Analysis and modeling of unsteady aerodynamics with application to wind turbine blade vibration at standstill conditions

Skrzypinski, Witold Robert

Publication date:
2012

Document Version
Publisher's PDF, also known as Version of record

Analysis and modeling of unsteady aerodynamics with application to wind turbine blade vibration at standstill conditions

By

Witold Skrzypiński (wisk@risoe.dtu.dk)

Ph.D. Thesis

DTU Wind Energy

February 2012

Abstract

Wind turbine blade vibrations at standstill conditions were investigated in the present work. These included vortex-induced and stall-induced vibrations. Thus, it was investigated whether the stand still vibrations are vortex-induced, stall-induced or a combination of both types. The work comprised analyzes based on engineering models and Computational Fluid Dynamics. Two-dimensional, three-degree-of-freedom, elastically-mounted-airfoil engineering models were created. These models aimed at investigating the effect of temporal lag in the aerodynamic response of an airfoil on the aeroelastic stability limits. The motivation for it was that the standard aerodynamics existing in state-of-the-art aeroelastic codes is effectively quasi-steady in deep stall. If such an assumption was incorrect, these codes could predict stall-induced vibrations inaccurately. The main conclusion drawn from these analyzes was that even a relatively low amount of temporal lag in the aerodynamic response may significantly increase the aerodynamic damping and therefore influence the aeroelastic stability limits, relative to quasisteady aerodynamic response. Two- and three-dimensional CFD computations included non-moving, prescribed-motion and elastically-mounted airfoil suspensions. 2D and 3D prescribed-motion CFD computations performed on a DU96-W-180 airfoil predicted vortex-induced vibrations at 90 degrees angle of attack at the frequency close to the stationary vortex shedding frequency predicted by 2D CFD computations. Significant discrepancies were observed between 2D and 3D computations around 25 degrees angle of attack. 3D computations predicted occurrence of vortex-induced vibrations while the wind speed necessary for the occurrence of stall-induced vibrations was predicted too high to occur in normal conditions. Analysis of the dynamic lift and drag resulting from 2D and 3D CFD computations carried out around 25 degrees angle of attack showed loops with the slopes of opposite signs indicating that further investigations are needed and that simple models in connection with aeroelastic simulations might not be sufficient to accurately predict vibrations at standstill conditions.

Resumé

Denne afhandling omhandler stilstandssvingninger af vindmøllevinger. Stilstandssvingningerne kan opdeles i hvirvelinducerede (vortex-induced) og separationsinducerede (stall-induced) svingninger. I denne afhandling er det undersøgt hvorvidt stilstandssvingninger af vindmøllevinger er af den hvirvelinducerede, af den separationsinducerede eller begge typer svingninger. Afhandlingen indeholder analyzer baseret på både ingeniørmæssige modeller og CFD (Computational Fluid Dynamics)-baserede modeller. Der er blevet opstillet to-dimensionelle ingeniørmodeller af en elastisk ophængt profilsektion med tre strukturelle frihedsgrader. Målet med disse modeller er at undersøge effekten af en tidsforsinkelse i det aerodynamiske respons på de aeroelastiske stabilitetsgrænser. Motivationen for denne undersøgelse er at aerodynamikken i de eksisterende "state-of-the-art" aeroelastiske beregningsmodeller effektivt er kvasistationær ved fuldt separerede strømninger. Konklusionen fra denne del af afhandlingens arbejde er at selv en relativt lille tidsforsinkelse i det aerodynamiske respons kan forøge den aerodynamiske dæmpning, og derved influere de aeroelastiske stabilitetsgrænser relativt til det der forekommer med et kvasistationært aerodynamisk respons. Ud over arbejdet med ingeniørmodellerne er der foretaget instationære to- og tre-dimensionelle CFD beregninger med såvel ikke bevæget, foreskrevet bevægelse og elastisk profilophængning. 2D og 3D CFD beregninger på et DU96-W-180 vingeprofil med foreskrevet harmonisk kantvis bevægelse indikerer hvirvelinducerede svingninger ved 90 graders indfaldsvinkel ved en frekvens tæt på hvirvelafkastningsfrekvensen fra 2D CFD beregninger med ikke-bevæget profilophængning. Der er fundet væsentlige uoverensstemmelser mellem 2D og 3D CFD beregninger omkring 25 graders indfaldsvinkel. 3D beregningerne foretaget i dette arbejde indikerer at muligheden for hvirvelinducerede svingninger på vindmøllevinger ikke kan afvises, hvorimod den fornødne fristrømshastighed for at separationsinducerede svingninger skulle kunne opstå er så høj at denne type svingninger baseret på disse beregninger forekommer usandsynlige. Analyze af dynamisk lift og drag fra 2D og 3D CFD beregninger foretaget omkring 25 graders angrebsvinkel viste loops med middelhældninger af forskelligt fortegn. Dette indikerer at yderligere undersøgelser er nødvendige, og at der skal udvises forsigtighed ved anvendelse af simple modeller i forbindelse med aeroelastiske simuleringer af vindmøller ved stilstand.

Acknowledgments

First of all, I would like to thank my main supervisor, Mac Gaunaa, for his guidance, patience and support over the last three years, especially for thorough reviews of every piece of written work I sent him.

I would not get even started with the CFD computations which became a substantial piece of my project if not the help of Niels Sørensen and Frederik Zahle who guided me through the intricate world of Computational Fluid Dynamics.

I would also like to thank Joachim Heinz for designing the CFD add-on for structural computations which helped me to understand some of the mechanisms involved in standstill vibrations.

The aforementioned computations were made possible by the use of the PC-cluster provided by Danish Center for Scientific Computing (DCSC) and the Risø-DTU central computing facility.

I would like to thank Nando Timmer for making the coordinates and aerodynamic characteristics of the DU96-W-180 airfoil used in this work available.

The study was funded by VEA, Risø DTU and by the project *EUDP-DanAero-II, Analysis*.

I would also like to express my gratitude to Aleksandra, for her love, patience, understanding and the great care taken of our new-born miracle, Marysia, allowing me to spend numerous evenings in the office.

I will always be grateful to my parents for their never-ending love and support (including making my stay in Denmark possible), my sisters (Iwona and Renata) because they've always been there for me, my dear friend Jurek for top-notch tutoring in physics and my grandmother who unfortunately passed away during my studies.

I also need to mention that the long hours spent in the office were certainly made more pleasant and productive because of the company of my dear friends and colleagues: Ivan, Leonardo, Joachim, Knud, Sri, Tilman, Carlo, David and Zuzana.

Podziękowania

Korzystając z okazji, chciałbym podziękować mojej kochanej żonie za pomoc, wyrozumiałość i wspaniałą opiekę nad Marysią, dzięki czemu mogłem spędzać na pisaniu doktoratu długie wieczorne godziny.

Chciałłbym wyrazić moją ogromną wdzięczność wobec rodziców za ich miłość i opiekę, w tym za umożliwienie mi pobytu i studiów w Danii.

Chciałbym podziękować również moim siostrom, Iwonie i Renacie, za to, że zawsze mogę na nie liczyć.

Dziękuję również mojemu drogiemu przyjacielowi Jurkowi za pomoc i zasianie we mnie zainteresowania mechaniką.

Nię mogę nie podziękować również mojej babci, która była pośród nas, kiedy zaczynałem studia doktorskie, a pamięć o której towarzyszy mi każdego dnia.

Table of Contents

1 Foreword

This dissertation is the outcome of a three-year Ph.D. study on *analysis and modeling of unsteady aerodynamics with application to wind turbine blade vibration at standstill conditions.* It is a partial fulfillment of the requirements for the degree of Doctor of Philosophy in Engineering at the Technical University of Denmark (DTU).

My work was supervised by Senior Scientist Mac Gaunaa (Risø DTU) and co-supervised by Program Leader Thomas Buhl, and Senior Scientists Christian Bak (Risø DTU) and Franck Bertagnolio (Risø DTU).

During these three years – from 2008 to 2011 – I worked at the Aeroelastic Design Programme (AED), Wind Energy Division (VEA), Risø DTU National Laboratory for Sustainable Energy.

This thesis is a collection of three papers submitted to international peer-reviewed journal, *Wind Energy*. It also comprises one paper that appeared in the proceedings of the EWEA 2010 international conference in Warsaw, and one to be submitted to the EWEA 2012 international conference in Copenhagen, that was granted an oral presentation. These papers are:

[I] Skrzypiński, Witold; Gaunaa, Mac: *Wind turbine blade vibration at standstill conditions – the effect of imposing time lag onto aerodynamic response*, in: Proceedings of *EWEC* 2010, Warsaw, Poland; April 2010

[II] Skrzypiński, Witold; Gaunaa, Mac: *Wind turbine blade vibration at standstill conditions – the effect of imposing lag on the aerodynamic response of an elastically mounted airfoil*; submitted to *Wind Energy* in July 2011

[III] Skrzypiński, Witold; Gaunaa, Mac; Sørensen, Niels; Zahle, Frederik; Heinz, Joachim: *Vortex-induced vibrations of a DU96-W-180 airfoil at 90 degrees angle of attack*; submitted to *Wind Energy* in January 2012

[IV] Skrzypiński, Witold; Gaunaa, Mac; Sørensen, Niels; Zahle, Frederik; Heinz, Joachim: *Self-induced vibrations of a DU96-W-180 airfoil in stall*; submitted to *Wind Energy* in January 2012

[V] Skrzypiński, Witold; Gaunaa, Mac; Sørensen, Niels; Zahle, Frederik: *Modeling of unsteady airfoil aerodynamics for the prediction of blade standstill vibrations*; to be submitted for EWEA 2012, Copenhagen, Denmark

The listed papers are included in the end of the thesis in their original form and layout. The papers are referred to throughout the thesis by the roman numbers. Further, the following chapters provide introduction, context and additional explanation to the aforementioned papers.

2 Work not directly included in the PhD thesis

One of the requirements for obtaining the PhD degree is that the student spends an equivalent of one semester working for the institution the student is employed at. The work carried out at that time does not necessarily need to be related to the PhD subject. During the course of the present PhD project, this requirement was fulfilled by processing the experimental data from the Danaero 2009 project [1]. In the experiment, the heavily instrumented LM 38.8 blade was installed on the 2MW NM80 wind turbine. The blade was equipped with strain gauges, accelerometers, microphones, four Pitot tubes and four pressure-tap sections. Measurements on that blade on which I worked were carried out between July and September 2009. The present work consisted of three parts, briefly described in the following chapters.

2.1 Calibration of measurement devices

Calibration of accelerometers, strain gauges and Pitot tubes used in the experiment was carried out in the present work and described in [1].

2.2 Correction of corrupted measurement data

During the experiment, a rupture of a hose inside the blade corrupted the measurement data from all the pressure taps. The hose was meant to supply control air to one of the valves in the blade. The valve, in turn, supplied purge air into the measurement system. After the valve lost its control pressure, it let the air through in an unknown manner. Fortunately, the defect was discovered before the following measurement day. However, it was not possible to reach the rupture point inside the blade. The furthest point reached was before the rupture and the control-pressure hose was blocked at this point. This restored the proper function of the measurement system at two inner sections of the blade. However, the two outer sections could not be repaired at that time.

The present work involved analysis of the corrupted data for the surface pressure measurements and recalibration that would enable further use of it. The approach was to find similar inflow and operational conditions before and after the rapture. Then, the differences in the measured data were analyzed in order to find a common relation between the correct and corrupted measurements. Such a relation was found and the data is now used for analyzing the MW rotor in operational conditions. Nevertheless, because of a significant level of noise in the stand still measurements, where the velocity and thereby the pressure is significantly lower than in operation, recalibration did not bring results of great accuracy.

2.3 Analysis of the data from standstill measurements

Standstill measurements carried out during the experiment were analyzed in the present work. Polars were extracted from pressure-distribution time series measured at one blade section. The angle-of-attack time series was computed in two alternative ways: with the aid of the yaw-misalignment measurement from the turbine's nacelle, and the wind-direction measurement from the nearby meteorology mast. The wind speed was also measured at both the nacelle and meteorology mast. Dynamic pressure was measured at the stagnation point at one blade section. Both the wind-speed and dynamic-pressure measurements were used alternatively for load normalization.

The quality of the resulting polars was, however, unsatisfactory. Simple error analysis was performed to indicate which of the measurements the main source of error was. While it was difficult to pinpoint a single faulty measurement (angle of attack, wind speed or pressure distribution), it appeared that an increase in quality of all the involved measurements, especially pressure distribution, was necessary to obtain reliable polars.

Note that the standstill measurements were not one of the main goals of the performed experiment, but an add-on meant to indicate whether the experimental setup designed for operational conditions is capable of performing reliable standstill measurements. Therefore, the measurement setup tuned for operational conditions showed relatively low signal to noise ratio as the involved wind speed values were lower than what the measurement setup was tuned for.

3 Introduction

Vibration of airfoils or whole wind turbine blades in standstill has recently received increased attention due to wind turbine failures potentially caused by blade vibration at standstill conditions. It is currently considered an important new subject of research although no one has officially reported any turbine failures due to standstill vibrations so far. A number of studies have approached different aspects of this problem. A short review of the key articles written on the subject is presented in one of the subsequent chapters. To the author's knowledge, standstill vibrations may potentially be one of two separate phenomena, i.e. vortex-induced vibrations (VIV) and stall-induced vibrations (SIV). A clear description of both phenomena is contained in the book by Sumer and Fredsøe [2], although in a context different than wind energy – namely, ocean engineering. Both types are also extensively described in the book by Dowell *et al.* [3] in the context of both aeroelasticity and civil engineering. Stall-induced vibrations are often referred to as galloping, stall flutter or bluff-body flutter. In stall-induced vibrations, a small velocity of the body causes an increase in the aerodynamic force in the direction of its motion, resulting in negative aerodynamic damping. The nature of vortex-induced vibrations is such that the body vibrates in a particular mode at a wind speed for which the von Karman frequency of vortex shedding coincides with the natural frequency of the structural mode. In such case, a resonance is created between the displacement and vortex shedding, resulting in an increase of vibrational amplitude.

One may argue that the distinction of vortex-induced and stall-induced vibrations is misleading because vortex-induced vibrations are also inherently related to stall. This is because a non-moving airfoil in steady flow will only shed vortices if it is stalling. On the other hand, an airfoil in attached flow will shed vortices if the aerodynamic loading on this airfoil changes. However, it is intuitive that vortex-induced vibrations of airfoils, if existent, occur in stall rather than as a result of a change of the aerodynamic loading in the attached flow. It is currently uncertain which of the two kinds of vibration is seen at wind turbines at standstill.

This thesis is organized as follows. In the next sections, a more detailed description of vortex-induced and stall-induced vibrations is presented. Then, the state of the art in modeling standstill vibrations of wind turbine blades is summarized. That summary is followed by a description of elastically-mounted-airfoil engineering models created as a part of the current work. The models were tools to analyze the influence that temporal lag in the aerodynamic response of an airfoil may have on the aeroelastic stability limits. The motivation for this part of the current work was to investigate whether the assumption of quasisteady aerodynamics in deep stall present in state-of-the-art aeroelastic codes may lead to inaccurate prediction of standstill vibrations. Description of these models and related results is followed by description of CFD computations that analyzed the risk of stall-induced and vortex-induced vibrations for airfoils. The computations were divided into 2D and 3D. Further, these were divided into non-moving, prescribed-motion and elastically-mounted airfoil computations. In the end, CFD analysis of dynamic aerodynamic response of an airfoil performing prescribed lead-lag and pitch oscillations in stall is presented and the most important conclusions are summarized.

Note that the present work simplified the problem of standstill vibrations by analyzing 2D and 3D airfoil sections which are not necessarily representative to the whole wind turbine blades. Some of the simplifications made in the present analysis were the lack of blade twist and taper as well as the lack of shear, turbulence and skew in the incoming flow. Further, the CFD computations were performed at a limited number of angles of attack while it is not known whether the conclusions presented in the end of this thesis would hold at other angles.

3.1 Vortex-induced vibrations

As it is stated in [2], a circular cylinder in steady flow will shed vortices if the Reynolds number exceeds 40. Then, the vortices form the so called von Karman vortex street which is a repeating pattern of vortices caused by unsteady flow separation. The dimensionless frequency at which the vortices are shed is denoted the Strouhal number:

$$St = \frac{f_v c}{V} \qquad (1)$$

where f_v is the frequency of vortex shedding expressed in Hertz, c is the characteristic length and V is the inflow velocity. Various factors influence St: Reynolds number, surface roughness, cross-sectional shape and incoming turbulence. A number of St values for various cross-sectional shapes is listed in the book by Blevins [4]. For example, approx. value of St for a cylinder from Re=40 to Re=$3 \cdot 10^5$ is 0.2. Above Re=$3 \cdot 10^5$, the value doubles and stays constant until Re=$2 \cdot 10^6$ from where it drops.

Vortex shedding results in periodic variation of the lift and drag. The lift oscillates with the frequency of vortex shedding while the drag oscillates with twice the vortex shedding frequency. If the oscillation frequency of either lift or drag coincides with the natural frequency of a structural mode, large-amplitude vibrations may be excited. A phenomenon associated with these vibrations is the so called lock-in, a thorough study of which is presented by Feng [5]. The lock-in occurs when the vortex shedding frequency described by the Strouhal number falls close to the frequency of a structural mode. Then, the vortex shedding frequency assumes the value of the vibration frequency which results in an increase of the vibration amplitude. As it is mentioned in [3], the width of the frequency band at which the lock-in occurs depends on the cross-sectional shape and is usually in the range of a few percent.

In the case of bluff bodies, the limit-cycle amplitude of the cross-flow vibration related to the oscillation of the lift is by an order of magnitude larger than the amplitude of the in-flow vibration related to the oscillation of the drag. The reasons are that the lift oscillations are of higher magnitude than the drag oscillations, and that the drag oscillation is of twice as high frequency as the lift oscillation. Therefore, according to Eq. (1), a lower flow speed and therefore loading is necessary for the onset of inline vibrations provided that the frequencies of structural modes in the inline and cross-flow directions are equal. The situation is, generally, different in the case of slender bodies like airfoils where the dominating direction of vibration is usually along the widest span of the body. This, in the case of airfoils, is in the chord-wise direction.

In order to visualize the mechanism of vortex shedding for airfoils, Figure 1 presents two snapshots of the pressure distribution around a section of a non-moving 3D DU96-W-180 airfoil at 90 degrees angle of attack, obtained using CFD which is explained in detail in chapter 6. The Reynolds number was $6 \cdot 10^6$ and the Strouhal number for the flow was 0.16. The bright areas in the figure indicate low pressure. The consecutive vortices shed from the leading and trailing edges of the airfoil are represented by low pressure areas and numbered.

One of major incidents in civil engineering associated with vortex-induced vibrations was the failure of the Brighton Chain Pier Bridge in 1836 [3].

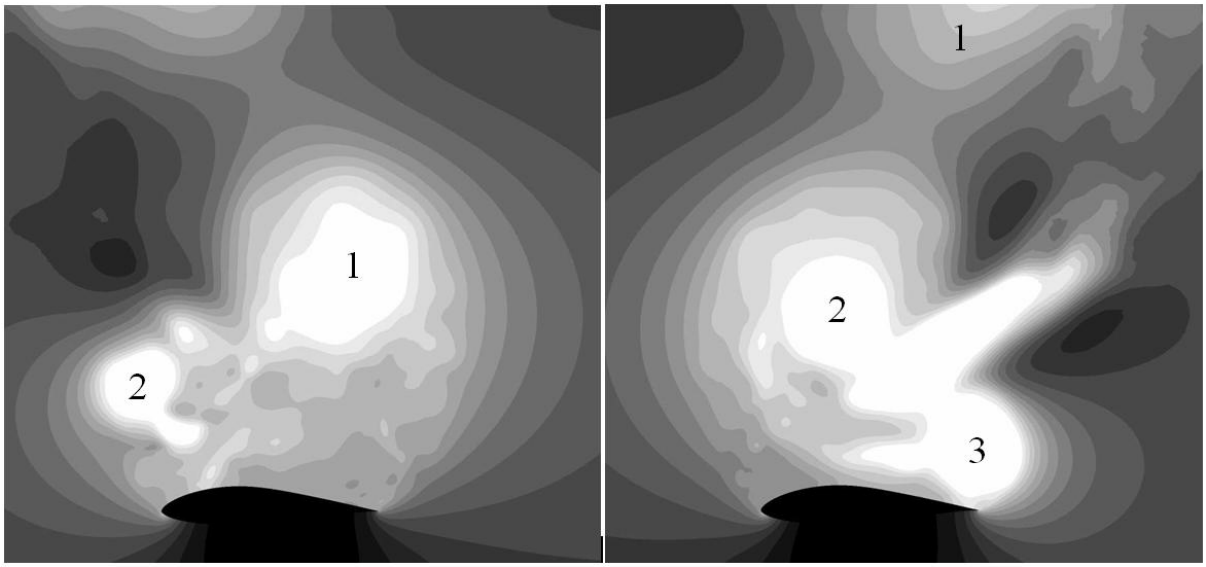

Figure 1: Snapshots presenting pressure distribution at a section of the 3D flow around the non-moving DU96-W-180 airfoil at 90 deg. angle of attack; white areas represent low pressure

3.2 Stall-induced vibrations

In the context of bluff bodies, stall-induced vibrations are often referred to as galloping. Note that there are two kinds of galloping: across-wind and wake. Only the former is addressed in the present work. As is pointed out in [2], the classic example of galloping is the vibration of ice-coated power lines. Dowell *et al.* [3] state that galloping of bluff bodies is governed primarily by quasi-steady aerodynamic forces.

Stall-induced vibrations in the context of airfoil structures are often referred to as stall flutter. As it is mentioned in [3], a number of structures could potentially experience this type of instability – from venetian blind slats, air deflectors and automobile spoilers to helicopter rotors and turbomachinery blades. Stall flutter was an issue during World War I as it occurred during sharp pull-up maneuvers of airplanes in combat. The problem was solved by stiffening the structures and avoiding dangerous maneuvers whenever possible. Dowell *et al.* [3] recognize that practical stall-flutter prediction for airfoils is either a semi-empirical or entirely empirical process as the dynamic aerodynamic forces are dependent on the frequency of airfoil vibration.

The following example describing stall flutter is adopted from Gaunaa and Larsen [6] and deals with an airfoil model exposed to steady flow. The setup of the presented model is shown in Figure 2. The aerodynamic response of the airfoil is assumed quasisteady. The airfoil is subject to rectilinear motion. The x axis is aligned with the free stream flow direction, as observed in the non-moving reference frame. The angle between the y axis and the oscillation direction, z, is denoted by β, positive clockwise. Linearization of the aerodynamic force in this example provides the equation for the aerodynamic damping.

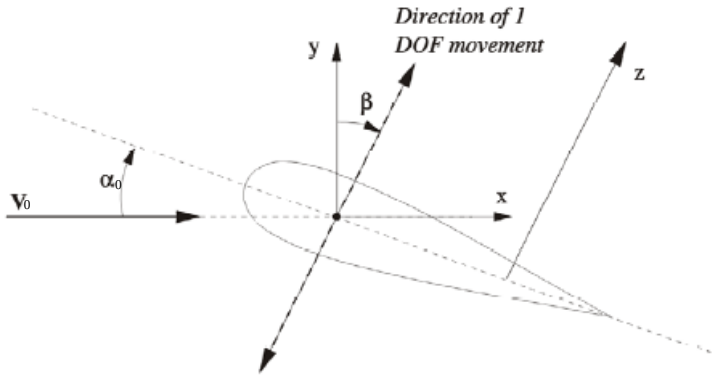

Figure 2: Definition of the angle of attack and angle of vibration; reproduced from Gaunaa and Larsen [6]

The lift and drag coefficients together with the coefficient of the force in the z direction are defined as:

$$C_l = \frac{l}{1/2\ \rho {V_{rel}}^2 c} \tag{2}$$

$$C_d = \frac{d}{1/2\ \rho {V_{rel}}^2 c} \tag{3}$$

$$C_z = \frac{F_z}{1/2\ \rho {V_{rel}}^2 c} \tag{4}$$

where ρ is density, V_{rel} is the relative flow speed and c is the chord length. The lift and drag are defined with respect to the relative inflow direction, V_{rel}.

The lift and drag coefficients may be linearized around α_0:

$$C_l(\alpha_{rel}) \cong C_l(\alpha_0) + \left.\frac{\partial C_l}{\partial \alpha}\right|_{\alpha_0} d\alpha = C_l + C_l' d\alpha \tag{5}$$

$$C_d(\alpha_{rel}) \cong C_d(\alpha_0) + \left.\frac{\partial C_d}{\partial \alpha}\right|_{\alpha_0} d\alpha = C_d + C_d' d\alpha \tag{6}$$

where the small change in the angle of attack due to airfoil motion is:

$$d\alpha = -\tan^{-1}\frac{\dot{y}}{V_0 - \dot{x}} = -\tan^{-1}\frac{\dot{z}\cos\beta}{V_0 - \dot{z}\sin\beta} \tag{7}$$

where V_0 is the steady inflow speed. Linearization of Eq. (7) results in:

$$d\alpha \cong -\frac{\dot{z}}{V_0}\cos\beta \tag{8}$$

Projecting both the lift and drag on the z axis yields:

$$F_z(\alpha_{rel}) = l(\alpha_{rel})\cos(\beta + d\alpha) + d(\alpha_{rel})\sin(\beta + d\alpha) \tag{9}$$

Substituting Eqs. (2), (3) and (4) into Eq. (9) yields:

$$C_z(\alpha_{rel}) = C_l(\alpha_{rel})\cos(\beta + d\alpha) + C_d(\alpha_{rel})\sin(\beta + d\alpha) \tag{10}$$

The relative velocity, V_{rel}, is influenced by the airfoil motion:

$$V_{rel}{}^2 = (V_0 - \dot{x})^2 + \dot{y}^2 = (V_0 - \dot{z}\sin\beta)^2 + (\dot{z}\cos\beta)^2 \quad (11)$$

Linearization of Eq. (11) yields:

$$V_{rel}{}^2 \cong V_0{}^2 - 2V_0 \sin\beta\, \dot{z} \quad (12)$$

Substituting Eqs. (5), (6), (8), (10) and (12) into Eq. (4) and introducing $\dot{z} = \dot{\tilde{z}}V_0$ yields:

$$F_z(\alpha_{rel}) \cong 1/2\,\rho c\big(V_0{}^2 - 2V_0{}^2 \sin\beta\,\dot{\tilde{z}}\big)\big[\big(C_l - C_l'\dot{\tilde{z}}\cos\beta\big)\cos(\beta - \dot{\tilde{z}}\cos\beta) + \big(C_d - C_d'\dot{\tilde{z}}\cos\beta\big)\sin(\beta - \dot{\tilde{z}}\cos\beta)\big] \quad (13)$$

After linearizing the terms $\cos(\beta - \dot{\tilde{z}}\cos\beta)$ and $\sin(\beta - \dot{\tilde{z}}\cos\beta)$ around $\dot{\tilde{z}} = 0$ by means of Taylor series expansion, removing higher-order terms and non-dimensionalizing with $\frac{1}{2}\rho V_{rel}{}^2 c$:

$$C_z(\alpha_{rel}) \cong C_z(\alpha_0) - [\sin\beta\cos\beta\,(C_l + C_d') + \cos^2\beta\, C_l' + (1 + \sin^2\beta)C_d]\dot{\tilde{z}} \quad (14)$$

Eq. (14) my be written as:

$$C_z(\alpha_{rel}) \cong C_z(\alpha_0) - C_{DA}\dot{\tilde{z}} \quad (15)$$

where C_{DA} is the dimensionless linear aerodynamic damping coefficient, defined as:

$$C_{DA} = \sin\beta\cos\beta\,(C_l + C_d') + \cos^2\beta\, C_l' + (1 + \sin^2\beta)C_d \quad (16)$$

When C_{DA} is negative, the aerodynamic damping of the system is negative which means that energy is transferred from the flow to the system. Therefore, the necessary condition for the occurrence of stall-induced vibrations reads:

$$\sin\beta\cos\beta\,(C_l + C_d') + \cos^2\beta\, C_l' + (1 + \sin^2\beta)C_d < 0 \quad (17)$$

If Eq. (17) is satisfied, depending on the amount of structural damping, the system may experience stall-induced vibrations. Eq. (16) is used extensively in the present work. The assumption of quasisteady aerodynamics under which Eq. (16) is derived may be a limitation as in stall-induced vibrations of airfoils the aerodynamic forces are dependent on the frequency of airfoil vibration [3]. The smaller the value of the reduced frequency ($k=\omega c/2V_0$) is, the more accurate Eq. (17) becomes.

If the direction of rectilinear vibration is perpendicular to the incoming flow, which is the case with bluff bodies or airfoils at 90 deg. angle of attack, β is zero and Eq. (17) reduces to so called den Hartog condition for galloping, described in [2,3], or the necessary condition for galloping:

$$C_l' + C_d < 0 \quad (18)$$

Eq. (18) states that stall-induced vibrations of bluff bodies may occur when the sum of the slope of the lift coefficient and the drag coefficient is negative. However, the actual occurrence of stall-induced vibrations in the case of bluff bodies where the aerodynamic forces can be considered quasi-steady is dependent on the amount of structural damping in the system. In the

case of airfoils, it may also dependent on the temporal lag in the aerodynamic response or non-linear effects.

4 State of the art in modeling standstill vibrations of wind turbine blades

The present chapter presents the state of the art in prediction of and modeling standstill vibrations of wind turbine blades. It shows a brief collection of papers that are closely related to the present work, in terms of their subject, findings or because they provided inspiration for it. Note that the number of presented paper is relatively small. This is because the subject of wind turbine blade vibrations at standstill conditions is new and a rather limited number of papers have been written on it so far.

4.1 Engineering models for the prediction of stall flutter

Gaunaa and Larsen [6] propose a two-dimensional engineering model for the prediction of stall flutter under the assumption of quasi-steady aerodynamics. The model was discussed in the preceding chapter. They also compare the dimensionless linear aerodynamic damping coefficient, C_{DA}, of a two-dimensional airfoil section with the corresponding results of three-dimensional aeroelastic computations performed with the predecessor of HAWC2. The results of HAWC simulations represent a whole isolated wind turbine blade including twist, taper, varying profiles and structural damping. In their HAWC simulations, the turbine including the shaft is stiff, a single blade is elastic, the flow comes from all directions, all azimuthal positions of the rotor are considered, dynamic-stall model is disabled and the angle of attack is evaluated at the 75% blade radius. The HAWC results are expressed in terms of the logarithmic decrement of the amplitude of vibration. Note that at high angles of attack, where the flow is fully separated, the dynamic aerodynamic response predicted by HAWC2 and its predecessor is quasisteady. The comparison is presented in Figure 3.

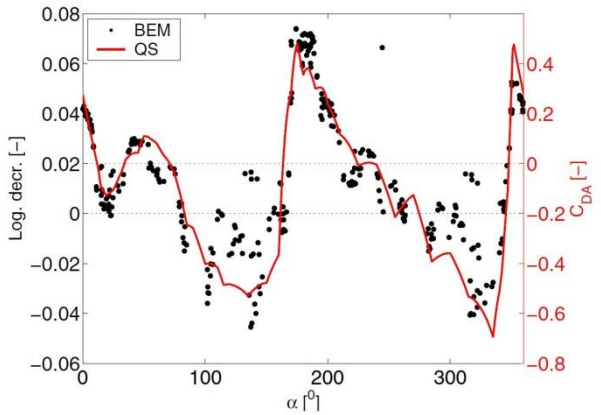

Figure 3: Comparison of the dimensionless linear aerodynamic damping coefficient, C_{DA}, of a two-dimensional airfoil section with the corresponding results of aeroelastic computations performed with HAWC expressed in therms of the logarithmic decreament of the amplitude of vibration; reproduced from Gaunaa and Larsen [6]

The curves representing the aerodynamic damping coefficient and the logarithmic decrement are in good agreement in the whole 360° ranges of angle of attack, even though a 2D airfoil section is not necessarily representative of a complex 3D blade. This indicates that some of the aerodynamic characteristics of whole blades, as simulated in an aeroelastic code, may be modeled by simple 2D engineering models. It also confirms that the dynamic aerodynamic response predicted by the aeroelastic code in deep stall is quasisteady.

Further, Gaunaa and Larsen present – based on Eq. (16) – how the lift and drag coefficient and their slopes contribute to the aerodynamic damping. The highest damping is associated with the drag coefficient, C_d, while the lowest with the slope of the lift coefficient, C_l'. In the other words, the slope of the lift coefficient subtracts the most from the aerodynamic damping. Gaunaa and Larsen also show that the changes made in the steady polars below the level of their accuracy may significantly change the values of the aerodynamic damping predicted by Eq. (16), even completely removing the negative damping in the whole 360° range of angles of attack. Assuming that Eq. (16) represented the real-life phenomena relatively good and that 2D modeling was representative of 3D blade aerodynamic characteristics, that would suggest the need for more accurate measurements of polars in deep stall. On the other hand, such measurements are problematic and tunnel-dependent because of wind tunnel effects, especially pronounced at high angles of attack.

Similar study to that of Gaunaa and Larsen was carried out by Hansen [7] who derives the equation for the aerodynamic damping using a different frame of reference than Gaunaa and Larsen:

$$C_{DA} = \sin(2\theta - 2\phi_0)\,(C_l + C_d') + [1 - \cos(2\theta - 2\phi_0)]C_l' + [3 + \cos(2\theta - 2\phi_0)]C_d \qquad (19)$$

The inflow angle, ϕ_0, and the angle of vibration, θ, used in Eq. (19) are defined in Figure 4 (left). Using his equation, Hansen presents different ranges of the direction of vibration relative to the inflow direction. Given by the three terms in Eq. (19), these ranges are presented in Figure 4 (right). The arrows indicate whether the corresponding term 'pushes' or 'pulls' the direction of vibration. The term 'pull' refers to a specific term enhancing the vibration at the corresponding direction while the term 'push' refers to a specific term mitigating the vibration at the corresponding direction. The drag pushes the direction of vibration away from the inflow direction. The negative gradient of the lift pulls the direction of vibration perpendicular to the inflow direction. The positive sum of the lift and drag coefficient pulls the vibration direction towards 45° angle relative to the inflow direction.

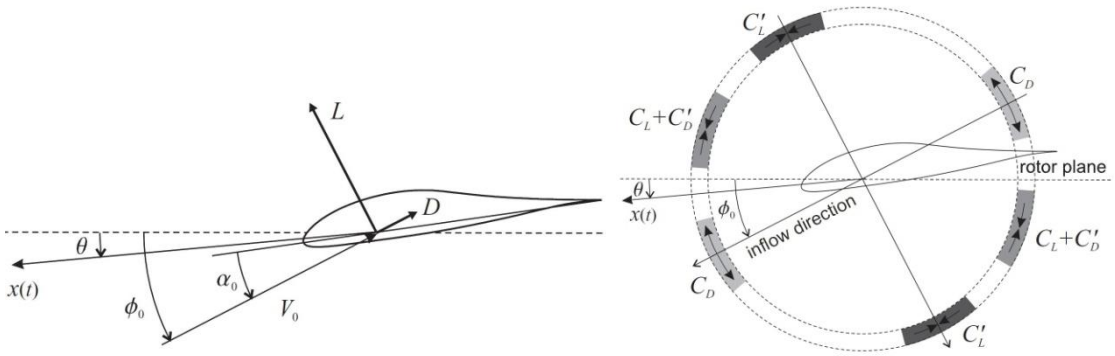

Figure 4: (left) Definition of the inflow angle, ϕ_0 , and the angle of vibration, θ; (right) different ranges of the direction of vibration relative to the inflow direction; reproduced from Hansen [7]

Hansen outlines three most important parameters governing the risk of stall flutter: airfoil characteristics, structural damping and the direction of vibration. He also mentions what was brought up in some of the other papers, i.e. the importance of the determination of the dynamic aerodynamic response in deep stall.

4.2 Prediction of standstill vibrations with an aeroelastic code

Aeroelastic simulations of wind turbine blades at standstill conditions, inspired by the work of Gaunaa and Larsen, were also carried out by Buhl [8]. Buhl extends the work of Gaunaa and Larsen by including two new turbine configurations, on top of the simulations with the isolated flexible blade: flexible rotor (including flexible shaft) and stiff tower, and a fully flexible turbine. In all the simulations, one of the blades is in the vertical position pointing upwards. The simulations cover the whole angle-of-attack range of the blade in the vertical position. As long as the angle of attack defined at 75% blade radius is varied by collectively pitching the blades which assures equal angles of attack at every blade, the three configurations mentioned above return very similar results in terms of the aeroelastic stability limits. The situation is different when the angle of attack of the blade in the vertical position is varied through yawing the whole turbine. This results in the expansion of one of the angle-of-attack regions corresponding to edgewise vibrations of the blade in the vertical position.

Comparison of the damping of the blade in the vertical position expressed by logarithmic decrement, δ, with and without the dynamic stall model [12], plotted as functions of the angle of attack is presented in Figure 5.

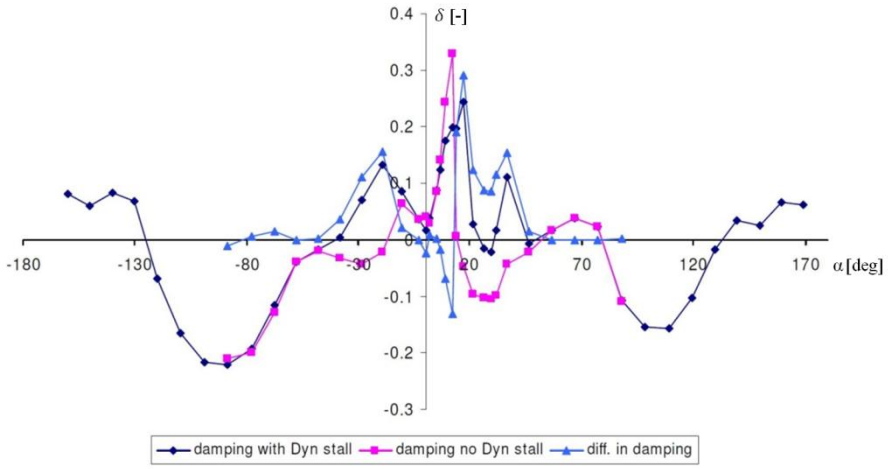

Figure 5: Comparison of the damping of the blade in the vertical position with and without the dynamic stall model included in the simulations; x axis corresponds to the angle of attack defined at 75% blade radius; reproduced from Buhl [8]

By performing simulations both with and without the dynamic stall model, Buhl shows that the flow over the entire blade is fully separated from approx. 50° angle of attack and upwards, and from approx. -40° angle of attack and downwards. By doing these simulations, Buhl also confirms that the dynamic stall model has no effect on the simulations in deep stall. The reason for it is that the separation point is used for modeling the dynamics of stall. Simulations carried out with different amounts of inflow turbulence level show a small dependency of the aeroelastic stability limits on the turbulence level.

Buhl concludes that if the problem of standstill vibrations is existent in real life, active pitch or yaw control could be adopted. On the other hand, if the problem is purely numerical, the models in the aeroelastic codes must be refined e.g. by implementing a model for dynamic aerodynamic response in deep stall.

4.3 Modeling phenomena related to vortex shedding

The subject of dynamic aerodynamic response in deep stall is taken up by Riziotis *et al.* [9] who also point out that the state-of-the art dynamic stall models [10,11,12] are not tuned to handle standstill conditions. These models are meant to provide the dynamic loading at angles of attack not higher than those at which the full flow separation occurs. However, in deep stall these models suppress wake induced hysteresis effects by assuming either quasisteady or inviscid aerodynamic response.

Riziotis *et al.* use a vortex-type deep-stall model to predict the aerodynamic damping characteristic of a stationary blade in the vicinity of +/- 90 deg. In their work, massive flow separation is taken into account by the use of so called 'double wake' concept in which vorticity is released to the wake not only from the trailing edge but also from the leading edge. The interaction of the two vortex sheets causes successive generation of vortices of opposite sign that form the von Karman vortex street. In order to reduce the computational effort, even when dealing with a full blade, a strip-like approach is employed. This means that each blade strip is considered two-dimensional and solved independently from all other strips. This approach neglects the interaction between the vortices released from different strips. In order to reduce the computational effort further, the hybrid wake concept is applied in which the contribution of the far wake, once calculated, is kept constant. All vortices that enter the far wake are eliminated which keeps the extent of the wake and the number of active vortices constant. The grid covering the near wake extends two to three diameters downstream and so does the grid covering the far wake.

In the computations, the blade is excited through variation of the pitch in the frequency of a certain mode. Then, the blade free vibration is analyzed by determination of the decay envelope signal of the transient response of blade deflections. The Hilbert transform of real valued time series is used for calculating directly the decaying signal. An example of the application of Hilbert method is presented in Figure 6.

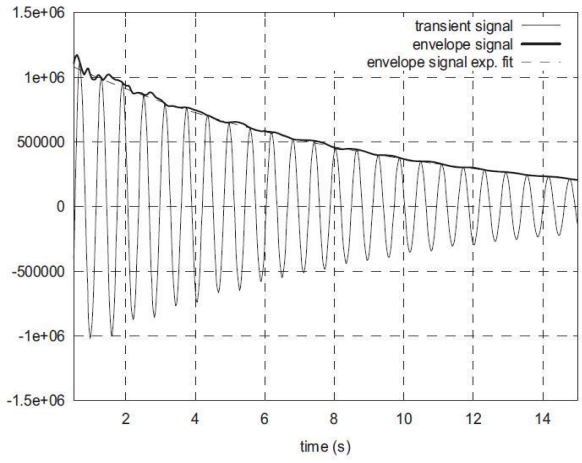

Figure 6: Example of the application of Hilbert damping identification method; reproduced from Riziotis *et al.* [9]

The results of the time domain aeroelastic simulations carried out with the vortex model are compared with the results of the linear eigenvalue analysis performed using steady-state aerodynamics. The vortex model is only applied in the inflow-angle ranges of [-120° -60°] and [60° 120°] because it is only applicable in the ranges where the flow is fully separated and the effect of airfoil thickness is negligible. The damping values of the first edgewise blade mode are

presented in Figure 7 in terms of the logarithmic decrement. At a given inflow angle, the damping predicted by the vortex model covers a range between the minimal and maximal values because of the non-linear character of the system. The time series predicted by the vortex model do not decay exponentially. Therefore, the exponential fit to the non-linear envelope is carried out several times for each time series.

Riziotis *et al.* report that the damping predicted by the vortex model is slightly higher than that predicted by the linear eigenvalue analysis in the inflow angle range of [75° 90°]. On the other hand, the damping predicted by the vortex model in the negative inflow-angle region is generally lower than that predicted by the linear eigenvalue analysis. This is pronounced at -120° inflow angle. At -60° the vortex model predicted limit cycle behavior that – according to Riziotis *et al.* – could under turbulent inflow conditions result in undamped edgewise vibrations of the system. Riziotis *et al.* conclude that the results indicate that the flow is highly non-linear and that damping of the system is not purely of viscous type.

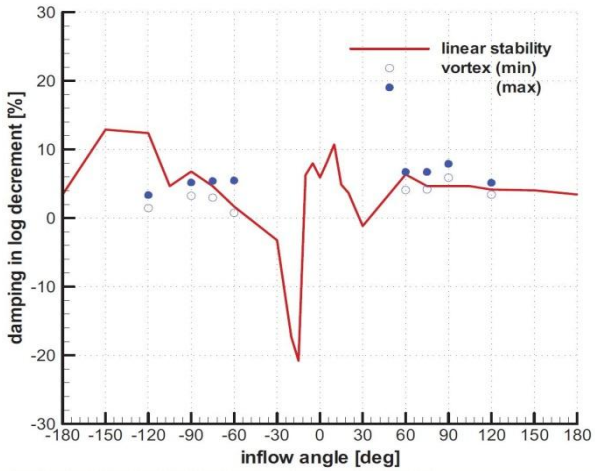

Figure 7: Damping of the first edgewise blade mode (linear vs. non-linear); reproduced from Riziotis *et al.* [9]

The authors of [9] do not explicitly discuss the possibility of the occurrence of vortex-induced vibrations even though large-scale vortex dynamics are resolved by their code. For a given blade and inflow angle, occurrence of vortex-induced vibrations largely depends on the inflow velocity which determines the frequency of vortex shedding. If the frequency of vortex shedding was close to the frequency of the first edgewise mode, lock-in could occur and vortex-induced vibrations could be induced.

The problem of vortex-induced vibrations is taken up by Bertagnolio *et al.* [13] who show that an aeroelastic code does not resolve load fluctuations related to vortex shedding (self-induced turbulent wake) that are clearly visible at wind tunnel measurements and 3D DES CFD numerical experiments. Such a comparison is reproduced in Figure 8 where the lift-coefficient time series obtained by the aeroelastic code HAWC2 [14] is validated against wind tunnel experiments performed at the National Renewable Energy Laboratory (NREL). As it is seen in the figure, independent of the intensity of turbulent inflow, HAWC2 is not able to resolve the high-frequency, high-amplitude fluctuations of the lift coefficient in static-stall. Analytical models developed to take into account specific unsteady wake flow features such as vortex shedding at lock-in are mainly related to bluff-body aerodynamics.

Bertagnolio *et al.* develop a model intended to reproduce unsteady effects at static stall originating from the self-induced turbulent wake of an airfoil. Due to certain limitations

discussed later, the model is not intended as quantitatively highly accurate while it is the first step towards obtaining this goal. In the model, the aerodynamic forces are described by their statistical properties. The input data may be extracted from measurements or 3D DES CFD computations. Note that stalled flows are inherently three-dimensional while in the model, each spanwise two-dimensional section of the blade where aerodynamic forces are modeled is independent of others.

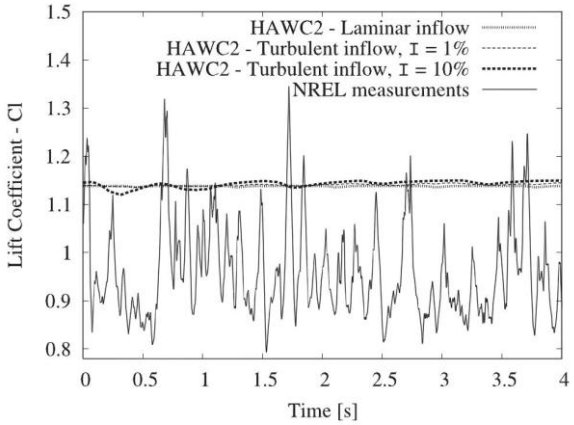

Figure 8: Time series of Cl from HAWC2 simulations without the static stall model compared with a wind tunnel experiment carried out at NREL; reproduced from Bertagnolio *et al.* [13]

The stochastic time series accounting for the effects of the self-induced turbulent wake is superimposed onto the time series of the aerodynamic forces predicted by an aeroelastic code. Another limitation may be that in the model, no interaction between the motion of the airfoil and the modeled unsteady effects is present. The drag and pitching moment are simulated by a conditional simulation technique in which the lift time series acts as the conditioning parameter. The cross correlations between the different forces are accurately described. The technique may be described as means to simulate unknown data at certain points when some data is known at other points, using the cross correlation between the data. As Bertagnolio *et al.* point out, it may be a limitation of this conditional simulation technique that it is only valid if the stochastic processes at work are Gaussian. However, large skewness in the probability distribution of low pressures typically observed in the separated flow regions can exist.

Bertagnolio *et al.* mention that the self-induced turbulent wake of an airfoil in stall is mostly characteristic of the flow and relatively independent of the airfoil itself. However, the characteristics of the turbulent wake are significantly dependent on the angle of attack which is taken into account in the model. Therefore, the measurements or CFD computations used as input to the model need to be performed at a number of distinct angles of attack. Note that the airfoil shape is decisive in defining both the onset of stall and the type of stall that occurs. Another important feature of the model is that it takes the spanwise load coherence into account. If no spanwise coherence was present, a large number of spanwise discretization points would result in mutual cancellation of the loads and constant loading when averaged over the whole blade span.

The stochastic stall model is validated by a comparison of the HAWC2 simulations including the model with the measurements of an operating rotor carried out in the NREL/NASA Ames Unsteady Aerodynamic Experiment Phase VI [15]. The HAWC2 simulations are also compared with corresponding 3D DES CFD rotor computations performed with EllipSys 3D [25,26,27]. Bertagnolio *et al.* report that both the experimental results and CFD computations show highly

fluctuating aerodynamic forces on the blades while HAWC2 simulations without the stochastic stall model predict nearly constant aerodynamic forces. However, the corresponding HAWC2 simulations with the stochastic stall model predict fluctuations corresponding to those seen in the measurements and CFD computations. Note that the frequency of vortex shedding predicted by the HAWC2 simulations including the model is slightly higher than that predicted by the measurements and CFD computations. Bertagnolio *et al.* discuss the possible reasons of this difference.

To further analyze the effect the model has on the results of aeroelastic simulations, several simulations are performed with the aeroelastic code HAWC2 within which the proposed model is implemented. Among others, the NREL 5MW reference offshore wind turbine [16,17] is modeled at parked condition with feathered blades. For this specific turbine, at this specific condition, for a specific range of yaw angles, aeroelastic computations predict negative aerodynamic damping of the first edgewise blade mode. The considered blade is in the vertical position. The predicted negative aerodynamic damping is associated with stall-induced vibrations. The inflow velocity in the simulations performed by Bertagnolio *et al.* is such that the frequency of stationary vortex shedding coincides with the frequency of the first structural edgewise blade mode. The yaw angle is such that an aeroelastic code without the static stall model would predict the negative aerodynamic damping of the first edgewise blade mode. The results of the computations performed by Bertagnolio *et al.* are presented in Figure 9 where the amplitude envelopes of the edgewise tip deflection from the HAWC2 simulations with the static stall model are compared with the results of the simulations performed without the model. The simulations with the model are carried out with and without the ambient turbulence. All the presented computations predict edgewise blade vibrations. However, the rates of the amplitude growth and the shape of the amplitude envelopes differ significantly. The oscillation amplitudes predicted in the simulations without the static stall model grow relatively slowly and the shape of the amplitude envelope might indicate exponential growth. The oscillation amplitudes predicted in the simulations with the static stall model grow rapidly and reach a limit-cycle oscillation of approx. 2 m displacement amplitude. The ambient turbulence level does not seem to have significant influence on the vortex-induced vibrations.

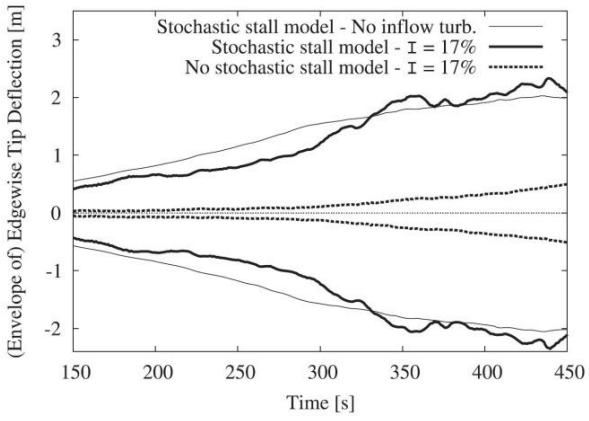

Figure 9: Amplitude envelopes of the edgewise tip deflection oscillations comparing HAWC2 simulations with and without the static stall model; reproduced from Bertagnolio *et al.* [13]

Bertagnolio *et al.* conclude that generally there is a good agreement between the results obtained with the stochastic stall model implemented into HAWC2 and the measurements of the full operating rotor as well as the corresponding 3D CFD computations. There is a slight discrepancy between the frequencies at which vortex shedding is predicted. The simulations of

the megawatt-sized wind turbine at park condition carried out with HAWC2 including the stochastic stall model show rapid growth of vortex-induced vibrations of one of the blades.

By looking at the shapes of the amplitude envelopes, one could wonder whether the stall-induced vibrations predicted in the simulations without the static stall model could, after a sufficiently long time, reach displacement amplitudes larger than vortex-induced vibrations predicted in the simulations with the static stall model.

The subject of self-induced turbulent wake is also taken up by Hansen [18] who investigates the effect it has on the stall-flutter limit of a two-dimensional airfoil section with one degree of freedom subject to quasi-steady aerodynamic forces. In his engineering model, the self-induced turbulent wake is modeled by stochastic fluctuations of the inflow velocity. The turbulent velocities are modeled independently from the airfoil motion assuming that the related stochastic processes are independent of inflow velocity and small changes in the angle of attack. Hansen also points out that the length scales of the self-induced turbulent structures in deep stall are up to the order of the chord length.

Figure 10 presents the most frequent amplitude of the limit-cycle oscillation as a function of the relative direction of vibration which is the angle between the direction of the free stream and the direction of rectilinear vibration, positive clockwise.

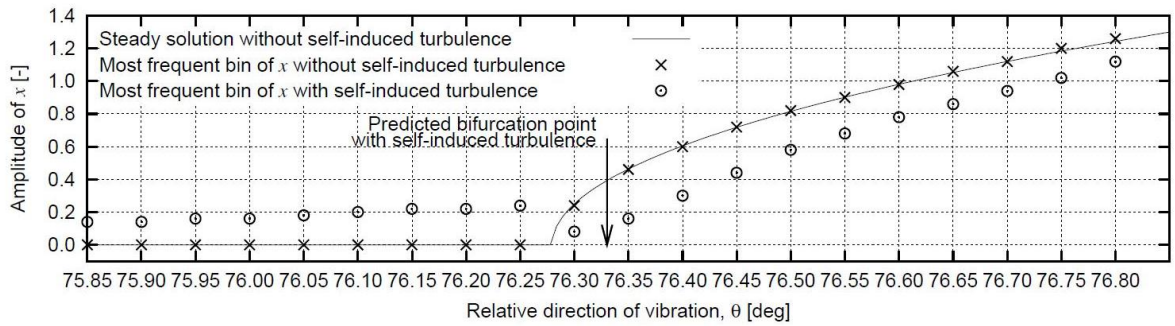

Figure 10: Comparison of the limit-cycle amplitudes of the engineering model with and without self-induced turbulence; reproduced from Hansen [18]

The numerical values of the amplitudes of limit-cycle oscillations without the self-induced turbulent wake are well predicted by the steady state solution proposed by Hansen. The self-induced turbulence increases the limit-cycle amplitudes below the stability limit while it decreases the amplitudes above the stability limit. The self-induced turbulent wake slightly delays the stability limit which is marked in the figure with the arrow.

Hansen concludes that the results show that the self-induced wake may add very small damping to the critical blade mode, if it is modeled as a stochastic inflow of the quasi-steady aerodynamic model. He also points out that more advanced models for the aerodynamic forces in deeps stall should be considered, possibly including a model for the dynamic aerodynamic response in deeps stall.

5 Elastically-mounted-airfoil aerodynamic model

The previous chapters introduced vortex-induced and stall-induced standstill vibrations and described the state of the art in prediction of and modeling these vibrations. The following chapters briefly summarize the methods used and results of the present work described in more detail in the five enclosed papers:

5.1 The effect of imposing time lag on the lift [I]

One of the conclusions drawn by Buhl [8] and Hansen [7,18] is that the dynamic aerodynamic airfoil loading in deep stall should be investigated as the assumption of quasisteady aerodynamics present in the state-of-the-art aeroelastic codes may be insufficient. An attempt to include temporal lag in the aerodynamic response of a wind turbine blade in deep stall is made by Riziotis *et al.* [9] who conclude that their vortex-type deep-stall model predicts either higher or lower aerodynamic damping than the model based on quasisteady aerodynamics, depending on the angle of attack. The part of the present work described in [I] analyzed whether temporal lag in the aerodynamic response of a simple engineering two-dimensional elastically-mounted-airfoil model may significantly influence the aeroelastic stability limits in deep stall predicted by this model. This was achieved by imposing different amounts of lag on the lift force of both nonlinear and linearized two-dimensional, three-degree-of-freedom engineering models of an elastically mounted airfoil. The models allowed for different inflow angles. The nonlinear model was solved in the time domain. The linearized model, in turn, was solved in both the time and frequency domains. The edgewise damping ratios were drawn from the analyzes of both models and compared.

5.1.1 Method

The setup used in this work was originally presented by Buhl *et al.* [19] together with the parameter values – such as airfoil mass – which were discussed in [I]. The setup is presented in Figure 11 where T and N are the chordwise and normal-to-chord aerodynamic force components.

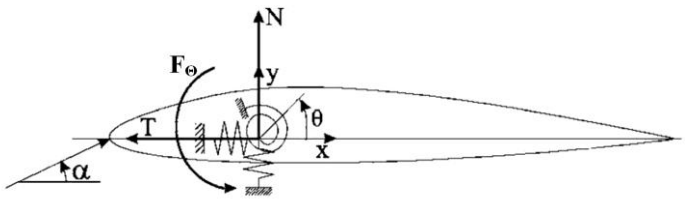

Figure 11: 2D 3-DOF aeroelastic model; reproduced from Buhl *et al.* [19]

F_Θ is the aerodynamic moment around the hinge point, positive counter-clockwise. The angle of attack is denoted by α. The degrees of freedom of the 2D aeroelastic system with linear stiffness and damping are denoted by x, y and Θ. The aforementioned system is governed by the following equations of motion:

$$\begin{aligned} M\ddot{X} + c_x\dot{X} + k_xX &= F_X + Ml\dot{\Theta}^2\cos(\Theta+\Theta_{geom}) + Ml\ddot{\Theta}\sin(\Theta+\Theta_{geom}) \\ M\ddot{Y} + c_y\dot{Y} + k_yY &= F_Y + Ml\dot{\Theta}^2\sin(\Theta+\Theta_{geom}) - Ml\ddot{\Theta}\cos(\Theta+\Theta_{geom}) \\ \ddot{\Theta}(I_{cg}+Ml^2) + c_\Theta\dot{\Theta} + k_\Theta\Theta &= F_\Theta + Ml\ddot{X}\sin(\Theta+\Theta_{geom}) - Ml\ddot{Y}\cos(\Theta+\Theta_{geom}) \end{aligned} \quad (20)$$

where Θ_{geom} is the angle between the x axis and the line through the elastic axis and the center of gravity when the profile is in the equilibrium state without the aerodynamic forces involved. F_X and F_Y are the aerodynamic force components. Further, l is the distance between the center of gravity and the hinge point, assuming that the center of gravity is behind the hinge point. The mass of the airfoil section is denoted by M, and the moment of inertia around the center of gravity is denoted by I_{cg}. Note that Figure 11 differs from the corresponding figure presented in [I].

In this work, the lift was governed by a model that may presumably reflect behavior of a wind turbine blade vibrating in deep stall better than a model assuming quasi-steady aerodynamics. The dynamic lift coefficient was calculated as the static lift coefficient at an effective angle of attack:

$$C_L^{Dyn} = C_L^{St}(\alpha_E) \tag{21}$$

The effective angle of attack, α_E, is a lagged angle of attack defined as:

$$\alpha_E = \alpha_{3/4}(1 - A_1 - A_2) + x_1 + x_2 \tag{22}$$

where $\alpha_{3/4}$ is the angle of attack as observed at the three-quarter chord. The use of the effective angle of attack in the model, and the way it is expressed resembles the dynamic stall model described by Hansen *et al.* [12]. A_1 and A_2 constitute the first half of the parameters defined in the subsequent description of the aerodynamic time lag. Further, x_1 and x_2 are the aerodynamic-state variables governed by the differential equations:

$$\dot{x}_i + T_u^{-1} b_i x_i = b_i A_i T_u^{-1} \alpha_{3/4} \qquad i = 1, 2 \tag{23}$$

where b_i constitute the second half of the parameters used for defining the aerodynamic time lag. The time-varying parameter, T_u, equals:

$$T_u = c/2V_{rel} \tag{24}$$

where c is chord length and V_{rel} is airflow velocity relative to the airfoil.

The choice of parameters – namely: A_1, A_2, b_1, b_2 – characterizes a specific temporal behavior of the aerodynamic model. Such a choice is visualized by means of the unit response function:

$$\varphi = 1 - A_1 e^{-b_1 s} - A_2 e^{-b_2 s} \tag{25}$$

where s is non-dimensional time, $t\frac{V_0}{c}$. The faster a particular function converges to 1, the closer the respective aerodynamic response is to quasi-steady. The choice of four exemplary parameter sets used for this study is presented in Figure 12, together with the respective parameters of the aerodynamic response function. The parameters of quasi-steady response function effectively bypass the lagging effect of the dynamic model. This corresponds to the aerodynamic response one would get from aeroelastic codes in deep stall. Aerodynamic response function No. 1 is an approximate representation of a thin airfoil's inviscid response [20]. Therefore, it is most likely faster than the response of a real-life airfoil in deep stall. However, the actual aerodynamic response of such an airfoil is currently unknown. The aerodynamic response functions No. 2 and No. 3 are both significantly slower than the response function No. 1. Function No. 3 is initially the same as No. 2. However, it introduces an overshoot in the response. The aeroelastic behavior, including damping characteristics, of the 3-DOF aeroelastic system depends on the

aforementioned response functions which, in turn, are defined by the parameters A_1, A_2, b_1, b_2. Functions No. 2 and No. 3 were not meant to represent any particular real-life aerodynamic system but are chosen to investigate how the aerodynamic damping is dependent on the shape of a response function.

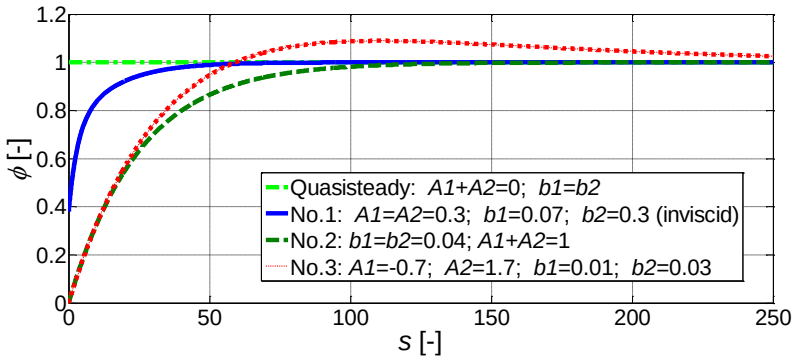

Figure 12: The four response functions corresponding to the aerodynamic-parameter sets

The main concern of the current investigation was stability analysis of the system at different angles of attack defined with respect to the free stream. For this reason, the aforementioned time-domain analysis of the nonlinear system was aided by both time-domain and eigenvalue analyzes of a linearized system. Eigenvalue analysis is more effective for investigating the aeroelastic stability limits of the system from both, a computational and practical perspective. It saves computational time and allows for easier interpretation of results than the time-domain analysis does. The linearized system of equations of motion, Eq. (1), is presented below:

$$\begin{aligned} M\ddot{X} + c_x\dot{X} + k_xX &= F_X^{lin} + Ml\ddot{\Theta}\sin(\Theta_{geom}) \\ M\ddot{Y} + c_y\dot{Y} + k_yY &= F_Y^{lin} - Ml\ddot{\Theta}\cos(\Theta_{geom}) \\ \ddot{\Theta}(I_{cg} + Ml^2) + c_\Theta\dot{\Theta} + k_\Theta\Theta &= F_\theta^{lin} + Ml\ddot{X}\sin(\Theta_{geom}) - Ml\ddot{Y}\cos(\Theta_{geom}) \end{aligned} \tag{26}$$

where F_X^{lin} and F_Y^{lin} are the aerodynamic force components. F_θ^{lin} is the aerodynamic moment. All components were linearized around equilibrium positions which depend on the inflow angle.

To obtain a fully linearized model, the aerodynamic coefficients were also linearized. The lift coefficient was expressed as:

$$C_L^{lin} = C_L^0 + \frac{dC_L^0}{d\alpha}\alpha_E^1 \tag{27}$$

where C_L^0 is the lift coefficient at the equilibrium state. Further, α_E^1 is a small perturbation of the effective angle of attack from its equilibrium value, calculated as:

$$\alpha_E^1 = \alpha_{3/4}^1\phi(0) + x_1^1 + x_2^1 \tag{28}$$

where $\phi(0)$ is the initial value of the respective unit response function. Variables x_1^1 and x_2^1 are small perturbations of the aerodynamic-state variables, x_i, around their equilibrium values. They were calculated by linearization of Eq. (23):

$$\dot{x}_i^1 + T_0^{-1}b_ix_i^1 = b_iA_iT_0^{-1}\alpha_{3/4}^1 \qquad i = 1,2 \tag{29}$$

where $T_0 = c/(2U_0)$. The variable $\alpha_{3/4}^1$ is a small perturbation of the three-quarter-chord angle of attack from its equilibrium value.

5.1.2 Results and discussion

The airfoil data used in the computations was for NACA 63-416. Both the nonlinear and linearized aeroelastic models were validated by comparing the chordwise damping ratios, ζ, obtained using the quasi-steady aerodynamic response with the damping ratio obtained by the use of Eq. (16). This comparison, which verified the present implementation, is presented in [I]. Note that positive damping ratio corresponds to negative aerodynamic damping and vice versa.

Figure 13 presents the damping ratios corresponding to the response functions presented in Figure 12 calculated on both the nonlinear and linearized models. The time-domain and eigenvalue analyzes of the linearized system returned identical results. The grey area in Figure 13 indicates the range of angles of attack approximately between -20° and 30° which was out of this work's focus because the airfoils' damping characteristics can be accurately determined by the state-of-the-art dynamic-stall models.

The main finding of [I] presented in Figure 13 was that the edgewise damping ratios corresponding to the lagged aerodynamic response were considerably higher than the damping ratio corresponding to the quasi-steady aerodynamic response. Most of the angle of attack regions corresponding to the negatively damped vibrations of the system characterized by the quasi-steady aerodynamic response vanished already in the case of the system characterized by the inviscid aerodynamic response No. 1. On the other hand, even though the actual aerodynamic response in deep stall is currently unknown, it is probable that such a response is slower than the inviscid response No. 1. Moreover, an increase in the aerodynamic damping was even more pronounced for responses slower than inviscid, i.e. No. 2 and No. 3. These facts indicate standstill blade vibrations may be overestimated by aeroelastic codes which assume quasi-steady aerodynamics in deeps stall. Note that delaying the aerodynamic response more than to what corresponds to inviscid flow caused an increase in the aerodynamic damping in the angle of attack regions which were already positively damped rather than expanded these regions. The regions around -20 and 20 degrees angle of attack remained negatively damped independent of the amount of lag in the response. However, it is questionable how well the present model represents the real behavior of the airfoil at these angles because of a possible existence of dynamic-stall effects. Another angle of attack region that seemed to be unaffected by the introduction of lag in the aerodynamic response was the vicinity of 180 degrees. Therefore, this region may create stability problems in real-life.

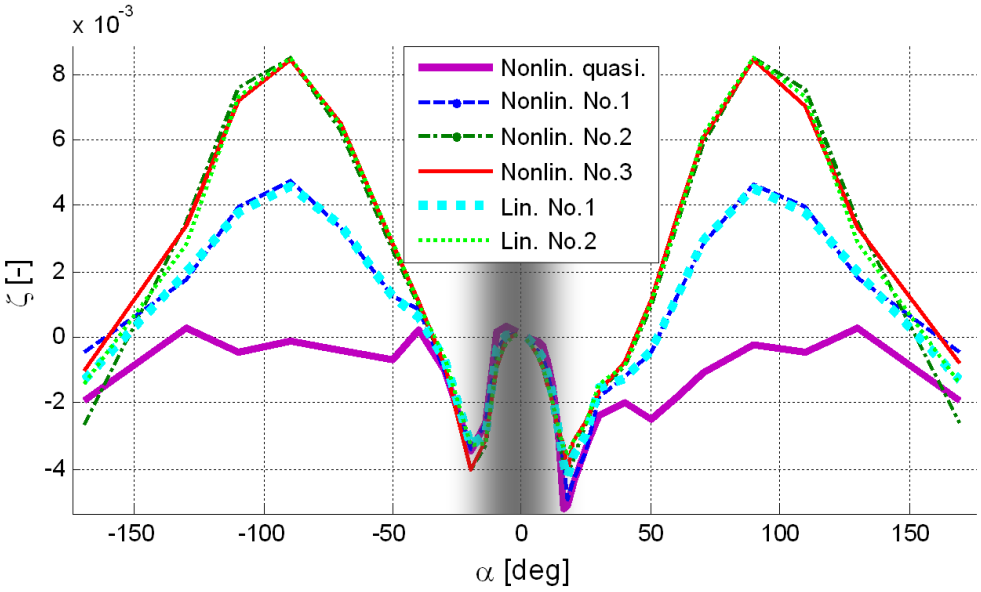

Figure 13: Edgewise damping ratios corresponding to the aerodynamic response functions from Figure 2, calculated on both the nonlinear and linearized models; the airfoil data used in the computations was for NACA 63-416; the grey area indicates the angle of attack range out of this work's focus

Moreover, introduction of an overshoot in the aerodynamic response made a very small change in the aerodynamic damping characteristic of the nonlinear model and no change in the linearized one. However, an overshoot in the response cannot alter the damping of the linearized system as its damping is dependent on the initial value of the response function. Therefore, the curve corresponding to the linearized response No. 3 is not plotted in Figure 13 for better clarity.

The aerodynamic damping characteristics obtained by the analyzes of the nonlinear and corresponding linearized models were similar. This indicates that the nonlinear effects in this aerodynamic model play a minor role in terms of the system's aeroelastic stability limits.

A sensitivity study involving spring stiffness performed in the present work showed that the influence of varying stiffness on the aerodynamic damping characteristics is relatively low.

Note that the presented results regard a simple engineering model and do not necessarily reflect the real-life phenomena. However, these results are meant as guidance to what parameters may influence the aerodynamic response in deep stall, and also to indicate that aeroelastic codes may inaccurately model standstill vibrations.

5.2 The effect of imposing time lag on the full aerodynamic response [II]

The effect that time lag on the aerodynamic lift, drag and moment has on the aeroelastic stability limits was analyzed in the part of the present work described in [II]. The main difference between the current model and the one presented in the preceding section was that here the temporal lag was imposed on all the force components – lift, drag and moment – and not just on the lift alone which makes the model more realistic. Moreover, a parameter study of the effect of alternating the position of the hinge point and centre of gravity was included together with a parameter study of the effect of varying spring stiffness. Finally, a discussion of the significance of including added-mass terms in the aerodynamic equations of the model was given. In order to allow for the aforementioned studies, the model described below differs from the one described in the preceding section.

5.2.1 Method

The current setup of the 2D 3-DOF elastically mounted airfoil model is presented in Figure 14. *C* is the chord line, *AA* is the aerodynamic axis, and *EA* is the elastic axis (hinge point). Both *AA* and *EA* are positioned on *C*. F_X and F_Y are the aerodynamic force components applied at *AA* in x and y directions, respectively. *AA* is positioned at the quarter chord. F_Θ is the aerodynamic moment applied at *AA*, positive counter-clockwise. Θ_g is the angle between *C* and the line (*C'*) through *EA* and the center of gravity (*CG*). *C* is parallel with x axis when the profile is in the equilibrium without the aerodynamic forces involved. In the case of symmetric profiles, *CG* lies on *C*. In such a case, *C'* coincides with *C*, and Θ_g is zero. In this study, Θ_g was approximated as zero even though the profiles considered are non-symmetric. Note that *AA* is not the aerodynamic center (*ac*) which is the point on an airfoil where the aerodynamic moment is independent of the angle of attack under fully attached flow conditions.

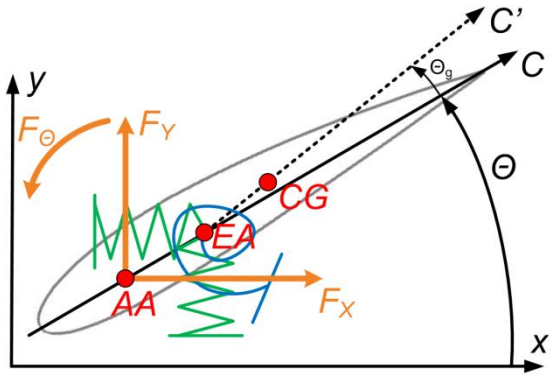

Figure 14: 2D 3-DOF elastically mounted airfoil model from [II].jpg

The nonlinear structural model consists of the following set of equations of motion:

$$\begin{aligned} M\ddot{X} + c_X\dot{X} + k_X X &= F_X + M\,C\,l_{EACG}\,\dot{\Theta}^2 cos(\Theta+\Theta_g) + M\,C\,l_{EACG}\,\ddot{\Theta} sin(\Theta+\Theta_g) \\ M\ddot{Y} + c_Y\dot{Y} + k_Y Y &= F_Y + M\,C\,l_{EACG}\,\dot{\Theta}^2 sin(\Theta+\Theta_g) - M\,C\,l_{EACG}\,\ddot{\Theta} cos(\Theta+\Theta_g) \\ \ddot{\Theta}\left(I_{cg} + M\,(C\,l_{EACG})^2\right) + c_\Theta\dot{\Theta} + k_\Theta\Theta & \\ = F_\Theta + F_X\,C\,l_{AAEA}\,sin\left(\Theta+\Theta_g\right) - F_Y\,C\,l_{AAEA}\,cos\left(\Theta+\Theta_g\right) & \\ + MC\,l_{EACG}\,\ddot{X}\,sin(\Theta+\Theta_g) - M\,C\,l_{EACG}\,\ddot{Y} cos(\Theta+\Theta_g) & \end{aligned} \tag{30}$$

where *X*,*Y* and Θ denote displacements in x, y and rotational directions, respectively. Further, l_{EACG} is the dimensionless distance from *EA* to *CG*, positive when *CG* is behind *EA*. The dimensionless distance from *AA* to *EA*, positive when *EA* is behind *AA*, is denoted as l_{AAEA}. *C* denotes the chord length.

The dynamic lift coefficient is calculated as a sum of the static lift coefficient at an effective angle of attack and the added-mass terms from the unsteady thin airfoil theory [21,22]:

$$C_L^{Dyn} = C_L^{St}(\alpha_E) + \frac{\pi\rho C^2}{4}\left[(\sin\gamma - \alpha\cos\gamma)\ddot{X} - (\cos\gamma + \alpha\sin\gamma)\ddot{Y} - V_{rel}\dot{\Theta} + \frac{C}{2}(2l_{EA}-1)\ddot{\Theta}\right] \tag{31}$$

where l_{EA} is the dimensionless distance from the leading edge to the elastic axis. V_{rel} is the airflow velocity relative to the airfoil. Further, γ is the angle between the *x axis and* V_0 where V_0 is the absolute airflow velocity The effective angle of attack (α_E) was defined in Eq. (22).

The dynamic drag coefficient was calculated as:

$$C_D^{Dyn} = C_D^{St}(\alpha_E) + (\alpha - \alpha_E)C_L^{Dyn} \tag{32}$$

The first term is the steady drag coefficient defined with respect to α_E. This term ensures that the dynamic drag converges to the static value. The second term represents the induced drag which is a concept stemming from thin airfoil theory [21,22]. This term arises due to the change of the effective inflow direction due to the effect of shed vorticity. The geometric angle of attack, α, is defined with respect to the relative velocity, V_{rel}, taking into account airfoil motion.

The dynamic moment coefficient is taken to be equal to the sum of the static moment coefficient at the effective aoa and the added-mass terms:

$$\begin{aligned} C_M^{Dyn} = C_M^{St}(\alpha_E) + \frac{\pi\rho C^3}{8}\Big[&(2l_{EA}-1)(\alpha\cos\gamma - \sin\gamma)\ddot{X} + (2l_{EA}-1)(\alpha\sin\gamma + \cos\gamma)\ddot{Y} \\ &+ \frac{1}{2}(4l_{EA}-3)V_{rel}\dot{\Theta} - \frac{C}{16}(32{l_{EA}}^2 - 32l_{EA} + 9)\ddot{\Theta}\Big] \end{aligned} \tag{33}$$

The specific parts of the added-mass terms in equations (31) and (33) will be referred to as the edgewise acceleration, flapwise acceleration, pitch rate and pitch acceleration terms of the lift and moment coefficients, respectively.

The unit response function and the parameter values were the same as in the preceding section.

The nonlinear structural model presented above was linearized in order to perform eigenvalue analysis of the system, resulting in the following set of linearized equations of motion:

$$\begin{aligned} M\ddot{X} + c_x\dot{X} + k_xX &= F_X^{lin} + M\ C\ l_{EACG}\ddot{\Theta}sin(\Theta_g) \\ M\ddot{Y} + c_y\dot{Y} + k_yY &= F_Y^{lin} - M\ C\ l_{EACG}\ddot{\Theta}cos(\Theta_g) \\ \ddot{\Theta}\left(I_{cg} + M(C\ l_{EACG})^2\right) + c_\Theta\dot{\Theta} + k_\Theta\Theta & \\ = F_\Theta^{lin} + F_X^{lin}\ C\ l_{AAEA}\ sin(\Theta_g) - F_Y^{lin}\ C\ l_{AAEA}\ cos(\Theta_g) + M\ C\ l_{EACG}\ \ddot{X}\ sin(\Theta_g) & \\ - MC\ l_{EACG}\ \ddot{Y}cos(\Theta_g) & \end{aligned} \tag{34}$$

where F_X^{lin} and F_Y^{lin} are the linearized aerodynamic force components. F_θ^{lin} is the linearized aerodynamic moment. Linearization was performed around equilibrium positions which depend on the inflow angle.

The aerodynamic equations were linearized as well in order to obtain a fully linearized system. The linearized dynamic lift coefficient was expressed as:

$$C_L^{lin} = C_L^0 + \frac{dC_L^0}{d\alpha}\alpha_E^1 + \frac{\pi\rho C^2}{4}\Big[(\sin\gamma - \alpha_0\cos\gamma)\ddot{X} - (\cos\gamma + \alpha_0\sin\gamma)\ddot{Y} - V_0\dot{\Theta} + \frac{C}{2}(2l_{EA}-1)\ddot{\Theta}\Big] \tag{35}$$

where C_L^0 and α_0 are the lift coefficient and the angle of attack at the equilibrium state. Further, l_{EA} is the dimensionless distance between the leading edge and *EA*. The small perturbation of the effective angle of attack from its equilibrium value, α_E^1, was calculated as in the preceding section.

The linearized dynamic drag coefficient was expressed as:

$$C_D^{lin} = C_D^0 + \frac{dC_D^0}{d\alpha}\alpha_E^1 + (\alpha^1 - \alpha_E^1)C_L^0 \tag{36}$$

where C_D^0 is the drag coefficient value at the equilibrium state, and α^1 is a small perturbation of the geometric angle of attack from its equilibrium value.

The linearized dynamic moment coefficient is:

$$C_M^{lin} = C_M^0 + \frac{dC_M^0}{d\alpha}\alpha_E^1 + \frac{\pi\rho C^3}{8}\Big[(2l_{EA}-1)(\alpha_0\cos\gamma-\sin\gamma)\ddot{X} + (2l_{EA}-1)(\alpha_0\sin\gamma+\cos\gamma)\ddot{Y} + \frac{1}{2}(4l_{EA}-3)V_0\dot{\Theta} - \frac{C}{16}\left(32{l_{EA}}^2 - 32l_{EA}+9\right)\ddot{\Theta}\Big] \quad (37)$$

where C_M^0 is the moment coefficient value at the equilibrium state.

The significance of the added-mass terms in the equations is discussed in the end of this section. Otherwise, the presented results were obtained with equations in which the added-mass terms were set to zero in order to allow for a more objective comparison with the model from the previous section where no such terms were present.

Parameter values of the setup used in this study – such as the mass or spring stiffness – were the same as in the preceding section and were discussed again in [II].

Airfoil data used in the computations was for NACA 63-416, DU96-W-180 and Risø-B1-18. The airfoil data for DU96-W-180 was obtained from measurements made by Timmer and van Rooij [23,24] from the Delft University of Technology, Faculty of Aerospace Engineering, Wind Energy Section. The data regarding Risø-B1-18 was obtained at Risø DTU National Laboratory for Sustainable Energy by a combination of wind tunnel measurements and EllipSys3D CFD computations. The EllipSys3D code was developed by Michelsen [25,26] and Sørensen [27,28], at Risø DTU and the Technical University of Denmark. The airfoil characteristics are presented in [II].

5.2.2 Results and discussion

Both the nonlinear and linearized aeroelastic models were validated by comparing the chordwise damping ratios, ζ, obtained using the quasi-steady aerodynamic response with the damping ratio obtained by the use of Eq. (16). This comparison, which verified the present implementation, is discussed in [II].

The damping ratios corresponding to the response functions from Figure 12 calculated by means of the linearized model from [II] are presented in Figure 15. The results are compared with the respective results obtained by the linearized model from [I] where lag was imposed exclusively on the lift. The airfoil coefficients used for the comparison regarded NACA_63-416 aerodynamic characteristics of which are presented in **[II**]. As it is seen in Figure 15, results obtained by means of both linearized models are very similar. This indicates that the lift is the main driver of the aeroelastic stability of the model from [II]. Moreover, the damping ratios corresponding to response function No. 3 were not plotted because the corresponding curves overlapped with the curves representing response function No. 2. This verifies what was mentioned earlier, i.e. that the overshoot in the corresponding unit response function is insignificant in terms of the damping of the linearized model. Analysis of additional response functions not presented here indicated that the damping is sensitive to the initial slope of the response function, as well as to its initial value. Note that the regions around -20 and 20 degrees

angle of attack remained negatively damped independent of the amount of lag in the response. However, it is questionable how well the present model represents the real behavior of the airfoil at these angles because of a possible existence of dynamic-stall effects. Another angle of attack region that seemed to be unaffected by the introduction of lag in the aerodynamic response was the vicinity of 180 degrees. Therefore, this region may create stability problems in real-life.

A parameter study of the influence of the positions of the elastic axis and center of gravity was performed in this work under the assumption of quasisteady aerodynamics. The study showed that the damping of the edgewise mode is independent of the position of both EA and CG. Further, also the flapwise mode is independent of these parameters. Only the torsional mode was found dependent on CG but it did not become unstable within physical displacement regime of CG which had to lie on the latter half of the profile in order for the torsional mode to become unstable.

Influence of the spring stiffness values on the aerodynamic damping was analyzed. In the study, the stiffness of each of the three springs was changed by 50% which influenced the shape of the curves representing the aerodynamic damping but did not influence the aeroelastic stability limits. Further discussion of the results is presented in [II].

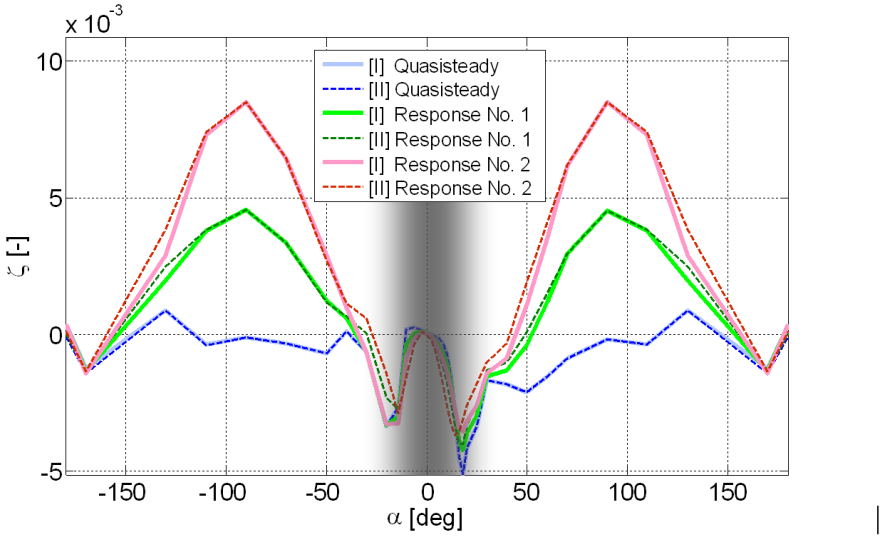

Figure 15: Comparison of the edgewise damping ratios obtained by the linearized models in [I] and [II]; added-mass terms excluded; the airfoil data used in the computations was for NACA 63-416; the grey area indicates the inflow direction out of the focus of the present work

Four distinct added-mass terms are present in the equations. These are: edgewise acceleration, flapwise acceleration, pitch rate and pitch acceleration. The influence of each of these terms on the aeroelastic stability limits of the linearized model was investigated which showed that only the flapwise-acceleration and pitch-rate terms had any influence on the aerodynamic damping. Their influence on the aeroelastic stability limits, which was relatively low, is discussed in more detail in [II].

Also, the influence of different airfoil characteristics on the aeroelastic stability limits was analyzed and is presented in Figure 16.

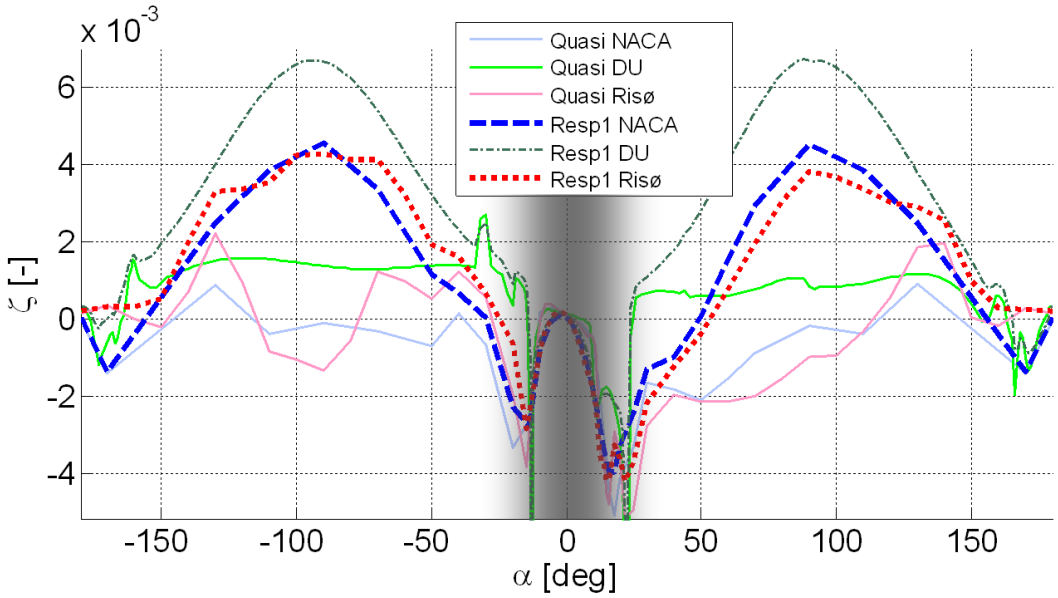

Figure 16: Comparison of the edgewise damping ratios corresponding to three different airfoils and two response functions; the grey area indicates the inflow direction out of the focus of the present work; added-mass terms excluded

The two aerodynamic response functions considered in this analysis were the quasisteady and No. 1 (inviscid). The three investigated airfoils were: NACA 63-416, DU96-W-180 and Risø-B1-18. The results showed that the damping was heavily dependent on the profile characteristics. Further, for every presented profile the damping corresponding to the aerodynamic response function No. 1 was higher than the damping corresponding to the quasisteady response function. Moreover it was verified that the flapwise and torsional modes of all the investigated profiles were characterized by positive aerodynamic damping for both response functions. This indicates that only the edgewise mode of an elastically mounted airfoil may be problematic. However, the simple engineering models presented in this work are not necessarily an accurate representation of an actual wind turbine blade. Therefore, further work needs to be carried out in order to verify the aforementioned results. Computational fluid dynamics could serve as a tool for verification of the present results.

6 Investigation of standstill vibrations by means of Computational Fluid Dynamics

6.1 Vortex-induced vibrations at 90 degrees angle of attack [III]

Locked-in vortex induced vibration is a potential threat to large wind turbine blades at standstill. The part of the present work described in this section and in more detail in [III] was a study of vortex-induced vibrations of the DU96-W-180 airfoil in which the response of the airfoil model in deep stall was investigated. The present study included 2D and 3D unsteady CFD computations. These included computations on non-moving, prescribed motion and elastically mounted airfoil suspensions. Stationary vortex shedding frequencies corresponding to the 2D and 3D computations were obtained by performing a frequency analysis of the loading on the non-moving airfoil models. In the prescribed motion computations the airfoil was forced to oscillate in the direction of the chord line. The elastically mounted airfoil computations were made with both one and three degrees of freedom of movement. The motivation for including both the prescribed motion and the elastically mounted airfoil computations was that, on the one hand, elastically mounted airfoil computations are the best reflection of real life blade vibration. On the other hand, prescribed motion computations allow us to learn about the basic mechanisms of fluid-structure interaction. It is also easier to derive engineering models from the data when well-defined forcing of prescribed motion computations was applied. Another motivation was to simply gain more insight into the involved phenomena by investigating it from two different perspectives.
Note that the present work simplified the problem of blade standstill vibrations by omitting the effects of blade twist and taper as well as the shear and turbulence in the incoming flow. The reason is to learn about the basic mechanisms involved in vortex-induced vibrations of wind turbine blades. Further, flows in the deep-stall regime are known to be highly three-dimensional. It is common to resolve such flows by means of computationally expensive 3D DES simulations. The motivation for including 2D computations in the present work was to investigate whether relevant flow characteristics may be captured by 2D computations. This could be beneficial because of the high computational efficiency of such simulations compared to 3D DES.

6.1.1 Method

The DU96-W-180 airfoil was used in the computations performed with EllipSys2D and EllipSys3D [25,26,27]. Elastically mounted airfoil computations were performed with an EllipSys add-on for structural computations developed by Heinz [29]. Detailed description of the parameter values used in the EllipSys2D and EllipSys3D computations as well as in the structural model is presented in [III].

Snapshots of the flow and the time series of the load in the edgewise direction were extracted from the non-moving computations (of the fixed airfoil). The snapshots visualized the mechanism of vortex shedding. The time series from both 2D and 3D CFD simulations were used to calculate the stationary Strouhal number, defined as:

$$St = \frac{f_v c}{V} \qquad (38)$$

where f_v is the vortex shedding frequency, c is the chord length and V is the inflow velocity.

Vortex induced vibration is by nature an aeroelastic problem. However, here an attempt was made to identify the aeroelastic stability limits by means of prescribed motion computations where the airfoil was subjected to forced oscillations along the chord line. The load-displacement plots and the mean power were extracted from the computations. The instantaneous aerodynamic power per unit length of the system was defined as the product of the instantaneous speed of the airfoil and the component of the aerodynamic loading per unit length in the displacement direction, $R_x(t)$. Then, the mean value during a whole number of periods was calculated:

$$\bar{P} = \frac{1}{nT}\int_0^{nT} R_x(t)\frac{dx}{dt}dt \qquad (39)$$

The time series length in the power calculations was 10 oscillation periods in the case of 2D flows, and 30 periods in the case of 3D. Assuming that the damping in the system is linear, the power is directly proportional to the damping coefficient. Therefore, even though the aerodynamic damping is not necessarily linear, using power to determine the aeroelastic stability limits is intuitive. When the power was positive, the flow fed energy to the oscillating system.

A number of computations were made at different vibration periods, *T*. Then, the mean dimensionless power was plotted as a function of the dimensionless vibration period $T^*=T\,V/c$. The dimensionless mean power was obtained by normalization of the mean power with density, chord length, vibration amplitude and vibration period:

$$P^* = \frac{T}{\rho c A V^2}\bar{P} \qquad (40)$$

The motivation for such a non-dimensionalization is that the power is the product of the loading and airfoil velocity, i.e. $P = R_x(t)\dot{x}$. Further, the loading is directly proportional to the square of the flow speed, i.e. $R_x \sim V^2$ while the airfoil velocity is directly proportional to the ratio of the amplitude and period of oscillation, i.e. $\dot{x} \sim \frac{A}{T}$. Therefore, the loading was non-dimensionalized by $\rho c V^2$, and the airfoil velocity was non-dimensionalized by $\frac{A}{T}$ which resulted with Eq. (40).

6.1.2 Results and discussion

The present approach was validated by performing computations on a circular cylinder and comparing the present results with the results of the experiment by Feng [5], detailed description of which is presented in [III].

The upper graph of Figure 17 presents the time series of the chordwise force coefficient, C_{Fx}, of the DU96-W-180 airfoil at 90 deg angle of attack. The figure shows both the results of the 2D RANS and 3D DES time-marching computations, both for 80 dimensionless time units, $s = t\,V_0\,c^{-1}$. The 2D time series was more regular than the 3D series, with amplitude twice as large as the 3D series. The differences were most likely due to the lower than unit spanwise coherence of the aerodynamic force in the 3D case. The 2D CFD case of course has a unit spanwise coherence by definition. The difference in the amplitude is also visible in the lower graph of Figure 17 which shows the single-sided amplitude spectrum of the load coefficient based on the time series of 100 dimensionless time units. The Strouhal number values of the 2D

and 3D computations were 0.13 and 0.16, respectively. The instantaneous 3D loading was spatially averaged in the spanwise direction of the extruded profile. The time series of C_{Fx} related to three equidistant cross sections of the extruded profile are presented in [III] together with a short discussion of these results. There, it is shown that the time series were well correlated.

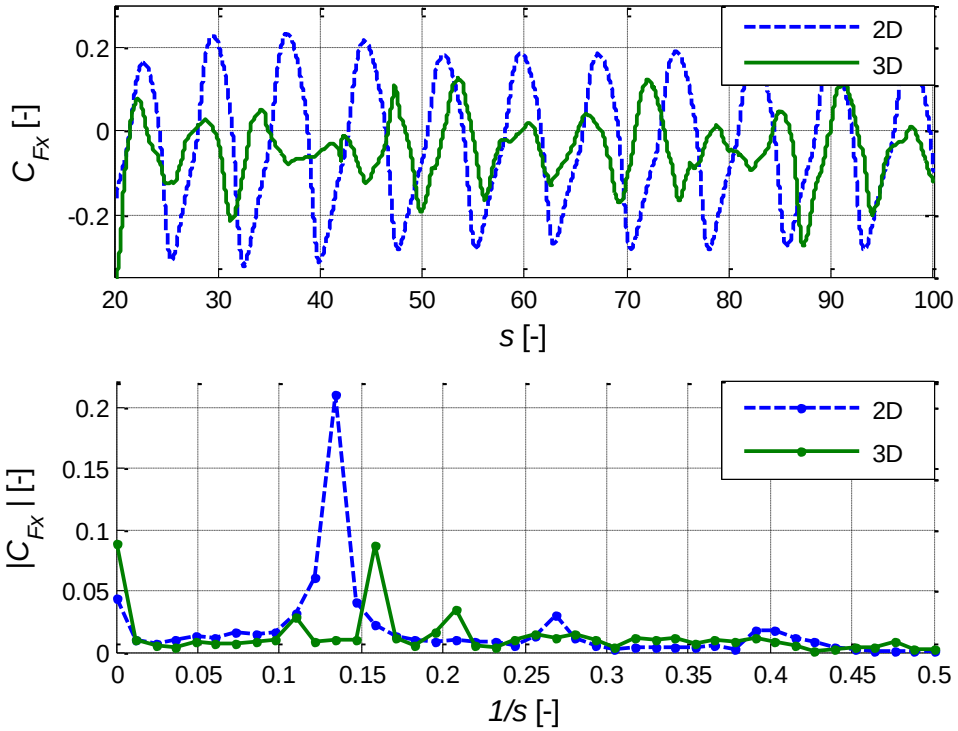

Figure 17: Non-moving DU96-W-180 airfoil at 90 deg angle of attack; (upper) Time series of the load coefficient in the chordwise direction, C_{Fx}; (lower) Single-sided amplitude spectrum of the chordwise load coefficient

To further illustrate that the force oscillations are caused by the vortex shedding, two snapshots of the 3D flow are presented in Figure 18. The figure presents vorticity magnitude. Dark areas correspond to high values. In the snapshot on the left side, a vortex is being shed off the leading edge. The vortex is marked with a circle. In the snapshot on the right side, a vortex is being shed off the trailing edge – also marked with a circle. This was confirmed by analysis of the animation showing pressure variation. Note that a 2D computation made on Risø A1-21 returned the Strouhal number value of 0.13 which was the same as that of the DU profile obtained with 2D CFD. This indicated that at high angles of attack where separation is well defined, the Strouhal number is relatively independent of the airfoil shape.

After the values of the Strouhal number were obtained from the non-moving computations, 2D and 3D prescribed motion computations were carried out. The reason was to investigate the aeroelastic stability limits of the airfoil at 90 deg angle of attack. Figure 19 presents the results of the 2D computations with three curves showing the dimensionless power, P^*, as a function of the dimensionless forced-oscillation period, T^*, of DU96-W-180. Each of the curves corresponds to simulations carried out at a specific A^*/T^* ratio. The reason was that A^*/T^* or f^*A^* – where f^* is the dimensionless oscillation frequency – can be thought of as the level of perturbation imposed by the airfoil motion on the flow. If A^* was constant in a set of

computations, then such a level of perturbation would grow with f^*. Then, computations with high oscillation frequency would drive the vortex shedding and create the lock-in.

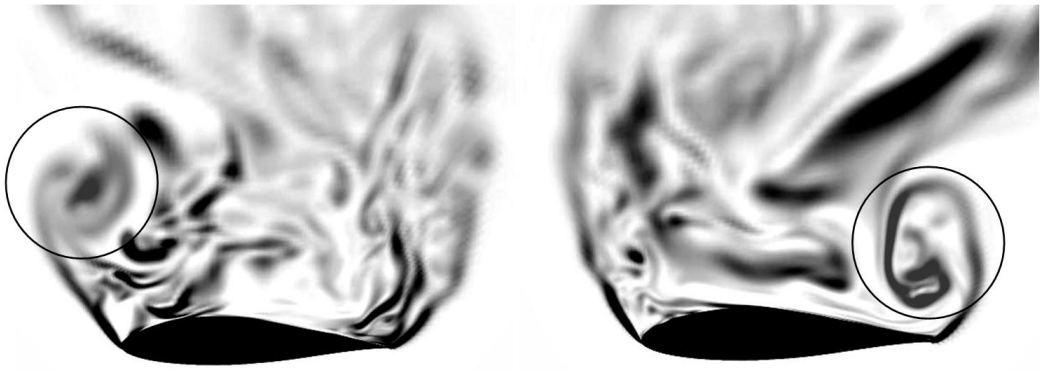

Figure 18: Snapshots presenting vorticity magnitude of the 3D flow around the DU96-W-180 airfoil at 90 deg angle of attack

After a simple calculation, one may show that there exists the following relation between the A^*/T^* ratio, airfoil maximum velocity, and the maximum variation in the angle of attack:

$$\frac{A^*}{T^*} = \frac{\frac{A}{c}}{\frac{TV}{c}} = \frac{A}{T\,V} = \frac{1}{2\pi}\frac{|\dot{x}|_{max}}{V} = \frac{1}{2\pi}\tan\alpha_{max} \qquad (41)$$

where $\dot{x}$ is the velocity of the airfoil and α is the angle of attack. Therefore, maintaining a constant A^*/T^* ratio in a series of computations assures a constant ratio between the maximum airfoil velocity and the flow velocity. It also assures a constant maximum variation in the relative angle of attack independent of the oscillation frequency.

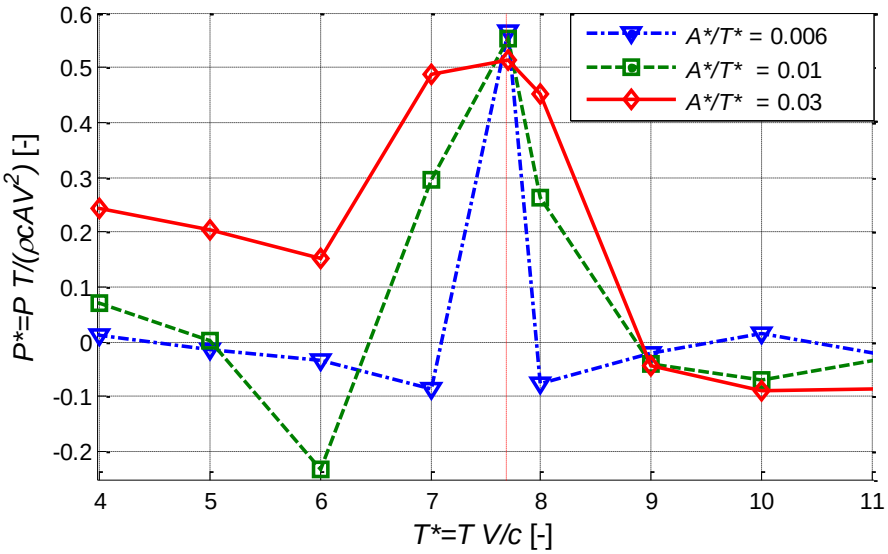

Figure 19: Dimensionless power related to prescribed oscillation of the DU96-W-180 airfoil at 90 deg angle of attack, oscillating perpendicular to the free stream; 3 different A^*/T^* ratios; 2D computations

The dimensionless vortex shedding period of the three cases was 7.7. As the figure shows, the dimensionless power in all three cases increased to a peak with positive sign when the

oscillation period reached 7.7. This indicated that an actual DU96-W-180 airfoil with the natural frequency of the edgewise mode close to the frequency of vortex shedding could have issues with dynamic instability. In order to confirm that the vortex shedding was in resonance with the oscillation, load-displacement plots of the 2D simulations of all three cases at $T^*=7.7$ are presented in Figure 20. In the figure, the direction of all the loops is clockwise.

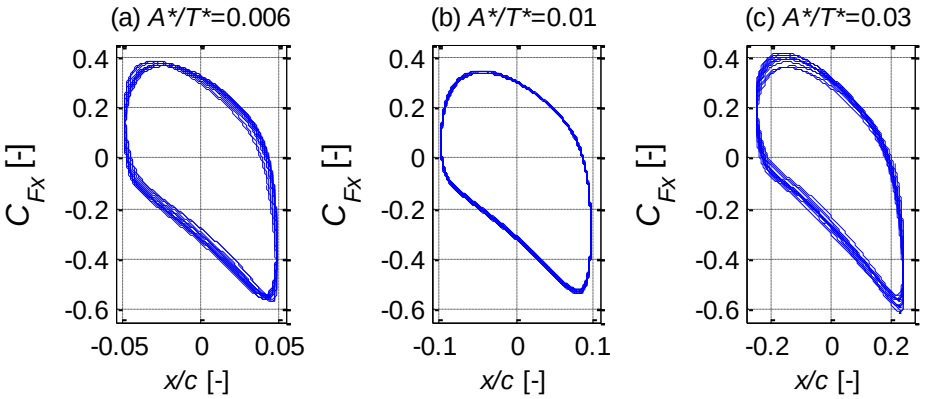

Figure 20: Load-displacement plots of DU96-W-180 at T^*=7.7 and A^*/T^*= (a) 0.006, (b) 0.01, (c) 0.03; all loops are clockwise; 2D computations.

Plots presented in Figure 19 also indicated what is mentioned by Sumer and Fredsøe [2] in the context of a vibrating cylinder, i.e. the larger the oscillation amplitude is, the wider the lock-in range is. Here, the larger the A^*/T^* ratio was, the wider the T^* band in which the power increased was. This was further indicated by the load-displacement plots of the three systems at $T^*=7$ presented in [III].

Also, the sensitivity of the dimensionless power with respect to the changes in the mean angle of attack and angle of vibration was studied. The results are presented in [III] where it shows that the dimensionless power in the model is more sensitive with respect to the change in the mean angle of attack than the angle of vibration.

Figure 21 presents the dimensionless power as a function of the dimensionless period of forced vibration, comparing 2D and 3D computations. It is a comparison of the results of the 3D DES computations made at A^*/T^*=0.03 with the results of the 2D RANS computations presented in Figure 19. Surprisingly, the power peaked at T*=7.7 although the dimensionless stationary vortex shedding period in the 3D computations was 6.3 while the period in the 2D computations was 7.7. This may be clarified by looking at Figure 22 which presents the load-displacement plots from the 3D computations with three different eigen periods: T^* = 6.3, 7.7 and 8. These curves consist of 30 oscillation periods each. They are in very good agreement with the 3D power characteristic presented in Figure 21. Resonance between the displacement and the loading was clearly visible at $T^*=7.7$ where the shape of the curve remained practically constant for the whole time of the simulation. Direction of the loop was clockwise. T^*=7.7 is also where the power in Figure 21 peaked. The load-displacement curves corresponding to T^*=6.3 and 8 were not identical for all displacement loops and the corresponding power values were relatively small. This indicates that even though the 3D stationary vortex-shedding period was 6.3, when the airfoil was forced to oscillate, the loading characteristic resembled that of the 2D computations. The 3D prescribed motion load time series was relatively regular and resembled that of the non-moving 2D computation more than that of the non-moving 3D. Analysis, which is not presented here, of the present computations showed that the spanwise load correlation in the 3D flow was higher for the oscillating airfoil than for the non-moving.

An increase in the spanwise correlation of the pressure distribution with increasing oscillation amplitude is also observed for a circular cylinder and described in [2,3,30,31]. One may therefore speculate that some characteristics of 2D simulations on oscillating airfoils may be applicable in 3D because the motion and the associated forcing can be in some sense thought to two-dimensionalize the flow pattern.

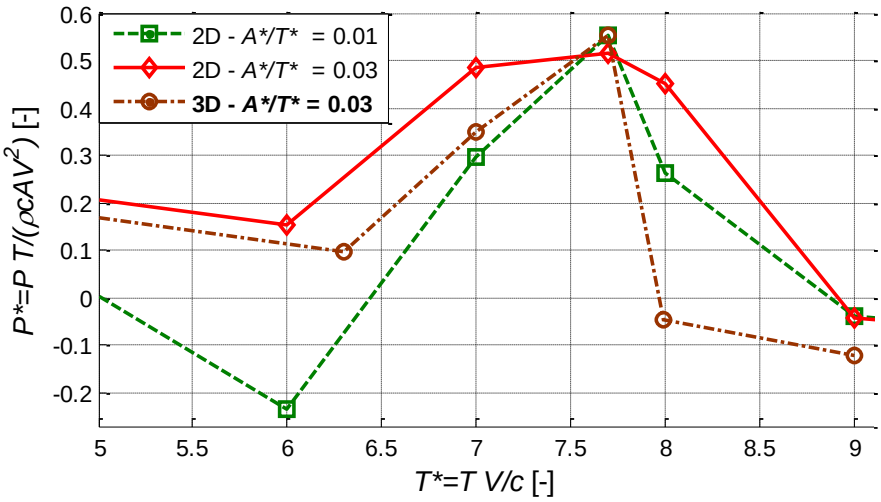

Figure 21: Dimensionless power related to prescribed oscillation of the DU96-W-180 profile at 90 deg angle of attack, oscillating perpendicular to the free stream; results of the 3D DES computations compared to the results of the 2D RANS computations

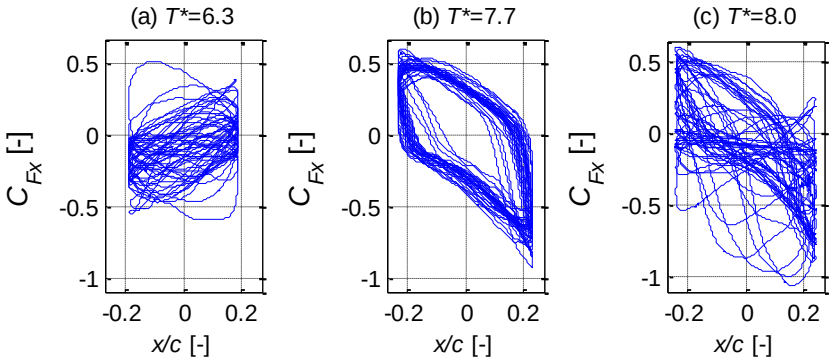

Figure 22: Load-displacement plots from the 3D DES computations of DU96-W-180 at *A*/T=0.03 and *T**= (a) 6.3, (b) 7.7 - clockwise loop direction, (c) 8.0**

The results obtained with the prescribed motion computations were verified with the computations on the elastically mounted 2D structural model of the DU96-W-180 airfoil coupled with 2D CFD, at 90 degrees angle of attack. The model had one degree of freedom of movement in the edgewise direction. Figure 23 presents the dimensionless edgewise displacement time series. In the case of the elastically mounted airfoil computations, *T** represented the edgewise eigen period of the isolated structural system which was not necessarily the exact period of the oscillation of the aeroelastic system. The results of these computations supported the results of the 2D CFD prescribed motion computations. The motion in the edgewise direction had increasing amplitude in time when the eigen frequency of the system approached the frequency of vortex shedding (Figure 23 c). The growth of the amplitude in the edgewise-displacement time series was approximately constant in time. This

made the calculation of logarithmic decrements inappropriate. A detailed investigation of limit cycles was outside the scope of the current work.

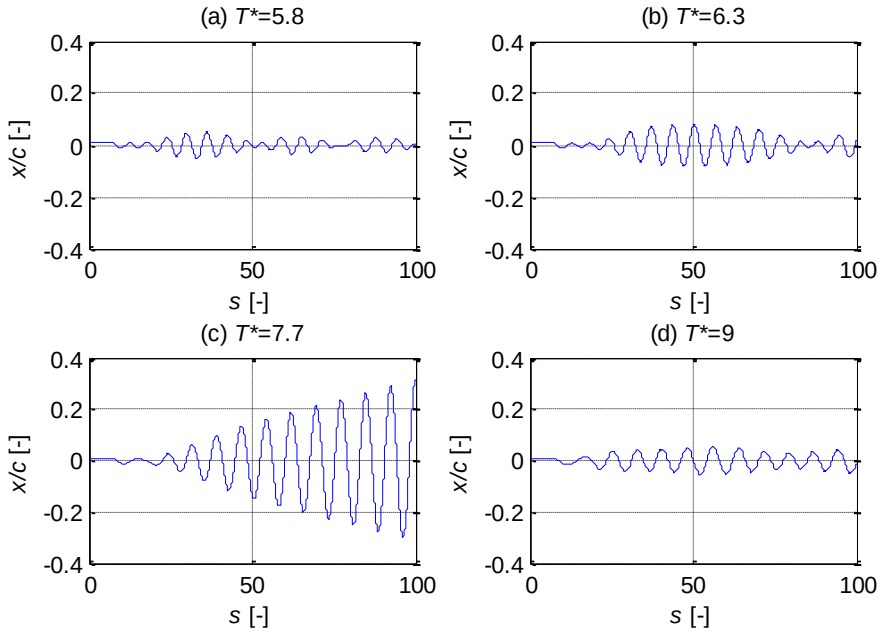

Figure 23: Dimensionless displacement in the edgewise direction of the elastically mounted 2D model of the DU96-W-180 at 90 deg angle of attack with one degree of freedom of movement. 2D CFD, 1DOF structural model.

Figure 24 shows the dimensionless displacement of the same setup except with three degrees of freedom. At the beginning of the time simulations, the model was displaced by the drag in the flapwise direction by approximately 0.3 of the chord length. In the three cases where no violent vibrations occurred (a, b and d), the flapwise and edgewise displacements were of the same order of magnitude. In the case where the model showed growth of its displacement amplitude in time (c) the edgewise mode was dominating.

Figure 25 presents dimensionless edgewise displacement time series of four different simulations made with the elastically mounted 2D, 3 DOF structural model of DU96-W-180 coupled with 3D CFD. The angle of attack was again 90 degrees As in the case of the 2D CFD computations, it was impossible to determine constant values of damping ratio of the system. The model - like in the 2D CFD case - had four variations with different eigen periods. Cases (b) T^*=6.3 and (c) T^*=7.7 showed the highest maximum amplitude values within 100 time units. It was shown previously that 6.3 was the period of the stationary vortex shedding of the 3D system. None the less, the displacement time series of the computation made with the eigen period 6.3 (c) did not indicate that there was a resonance between the system and the vortex-generated forcing. Moreover, the displacement time series (a),(b) and (c) were similar to that of a dynamic system subject to the beating phenomenon in which the frequency of forcing is relatively close to the system's eigen frequency, but not close enough to create a resonance. This indicated that the period of vortex shedding of the 3D CFD aeroelastic system in motion might be different than the period of stationary vortex shedding (6.3) or the period of vortex shedding of the system in prescribed motion (7.7). This was verified by a frequency analysis of the load time series of the computations (b) and (c). The analysis of both time series showed single peaks in the response corresponding to a period of 6.8 in the case of computation (b) and 7.1 in the case of computation (c). One may speculate that the difference comes from the

elastically mounted system having three degrees of freedom while the prescribed motion system oscillated in a single direction.

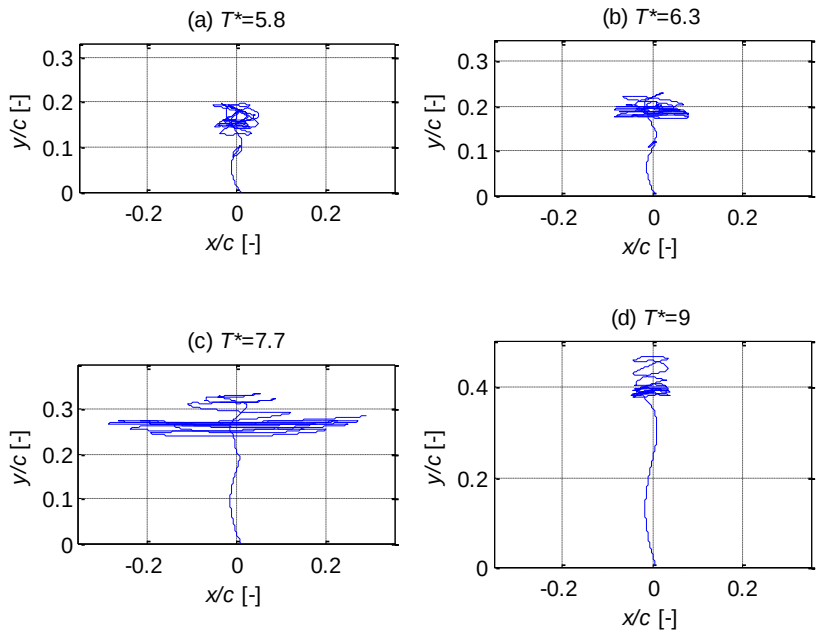

Figure 24: Displacement of the elastically mounted 2D, 3DOF structural model of DU96-W-180 coupled with 2D CFD; 90 deg angle of attack

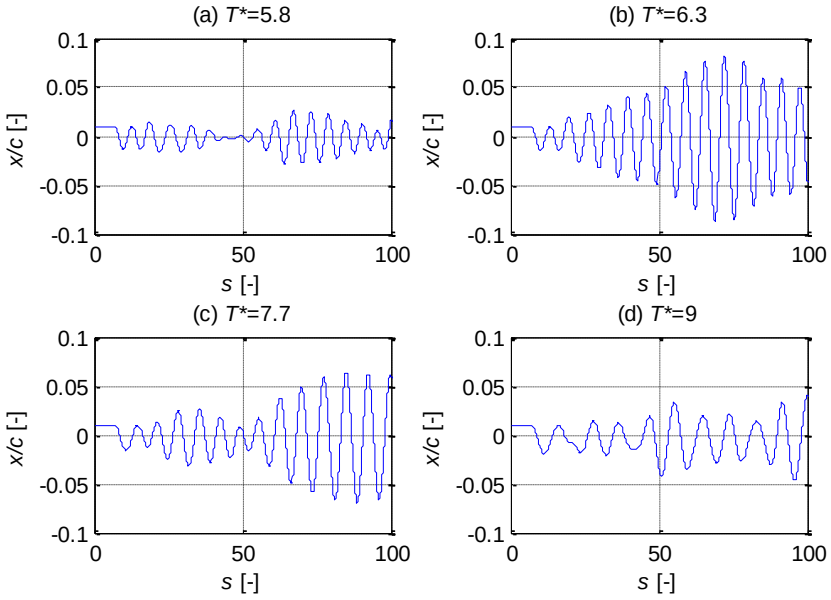

Figure 25: Dimensionless displacement in the edgewise direction of the elastically mounted 2D, 3DOF structural model coupled with 3D CFD; DU96-W-180 at 90 deg angle of attack; four different eigen periods of the edgewise mode

This fact spurred another computation with the eigen period of 7.0. The edgewise-displacement time series of that computation is presented in Figure 26. The displacement reached higher amplitude than any of the 3D displacements presented above. The time series resembled more that of a dynamic system at resonance than at beating conditions.

A comparison of the 1 DOF and 3 DOF 2D CFD models with the 3 DOF 3D CFD model in terms of the maximum amplitude reached within 100 time units is presented in Figure 27. The comparison showed that the 1 DOF 2D CFD model over predicted the amplitudes at T^*=7.7 and 9 relative to the 3 DOF 2D CFD model. Both 2D CFD models showed the same tendency. The amplitudes were the highest at T^*=7.7 which was the 2D CFD stationary vortex shedding period. In the case of the 3D CFD model – as it was mentioned above - the maximum amplitude showed at T^*=7.0.

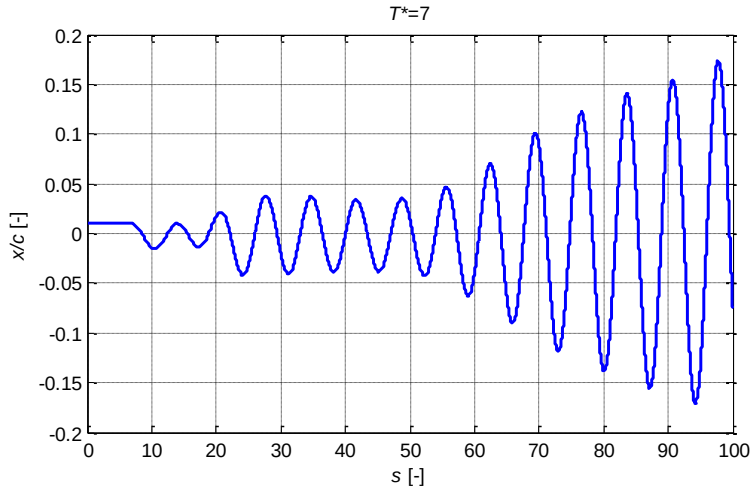

Figure 26: Dimensionless displacement in the edgewise direction of the elastically mounted 2D, 3DOF structural model coupled with 3D CFD; DU96-W-180; 90 deg angle of attack; edgewise dimensionless eigen period of 7.0

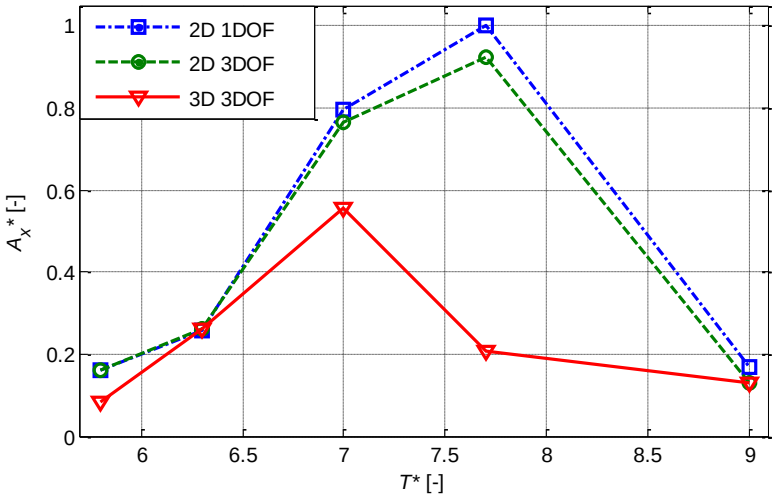

Figure 27: Comparison of the maximum amplitude reached within 100 time units by the 1 DOF and 3 DOF 2D CFD models with the 3 DOF 3D CFD model.

An important observation is that, the 3D CFD computations showed significantly lower maximum displacement, and occurring at a different eigen period than the corresponding 2D computations. Assuming that 3D CFD is more accurate in the present context, the results indicated that 2D computations can simulate the qualitative behavior of the aeroelastic system while 3D computations are necessary to deliver more accurate quantitative results. However, it was not explicitly shown in the present work that 3D CFD is a better representation of the real life situation.

Several of the computations presented in this work were also performed on the Risø-A1-21 airfoil. The results were similar to those of the DU96-W-180 indicating that the phenomena described here were rather general and not exclusively specific to the DU profile.

One of the most significant implications of the current findings is that – according to the dimensionalization of T^* at which the vibrations occurred in the simulations – vortex-induced vibrations may show on modern wind turbine blades, assuming that the average chord length is 2 m and the frequency of the first edgewise mode is approximately 1 Hz.

Besides vortex-induced vibrations, another potential kind of blade vibrations is stall-induced vibrations also referred to as galloping. However, the phenomena presented in this section were most likely solely related to vortex shedding. This was verified by the analysis of basic characteristics of galloping of bluff bodies [2]. The fact that vibrations modeled in 2D and 3D CFD occurred only in frequency bands around the corresponding frequencies of vortex shedding indicated that they were vortex related. Moreover, if these vibrations were stall related they would most likely show in lower frequencies, cover a wider range of frequencies and grow with the vibration period.

6.2 Vortex-induced and stall-induced vibrations in stall [IV]

This section presents an analysis of 2D and 3D non-moving, prescribed motion and elastically mounted CFD computations of the DU96-W-180 airfoil in the angle of attack region potentially corresponding to the highest risk of stall-induced vibrations. The computations aimed at investigating the mechanisms of both vortex-induced and stall-induced vibrations.

6.2.1 Method

The CFD computations were carried out with EllipSys2D and EllipSys3D [25,26,27] Navier-Stokes solvers. Elastically mounted airfoil computations were performed with an EllipSys add-on for structural computations developed by Heinz [29]. Detailed description of the parameter values used in the CFD computations as well as in the structural model is presented in [IV].

The aeroelastic stability limits were investigated by calculating the mean dimensionless aerodynamic power, P^*, defined as in the preceding section.

6.2.2 Results and discussion

In order to perform the computations at a Reynolds number representing a modern wind turbine blade subject to stall-induced standstill vibrations, the prescribed motion and elastic computations were performed at the Reynolds number of $6 \cdot 10^6$. This was because preliminary computations indicated that stall-induced vibrations occur at relatively high wind speeds.

In order to facilitate the process of finding the angle-of-attack region of the highest risk of stall-induced edgewise vibrations, Eq. (16) was applied to the aerodynamic characteristics of the DU96-W-180 airfoil measured at the $Re=0.7 \cdot 10^6$ [24], indicating where the vibrations could emerge. After comparing this result, presented in Figure 28, with the results of CFD simulations carried out at $Re=6 \cdot 10^6$, presented in Figure 29, it was decided that 26 degrees and 24 degrees were the angles of attack investigated further in 2D and 3D, respectively. Additionally, results of CFD computations carried out at various Reynolds numbers as well as a discussion of these results are presented in [IV] together with a study of flow separation.

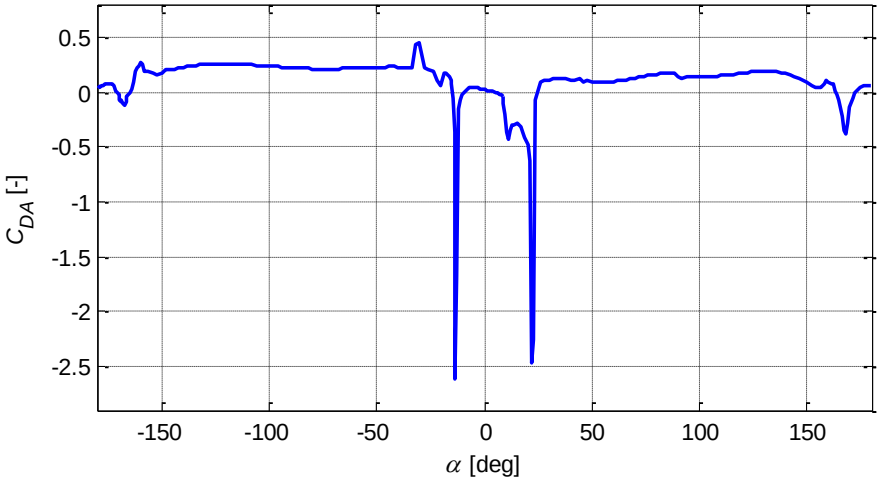

Figure 28: Dimensionless aerodynamic damping coefficient resulting from Eq. (16) being applied to the aerodynamic characteristics of the DU96-W-180 airfoil [23,24] assuming edgewise direction of vibration

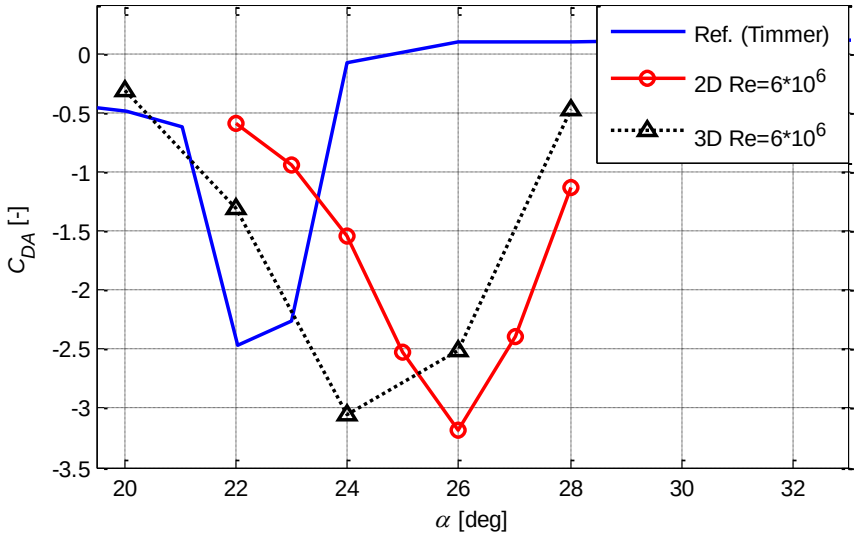

Figure 29: Dimensionless aerodynamic damping coefficient resulting from Eq. (16) being applied to the aerodynamic characteristics obtained by CFD computations on the DU96-W-180 airfoil [25,26] assuming edgewise direction of vibration

Figure 30 presents the results of both 2D and 3D prescribed motion computations of the DU96-W-180. The dimensionless power was plotted as a function of the dimensionless displacement period for A^*/T^*=0.01 which corresponds to the angle of attack amplitudes of 1.6 deg in 2D and 1.5 deg in 3D. The difference comes from the fact that different mean angles of attack were used in 2D and 3D. The curves representing 2D and 3D computations differed significantly. Detailed analysis of the aerodynamic force time series underlying the presented aerodynamic power characteristics is presented in [IV].

Figure 31 presents the curve corresponding to the 3D computations from Figure 30. The power appeared positive in two T^* regions. The first was approximately between 1 and 15 while the second was approximately above 44. The first region contained relatively high values of P^* with steep rise and fall. The underlying values of T^* contained the dimensionless period of stationary vortex shedding. These facts indicated that the increase in power was associated with

vortex induced vibrations. The same kind of vibrations is shown by both 2D and 3D prescribed motion and elastically mounted airfoil CFD simulations of the same airfoil at 90 deg angle of attack, presented in the preceding section.

Note that – according to the present work – vortex-induced vibrations are likely to occur on modern wind-turbine blades. This is because the predicted frequency of vortex shedding for realistic dimensional parameter values is relatively close to the frequency of the first edgewise mode being approximately equal to 1 Hz.

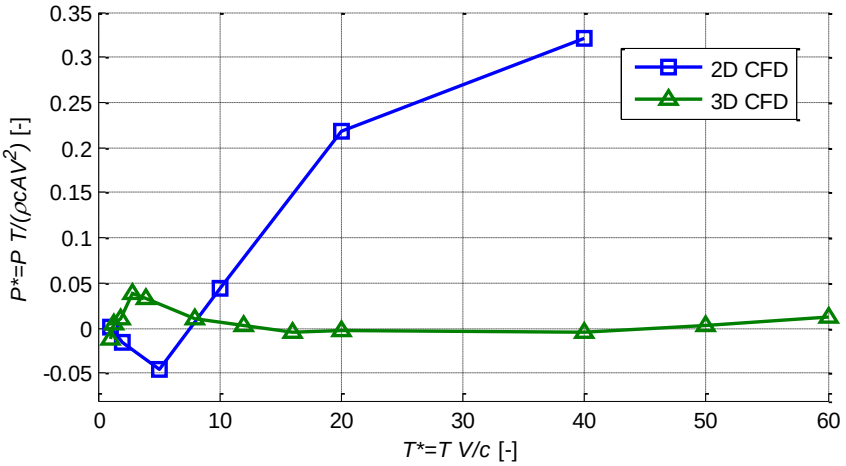

Figure 30: Dimensionless power related to prescribed motion 2D and 3D CFD simulations of DU96-W-180 at 26 and 24 deg angle of attack, respectively; oscillating in chordwise direction

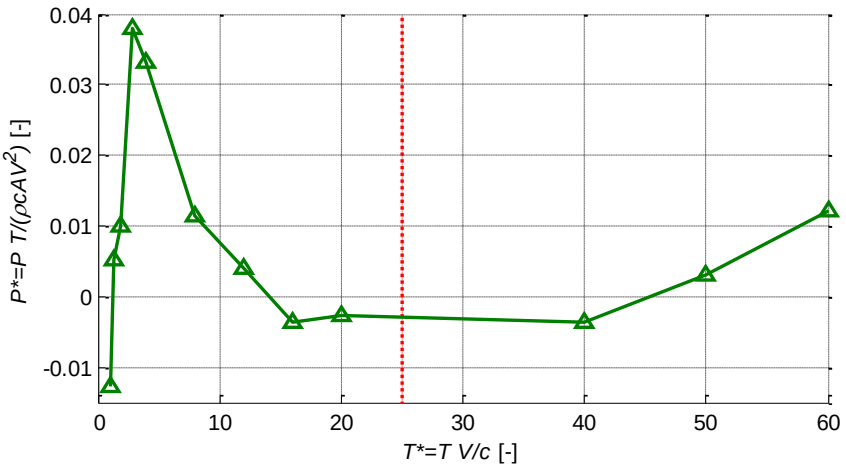

Figure 31: Dimensionless power related to prescribed motion 3D CFD simulations of DU96-W-180 at 24 deg angle of attack; oscillating in chordwise direction

The second region contained T^* values larger than the frequency of stationary vortex shedding by an order of magnitude. This indicated the presence of stall induced vibrations. However, the present model indicated that if such vibrations occurred on a modern wind turbine, the associated wind speed would be far from any realistic regime. Assuming that the chord length of the blade section was 2 m and the frequency of the first edgewise mode 1Hz, that mode would be excited if the wind speed exceeded 88 m/s. The thick vertical dotted line in Figure 31 shows the value of T^* corresponding to the wind speed of 50 m/s. On the other hand, in order for the T^* value of 44 to correspond to the wind speed of 50 m/s, the frequency of the first

edgewise mode of the blade with 2 m chord would need to be as low as 0.56 Hz. In the case of a blade with 1 m chord this frequency would need to be 1.1 Hz. Given the average relation between the blade chord length and the frequency of the first edgewise mode of modern wind turbine blades, the risk of the onset of stall induced vibrations seems small.

Note that the present simulations included only a single angle of attack, airfoil design and direction of rectilinear vibrations. Therefore, the present results may not generally describe vibrations at different conditions. Further, the conclusions based on the 2D results are drastically different, predicting vibrations at a wide range on T^* values while it was not explicitly shown in the present work that 3D simulations represent the real-life mechanisms of airfoil vibrations under the current flow conditions better than 2D. However, Shur *et al.* [32] and Strelets [33] indicate that 3D DES computations resolve stalled flows around airfoils better than 2D RANS.

It may also be concluded that CFD computations confirmed Eq.(16). This is because both 2D and 3D CFD simulations indicated a growth of stall-induced vibrations with increasing T^*. The higher the T^* value is, the slower the oscillation is and the closer the aerodynamic response is to quasi-steady. On the other hand, Eq. (16) was derived based on the assumption of quasi-steady aerodynamics. Therefore, when the aerodynamic response approaches quasi-steady characteristics, the aerodynamic damping predicted by CFD approaches the negative value predicted by Eq.(16).

The effective differences between using one, two and three degrees of freedom in the 2D elastically mounted airfoil model coupled with 2D CFD were investigated by comparison of predicted displacement amplitudes. The airfoil under consideration was DU96-W-180 at 26 degrees angle of attack and a Reynolds number of $6 \cdot 10^6$. The models had an edgewise dimensionless eigen period of 3 which in the case of elastic computations was denoted by T^*. The ratio between the periods of the edgewise and flapwise modes of the isolated structure was 0.7. The ratio between the periods of the edgewise and rotational modes was 7. Compared to the 3 DOF structural system, the 2 DOF system was constrained in rotation. The 1 DOF structural system was only free to move in the edgewise direction. The amplitude values of edgewise displacement were compared after 10 and 100 periods of oscillation. All three systems showed an increase in the amplitude in time. The highest amplitude was shown by the 1 DOF system. The 3 DOF system showed the lowest. The differences relative to the 3 DOF system are listed in Table 1.

Table 1: The effective differences between using one, two and three degrees of freedom in the 2D elastically mounted airfoil model coupled with 2D CFD; the amplitude of edgewise displacement after 10 and 100 periods of oscillation

	Number of periods [-]	**10**	**100**
2 DOF system	$\left\lvert\frac{A_{3DOF} - A_{2DOF}}{A_{3DOF}}\right\rvert$ [%]	**0.7 %**	**5.6 %**
1 DOF system	$\left\lvert\frac{A_{3DOF} - A_{1DOF}}{A_{3DOF}}\right\rvert$ [%]	**1.0 %**	**7.3 %**

One of the problems with using the 3 DOF model was that the springs needed to be preloaded in order to avoid unwanted nonlinear effects. Secondly, some of the investigated values of T^* were relatively high. Therefore the corresponding values of spring stiffness were low. Accordingly, the airfoils needed to be displaced by a large distance in order to preload the springs. In the case of the rotational degree of freedom, that would correspond to a large change

in the angle of attack which would change the aerodynamic characteristics of the system, and make the study very difficult. Because of this issue, and the fact that after a moderate number of oscillation periods the differences in the amplitude were relatively low, the elastic computations employed the 2 DOF system, results of which are presented in Figure 32. Note that the y-axis range differs between subfigures. The displacement time series are presented in Subfigures (a), (b) and (c). The dimensionless eigen periods of the first model coupled with 2D CFD presented in Subfigures (b) and (e), and the model coupled with 3D CFD presented in Subfigures (c) and (f), were T^*=3. The dimensionless eigen period of the second model coupled with 2D CFD presented in Subfigures (a) and (d) was T^*=1.8. This was the period of stationary vortex shedding in 2D. The ratio between the frequencies of the flapwise and edgewise modes was 0.7 – similar to that on modern wind turbines. Viscous damping was set to zero. The 3D CFD model showed negative aerodynamic damping with an exponential growth in its displacement amplitude presented in Subfigure (c). The corresponding plot of the displacement history indicated lock-in (Subfigure (f)) by showing that the displacements in three consecutive periods were of similar shape. The direction of the loop was clockwise. The 2D CFD model with T^*=3 showed positive aerodynamic damping (Subfigure (b)) and a lack of lock-in (Subfigure (e)) as the plot of the displacement history changed shape in consecutive periods. The 2D model with T^*=1.8 showed lock-in (Subfigure (d)) and negative aerodynamic damping (Subfigure (a)). The direction of the loop in Subfigure (d) was clockwise. However, the displacement amplitude showed asymptotic growth with relatively small limit. Further, the limit was lower than the displacement amplitude used in the prescribed motion computations. That explains why the prescribed motion computation showed negative power while the elastically mounted computation showed an increase in the displacement amplitude. Generally, the three elastic computations verified the conclusions from the respective prescribed motion computations.

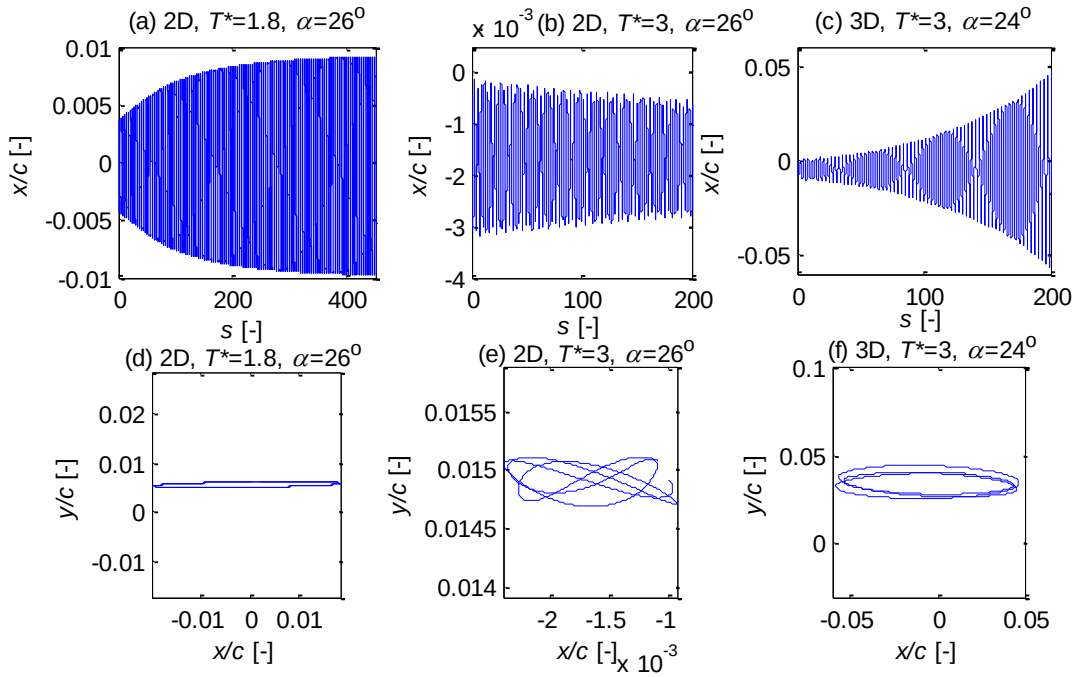

Figure 32: Displacement time series and displacement history of the elastic computations; displacement history plotted over 3 consecutive displacement periods

6.3 Modeling of unsteady airfoil aerodynamics in stall [V]

In one of the preceding sections, it was shown that even a relatively low amount of temporal lag in the aerodynamic response of an airfoil model in deep stall may dramatically decrease the range of angles of attacks at which the aerodynamic damping of this model is negative. Under the assumption that the actual aerodynamic response of airfoils in deep stall is slower than quasi-steady, this indicates that present aeroelastic codes may over-predict deep stall standstill vibrations. To analyze this issue further, the focus of the current work was on determining the amount of temporal lag of an airfoil in deep-stall.

6.3.1 Method

2D and 3D prescribed motion CFD computations respectively carried out at 26 and 24 degrees angle of attack, respectively, at the Reynolds number of $6 \cdot 10^6$ were analyzed. The CFD computations analyzed in this section were a part of the computations utilized for calculation of the aerodynamic power presented in the preceding chapter. Temporal lag of the aerodynamic response was quantified by means of the engineering aerodynamic model presented in section 5.2.1. In the model, the parameters were adjusted to match the dynamic lift coefficient and dynamic drag coefficient loops obtained during the CFD simulations. Then, these parameters were considered representative of the respective CFD simulations. Note that the angles of attack used in the present work were defined with respect to the flow velocity relative to the airfoil. The motion of the airfoil was therefore taken into account.

In the engineering model presented in section 5.2.1, the dynamic lift coefficient is calculated as the static lift coefficient at the effective angle of attack. Eq. (31) includes four added-mass terms, i.e. edgewise-acceleration, flapwise-acceleration, pitch-rate and pitch-acceleration terms. However, it was shown that only the pitch-rate and flapwise-acceleration terms have any influence on the stability limits while there was no motion in the flapwise direction or rotation in the present computations. Therefore, all the added-mass terms were excluded in the present application:

$$C_L^{Dyn} = C_L^{St}(\alpha_E) \qquad (42)$$

The dynamic drag coefficient was calculated as in Eq. (32).

6.3.2 Results and discussion

A number of prescribed motion computations was carried out in order to analyze the dependency between the aerodynamic forces and the geometric angle of attack. The reduced frequency of the prescribed oscillations in the chordwise direction was k=0.079 (with $k=\omega C/2U$). The amplitude of the oscillation was $A=0.4C$. Figure 33 presents the following curves plotted against the geometric angle of attack:

- Static lift coefficient resulting from the time-marching 2D CFD with the non-moving DU96-W-180
- Dynamic lift coefficient loop resulting from the prescribed motion 2D CFD
- Dynamic lift coefficient loop modeled to match the dynamic 2D CFD response based on the 2D CFD polars

- Dynamic lift coefficient loop modeled assuming inviscid response; based on the 2D CFD polars
- Dynamic lift coefficient loop modeled using Beddoes-Leishman type [10,12] dynamic stall model; based on the 2D CFD polars

The direction of the presented loops was clockwise. The results showed that the dynamic-lift response resulting from prescribed motion 2D CFD was slower than the one modeled using the inviscid parameters for the temporal response. Neither the dynamic lift coefficient loop modeled using the Beddoes-Leishman type dynamic stall model [10,12] resembled that of the prescribed motion CFD computations.

The approximate dynamic 2D CFD response was modeled by tuning values of two (A_1 and b_1) out of four available parameters in the aforementioned engineering model. The other two were set to zero. However, the exact shape of the CFD response was impossible to obtain. The dynamic lift coefficient loop resulting from the prescribed motion 2D CFD was averaged over 20 periods of oscillation in order to decrease the influence of the higher-frequency fluctuations associated with vortex shedding.

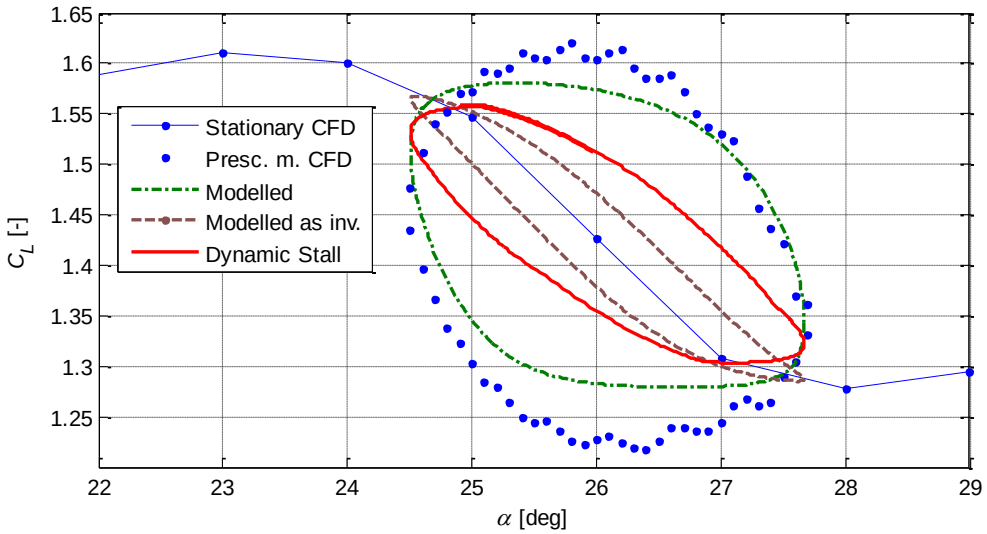

Figure 33: Lift coefficients from the 2D CFD with the non-moving DU96-W-180, 2D prescribed motion CFD and from two engineering models.

Apart from the dynamic lift, the characteristics of the dynamic drag were analyzed in the same fashion. The analysis is presented in Figure 34:

- Static drag coefficient resulting from the time-marching 2D CFD with the non-moving DU96-W-180
- Dynamic drag coefficient loop modeled using the same parameters as for modeling the dynamic 2D CFD response of C_L
- Dynamic drag coefficient loop modeled assuming inviscid response; based on the 2D CFD polars
- Dynamic drag coefficient loop resulting from the prescribed motion 2D CFD
- Dynamic drag coefficient loop modeled using Beddoes-Leishman type [10,12] dynamic stall model; based on the 2D CFD polars

The direction of the presented loops was counter-clockwise. The opening of the loop resulting from the prescribed motion 2D CFD simulation resembled that of the inviscid response and the one modeled using the Beddoes-Leishman model. However, the mean slope of the CFD loop was higher than of that representing inviscid response and the Beddoes-Leishman model.

From the results it was evident that it was not possible to model C_L and C_D simultaneously with the model described in section 5.2.1 as after tuning the parameters to match the prescribed motion CFD dynamic lift, the opening of the corresponding dynamic-drag loop was larger than that of the prescribed motion CFD. On the other hand, it was shown in the present work that the aerodynamic damping is more sensitive with respect to the lift than drag. Therefore, it is possible that modeling the dynamic lift is sufficient in order to predict stall-induced vibrations.

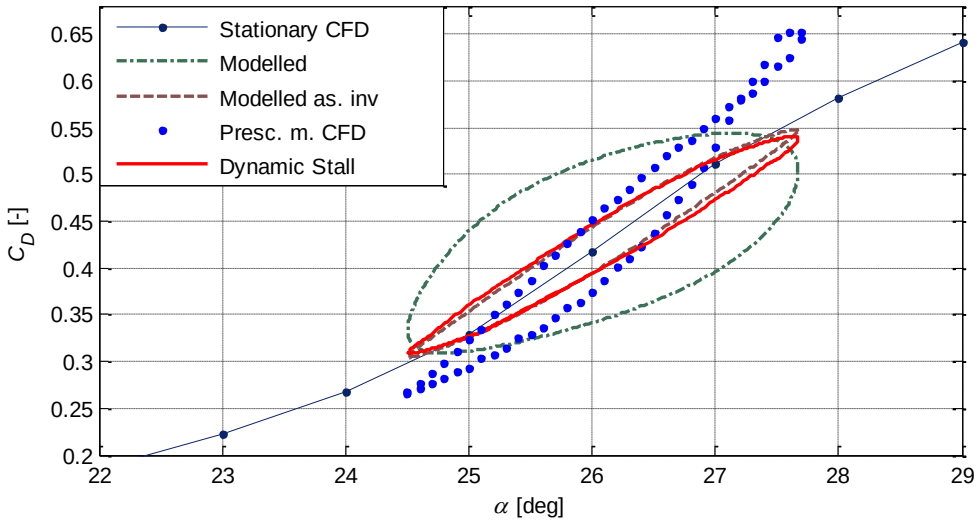

Figure 34: Drag coefficients from the 2D CFD with the non-moving DU96-W-180, 2D prescribed motion CFD and from two engineering models; chordwise oscillation

Additionally, a comparison of the unsteady aerodynamics in the aforementioned prescribed motion was made with the unsteady aerodynamics regarding the same airfoil performing prescribed pitching motion. The reason for such a comparison was to analyze whether, in stall, the same geometric angle of attack may be used to describe or model airfoils performing different kinds of motion in stall. The comparison of lift and drag loops plotted as functions of the geometric angle of attack, regarding the DU96-W-180 airfoil 2D CFD models performing chordwise and pitching oscillations, is presented in Figure 35. The comparison is satisfactory as even though some discrepancies are visible between the corresponding curves, these curves are relatively close to each other.

The comparison of lift and drag loops plotted as functions of the geometric angle of attack, regarding the DU96-W-180 airfoil 3D CFD models performing chordwise and pitching oscillations, is presented in Figure 36. As in the case of the 2D simulations presented above, the comparison is satisfactory as even though some discrepancies are visible between the corresponding curves, these curves are relatively close to each other. This indicates that the geometric angle of attack may be used to model airfoils performing different kinds of motion in stall.

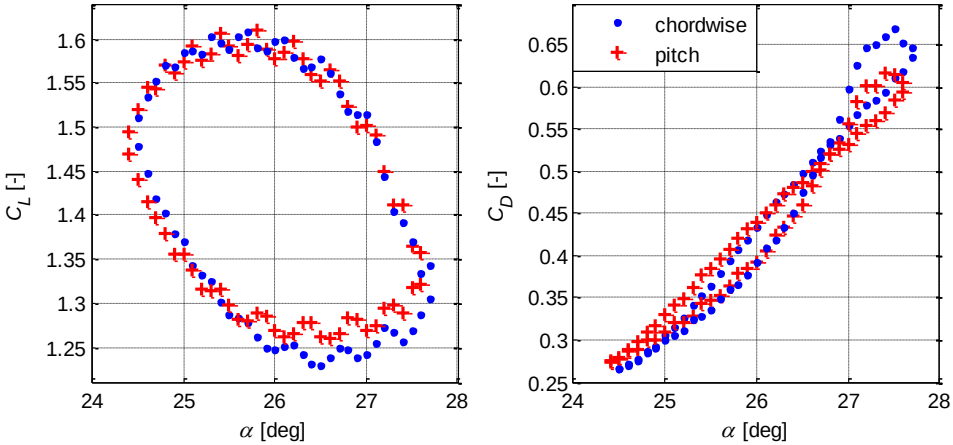

Figure 35: Comparison of dynamic lift and drag loops regarding 2D airfoil models performing chordwise rectilinear oscillation and pitching motion

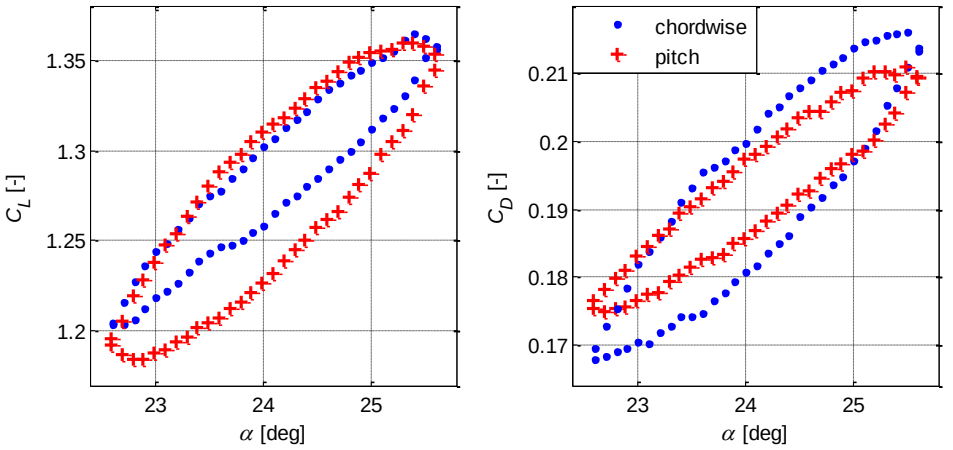

Figure 36: Comparison of dynamic lift and drag loops regarding 3D airfoil models performing chordwise rectilinear oscillation and pitching motion

An analysis of the dependency between the aerodynamic forces and the geometric angle of attack similar to that carried out in 2D was carried out in 3D. Results concerning the lift force are presented in Figure 37 where the included curves correspond to:

- Static lift coefficient resulting from the time-marching 3D CFD with the non-moving DU96-W-180
- Dynamic lift coefficient loop resulting from the prescribed motion 3D CFD
- Dynamic lift coefficient loop modeled assuming inviscid response; based on the 3D CFD polars
- Dynamic lift coefficient loop modeled using Beddoes-Leishman type [10,12] dynamic stall model; based on the 3D CFD polars

The direction of the presented loops was clockwise. The results were surprising as the characteristic of the prescribed motion CFD dynamic-lift loop was completely different from the corresponding 2D loop. The loop averaged over 30 oscillation periods had the opposite slope, as if the static values were of positive instead of negative slope. Modeling the 3D CFD dynamic lift with the tools from section 5.2.1 or the Beddoes-Leishman model [10,12] was difficult and will require further investigation and possibly another approach. This is because

these models are not developed to model loops with a slope of opposite sign to that of the steady values.

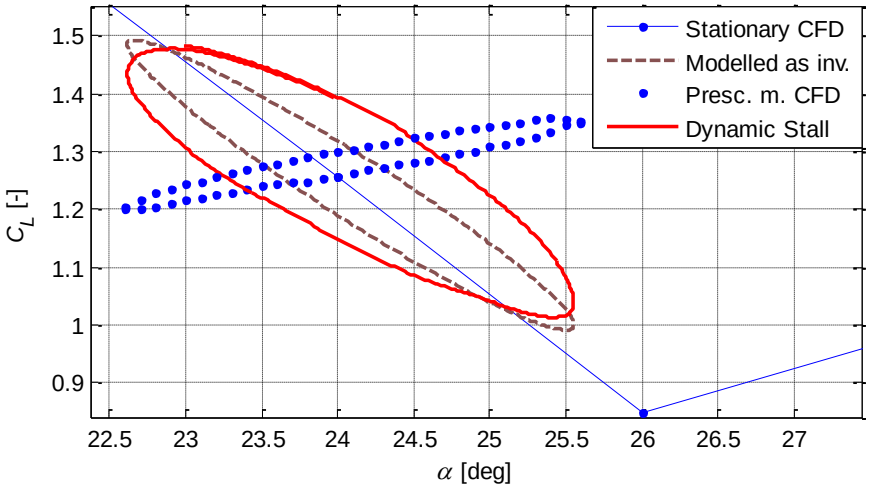

Figure 37: Lift coefficients from the 3D CFD with the non-moving DU96-W-180, 3D prescribed motion CFD and from two engineering models.

Characteristics of 3D drag were analyzed and the results are presented in Figure 38:

- Static drag coefficient resulting from the 3D CFD with the non-moving DU96-W-180
- Dynamic drag coefficient loop resulting from the prescribed motion 3D CFD
- Dynamic drag coefficient loop modeled assuming inviscid response; based on the 3D CFD polars
- Dynamic drag coefficient loop modeled using Beddoes-Leishman type [10,12] dynamic stall model; based on the 3D CFD polars

The direction of the presented loops was counter-clockwise. The opening of the CFD loop was similar to that representing inviscid response. The opening of the loop obtained by the Beddoes-Leishman model [10,12] was larger. The slope of the CFD loop did not follow the slope of the static drag coefficient while the slope of the loops representing the two models did.

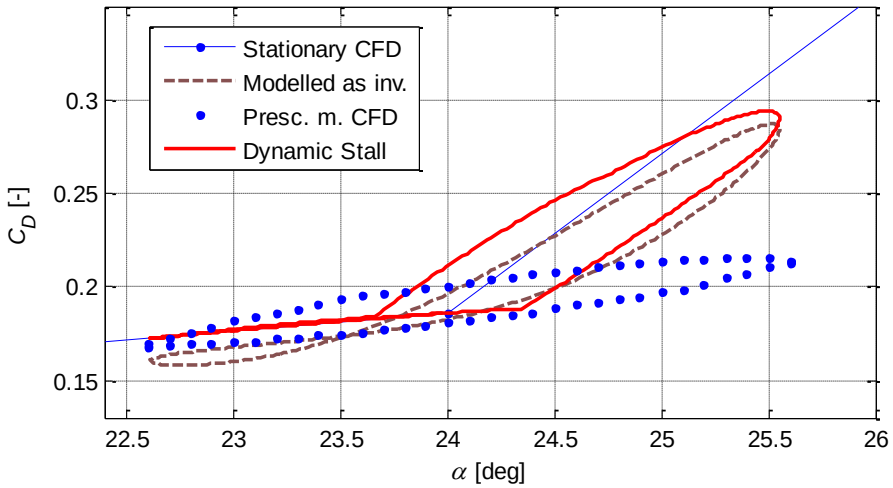

Figure 38: Drag coefficients from the 3D CFD with the non-moving DU96-W-180, 3D prescribed motion CFD and from two engineering models.

Generally, both 2D and 3D simulations showed some temporal lag of the dynamic lift and dynamic drag coefficients indicating that the state-of-the-art in modeling the dynamic lift and drag in deep stall in the aeroelastic codes may be inaccurate. Therefore, the present results indicate that the aeroelastic codes may inaccurately model edgewise vibrations. Further, it was indicated that the positive slope of the lift loop of 3D computations may correspond to an increased aerodynamic damping compared to the negative slope of 2D computations. This is because a prescribed motion 3D CFD computation presented in section 6.2.2, corresponding to the one analyzed in this section, was shown to poses positive aerodynamic damping while a corresponding prescribed motion 2D CFD computation was shown to poses negative aerodynamic damping.

Further, it should be investigated whether 2D or 3D CFD simulations reflect the actual stall characteristics better as it was not explicitly shown in the present work that 3D simulations represent the real-life flow conditions better than 2D. However, Shur *et al.* [32] and Strelets [33] indicate that 3D DES computations resolve stalled flows around airfoils better than 2D RANS.

It should also be investigated whether it is possible to tune the parameters of the Beddoes-Leishman [10,12] model to accurately represent the dynamic lift and drag loops obtained by CFD. The inability of the present model to predict the dynamic lift and drag using the same set of parameters in 2D, and inability to model the lift in 3D, indicate that the present engineering approach may be insufficient.

Note that the present work performed in the context of blade standstill vibrations, simplifies the problem by omitting the effects of blade twist and taper as well as the shear, turbulence and skew in the incoming flow. The reason for this is to learn about the most basic mechanisms involved in vibrations of wind turbine blades, before embarking on the full very complex problem as it occurs on actual turbines

7 Conclusions

This section briefly outlines the main conclusions drawn from the present work described in the enclosed papers:

1. Even a relatively low amount of temporal lag added to the aerodynamic response of a quasi-steady-aerodynamics airfoil model in stall may significantly increase the aerodynamic damping and therefore influence the aerodynamic stability limits. This indicates that stat-of-the-art aeroelastic codes may inaccurately model airfoil aerodynamic response and therefore blade standstill vibrations in deep stall. *

2. Vortex-induced vibrations may occur on modern wind turbine blades as the frequency of vortex shedding at which lock-in may occur was predicted close to the natural frequency of the first edgewise blade mode.**

3. Stall-induced vibrations indicated by 3D CFD computations are unlikely to occur on modern wind turbine blades at standstill conditions as the wind speed necessary for the onset of such vibrations was predicted too high to occur in normal conditions.**

4. Significant discrepancies were observed between the 2D and 3D CFD computations both in terms of the predicted aerodynamic damping and the characteristics of the dynamic aerodynamic response in stall.

* The conclusion was based on the results obtained by a simple engineering aerodynamic model which may represent the real-life phenomena better than a model assuming quasi-steady aerodynamics for airfoils in stall. However, the actual dynamic aerodynamic response of airfoils in stall is currently unknown. The work described in [V] is the first step towards analyzing such a response.

** Further work is required to verify conclusions (2) and (3) as the underlying computations were performed on 2D and 3D airfoils which are not necessarily representative to the whole wind turbine blades. Some of the simplifications made in the present computations were the lack of blade twist and taper as well as the lack of shear, turbulence and skew in the incoming flow. Further, the computations were performed at a limited number of angles of attack while it is not known whether the conclusions would hold at other angles.

7.1 Future work

Below is the list of the most important issues that need to be investigated in the future work:

1. Verify whether 2D or 3D CFD computations reflect real-life mechanisms of vibrations better as significant discrepancies were observed in the present work at angles of attack around 25 deg.

2. Investigate the effects of shear, turbulence and skew in the incoming flow. Experiments carried out on circular cylinders showed that both the shear and turbulence decrease the amplitude of vortex-induced vibrations.

3. Perform computations at other angle-of-attack regimes to investigate whether the phenomena studied in the present work retain the same characteristics at other angles of attack.

4. Investigate the amplitudes of limit cycles. Knowing the levels of these amplitudes would help to determine the risk of turbine failure due to specific kinds of vibration..

5. Investigate the effects of blade twist and taper as well as of airfoil shape on the aeroelastic stability limits.

6. Perform a 3D DES time-marching computation on a full wind turbine blade to investigate further the limitations of 2D and 3D CFD computations on airfoils.

7. Investigate further the characteristics of the dynamic aerodynamic response in stall and create accurate engineering models for predicting stall-induced and vortex-induced vibrations in aeroelastic codes.

References

[1] Bak, C.; Madsen, H.Aa.; Gaunaa, M.; Skrzypiński, W.; Paulsen, U.; Møller, R.; Hansen, P.; Rasmussen, M.; Fuglsang, P.: *DANAERO MW: Instrumentation of the NM80 2.3MW wind turbine including the LM 38.8 m blade and the meteorology mast at Tjæreborg*; Risø Internal Report

[2] Sumer, M.; Fredsøe, J.: *Hydrodynamics around cylindrical structures, Advanced Series on Ocean Engineering* – Volume 12; World Scientific; 1997

[3] Dowell, E.H.; Clark, R.; Cox. D.; Curtiss, H.C. Jr.; Edwards, J.W.; Hall, K.C.; Peters, D.A.; Scanlan, R.; Simiu, E.; Sisto, F.; Strganac, T.W.: *A Modern Course in Aeroelasticity*; Fourth Revised and Enlarged Edition; Kluwer Academic Publishers; 2004

[4] Blevins, R.D.: *Flow-induced Vibrations*; Van Nostrand; 1977

[5] Feng, C.C.: *The measurement of vortex-induced effects on flow past stationary and oscillating circular and D-section cylinders*; M.Sc. Thesis; The University of British Columbia; 1968

[6] Gaunaa, M.; Larsen, T.J.: *Stilstandslaster;* chapter in *Forskning i Aeroelasticitet*; ed. Bak, C.; Risø-R-1434(DA) in Danish, Risø DTU National Laboratory for Sustainable Energy; Roskilde; 2002

[7] Hansen, M.H.: *Aeroelastic instability problems for wind turbines*; *Wind Energy*; 10:551–577; 2007

[8] Buhl, T.: *Edgewise vibrations in stand still*; chaprer in *Research in Aeroelasticity EFP-2006*; ed. Bak, C.; Risø-R-1611(EN), pages 63–72; Risø National Laboratory for Sustainable Energy, Technical University of Denmark; Roskilde; June 2007

[9] Riziotis, V.A.; Voutsinas, S.G.; Politis, E.S.; Chaviaropoulos, P.K.: *Stability analysis of parked wind turbine blades using a vortex model*, Proceedings of TORQUE 2010: The Science of Making Torque from Wind; Crete, Greece; June 28-30 2010

[10] Leishman, J.G.; Beddoes, T.S.: *A semi empirical model for dynamic stall;* Journal of the American Helicopter Society 34, 3 (1989); DOI:10.4050/JAHS.34.3 (15 pages); 1989

[11] Øye, S.: *Dynamic stall simulated as time lag of separation*; Proceedings of the EWEC; Thessaloniki, Greece; Oct. 1994

[12] Hansen, M.; Gaunaa, M.; Madsen, H.Aa.: *Beddoes-Leishman type dynamic stall model in state-space and indicial formulations*; Risø-R-1354(EN); 40 p.; 2004

[13] Bertagnolio, F.; Rasmussen, F.; Sørensen N.N.; Johansen, J.; Madsen, H.Aa.: *A stochastic model for the simulation of wind turbine blades in stochastic stall*; Wind Energy; 13:323-338; 2010

[14] Larsen, T.J.; *How 2 HAWC2, the users manual*; Technical Report Risø-R-1597(EN); Risø National Laboratory; Roskilde, Denmark; 2007.

[15] Hand, M.M.; Simms, D.; Fingersh, L.J.; Jager, D.W.; Cotrell J.R.; Schreck, S.; Larwook, S.M.: *Unsteady aerodynamics experiment Phase VI: wind tunnel test confi gurations and available data campaigns*; *NREL/TP-500-29955*; National Renewable Energy Laboratory; Golden, CO; 2001

[16] Jonkman, J.; Butterfield, S.; Musial, W.; Scott, G.: *Definition of a 5-MW reference wind turbine for offshore system development*; *NREL/TP-500-38060*; National Renewable Energy Laboratory; 2007

[17] *IEA Wind, Task 23. Offshore wind energy technology deployment*; [Online]; Available: http://www.ieawind.org/Annex_XXIII.html; Accessed January 2012

[18] Hansen, M.H.: *Bias effect of self-induced turbulence on the stall-flutter limit of an airfoil section*; The sixteenth international congress on sound and vibration; Kraków; 5-9 July 2009

[19] Buhl, T.; Gaunaa, M.; Bak, C.: *Potential Load Reduction Using Airfoils with Variable Trailing Edge Geometry*; Journal of Solar Energy Engineering; Vol. 127; Nov. 2005

[20] Jones, R.T.: *The Unsteady Lift of a Wing of Finite Aspect Ratio*; Tech. Rep. 681; NACA Report; 1940

[21] Theodorsen, T.: *General theory of aerodynamic instability and the mechanism of flutter;* National Advisory Committee for Aeronautics; Report No. 496; 1949

[22] Øye, Stig: Instationære, aerodynamiske kræfter på todimensionalt vingeprofil, Afdelingen for Fluid Mekanik, Den Polytekniske Læreanstalt Lyngby, Nov. 1981

[23] Timmer, W.A.; van Rooij, R.P.J.O.M: *Summary of the Delft University wind turbine dedicated airfoils*; AIAA-2003-0352; 2003

[24] Timmer, W. A.: *Two-dimensional aerodynamic characteristics of wind turbine airfoils at high angles-of-attack*; 3rd Conference on The science of making Torque from Wind, Crete, Greece; June 2010

[25] Michelsen J.A.: *Basic3D – a platform for development of multiblock PDE solvers.* Report AFM 92-05, Dept. of Fluid Mechanics, Technical University of Denmark, DTU, Denmark; 1992

[26] Michelsen J.A.: *Block structured multigrid solution of 2D and 3D elliptic PDE's.* Report AFM 94-06, Dept. of Fluid Mechanics, Technical University of Denmark, DTU, Denmark; 1994

[27] Sørensen N.N.: *General purpose flow solver applied to flow over hills.* PHD Dissertation, Risø-R-827(EN), Risø National Laboratory, Roskilde, Denmark; 1995

[28] Sørensen N.N.: *HypGrid a 2-D Mesh Generator* Risø National Laboratory, Roskilde, Denmark; 1998

[29] Heinz, J., Sørensen, N.N.; Zahle, F.: *Investigation of the load reduction potential of two trailing edge flap controls using CFD*; Wind Energy; 14: 449–462; DOI: 10.1002/we.435; 2011

[30] Pantazopoulos, M.S.: *Vortex-induced vibration parameters: critical review*; Proceedings of the International Conference on Offshore Mechanics and Arctic Engineering; American Society of Mechanical Engineers; 1994

[31] Novak, M.; Tanaka, H.: *Pressure Correlations on a Vibrating Cylinder*; Proceedings of the Fourth International Conference, Wind Effects on Buildings and Structures; pp. 227-232; Heathrow, England; 1975

[32] Shur, M.; Spalart P.R.; Strelets, M.; Travin, A.: *Detached-eddy simulation of an airfoil at high angle of attack*; Engineering Turbulence Modelling and Experiments – 4; Elsevier Science Ltd.; 1999

[33] Strelets, M.: *Detached Eddy Simulation of Massively Separated Flows*; AIAA 2001-0879; 39th AIAA Aerospace Sciences Meeting and Exhibit January; Reno, NV; 8-11 January 2011

[I]

ewec 2010 WARSAW
Europe's premier wind energy event
Warsaw, Poland, 20-23 April 2010

Wind turbine blade vibration at standstill conditions – the effect of imposing time lag onto aerodynamic response

Witold Skrzypiński
Risø DTU
wisk@risoe.dtu.dk

Mac Gaunaa
Risø DTU
macg@risoe.dtu.dk

Abstract

Aeroelastic codes used for full-turbine computations assume quasi-steady aerodynamics at standstill when the blades are in deep stall. Under these conditions these codes often show negatively damped edgewise blade vibrations. On the other hand, it is unlikely that the real-life aerodynamic response in deep stall is quasi-steady. This work focuses on analyzing how the aerodynamic damping is influenced by temporal lag in aerodynamic response. Therefore, it investigates whether it is inaccurate to model turbines at standstill with present aerodynamic codes. This is achieved by introducing different amounts of temporal lag onto aerodynamic response of an elastically-mounted-airfoil model. Both the time-domain and frequency-domain analyses show that aerodynamic damping is significantly increased even when relatively low amount of lag is introduced in the model. This indicates that the aeroelastic codes may overpredict edgewise vibrations in deep stall.
Keywords: standstill, parked, vibrations, edgewise

1 Introduction

The introduction of computational models for the dynamic aeroelastic response of wind turbines spurred numerous investigations of various dynamic issues. These investigations have assisted in understanding and overcoming problems as well as have helped designing reliable turbines. In some cases specific problems have necessitated evolution of new or improved sub-models in the aeroelastic computational tools. An example of such models are the so called dynamic stall models by Øye [1] as well as by Hansen, Gaunaa and Aagard-Madsen [2] which model the dynamic aerodynamic response from the onset of separation until the flow over the airfoil is fully separated.

The existing aeroelastic tools for investigating the dynamic response of wind turbines in standstill indicate that the edgewise vibrational mode of the wind turbine blades may be negatively damped. This would lead to very big fatigue loads or even failure. Such vibrations may be exhibited at newly erected wind turbines' blades before the turbines are connected to the grid, as well as at turbines undergoing maintenance or suffering from power loss. The aerodynamically unstable regions occur in deep stall, for angles of attack far from normal operation. Under these conditions the underlying aerodynamic coefficients are uncertain. Therefore, it was initially assumed that the vibrations existed only in computations. In recent years, however, turbine failures at standstill conditions reported from the industry have spurred new analytic and numeric investigations by Gaunaa and Larsen [3] as well as by Buhl [4]. These investigations concluded that the standard aerodynamics existing in aeroelastic codes for deep stall is effectively quasi-steady. Simultaneously, it is feasible that the real-life aerodynamic response is slower than quasi-steady. Moreover, it was demonstrated that the aerodynamic damping can be either augmented or removed by adjusting the steady aerodynamic coefficients within the limits of uncertainty of the underlying aerodynamic data.

The aim of this work was to analyze how the aforementioned aerodynamic damping is sensitive to time lag in the aerodynamic response. This was achieved by imposing different amounts of lag in the aerodynamic response of both nonlinear and linearized two-dimensional, three-degree-of-freedom models of an elastically mounted airfoil. The models allow for different inflow angles. The nonlinear model was solved in the time domain. The linearized model, in turn, was solved in both the time and frequency domains. The relevant damping ratios were drawn from the analyses of both models and compared.

2 Computational tool

2.1 Setup

The setup used in this work was originally presented by Buhl, Gaunaa and Bak [5]. It is shown in Figure 1. *T* and *N* are the chordwise and normal-to-chord aerodynamic force components.

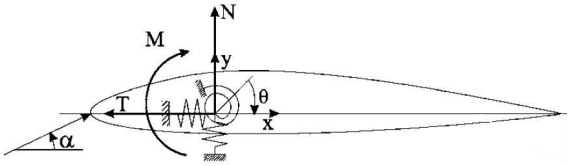

Figure 1: 2-D 3-DOF aeroelastic model, reproduced from Buhl *et al* [5]

M is the aerodynamic moment, α is the angle between the chord and the inflow, *x*, *y* and Θ are degrees of freedom of the 2-D aeroelastic system with linear stiffness and damping. The airfoil data used in the computations is for NACA 63-416. The chord length is 1 m, and the unit-depth mass of the airfoil equals 40 kg. The hinge point is assumed to be at a quarter chord. The spring constants are chosen in such a way that the vibrations in flapwise, edgewise and torsional directions have frequencies of 1, 2 and 10 Hz, respectively. Viscous damping is set to zero. Inflow velocity equals 10 m/s, and air density equals 1.225 kg/m^3.

2.2 Nonlinear structural model

The aforementioned system is governed by the following equations of motion:

$$\begin{aligned} M\ddot{X} + c_x\dot{X} + k_xX &= F_X + Ml\dot{\Theta}^2\cos(\Theta+\Theta_{geom}) + Ml\ddot{\Theta}\sin(\Theta+\Theta_{geom}) \\ M\ddot{Y} + c_y\dot{Y} + k_yY &= F_Y + Ml\dot{\Theta}^2\sin(\Theta+\Theta_{geom}) - Ml\ddot{\Theta}\cos(\Theta+\Theta_{geom}) \\ \ddot{\Theta}(I_{cg}+Ml^2) + c_\Theta\dot{\Theta} + k_\Theta\Theta &= F_\Theta + Ml\ddot{X}\sin(\Theta+\Theta_{geom}) - Ml\ddot{Y}\cos(\Theta+\Theta_{geom}) \end{aligned} \quad (1)$$

where Θ_{geom} is the angle between the x axis and the line through the elastic axis and the center of gravity when the profile is in the equilibrium state without the aerodynamic forces involved. F_X and F_Y are the aerodynamic force components. F_θ is the aerodynamic moment around the hinge point, positive clockwise. Further, *l* is the distance between the center of gravity and the hinge point. It is necessary to calculate the moment of inertia with respect to the hinge point, given the moment of inertia with respect to the center of gravity, according to the Steiner theorem.

2.3 Nonlinear aerodynamic model

Dynamic stall models used in aeroelastic codes for full-blade computations deal with dynamics of the separation point. Such an approach is only valid for partly attached flows and cannot govern airfoils in deep stall. In deep stall, these models assume quasi-steady aerodynamics. In this work, the lift is governed by a model that may presumably reflect behavior of a wind turbine blade vibrating at standstill conditions – in deep stall – better than a model assuming quasi-steady aerodynamics.

The dynamic lift coefficient is calculated as the static lift coefficient at an effective angle of attack:

$$C_L^{Dyn} = C_L^{St}(\alpha_E) \quad (2)$$

The effective angle of attack (α_E) is the angle between the airfoil's chord and a line representing the disturbed airflow relative to the airfoil. It is calculated as:

$$\alpha_E = \alpha_{3/4}(1 - A_1 - A_2) + x_1 + x_2 \quad (3)$$

where $\alpha_{3/4}$ is the angle of attack as observed at the three-quarter chord. A_1 and A_2 constitute the first half of the parameters defined in the subsequent description of the aerodynamic time lag. Further, x_1 and x_2 are the aerodynamic-state variables governed by the differential equations:

$$\dot{x}_i + T_u^{-1}b_ix_i = b_iA_iT_u^{-1}\alpha_{3/4} \qquad i = 1,2 \quad (4)$$

where b_i constitute the second half of the parameters used for defining the aerodynamic time lag. The time-varying parameter, T_u, equals:

$$T_u = c/2V_{rel} \quad (5)$$

where *c* is chord length and V_{rel} is airflow velocity relative to the airfoil.

The choice of parameters – namely: A_1, A_2, b_1, b_2 – characterizes a specific temporal behavior of the aerodynamic model. Such a choice is visualized by means of the unit response function:

$$\varphi = 1 - A_1e^{-b_1s} - A_2e^{-b_2s} \quad (6)$$

where s is non-dimensional time, $\frac{2}{c}\int_0^t V_{rel}dt$. The faster a particular function converges to 1, the closer the respective aerodynamic response is to quasi-steady. The choice of four exemplary parameter sets used for this study is presented in Figure 2, together with the respective

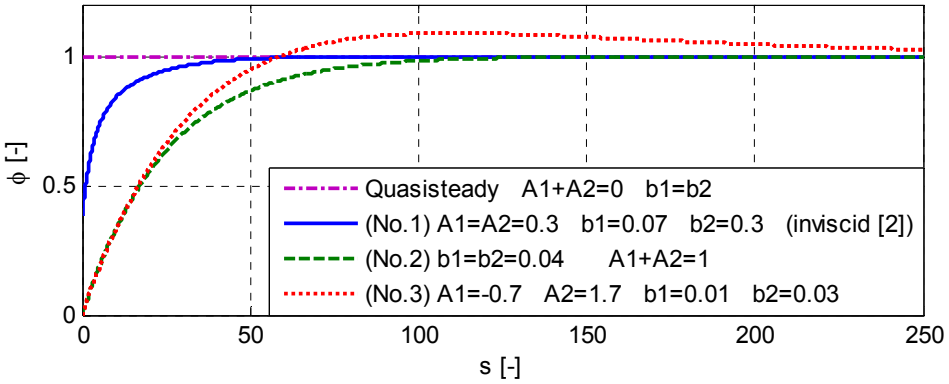

Figure 2: The four response functions corresponding to the aerodynamic-parameter sets

aerodynamic response functions. The quasi-steady response function corresponds to no time lag because its parameters effectively bypass the lagging effect of the dynamic model. This corresponds to the aerodynamic response one would get from standard aeroelastic codes in deep stall. The aerodynamic response function No. 1 is an approximate representation of a thin airfoil's inviscid response [6]. Therefore, it is most likely faster than the response of a real-life airfoil in deep stall. However, the actual aerodynamic response of such an airfoil is currently unknown.
The aerodynamic response functions No. 2 and No. 3 are both significantly slower than the response function No. 1. Function No. 3 is initially the same as No. 2. However, it introduces an overshoot in the response. The aeroelastic behavior, including damping characteristics, of the 3-DOF aeroelastic system depends on the aforementioned response functions which, in turn, are defined by the parameters A_1, A_2, b_1, b_2. Functions No. 2 and No. 3 are not meant to represent any particular real-life aerodynamic system but to investigate how the aerodynamic damping depends on the response-function shape.

2.4 Linearized structural model

The main concern of the current investigation is stability analysis of the system at different inflow angles. For this reason the aforementioned time-domain analysis of the nonlinear system is aided by both time-domain and eigenvalue analyses of a linearized system. Eigenvalue analysis is more effective for investigating system's stability from both, a computational and practical perspective. It saves computation time and allows for easier interpretation of results than the time-domain analysis does. The linearized system of equations of motion, Eq. (1), is presented below:

$$M\ddot{X} + c_x\dot{X} + k_xX = F_X^{lin} + Ml\ddot{\Theta}\sin(\Theta_{geom})$$
$$M\ddot{Y} + c_y\dot{Y} + k_yY = F_Y^{lin} - Ml\ddot{\Theta}\cos(\Theta_{geom})$$
$$\ddot{\Theta}(I_{cg} + Ml^2) + c_\Theta\dot{\Theta} + k_\Theta\Theta = F_\theta^{lin} + Ml\ddot{X}\sin(\Theta_{geom}) - Ml\ddot{Y}\cos(\Theta_{geom}) \quad (7)$$

where F_X^{lin} and F_Y^{lin} are the aerodynamic force components. F_θ^{lin} is the aerodynamic moment. All components are linearized around equilibrium positions which depend on the inflow angle.

2.5 Linearized aerodynamic model

To obtain a fully linearized model, the aerodynamic coefficients are also linearized. The lift coefficient is expressed as:

$$C_L^{lin} = C_L^0 + \frac{dC_L^0}{d\alpha}\alpha_E^1 \quad (8)$$

where C_L^0 is the lift coefficient at the equilibrium state. Further, α_E^1 is a small perturbation of the effective angle of attack from its equilibrium value, calculated as:

$$\alpha_E^1 = \alpha_{3/4}^1\phi(0) + x_1^1 + x_2^1 \quad (9)$$

where $\phi(0)$ is the initial value of the respective response function. Variables x_1^1 and x_2^1 are small perturbations of the aerodynamic-state variables, x_i, around their equilibrium values. They are calculated similarly to what is done in [2], by linearization of Eq. 4:

$$\dot{x}_i^1 + T_0^{-1}b_ix_i^1 = b_iA_iT_0^{-1}\alpha_{3/4}^1 \qquad i = 1,2 \quad (10)$$

where $T_0 = c/(2U_0)$. The variable $\alpha_{3/4}^1$ is a small perturbation of the three-quarter-chord angle of attack from its equilibrium value.

3 Validation of the models

The dependence of the chordwise damping ratio on the choice of the response function is

presented later in the paper. In the time-domain analysis, the aforementioned damping ratio is calculated as:

$$\zeta = \frac{\delta}{\sqrt{(2\pi)^2+\delta^2}} \tag{11}$$

where δ is the logarithmic decrement. It is calculated as:

$$\delta = \frac{1}{n} ln \frac{x_0}{x_n} \tag{12}$$

where, in a given time span, x_0 is the first displacement peak and x_n is a peak n periods away. The peaks are found in a time series of the profile's chordwise displacement.

In eigenvalue analysis of the linearized system, the damping ratio is calculated differently than in the time-domain analysis, i.e.:

$$\zeta_i = \frac{-Re(\lambda_i)}{\varpi_{n\,i}} \qquad i=1,\ 2,\ 3 \tag{13}$$

where $Re(\zeta_i)$ is a real part of the eigenvalue entry corresponding to a given mode. Further, $\omega_{n\ i}$ is the undamped natural frequency of that mode defined as:

$$\varpi_{n\,i} = \sqrt{Re(\lambda_i)^2+Im(\lambda_i)^2} \tag{14}$$

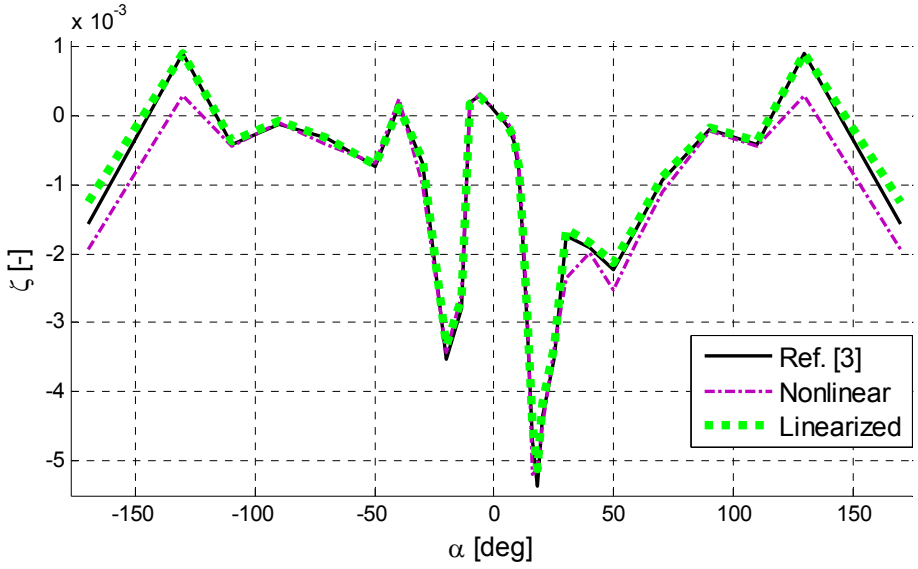

Figure 3: Validation of the damping ratios of the nonlinear and linearized models with the reference linear model [3]; quasi-steady aerodynamic response

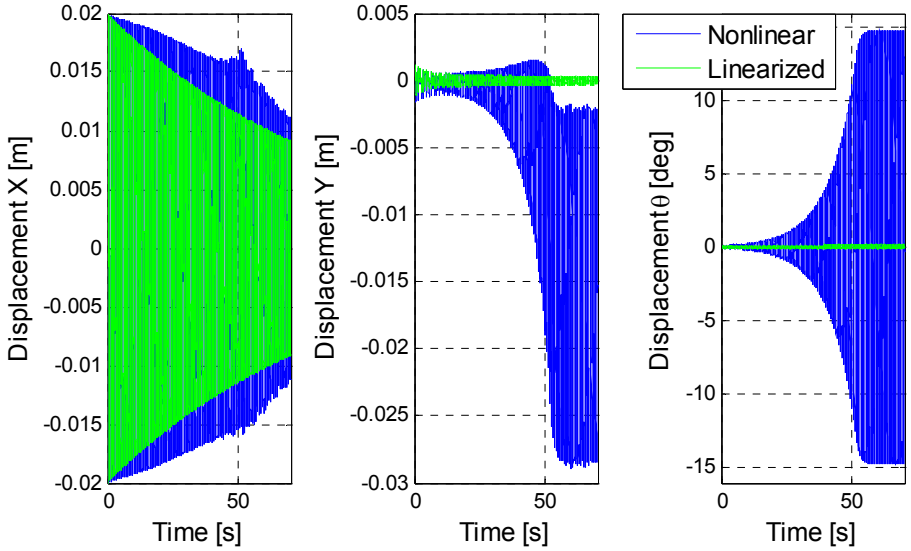

Figure 4: Displacement time series in the x, y and Θ directions of both the nonlinear and the linearized models; quasisteady aerodynamic response; inflow at 130 deg

Both the nonlinear and linearized aeroelastic models are validated by comparing the chordwise damping ratios obtained using the quasi-steady aerodynamic response with the reference damping ratio from the analytical linearized 1-DOF quasi-steady model [3]. This comparison is presented in Figure 3. It verifies the present implementation. In fact, the linearized model fits the reference model better than the nonlinear does. This is understandable as the reference model is linear. The difference between the nonlinear and linear models is mostly visible in the inflow-angle region above 110 and below -110 degrees. There, the nonlinear curve presents a certain offset relative to the other two. A comparative plot of the displacement time series at the inflow angle of 130 deg is presented in Figure 4. It is made in order to gain an insight into the differences visible in Figure 3. As it is seen in Figure 3, the damping ratio in the x direction corresponding to the nonlinear model depends on time which is not the case in the linearized

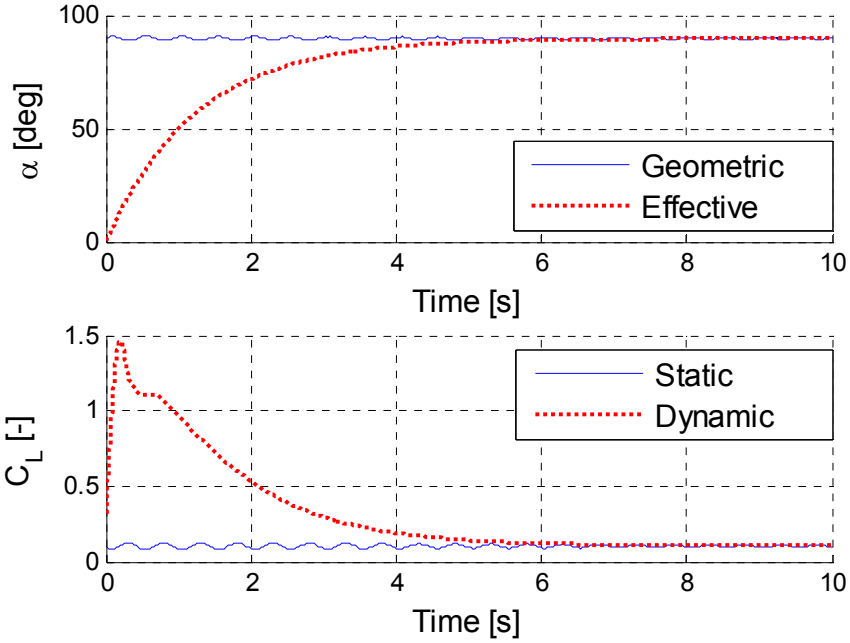

Figure 5: Aoa and C_L time series at 90 deg inflow; response function No. 2

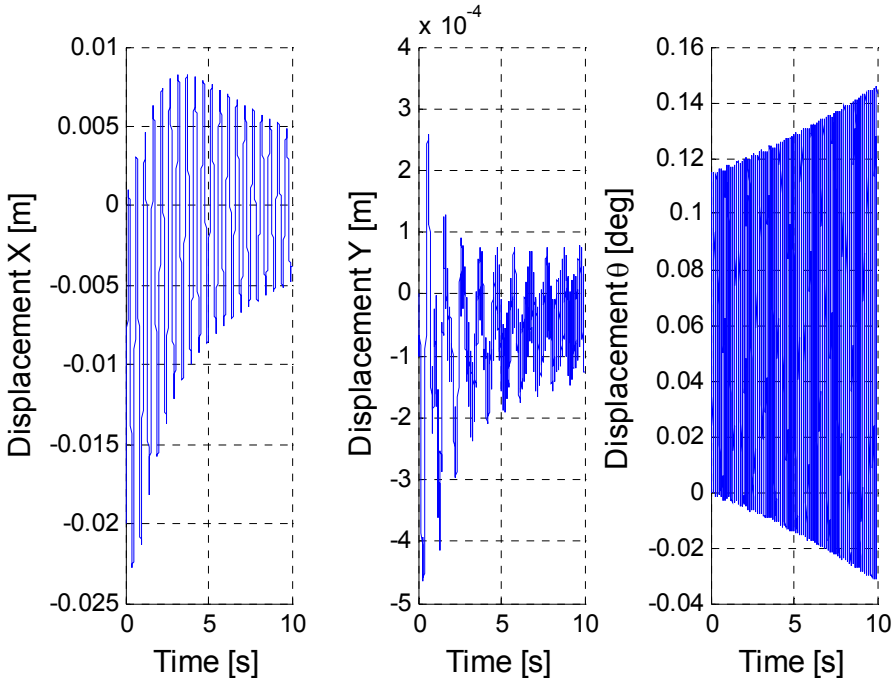

Figure 6: Displacement time series in x, y and Θ directions at 90 deg inflow; response function No. 2

model. This difference creates the aforementioned offset in Figure 3. In the nonlinear case, the amplitude in the Θ direction increases ending in a limit cycle. The equilibrium position in the y direction shifts downwards whereas the amplitude increases ending in a limit cycle as well. Such phenomena are not present in the results from linearized models.

The time span used for calculating the damping ratio in the nonlinear model was chosen in such a way that the damping-ratio curves corresponding to the two models fit well. This is possible since the damping ratio in the nonlinear model is time-dependent. This time span equals 10-13 seconds, except one case described later. 3 seconds is long enough for the displacement time series to exhibit a satisfactory number of amplitudes. This makes the calculation of the damping accurate. The first 10 seconds is disregarded to allow for the initial transients to subside. The effective angle of attack was defined in Eq. 3. Its value is a sum of the unit response function's initial value and the aerodynamic state variables defined in Eq. 4. The effective angle of attack initially equals the unit response function's initial value because the aerodynamic state variables are set to zero.

The dynamic lift is defined as the static lift at the

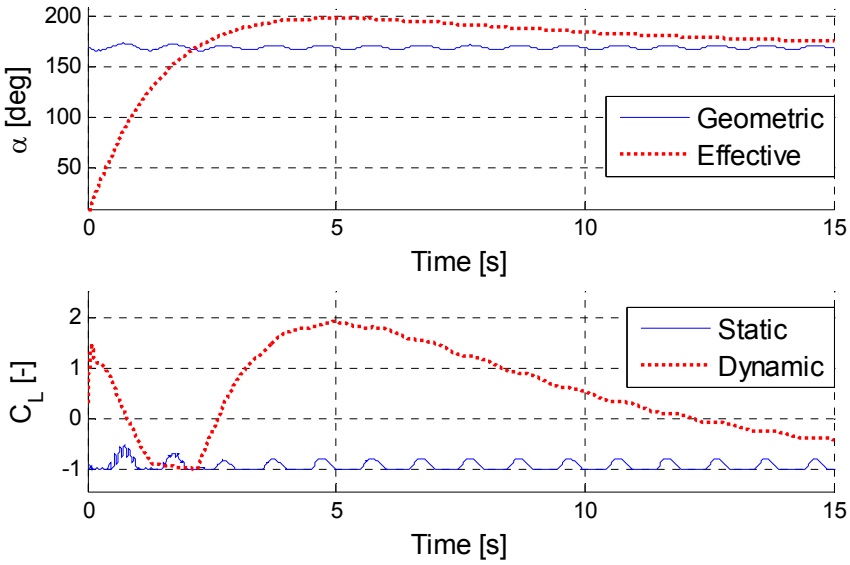

Figure 7: Aoa and C_L at 170 deg inflow angle; aerodynamic response function No. 3

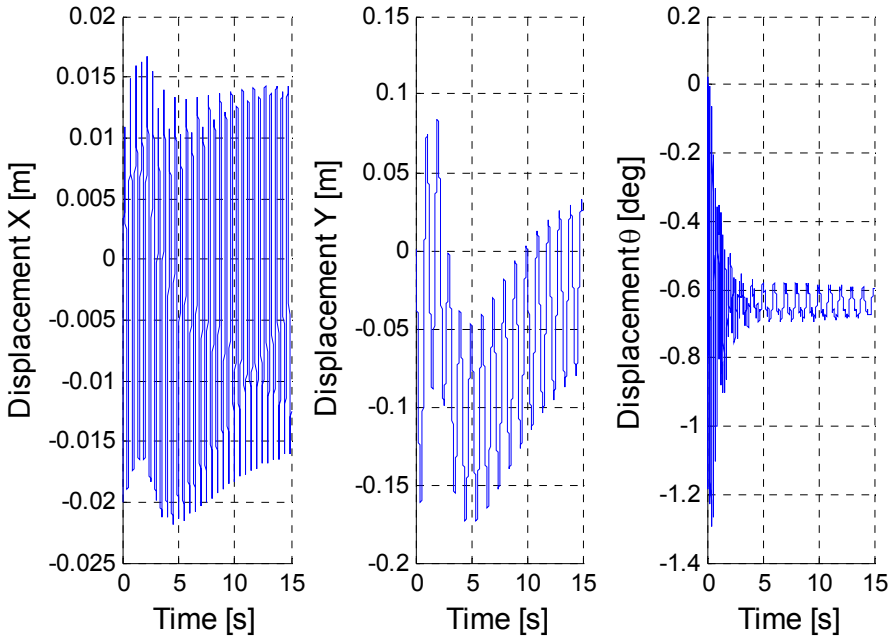

Figure 8: Displacement time series in x, y and Θ directions at 170 deg inflow; response No. 3

effective aoa (Eq. 2). Therefore, it requires the same amount of time to reach the static lift's vicinity as the effective aoa to reach the geometric aoa's vicinity. Hence, the first 10 sec of the simulation include transient response. This is especially important at high inflow angles characterized by low lift. Then, the dynamic lift overshoots as it passes through the separation point on its way to the static lift's vicinity. This can lead to some unphysical behavior of the model, e.g. temporary shift of the equilibrium position. The phenomenon is visualized in figures 5 and 6. The aforementioned overshoot of the lift is visible in Figure 5 (bottom) approx. during the first 6 seconds. The corresponding shift of the equilibrium position in x direction is visible in Figure 6 (left).

A similar problem is related with the overshooted aerodynamic response function No. 3 when the inflow angle equals approx. 170 or -170 degrees. This is because of the following reason. First, the dynamic lift overshoots around the separation point and then decreases in value as the effective aoa increases towards 170 degrees. Subsequently, after the effective aoa reaches 170 degrees, it overshoots by approx 20 degrees during the next few seconds. The dynamic lift overshoots correspondingly. This is because the lift is relatively high around 180 deg of aoa. This phenomenon is visualized in figures 7 and 8. As it is seen in Figure 8, the overshoots in the lift result in a shift of the equilibrium position which, in turn, influences calculation of the damping ratio. In order to exclude the effect of this phenomenon in further considerations, the damping ratios corresponding to response function No. 3 at both -170 deg and 170 deg of inflow angle are calculated in a 50-53 sec time interval, instead of otherwise used 10-13 sec.

It should be mentioned that the response of a real-life airfoil at approx. 180 deg of inflow angle is relatively complex. This is because the flow at 180 deg may be partly attached. In other words, an airfoil at 180 deg can be thought of as an airfoil with a sharp leading edge (the actual trailing edge) and a wide and blunt trailing edge (the actual leading edge). This increases complexity and unpredictability of its aerodynamic response around 180 deg of inflow angle.

4. Results of the time-domain analysis

Figure 9 presents the damping ratios corresponding to the response functions presented in Figure 2. These are calculated on both the nonlinear and linearized models. The grey rectangle in Figure 9 as well as in some other figures presented below indicate the range of inflow angles in which the usual dynamic stall models work properly, i.e. approx. between -20

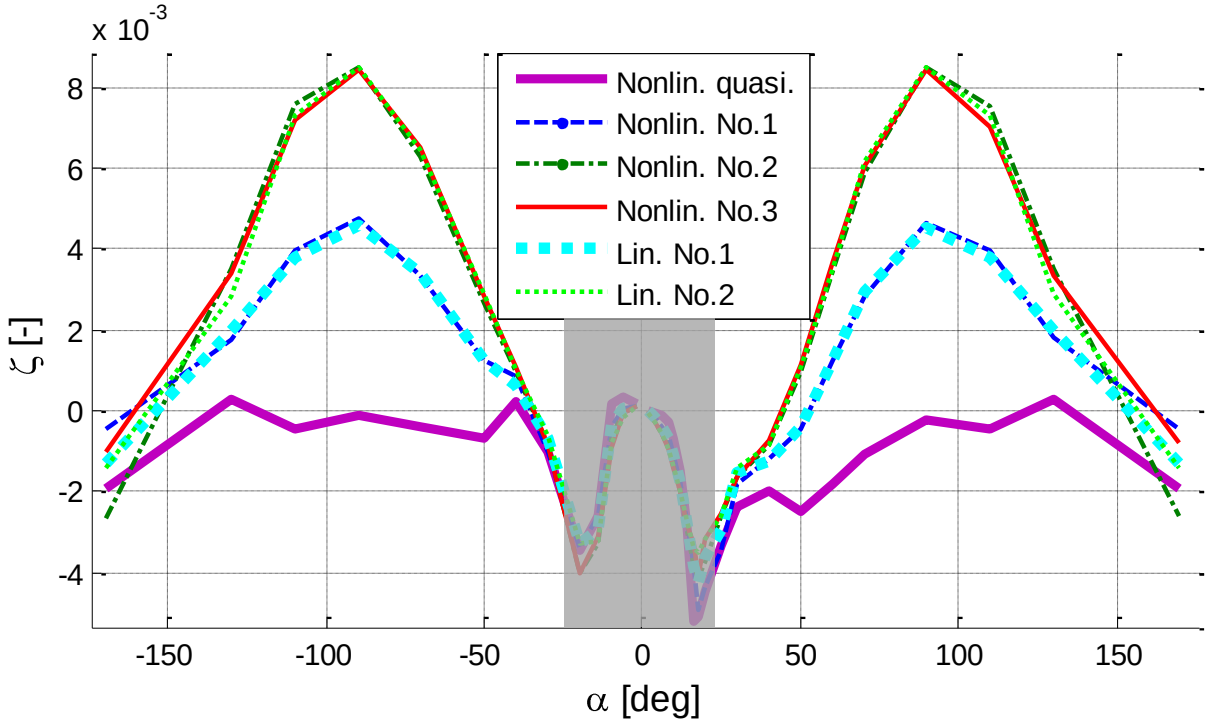

Figure 9: Edgewise damping ratios corresponding to the aerodynamic response functions from Figure 2, calculated on both the nonlinear and linearized models; the grey rectangle indicates inflow-angle range out of this work's focus

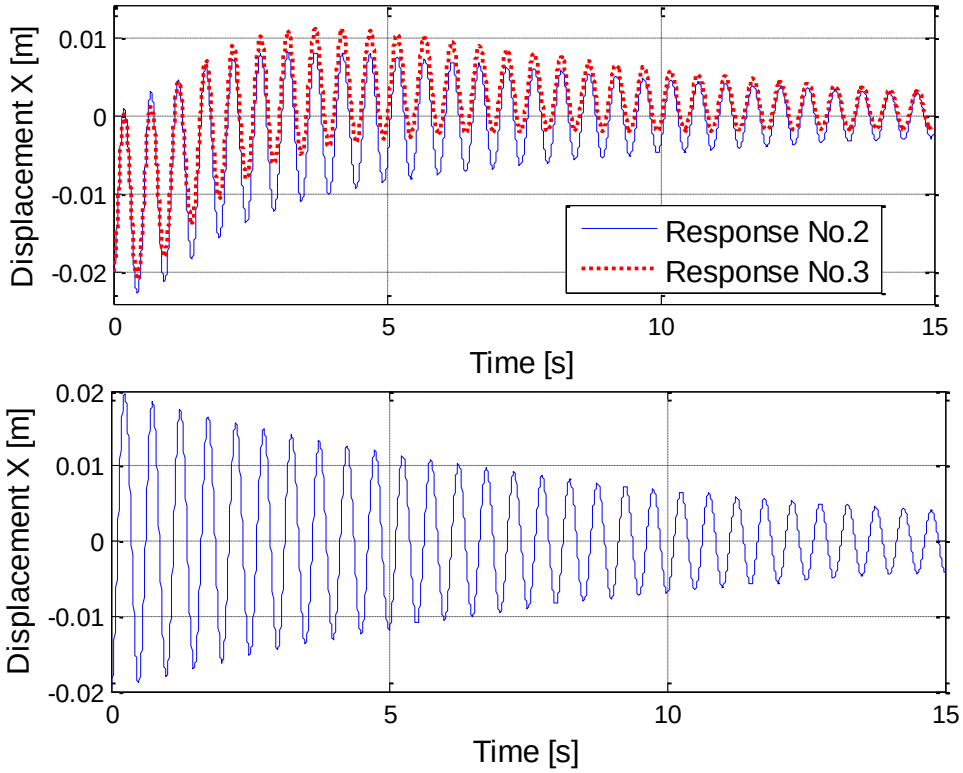

Figure 10: Displacement time series of the nonlinear (up) and linearized (down) models at 90 deg inflow, corresponding to aerodynamic responses No. 2 and No. 3 (overshooted)

and 30 deg. This region is out of this work's focus because the airfoils' damping characteristics can be accurately determined by the usual dynamic-stall models, which is not a part of the present work.

The main finding of the current paper is presented in Figure 9. The edgewise damping ratios corresponding to the lagged aerodynamic response are considerably higher than the damping ratio corresponding to the quasi-steady response. Most of the inflow-angle regions corresponding to the negatively damped vibrations in case of the quasi-steady aerodynamic response vanish already in case of aerodynamic response No. 1. Aerodynamic response function No. 1 corresponds to inviscid flow. On the other hand, even though the actual aerodynamic response in deep stall is currently not known, it is probable that such response is slower than the inviscid response No. 1. Moreover, an increase in the damping is even more pronounced in cases No. 2 and No. 3, i.e. responses slower than inviscid. These facts indicate that in real life edgewise vibration may be more damped than the aeroelastic codes – which assume quasi-steady aerodynamics – predict.

It is also worth mentioning that delaying the response more than what corresponds to inviscid flow causes an increase in the damping in the inflow-angle regions which are already positively damped rather than expanding this region. Otherwise stated, inflow-angle region approx. between -30 degrees and -20 degrees as well as between 30 degrees and 40 degrees remains negatively damped independent on the amount of aerodynamic lag, compared with the damping characteristic of response function No. 1. However, it is questionable whether these inflow-angle regions are not within the operating range of the usual dynamic stall models.

Another intriguing observation is that introducing an overshoot in the response doesn't change the damping characteristic. Introducing an overshoot makes a very small change in the nonlinear model and no change in the linearized one. Therefore, the curve corresponding to the linearized response No. 3 is not plotted in Figure 9 for better clarity. Figure 10 shows displacement time series of the nonlinear and linearized models at 90 deg of inflow angle, corresponding to response functions No. 2 and No. 3 (overshooted). The linearized model appears only as one curve because the two time responses are identical. Figure 10 (upper) shows the difference between responses No. 2 and No. 3 in the nonlinear model. The overshoot in response No. 3 creates even higher temporary equilibrium-position shift than response function No. 2 does.

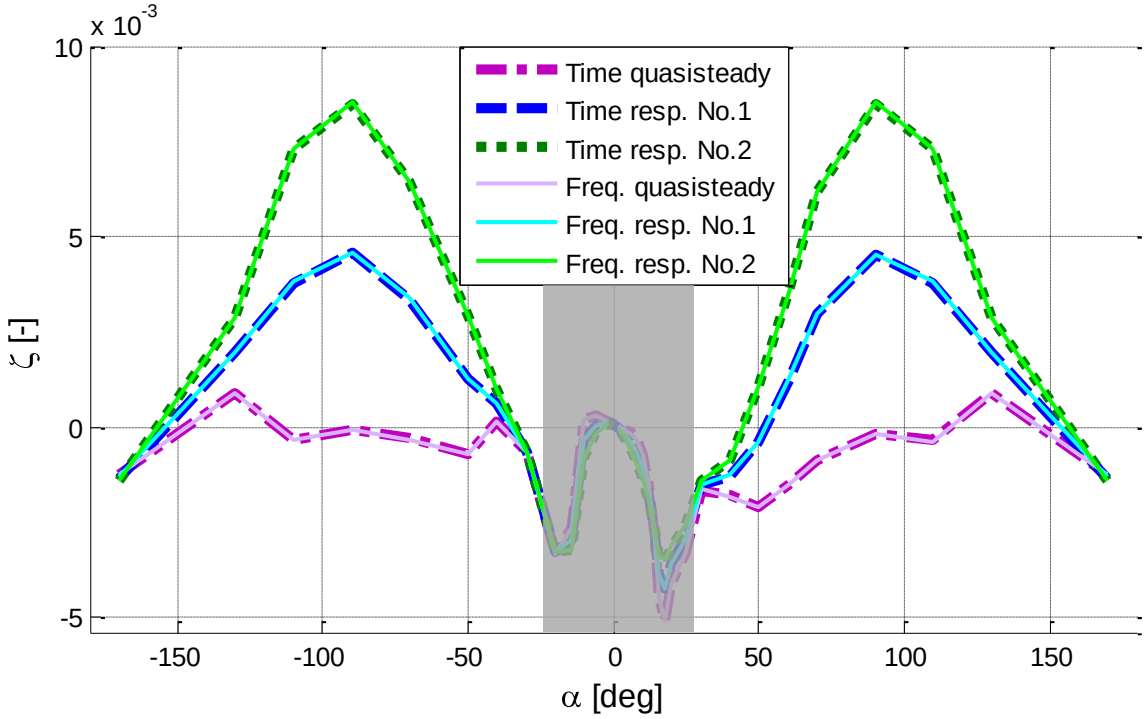

Figure 11: The edgewise damping ratios coming from the eigenvalue and time-domain analyses, applied to the linearized model; the grey rectangle indicates inflow-angle range out of this work's focus

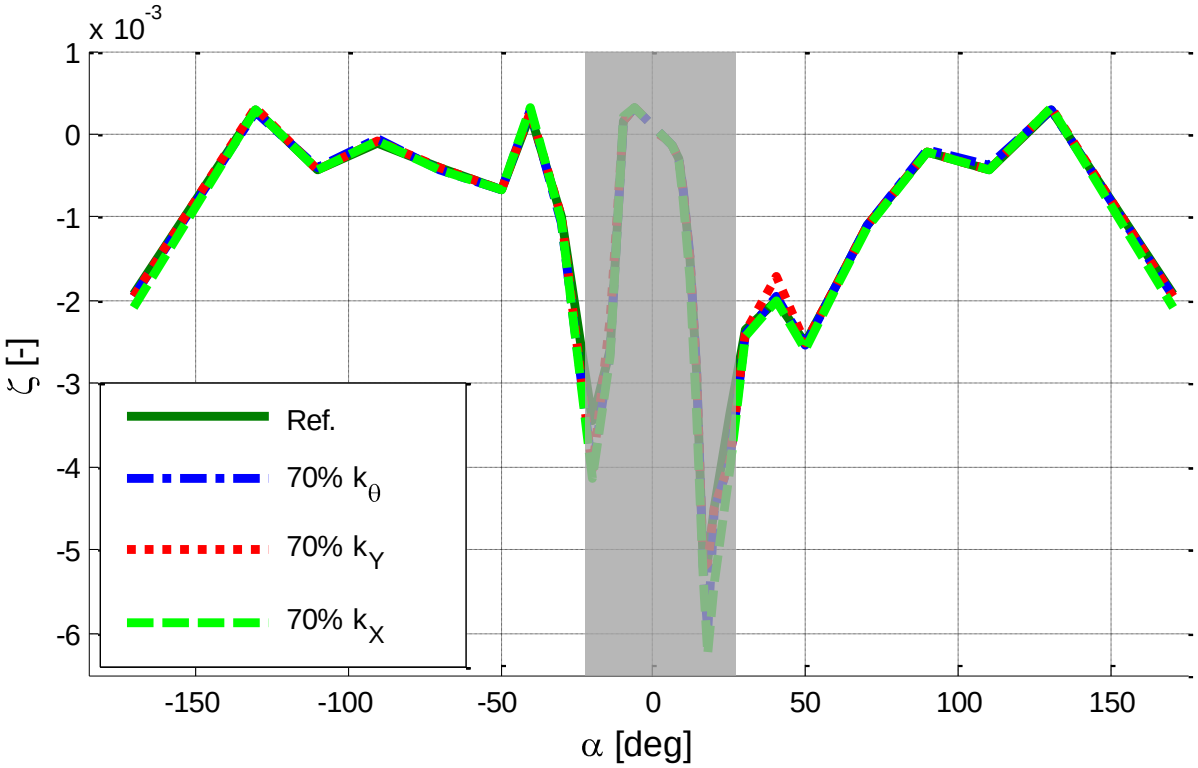

Figure 12: The edgewise damping ratio of the nonlinear system; quasi-steady aerodynamic response; comparison of the models with reduced elastic coefficients; the grey rectangle indicates inflow-angle range out of this work's focus

5. Results of the frequency-domain analysis

The linearized model is subjected to an eigenvalue analysis. The edgewise damping ratio coming from the eigenvalue analysis is plotted together with the edgewise damping ratio resulting from the time-domain analysis of the linearized model in Figure 11. This is done in order to investigate whether there is any difference between the results obtained by the two methods – the eigenvalue and time-domain – at any inflow angle or aerodynamic response, applied to the same linearized model. The damping-ratio comparison presented in Figure 11 shows that the damping ratios obtained by the eigenvalue and time-domain analyses are identical. For this reason the stability analysis considering edgewise vibration can be performed by the much faster eigenvalue method exclusively.

6. Sensitivity study

The next step is a sensitivity study of the relation between the system's elastic coefficients and its aerodynamic damping characteristic. Elastic coefficients corresponding to the system's edgewise, flapwise and torsional degrees of freedom are reduced by 30%. Then, the damping ratio is calculated from the results of the nonlinear model with the quasi-steady aerodynamic response. The results are presented in Figure 12. The average discrepancy between the damping of the original and altered models is small compared to the relatively high change in elastic coefficients, i.e. 30%. The most significant difference – 15% – is made at the inflow angle of 40 deg when the elastic coefficient in y direction, k_Y, is altered.

7. Conclusions

The essential finding of this paper is that introducing a relatively low time lag in the aerodynamic response of a 2-D 3-DOF elastically mounted airfoil model significantly increases aerodynamic damping in deep stall. On the other hand, it was previously demonstrated that the standard aerodynamics existing in aeroelastic codes for deep stall is effectively quasi-steady. These two findings indicate that these aeroelastic codes may overpredict vibration in deep stall. In addition, the aerodynamic response in deep stall – where the flow is massively separated – is presumably slower than for the inviscid flow, i.e. aerodynamic response function No. 1 presented in the paper.

This work also included a comparison of the results obtained by the time-domain analysis of the nonlinear model with the results of both the time-domain and eigenvalue analyses of the corresponding linearized model. The results indicate that the nonlinear effects play a minor role in terms of the system's damping characteristic.

The paper is closed by a parameter study of the influence of the system's elastic coefficients on the damping. This study indicated that this influence is relatively low.

The next step of the current work is to investigate whether a model like the present aerodynamic model can be used to describe the main unsteady aerodynamic response in deep stall. Further, if it shows to be achievable, to find one or more sets of parameters for the response function that can be used for reliable prediction of wind-turbine standstill response.

References

[1] Øye, Stig: *Dynamic stall simulated as time lag of separation*, in: Proceedings of the EWEC, Thessaloniki, Greece, Oct. 1994.

[2] Hansen, Morten; Gaunaa, Mac and Aagard-Madsen; Helge: *Beddoes-Leishman type dynamic stall model in state-space and indicial formulations*. Risø-R-1354(EN) (2004) 40 p.

[3] Gaunaa, Mac; Larsen, Torben J.: *Stilstandslaster;* chapter in "Forskning i Aeroelasticitet" 2002, ed. Christian Bak, Risø-R-1434(DA) in Danish, Risø DTU National Laboratory for Sustainable Energy

[4] Buhl, Thomas: *Edgewise vibration in stand still*, chapter in "Research in Aeroelasticity EFP-2006", ed. Christian Bak, Risø-R-1611.

[5] Buhl, Thomas; Gaunaa, Mac; Bak, Christian: *Potential Load Reduction Using Airfoils with Variable Trailing Edge Geometry,* Journal of Solar Energy Engineering, Nov. 2005, Vol. 127

[6] Jones, R. T.: *The Unsteady Lift of a Wing of Finite Aspect Ratio,* Tech. Rep. 681, NACA Report, 1940

[II]

Wind turbine blade vibration at standstill conditions – the effect of imposing lag on the aerodynamic response of an elastically mounted airfoil

Witold Skrzypiński (wisk@risoe.dtu.dk)

Mac Gaunaa (macg@risoe.dtu.dk)

DTU Wind Energy

Abstract

An elastically-mounted-airfoil model was developed in this work in order to investigate the influence of temporal lag in the aerodynamic response of an airfoil on the aeroelastic stability in deep stall. The study indicated that existence of even relatively low lag significantly increases the damping of the model. A comparison made between the current implementation and a model with lag imposed exclusively on the lift showed only marginal difference between the damping predicted by both models. A parameter study involving positions of the hinge point and the center of gravity indicated that the stability is relatively independent of these parameters. Another parameter study involving spring constants showed that the stability of each mode is dependent only on the spring constant acting in the direction of the leading motion of the mode. An investigation of the influence of the added-mass terms showed that only the pitch-rate and flapwise-acceleration terms have any influence on the stability. An investigation of three different profiles showed that the stability is heavily dependent on the aerodynamic characteristics of the profiles – mainly on the lift. It was also shown that only the edgewise mode is unstable in deep stall. Moreover, independent of the amount of temporal lag in the aerodynamic response of the model, the inflow-angle region in the vicinity of 180 deg remains unstable in the edgewise mode. Therefore, this inflow-angle region may create stability problems in real life.

1 Introduction

The introduction of computational models for the dynamic aeroelastic response of wind turbines has made possible investigation of numerous dynamic issues. This has assisted in understanding and overcoming many problems. In some cases specific problems have necessitated development of new or improved sub-models in the aeroelastic computational tools. An example of such models would be the so called dynamic stall models [1,2,3]. These models deal with the dynamic aerodynamic response from the onset of separation until the flow over the airfoil is fully separated.

Applying the existing aeroelastic tools to investigate the dynamic response of wind turbines in standstill has indicated that, under certain conditions, the edgewise vibrational mode of the wind turbine blades is characterized by a negative aeroelastic damping. If these tools predict correctly, this may lead to large fatigue loads or even failure.

Standstill conditions may exist at newly erected turbines before they are connected to the grid, as well as at turbines which undergo maintenance, experience extreme wind conditions or breakdown.

Some of the unstable regions in the computations occur in deep stall which corresponds to angles of attack far from normal operation. For this reason the underlying aerodynamic coefficients are uncertain, and it was initially assumed that the problem existed only in computations. In recent years, however, turbine failures at standstill conditions reported from the industry spurred new investigations. Politis *et al.* focuses on the investigation of stall-induced vibrations (SIV) [4]. In SIV, small-amplitude vibrations generate forces which increase the amplitudes to large values. This is one of the two mechanisms suspected of being related to blade standstill vibrations.

The other is vortex-induced vibrations (VIV) [5]. In VIV, the body vibrates in a particular mode over a small range of wind speeds containing that at which the von Karman frequency of vortex shedding coincides with the natural frequency of the mode. The non-dimensional von Karman frequency is the well-known Strouhal number. The mechanism of the von Karman frequency coinciding with the natural frequency of the mode is called the lock-in. Attempts of incorporating the VIV effects in computations of blade standstill stability were already made by several authors [6, 7, 8].

This article, however, focuses on the issues characteristic for the stall induced vibrations. SIV is well recognized in general aeroelasticity [9] and civil engineering. It is often referred to as galloping, stall flutter or bluff-body flutter. Square-like sections are relatively prone to such instability [10]. Regarding SIV, several investigations [11,12] concluded that the standard aerodynamics existing in aeroelastic codes for deep stall is effectively quasi-steady. Moreover, the aeroelastic damping can be either augmented or removed by adjusting the steady aerodynamic coefficients within the limits of uncertainty of the underlying aerodynamic data. In addition, another study [13] indicated that introducing even relatively low amount of temporal lag onto the dynamic lift of the airfoil considerably increases the damping. Thereby, it removes most of the negatively damped inflow-angle regions of an airfoil.

The present work investigates the effect of imposing different amounts of temporal lag onto the lift, drag and moment of different profiles. Moreover, a parameter study of the effect of alternating the position of the hinge point and center of gravity on the aeroelastic stability is included. It also includes a parameter study of the influence of the spring constants' on the damping. Finally, a discussion of the significance of including the added-mass terms in the aerodynamic equations of the model is given.

2 Computational model

2.1 Setup

The setup used in the simulations is presented in Figure 1. It is a 2-D 3-DOF elastically-mounted airfoil. *C* is the chord line. *AA* is the aerodynamic axis, and *EA* is the elastic axis (hinge point). Both *AA* and *EA* are positioned on *C*. F_X and F_Y are the aerodynamic force components applied at *AA* in x and y directions, respectively. F_Θ is the aerodynamic moment applied at *AA*, positive counter-clockwise. Θ_g is the angle between *C* and the line (*C'*) through *EA* and the center of gravity (*CG*). *C* is parallel with x axis when the profile is in the equilibrium without the aerodynamic forces involved. In case of symmetric profiles, *CG* lies on *C*. In such a case, *C'* coincides with *C*, and Θ_g is zero. In this study, Θ_g was approximated as zero even though the profiles considered are non-symmetric. *AA* is not to be confused with the aerodynamic center (*ac*) which is a point on an airfoil where the aerodynamic moment is independent of the angle of attack under fully attached flow conditions.

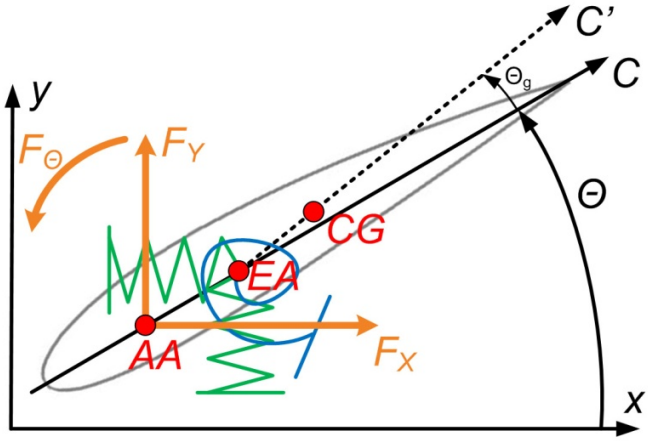

Figure 1: 2-D 3-DOF elastically mounted airfoil model

2.2 Non-linear structural model

The non-linear structural model [14] used in this study consists of the following set of equations of motion:

$$M\ddot{X} + c_X\dot{X} + k_X X = F_X + M\,C\,l_{EACG}\,\dot{\Theta}^2\cos(\Theta+\Theta_g) + M\,C\,l_{EACG}\,\ddot{\Theta}\sin(\Theta+\Theta_g)$$

$$M\ddot{Y} + c_Y\dot{Y} + k_Y Y = F_Y + M\,C\,l_{EACG}\,\dot{\Theta}^2\sin(\Theta+\Theta_g) - M\,C\,l_{EACG}\,\ddot{\Theta}\cos(\Theta+\Theta_g)$$

$$\begin{aligned}\ddot{\Theta}\left(I_{cg} + M\,(C\,l_{EACG})^2\right) + c_\Theta\dot{\Theta} + k_\Theta\Theta \\ = F_\Theta + F_X\,C\,l_{AAEA}\sin(\Theta+\Theta_g) - F_Y\,C\,l_{AAEA}\cos(\Theta+\Theta_g) + MC\,l_{EACG}\,\ddot{X}\sin(\Theta+\Theta_g) \\ - M\,C\,l_{EACG}\,\ddot{Y}\cos(\Theta+\Theta_g)\end{aligned} \quad (1)$$

where X,Y and Θ denote displacements in x, y and rotational directions, respectively. Further, l_{EACG} is the dimensionless distance from *EA* to *CG*, positive when *CG* is behind *EA*. Analogically, l_{AAEA} is the dimensionless distance from *AA* to *EA*, positive when *EA* is behind *AA*. The remaining symbols correspond to the description of the setup presented above.

2.3 Non-linear aerodynamic model

The aerodynamic loads, applied at *AA*, are governed by a deep-stall model. The new model may reflect behavior of a wind turbine blade vibrating in deep stall better than a model assuming quasisteady aerodynamics. A similar yet simpler model was introduced in [13]. In the current model, the dynamic lift coefficient is calculated as a sum of the static lift coefficient at an effective angle of attack and the added-mass terms from the unsteady thin airfoil theory [15,16]:

$$C_L^{Dyn} = C_L^{St}(\alpha_E) + \frac{\pi\rho C^2}{4}\left[(\sin\gamma - \alpha\cos\gamma)\ddot{X} - (\cos\gamma + \alpha\sin\gamma)\ddot{Y} - V_{rel}\dot{\Theta} + \frac{C}{2}(2l_{EA} - 1)\ddot{\Theta}\right] \quad (2)$$

where l_{EA} is the dimensionless distance from the leading edge to the elastic axis. The geometric angle of attack (α) is the angle between *C* and a line representing the absolute inflow velocity (V_0). V_{rel} is the airflow velocity relative to the airfoil. Further, γ is the angle between the *x axis and* V_0. The effective angle of attack (α_E) is a lagged angle of attack defined as:

$$\alpha_E = \alpha_{3/4}(1 - A_1 - A_2) + x_1 + x_2 \quad (3)$$

where $\alpha_{3/4}$ is the angle of attack as observed at the three-quarter chord. The use of the effective angle of attack in the model, and the way α_E is expressed resembles the dynamic stall model described by Hansen *et al.* [2]. A_1 and A_2 constitute the first half of the parameters defined in the subsequent description of the unit response function. Further, x_1 and x_2 are the aerodynamic-state variables governed by the differential equations:

$$\dot{x}_i + \frac{2V_{rel}}{C} b_i x_i = b_i A_i \frac{2V_{rel}}{C}\alpha_{3/4}; \quad i = 1,2 \quad (4)$$

Where V_{rel} is the airflow velocity relative to the airfoil, and b_i constitute the second half of the parameters used for defining the unit response function. The dynamic drag coefficient is calculated as:

$$C_D^{Dyn} = C_D^{St}(\alpha_E) + (\alpha - \alpha_E)C_L^{Dyn} \quad (5)$$

The first term is the drag coefficient defined with respect to α_E, which ensures that the dynamic drag eventually converges to the static drag. The second term represents the induced drag – a concept stemming from thin airfoil theory. This is because the dynamic lift is defined with respect to α_E.

Therefore, it has a component in the drag direction defined by the geometric angle of attack. The dynamic moment coefficient is taken to be equal to the sum of the static moment coefficient at the effective aoa and the added-mass terms:

$$C_M^{Dyn} = C_M^{St}(\alpha_E) + \frac{\pi\rho C^3}{8}\left[(2l_{EA}-1)(\alpha\cos\gamma-\sin\gamma)\ddot{X} + (2l_{EA}-1)(\alpha\sin\gamma+\cos\gamma)\ddot{Y} + \frac{1}{2}(4l_{EA}-3)V_{rel}\dot{\Theta} - \frac{C}{16}(32{l_{EA}}^2 - 32l_{EA}+9)\ddot{\Theta}\right] \quad (6)$$

The specific parts of the added-mass terms in equations (2) and (6) will be referred to throughout this article as the edgewise acceleration, flapwise acceleration, pitch-rate and pitch acceleration terms of the lift and moment coefficients, respectively.

All the added-mass terms are dependent on the angle of attack in such a way that they would vanish if the angle of attack, defined with respect to V_{rel}, was equal to zero. In the other words, the added mass terms are driven by the angle of attack.

The choice of parameter values (A_1, A_2, b_1, b_2) characterizes a specific temporal behavior of the aerodynamic model. Such a choice may be represented by the unit response function, defined as:

$$\phi = 1 - A_1 e^{-b_1 s} - A_2 e^{-b_2 s} \quad (7)$$

where s is the non-dimensional time, $t\frac{V}{c}$. The choice of four exemplary parameter sets used for the study is presented in Figure 2, together with the respective unit response functions.

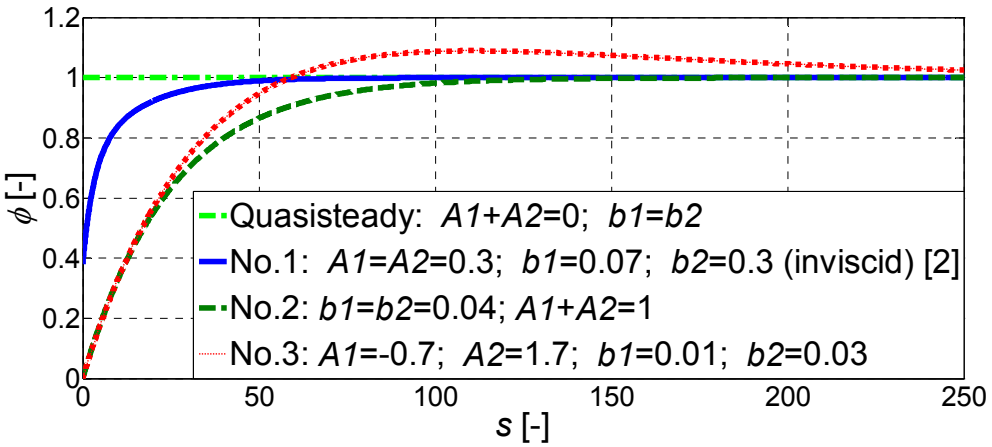

Figure 2: Aerodynamic unit response functions corresponding to the aerodynamic-parameter sets

Aerodynamic response function No. 1 is an approximate representation of the inviscid response of a thin airfoil [17]. This function is therefore probably associated with a faster response than the response of a real-life airfoil in deep stall. Aerodynamic response functions No. 2 and 3 are both significantly

slower than function No. 1. Function No. 3 – initially being the same as No. 2 – includes an overshoot. The parameters of the quasisteady response function effectively bypass the lagging effect of the dynamic model. Consequently, the quasisteady function corresponds to the aerodynamic response one would get from standard aeroelastic codes in deep stall. Mind that response functions No. 2 and 3 do not represent any particular aerodynamic system, and that the actual dynamic aerodynamic response of an airfoil in deep stall is currently not known, i.e. has not been verified by any computations or measurements, to the authors' knowledge.

2.4 Linearized structural model

In this work, the non-linear model presented above was linearized in order to perform eigenvalue and further stability analyses of the system. Eigenvalue analysis is far more effective computationally than time-domain analysis is. Therefore, it is a suitable tool for further parameter studies. The set of respective linearized equations is as follows:

$$M\ddot{X} + c_x\dot{X} + k_xX = F_X^{lin} + M\ C\ l_{EACG}\ddot{\Theta}sin(\Theta_g)$$

$$M\ddot{Y} + c_y\dot{Y} + k_yY = F_Y^{lin} - M\ C\ l_{EACG}\ddot{\Theta}cos(\Theta_g)$$

$$\begin{aligned}\ddot{\Theta}\left(I_{cg} + M(C\ l_{EACG})^2\right) + c_\Theta\dot{\Theta} + k_\Theta\Theta \\ = F_\Theta^{lin} + F_X^{lin}\ C\ l_{AAEA}\ sin(\Theta_g) - F_Y^{lin}\ C\ l_{AAEA}\ cos(\Theta_g) + M\ C\ l_{EACG}\ \ddot{X}\ sin(\Theta_g) \\ - MC\ l_{EACG}\ \ddot{Y}cos(\Theta_g)\end{aligned} \quad (8)$$

where F_X^{lin} and F_Y^{lin} are the linearized aerodynamic force components. F_θ^{lin} is the linearized aerodynamic moment. Linearization is performed around equilibrium positions which depend on the inflow angle.

2.5 Linearized aerodynamic model

The aerodynamic equations need to be linearized as well in order to obtain a fully linearized system. The lift, drag and moment are linearized around the equilibrium states of the system. The linearized dynamic lift coefficient is expressed as:

$$C_L^{lin} = C_L^0 + \frac{dC_L^0}{d\alpha}\alpha_E^1 + \frac{\pi\rho C^2}{4}\left[(\sin\gamma - \alpha_0\cos\gamma)\ddot{X} - (\cos\gamma + \alpha_0\sin\gamma)\ddot{Y} - V_0\dot{\Theta} + \frac{C}{2}(2l_{EA} - 1)\ddot{\Theta}\right] \quad (9)$$

where C_L^0 and α_0 are the lift coefficient and the angle of attack at the equilibrium state. Further, l_{EA} is the dimensionless distance between the leading edge and *EA*, and α_E^1 is a small perturbation of the effective angle of attack from its equilibrium value, calculated as:

$$\alpha_E^1 = \alpha_{3/4}^1\phi(0) + x_1^1 + x_2^1 \quad (10)$$

where $\phi(0)$ is the initial value of the respective aerodynamic unit response function. The variables x_1^1 and x_2^1 are small perturbations of the aerodynamic-state variables, x_i. They are calculated by linearization of Eq. (4):

$$\dot{x}_i^1 + T_0^{-1} b_i x_i^1 = b_i A_i T_0^{-1} \alpha_{3/4}^1; \quad i = 1, 2 \tag{11}$$

where variable $\alpha_{3/4}^1$ is a small perturbation of the quarter-chord angle of attack from its equilibrium value. The linearized dynamic drag coefficient is expressed as:

$$C_D^{lin} = C_D^0 + \frac{dC_D^0}{d\alpha}\alpha_E^1 + (\alpha^1 - \alpha_E^1)C_L^0 \tag{12}$$

where C_D^0 is the drag coefficient value at the equilibrium state, and α^1 is a small perturbation of the geometric angle of attack. The linearized dynamic moment coefficient is:

$$\begin{aligned} C_M^{lin} = C_M^0 + \frac{dC_M^0}{d\alpha}\alpha_E^1 \\ + \frac{\pi\rho C^3}{8}\Big[(2l_{EA} - 1)(\alpha_0 \cos\gamma - \sin\gamma)\ddot{X} + (2l_{EA} - 1)(\alpha_0 \sin\gamma + \cos\gamma)\ddot{Y} \\ + \frac{1}{2}(4l_{EA} - 3)V_0\dot{\Theta} - \frac{C}{16}\left(32{l_{EA}}^2 - 32l_{EA} + 9\right)\ddot{\Theta}\Big] \end{aligned} \tag{13}$$

where C_M^0 is the moment coefficient value at the equilibrium state. The significance of the added-mass terms in the equations is discussed in the end of this article. Until then, the added-mass terms are excluded from the loading. Therefore, the reduced versions of lift and drag coefficients are equal:

$$C_L^{lin} = C_L^0 + \frac{dC_L^0}{d\alpha}\alpha_E^1 \tag{14}$$

$$C_M^{lin} = C_M^0 + \frac{dC_M^0}{d\alpha}\alpha_E^1 \tag{15}$$

2.6 Parameters

Characteristics of the airfoil used in this study were previously proposed by Buhl *et al.* [14]. The chord length is 1 m. The unit-depth mass of the airfoil is M= 40 kg. The hinge point and aerodynamic axis are at quarter chord. The center of gravity is at 30% chord. The spring constants (k_X, k_Y, k_Θ) are chosen in such a way that the vibrations in flapwise, edgewise and torsional directions have frequencies of 1, 2 and 10 Hz, respectively. Viscous damping (c_X, c_Y, c_Θ) is set to zero. The inflow velocity is 10 m/s. Air density is 1.225 kg/m^3. These parameters are not meant to represent any specific position on a specific

blade. However, the section should be representative of blade sections on the outer parts of general wind-turbine blades. It should also be pointed out that aeroelastic characteristic of a 2-D section is not necessarily representative for a whole blade. However, a very good agreement has been seen previously between such a "strip model" and a full blade [11].

2.7 Airfoil data

Airfoil data used in the computations is for NACA 63-416, DU96-W-180 and Risø-B1-18. The airfoil data for NACA 63-416 is an example of full polars that would usually be used in aeroelastic analysis. The airfoil data for DU96-W-180 was obtained from measurements made by Timmer [18,19] from Delft University of Technology, Faculty of Aerospace Engineering, Wind Energy Section. The data regarding Risø-B1-18 was obtained at Risø by a combination of the Ellipsys3D CFD computations and wind tunnel measurements. The lift, drag and moment coefficients of the airfoils are presented in Figure 3.

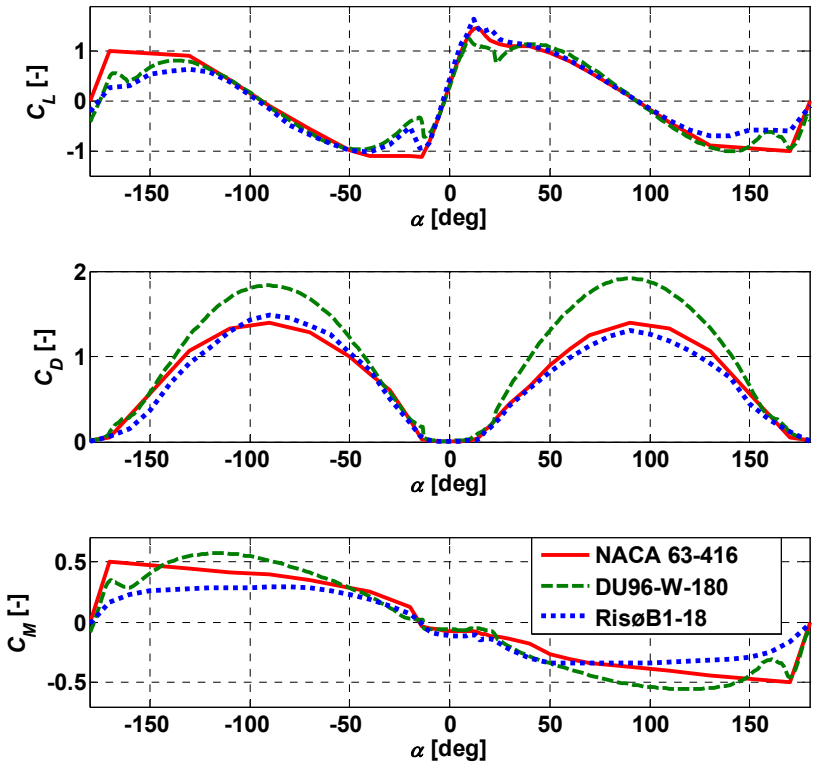

Figure 3: Airfoil aerodynamic data used in the computations

As it is seen, C_D of Risø-B1-18 is higher in the negative angle-of-attack region than in the positive. This seems unrealistic, as this is a cambered airfoil. The fact that the data comes from a blend of the CFD computations and experiments may be the reason for this.

It is also visible in the figure that the data regarding NACA 63-416 is of low resolution relative to the other two datasets, which may influence the damping assessment. However, it is often the case as polars are usually measured or computed with higher resolution in the normal operational region of an airfoil than at high angles of attack.
It is also important to realize that aerodynamic data is in general relatively uncertain at high angles of attack. According to the work of Sørensen and Michelsen [20], three-dimensional effects influence the forces considerably. Therefore, the results presented in this article should be treated rather as a general study of the stability of the elastically-mounted-airfoil model rather than the specific study of the aeroelastic stability when using the airfoils presented above.

3 Model validation

Both the non-linear and linearized models are validated by comparing the respective damping ratios with the damping ratio of the reference linearized 1-DOF model [11]. The predictions presented in this section concern steady-state aerodynamics solely because the response function used is quasisteady. The airfoil used is NACA_63-416. The added mass terms in the present models are currently excluded as the reference model does not include such. The comparison is presented in Figure 4.

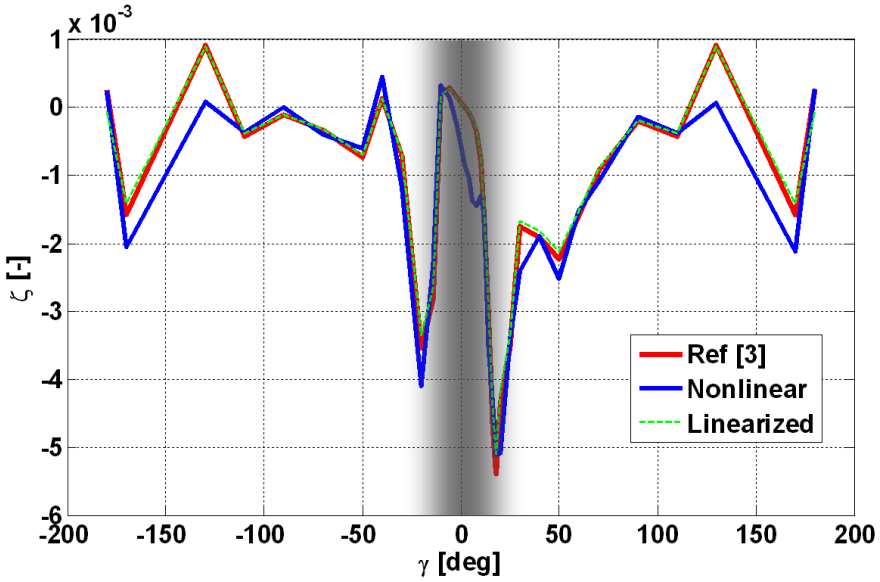

Figure 4: Comparison of the edgewise damping ratios obtained by the non-linear and linearized models with the damping ratio obtained by the reference model [11]; the added mass terms are excluded; the grey area indicates the inflow-angle region out of the focus of this work

The grey area indicates the inflow-angle region where the usual dynamic-stall models alter the dynamic aerodynamic response. This area is therefore out of the focus of the present work. However, it remains a little vague what the exact angle-of-attack region where the present considerations apply is. That is because the angle of attack at which the full separation occurs depends on the specific airfoil as well as on the flow conditions and other factors like surface contamination. On average, we consider airfoils being in either attached or partly separated flow between -25 and 25 degrees of the angle of attack.

As the figure shows, both the non-linear and linearized models fit well to the reference. Actually, it is the linearized model that fits better than the non-linear. Given this fact and the fact that eigenvalue analysis is far more effective computationally than time-domain analysis is, further considerations presented in this article are based on the eigenvalue analysis of the linearized system.
The edgewise vibration is the main focus of this work. This is because it is the edgewise mode that becomes unstable in deep stall. Nevertheless, the other two modes are shown as well in Figure 5 in order to give a better overview of the subject.

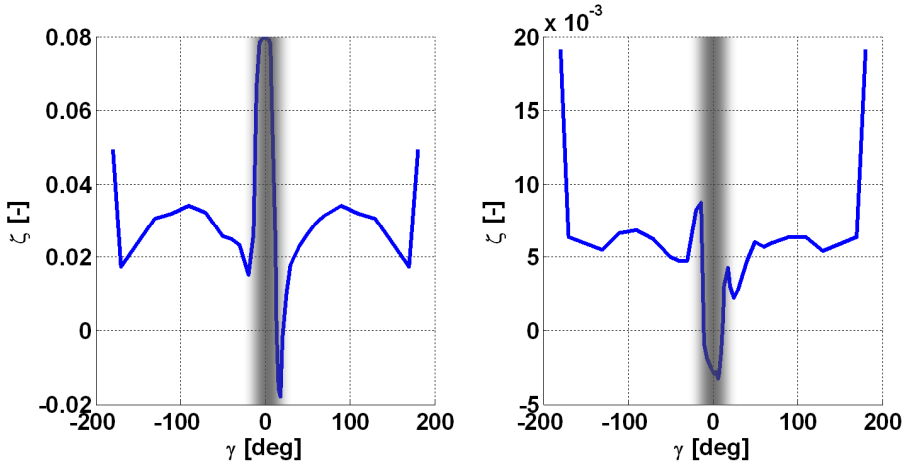

Figure 5: The flapwise (left) and torsional (right) modes of the model; quasisteady response function; the grey area indicates the inflow-angle region out of the focus of this work; quasisteady aerodynamic response

As it is seen in the figures, the flapwise and torsional modes are positively damped in deep stall, while the edgewise mode is damped negatively in most of the deep-stall inflow-angle regions.

4 Results

4.1 Lagged response

The damping ratios corresponding to the response functions from Figure 2 are presented in this chapter. The results are also compared with the respective results obtained by the simpler model [13] where lag is imposed exclusively on the lift. The added mass terms are currently excluded to allow for a more objective comparison with the reference model where no such terms are present. The airfoil force coefficients used regard NACA_63-416. The results are presented in Figure 6. As it is seen in the figure, results obtained by means of the current model are very similar to the previous implementation. This indicates that the lift is the main driver of the aeroelastic stability of the model in this case. Moreover, the damping ratios corresponding to response function No. 3 have not been plotted because the corresponding curves overlapped with the curves representing response function No. 2. This indicates that the convergence rate of the response function, as well as the existence of the overshoot, is insignificant in terms of the damping. Analysis of additional response functions indicated that the damping is sensitive to the initial slope of the response function, as well as to its initial value. The slope of the function is:

$$\dot{\varphi} = A_1 b_1 e^{-b_1 s} + A_2 b_2 e^{-b_2 s} \tag{16}$$

Correspondingly, the slope at the zero time is:

$$\dot{\varphi}(0) = A_1 b_1 + A_2 b_2 \tag{17}$$

The initial value of the response function is:

$$\varphi(0) = 1 - A_1 - A_2 \tag{18}$$

Increasing the initial slope, as well as increasing the initial value, decreases the aeroelastic damping of the model.
In the responses No. 1 and 2 only the inflow-angle regions in the vicinity on 180 deg are unstable.

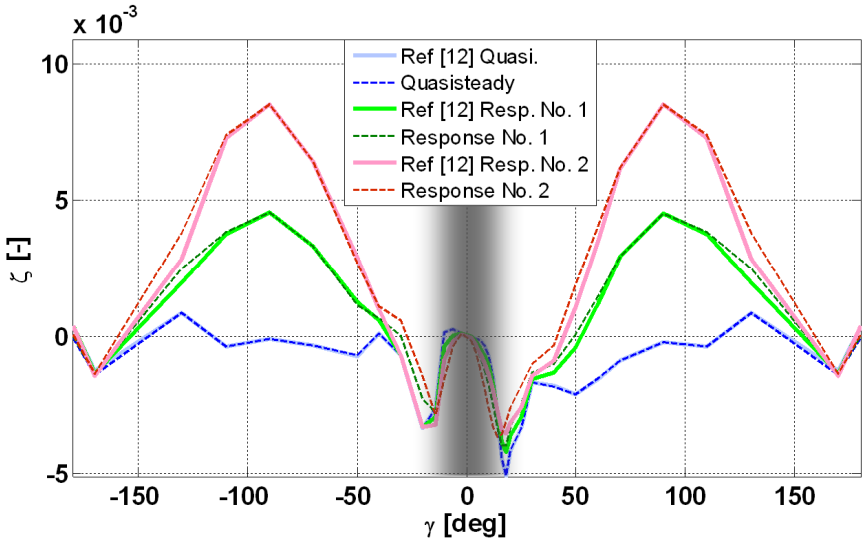

Figure 6: Comparison of the edgewise damping ratios obtained by the linearized model with the damping ratios obtained by the reference [13] linearized model; added-mass terms excluded; the grey area indicates the inflow-angle region out of the focus of this work

4.2 EA and CG parameter study

A parameter study of the influence of the positions of the elastic axis and center of gravity was performed in this work. The profile used was NACA 63-416. Quasisteady aerodynamics was assumed. The study showed that the damping of the edgewise mode is independent of the position of both EA and CG. Further, also the flapwise mode is independent of these parameters. Only the torsional mode was found dependent on CG. However, the torsional mode did not become unstable within physical displacement of CG which had to lie on the latter half of the profile in order for the torsional mode to become unstable.

4.3 Spring-constant parameter study

Influence of the spring constants on the damping is described in this section. In the baseline case the constants are chosen in such a way that the frequencies of the flapwise, edgewise and torsional modes are equal to 1, 2 and 10 Hz, respectively. In the study, the stiffness was changed by 50%.

The study showed that deviation of each constant influences only the aeroelastic damping of the respective mode. The damping deviation of the edgewise mode is presented in Figure 7. In general, increasing the corresponding stiffness increases the damping in the unstable regions and decreases it in the stable regions. In other words, increasing the stiffness corresponds to the aeroelastic damping approaching zero.

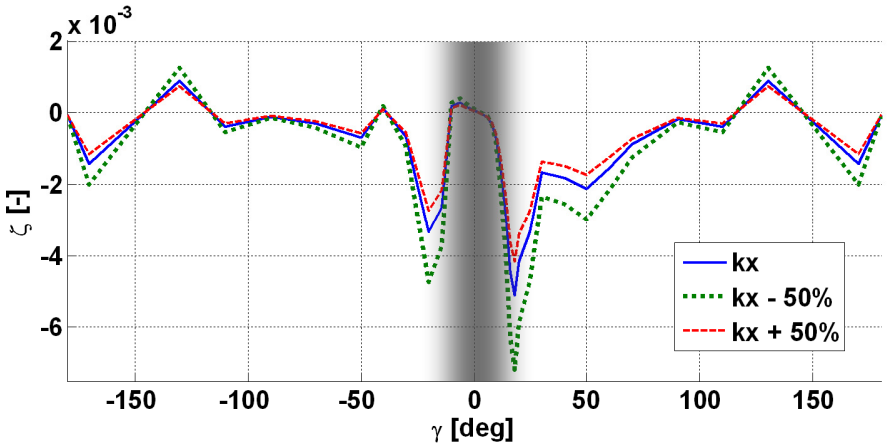

Figure 7: Influence of the edgewise spring constant on the stability of the edgewise mode; quasisteady response; the grey area indicates the inflow-angle region out of the focus of this work

4.4 Added-mass-terms study

Four distinct added-mass terms are present in the equations. These are: edgewise acceleration, flapwise acceleration, pitch rate and pitch acceleration. The influence of each of these terms on the stability of the model was investigated in this work.

It turned out that only the flapwise-acceleration and pitch-rate terms have some influence on the damping. The flapwise-acceleration term influences the damping of the edgewise mode while the pitch-rate term influences the damping of the torsional mode. This is presented in Figure 8. In the edgewise mode, the added-mass term increases the damping in the inflow-angle region between -90 and 90 deg, while it decreases the damping in the remaining region. In the torsional mode, the added-mass term acts on the contrary, decreasing the damping in the inner inflow-angle region, and increasing in the outer.

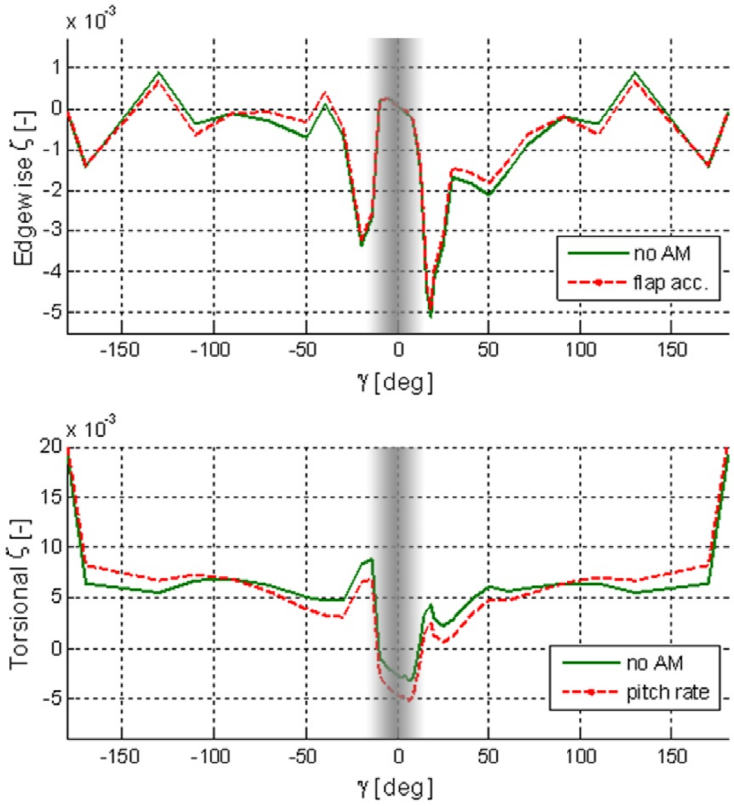

Figure 8: (up) Influence of the flapwise-acceleration added-mass term on the stability of the edgewise mode; (down) Influence of the pitch-rate added-mass term on the stability of the torsional mode; the grey area indicates the inflow-angle region out of the focus of this work

4.5 Airfoil comparison

The influence of different airfoil characteristics on the stability is presented in this section. The two aerodynamic response functions considered are the quasisteady and No. 1 (inviscid). Function No.1 is believed to be significantly slower than what could be in real life. Therefore, it may be a conservative estimate for the stability limits. The three investigated airfoils are: NACA 63-416, DU96-W-180 and Risø-B1-18. The results are presented in Figure 9 which shows that the damping is heavily dependent on the profile characteristics. Further, for every presented profile the damping corresponding to aerodynamic response function No. 1 is higher than the damping corresponding to the quasisteady response function.

The only inflow-region that seems to be unaffected by the introduction of lag in the aerodynamic response is the vicinity of 180 degrees. This region is therefore likely to create stability problems in real-life. Moreover it was verified that the flapwise and torsional modes of all the investigated profiles are stable for both response functions in the inflow-angle region considered in this work. Therefore, it is probably only the stability of the edgewise mode that is problematic.

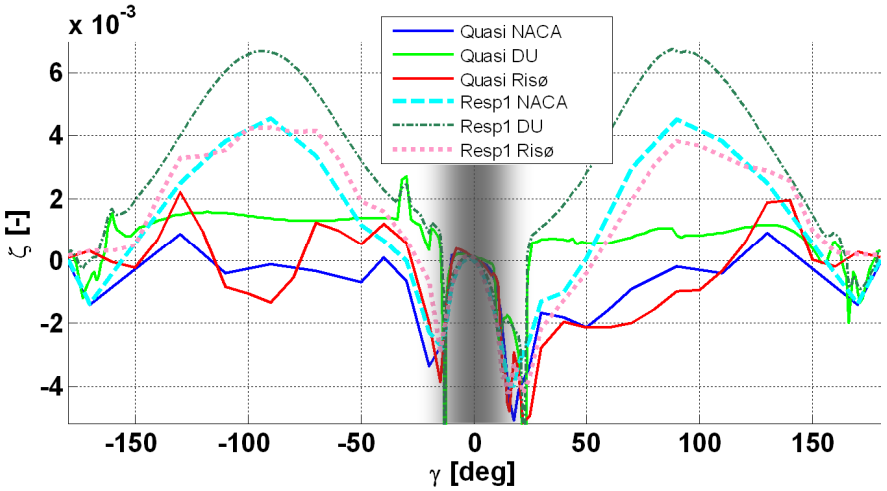

Figure 9: Comparison of the edgewise damping ratios corresponding to the three airfoils and two response functions; the grey area indicates the inflow-angle region out of the focus of this work; added-mass terms excluded

5 Conclusions

An elastically-mounted-airfoil model was developed in this work in order to investigate the influence of temporal lag in the aerodynamic response of an airfoil on the aeroelastic stability in deep stall. The aerodynamic model included lag imposed on the lift, drag and moment. It also included four distinct added-mass terms.

The study indicated that existence of even relatively low lag in the aerodynamic response significantly increases the damping of the model. A comparison made between the current implementation and a simpler model with lag imposed exclusively on the lift showed only marginal difference between the damping predicted by both models. A parameter study involving positions of the hinge point and the center of gravity indicated that the stability is relatively independent of these parameters. Another parameter study involving spring constants showed that the stability of each mode is dependent only on the respective spring constant, i.e. the one acting in the same direction as the leading motion of the mode. Investigation of the influence of the added-mass terms showed that only the pitch-rate and flapwise-acceleration terms have any influence on the stability. An investigation of three different profiles showed that the stability is heavily dependent on the aerodynamic characteristics of the profiles – mainly on the lift. It was also shown that only the edgewise mode is unstable in deep stall. Moreover, independent of the amount of temporal lag in the aerodynamic response of the model, the inflow-angle region in the vicinity of 180 deg remains unstable in the edgewise mode. Therefore, this inflow-angle region may create stability problems in real life.

It is noteworthy that this work exclusively regards the stall induced vibrations, while the relative importance and interaction of the stall and vortex induced vibrations remains in question. This interaction has been investigated by several authors. Nonetheless, a study shedding more light on this issue would help to guide future work on the standstill vibrations.

Nomenclature

A_i = parameters used for defining the unit response function
AA = aerodynamic axis
b_i = the parameters used for defining the unit response function
C = chord line
C' = line through *EA* and *CG*
C_D^{lin} = dynamic drag coefficient linearized around the system's equilibrium state
C_D^0 = drag coefficient value at the equilibrium state
C_D^{Dyn} = dynamic drag coefficient
C_D^{St} = static drag coefficient
C_L^{lin} = dynamic lift coefficient linearized around the system's equilibrium state
C_L^0 = lift coefficient value at the equilibrium state
C_L^{Dyn} = dynamic lift coefficient
C_L^{St} = static lift coefficient
C_M^{lin} = dynamic moment coefficient linearized around the system's equilibrium state
C_M^0 = moment coefficient value at the equilibrium state
C_M^{Dyn} = dynamic moment coefficient
C_M^{St} = static moment coefficient
CG = center of gravity
c_X = viscous-damping coefficient in x direction
c_Y = viscous-damping coefficient in y direction
c_Θ = viscous-damping coefficient in θ direction
EA = elastic axis (hinge point)
F_X = aerodynamic force component applied at AA in x direction
F_X^{lin} = linearized aerodynamic force component applied at AA in x direction
F_Y = aerodynamic force component applied at AA in y direction
F_Y^{lin} = linearized aerodynamic force component applied at AA in y direction
F_Θ = aerodynamic moment applied at AA, positive counter-clockwise
F_Θ^{lin} = linearized aerodynamic moment applied at AA, positive counter-clockwise
l_{EACG} = dimensionless distance from the elastic axis (hinge point) to the center of gravity
l_{AAEA} = dimensionless distance from the aerodynamic axis to the elastic axis (hinge point)
l_{EA} = dimensionless distance from the leading edge to the elastic axis (hinge point)
M = mass of a unit-depth airfoil section
s = non-dimensional time
V_0 = absolute inflow velocity
V_{rel} = airflow velocity relative to the airfoil
X = displacement in x direction
x_i = aerodynamic state variables
x_i^1 = small perturbation of the aerodynamic state variables
Y = displacement in y direction
α = geometric angle of attack
α_0 = angle of attack at equilibrium position
α^1 = small perturbation of the geometric angle of attack from its equilibrium value

$\alpha_{3/4}$ = angle of attack as observed at the three-quarter chord
$\alpha_{3/4}^{1}$ = small perturbation of the quarter-chord angle of attack from its equilibrium value
α_E = effective angle of attack: the angle between the airfoil's chord and a line representing the disturbed airflow relative to the airfoil
α_E^1 = small perturbation of the effective angle of attack from its equilibrium value
γ = angle between x *axis* and V_0
ϕ = unit response function
$\dot{\Theta}^1$ = small perturbation of the pitch rate from its equilibrium value
Θ = rotational displacement, positive counterclockwise
Θ_g = the angle between *C* and *C'*

References

[1] Øye, Stig: *Dynamic stall simulated as time lag of separation*, in: *Proceedings of the EWEC*, Thessaloniki, Greece, Oct. 1994.

[2] Hansen, Morten; Gaunaa, Mac, Aagard-Madsen; Helge: *Beddoes-Leishman type dynamic stall model in state-space and indicial formulations*; Risø-R-1354(EN) (2004) 40 p.

[3] Larsen, J. W.; Nielsen, S. R. K.; Krenk, S.: *Dynamic stall model for wind turbine airfoils;* Journal of Fluids and Structures 23 (2007) 959-982

[4] Politis, E.S.; Chaviaropoulos, P.K.; Riziotis, V.A.; Voutsinas, S.G.; Romero-Sanz, I.: *Stability analysis of parked wind turbine blades, Proceedings of the EWEC '09, Scientific Track*, Marseille, France, March 16-19, 2009

[5] Sumer, M.; Fredsøe, J.: *Hydrodynamics around cylindrical structures, Advanced Series on Ocean Engineering – Volume 12*, World Scientific, 1997

[6] Bertagnolio, F.; Rasmussen, F.; Sørensen N.N.; Johansen, J.; Madsen, H.Aa.: *A stochastic model for the simulation of wind turbine blades in stochastic stall,* Wind Energy 2010; 13:323-338

[7] Riziotis, V.A.; Voutsinas, S.G.; Politis, E.S.; Chaviaropoulos, P.K.: *Stability analysis of parked wind turbine blades using a vortex model, Proceedings of TORQUE 2010: The Science of Making Torque from Wind*, June 28-30, Crete, Greece, 2010

[8] Hansen, M.H.: *Bias effect of self-induced turbulence on the stall-flutter limit of an airfoil section, The sixteenth international congress on sound and vibration*, Kraków, 5-9 July 2009

[9] Dowell, E.H.; Clark, R.; Cox. D.; Curtiss, H.C. Jr.; Edwards, J.W.; Hall, K.C.; Peters, D.A.; Scanlan, R.; Simiu, E.; Sisto, F.; Strganac, T.W.: *A Modern Course in Aeroelasticity, Fourth Revised and Enlarged Edition*, Kluwer Academic Publishers, 2004

[10] Parkinson, G.V.; Smith, J.D.: *A square prism as an aeroelastic non-linear oscillator, The Quarterly Jonrnal of Mechanics and Applied Mathematics, Vol. XVH, Ft. 3,* 1964

[11] Gaunaa, Mac; Larsen, Torben J.: *Stilstandslaster*; chapter in *"Forskning i Aeroelasticitet"* 2002, ed. Christian Bak; Risø-R-1434(DA) in Danish, Risø DTU National Laboratory for Sustainable Energy

[12] Buhl, Thomas: *Edgewise vibration instand still*, chapter in *"Research in Aeroelasticity EFP-2006"*, ed. Christian Bak; Risø-R-1611.

[13] Skrzypinski, Witold; Gaunaa, Mac: *Wind turbine blade vibration at standstill conditions – the effect of imposing time lag onto aerodynamic response*, in: *Proceedings of EWEC 2010*, Warsaw, Poland, April 2010.

[14] Buhl, Thomas; Gaunaa, Mac; Bak, Christian: *Potential Load Reduction Using Airfoils with Variable Trailing Edge Geometry,* Journal of Solar Energy Engineering, Nov. 2005, Vol. 127

[15] Theodorsen, T.: *General theory of aerodynamic instability and the mechanism of flutter;* National Advisory Committee for Aeronautics; Report No. 496; 1949

[16] Øye, Stig: Instationære, aerodynamiske kræfter på todimensionalt vingeprofil, Afdelingen for Fluid Mekanik, Den Polytekniske Læreanstalt Lyngby, Nov. 1981

[17] Jones, R. T.: *The Unsteady Lift of a Wing of Finite Aspect Ratio,* Tech. Rep. 681, NACA Report, 1940

[18] Timmer, W.A.; van Rooij, R.P.J.O.M: *Summary of the Delft University wind turbine dedicated airfoils*; AIAA-2003-0352; 2003

[19] Timmer, W. A.: *Two-dimensional aerodynamic characteristics of wind turbine airfoils at high angles-of-attack*; 3rd Conference on The science of making Torque from Wind, Crete, Greece, June 2010

[20] Sørensen, N. N.; Michelsen, J. A.: *Drag prediction for blades at high angle of attack using CFD*; J. Solar Energy Eng. (2004) 126 , 1011-1016

[III]

Vortex-induced vibrations of a DU96-W-180 airfoil at 90 degrees angle of attack

Witold Skrzypiński (wisk@risoe.dtu.dk)

Mac Gaunaa (macg@risoe.dtu.dk)

Niels Sørensen (nsqr@risoe.dtu.dk)

Frederik Zahle (frza@risoe.dtu.dk)

Joachim Heinz (jhei@risoe.dtu.dk)

DTU Wind Energy

Abstract

This work presents an analysis of vortex-induced vibrations of a DU96-W-180 airfoil in deep stall at 90-degree angle of attack. The analysis was based on 2D and 3D unsteady CFD computations with non-moving, prescribed motion, and elastically mounted airfoil suspensions. In the prescribed motion computations the airfoil oscillated in the direction of the chord line. Negative aerodynamic damping in the vicinity of the corresponding stationary vortex-shedding frequencies was found. However, 2D and 3D CFD predicted different vibration frequencies. Both the 2D and 3D prescribed motion computations showed negative aerodynamic damping around the 2D stationary vortex shedding period. A shorter time series was sufficient to verify the sign of the aerodynamic damping in the case of the elastic computations than the prescribed motion. Even though the 2D computations seemed to be capable of indicating the presence of vortex induced vibrations, the 3D computations appeared as more accurate.

1 Introduction

Vibration of airfoils or whole wind turbine blades in standstill has recently received increased attention due to wind turbine failures potentially caused by blade vibration at standstill conditions. It is currently considered an important subject of research although no one has officially reported any turbine failures due to standstill vibrations so far. Blade vibration at standstill is potentially related to two separate phenomena: vortex-induced vibration (VIV) and stall-induced vibration (SIV).

SIV is well recognized in general aeroelasticity [1,2,3,4] and civil engineering. It is often referred to as galloping, stall flutter or bluff-body flutter. In SIV, a small displacement of the body causes an increase in the force in the direction of its motion, resulting in an aeroelastically unstable equilibrium. Square-like sections are relatively prone to this type of instability [5].

In VIV, the body vibrates in a particular mode at a wind speed for which the von Karman frequency of vortex shedding coincides with the natural frequency of the structural mode. An extensive review of experimental data concerning vortex-induced vibrations of circular cylinders is presented by Pantazopoulos [6]. The author lists the most important parameters affecting VIV response: the lift coefficient, the correlation length, the vortex shedding frequency, Reynolds number and the vortex shedding frequency bandwidth. The frequency bandwidth which is the standard deviation of the shedding frequency is further associated with the flow shear and incoming turbulence. Both shear and turbulence increase the bandwidth and decrease vibration amplitudes. To the aforementioned list Dowell [1] adds surface roughness which limits the influence of the Reynolds number. Attempts of incorporating the VIV effects in computations of wind turbine blade stability at standstill conditions were already made by several authors [7,8,9].

The present work, dealing exclusively with vortex-induced vibrations, was partly inspired by the experiment of Feng [10] from 1968. The experiment is also described in the book by Sumer and Fredsøe [11]. In the experiment, a flexibly-mounted circular cylinder with one degree of freedom of movement is exposed to air flow of varying speed. The direction in which the circular cylinder is allowed to move is in the direction perpendicular to the free stream. For each flow speed, V, the following quantities are measured: the vortex-shedding frequency, f_v, the vibration frequency, f, the vibration amplitude, A, and the phase angle between the cylinder vibration and the lift force, φ. The measured quantities are plotted as a function of the dimensionless flow velocity $V_r = V/Df_n$ where f_n is the natural frequency of the vibrating cylinder expressed in Hz. The results of the experiment are presented in Figure 1. In the experiment no vibration is experienced until the dimensionless flow speed reaches 4. For dimensionless flow speeds between 4 and 5, vibrations of small amplitude of the natural frequency of the cylinder emerge. The vortices are shed at the frequency corresponding to the Strouhal number of the cylinder. This frequency is presented in the upper graph of Figure 1 by the dashed line. When the dimensionless flow velocity exceeds 5, the frequency of vortex shedding begins to follow the natural frequency of the cylinder. In other words, the vortex-shedding frequency locks into the natural frequency of the system, or the vortex-shedding frequency is controlled by the vibration of the cylinder. The flow visualization work of Williamson and Roshko [12] shows how the vortices are forced to interact with the vibration of the cylinder. This phenomenon is known as lock-in. The vortex-shedding frequency unlocks and jumps back to the Strouhal value as the dimensionless flow velocity reaches 7. The width of the lock-in range in terms of the flow velocity may increase with the vibration amplitude. The lower graph in Figure 1 shows the increase in the vibration amplitude during the lock-in.

Locked-in vortex induced vibration is a potential threat to large wind turbine blades at standstill. In the present work - which was a study of vortex induced vibrations (VIV) of the

DU96-W-180 airfoil – similarities between the response of the cylinder in the aforementioned experiment and the response of the airfoil model in deep stall were investigated. The present study included 2D and 3D unsteady CFD computations. These included computations on non-moving, prescribed motion and elastically mounted airfoil suspensions. Stationary vortex shedding frequencies corresponding to the 2D and 3D computations were obtained by performing a frequency analysis of the loading on the non-moving airfoil models. In the prescribed motion computations the airfoil was forced to oscillate in the direction of the chord line. The elastically mounted airfoil computations were made with both one and three degrees of freedom of movement. The motivation for including both the prescribed motion and the elastically mounted airfoil computations was that, on the one hand, elastically mounted airfoil computations are the best reflection of real life blade vibration. On the other hand, prescribed motion computations allow us to learn about the basic mechanisms of fluid-structure interaction. It is also easier to derive engineering models from the data when well-defined forcing of prescribed motion computations was applied. Another motivation was to simply gain more insight into the involved phenomena by investigating it from two different perspectives.
Note that the present work simplified the problem of blade standstill vibrations by omitting the effects of blade twist and taper as well as the shear and turbulence in the incoming flow. The reason is to learn about the basic mechanisms involved in VIV of wind turbine blades. Further, flows in the deep-stall regime are known to be highly three-dimensional. It is common to resolve such flows by means of computationally expensive 3D DES simulations. The motivation for including 2D computations in the present work was to investigate whether relevant flow characteristics may be captured by 2D computations. This could be beneficial because of the high computational efficiency of such simulations compared to 3D DES.

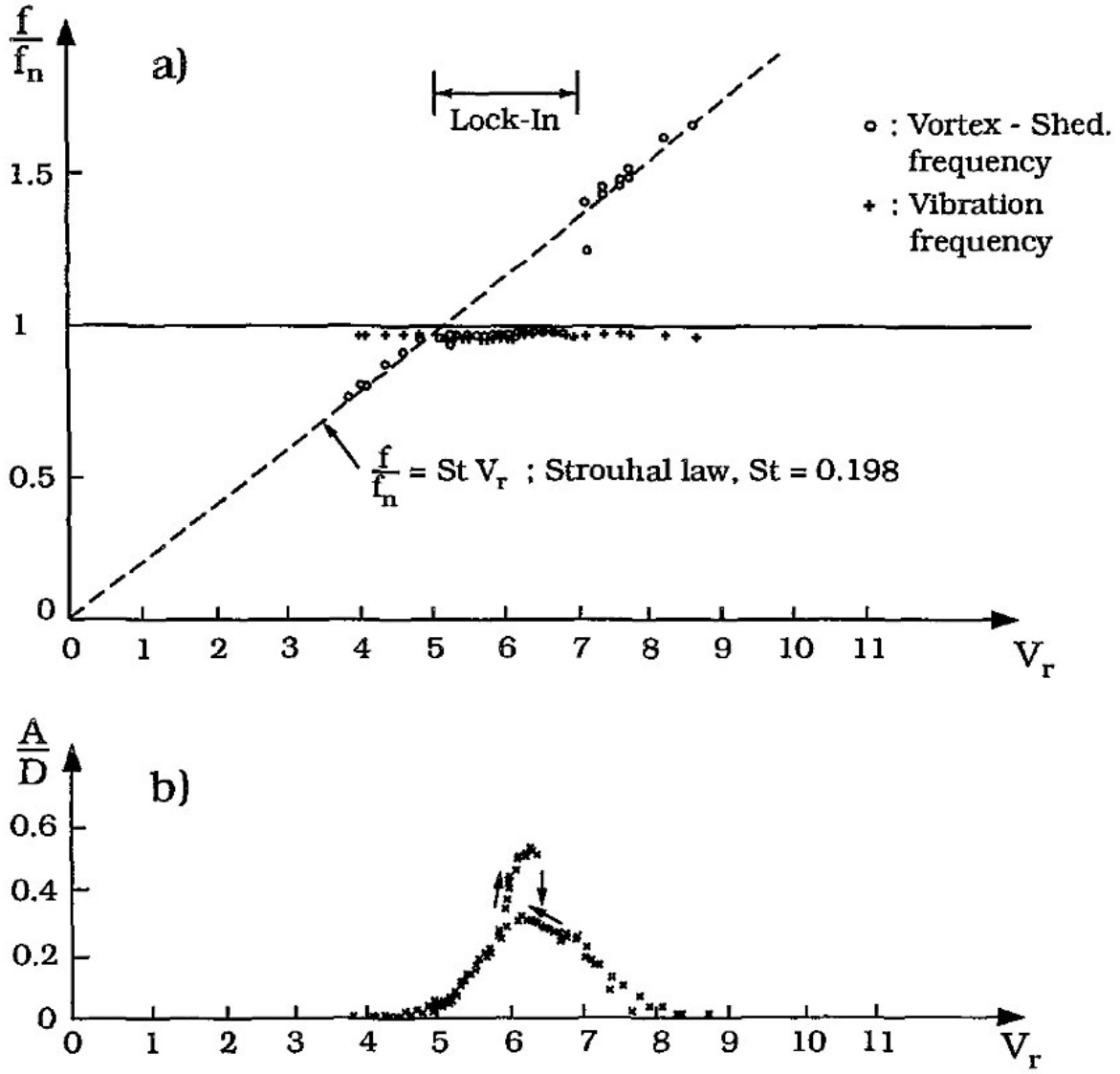

Figure 1: Results of the experiment by Feng [10]; reproduced from Sumer [11]

2 Method

2.1 Airfoil aerodynamic data

The DU96-W-180 airfoil was used in the computations. The airfoil was designed at TU Delft at the Faculty of Aerospace Engineering [13]. The aerodynamic performance of the airfoil, including its performance at high angles of attack, is investigated by Timmer [14]. The results of this investigation are presented in Figure 2. The DU96-W-180 airfoil, due to its relatively low thickness, good aerodynamic properties and publically available coordinates, is a good candidate for use on the outer parts of modern wind turbine blades.

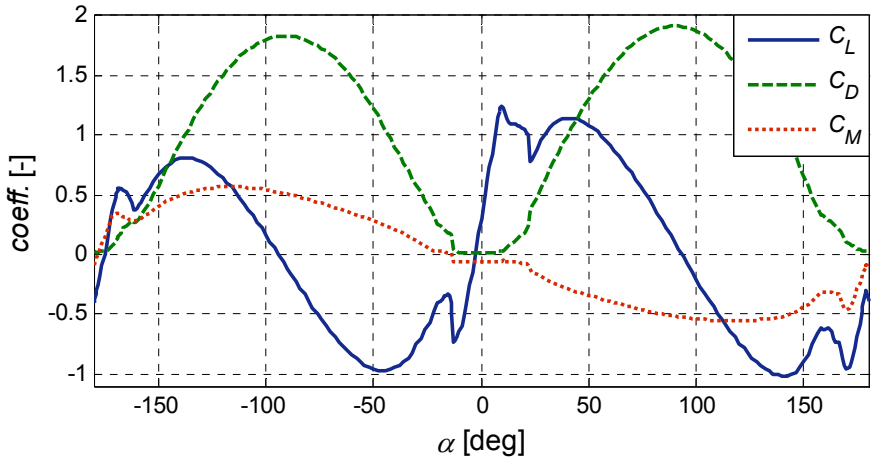

Figure 2: Aerodynamic force coefficients of the DU96-W-180 airfoil measured by Timmer [14]

2.2 Setup of the 2D and 3D Navier-Stokes solvers

All the computations were unsteady, made both in 2D RANS and 3D DES. The Navier-Stokes solvers used in the present work were EllipSys2D and EllipSys3D, developed by Michelsen [15,16] and Sørensen [17] at Risø DTU National Laboratory for Sustainable Energy and the Technical University of Denmark. The turbulence model used was the k-ω shear-stress transport (SST) [18]. It was used in both its standard RANS form and as a DES model as proposed by Strelets [19] with the delayed DES (DDES) technique of Menter and Kuntz [20]. The effects of laminar-to-turbulent transition in the boundary layer on the airfoil were modelled with the $\gamma - \widetilde{Re}_\theta$ correlation-based transition model of Menter [21]. For the present implementation, see Sørensen [22,23].

The airfoil motion was simulated by a moving mesh method. The grid points in the computational mesh were all moved together as a solid body. EllipSys2D and EllipSys3D are second-order accurate in time. The codes use a second-order backward differencing time discretization. Sub-iterations are used within each time step. In the present 2D and 3D computations, the diffusive terms were discretized with a second-order central differencing scheme. The convective fluxes in 2D and 3D RANS regions were computed using the third-order accurate QUICK scheme of Leonard [24]. The convective fluxes in 3D where the DDES model switched to large-eddy-simulation technique were computed with a fourth-order central differencing scheme.

The grids for 2D and 3D computations were made in HypGrid2D [25]. The 2D computations were made in an O-grid with $32.8 \cdot 10^3$ grid cells. The height of the domain in both 2D and 3D was 30 m. The dimensions of the 2D grid were 256 cells (parallel to the airfoil surface) by 128 cells (perpendicular to the airfoil surface). The 3D computations were made in an O-grid with $12.6 \cdot 10^6$ grid cells. The mesh was extruded in the span-wise direction by a single chord length. The dimensions were 256 cells (parallel to the airfoil surface) by 384 cells (perpendicular to the airfoil surface) by 128 cells (spanwise direction). The grid around the profile used in the 2D computations is presented in Figure 3.

The angle of attack was 90 degrees The boundary condition on the 3D lateral boundaries was periodic. The aim of setting such a boundary condition was to limit the effect of finite span. The airfoil surface was specified by a no-slip condition. Outlet condition was specified at angles +/-

45 degrees downstream the airfoil, in the perimeter of the O-grid. The rest of the perimeter was specified by the inlet condition.

The time step was 0.01 seconds. The Reynolds number of all the computations was $2 \cdot 10^6$. The airfoil boundary layer was simulated assuming free transition with ambient flow turbulence intensity, I, of $1.1 \cdot 10^{-3}$%. This corresponded to the turbulent kinetic energy, k, of $1.5 \cdot 10^{-4}$ m^2/s and the specific dissipation, ω, of 10^6 s^{-1} at the inlet.

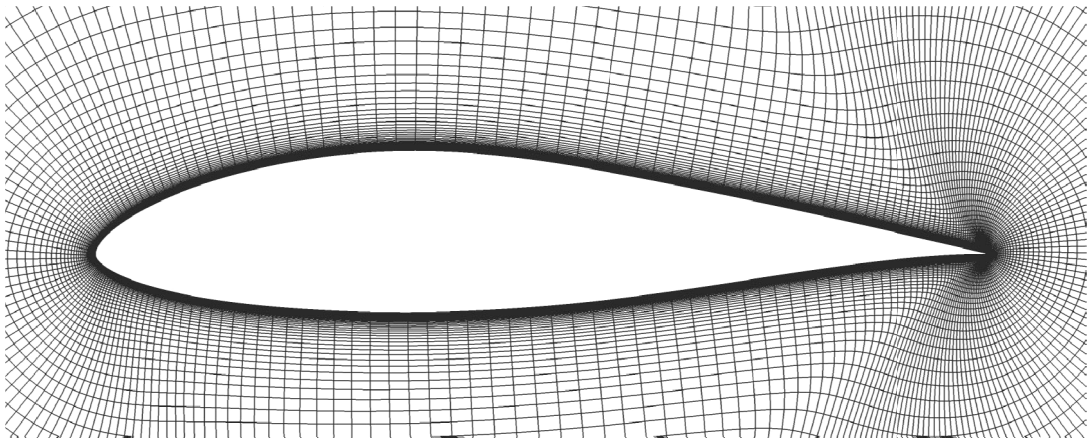

Figure 3: CFD grid around the DU96-W-180 airfoil, used in the 2D CFD computations

2.3 2D elastic model

The EllipSys add-on for elastically mounted airfoil computations was developed by Heinz [26]. It dimensionalized the system using the parameters proposed by Buhl *et al.* [27]. The parameters are presented in Table 1. The coefficients of viscous damping in all three directions were zero. The structural parameters from Table 1 were not meant to represent any specific position on a specific blade. However, the section should be representative of blade sections on the outer parts of general wind turbine blades. The eigenfrequency varied within the limits specified in Table 1 in order to match specific oscillation periods of the prescribed motion computations.

Table 1: Parameters used in the dimensionalization of the DU96-W-180 airfoil model in the structural code

Rotational centre x/c [-]	0.25
Chord length [m]	1
Air density [kg/m^3]	1.225
Centre of gravity x/c [-]	0.35
Airfoil mass [kg/m]	40
Moment of inertia [kg m^2]	2
Flapwise eigenfrequency [Hz]	3.5-5.4
Edgewise eigenfrequency [Hz]	1.7-2.7
Torsional eigenfrequency [Hz]	17.4-27.0

Note that time consumption of the elastic model is negligible compared with time consumption of 3D or even 2D CFD computations.

2.4 Data processing

Snapshots of the flow and the time series of the load in the edgewise direction were extracted from the non-moving computations (of the fixed airfoil). The snapshots visualized the mechanism of vortex shedding. The time series from both 2D and 3D CFD simulations were used to calculate the stationary Strouhal number, defined as:

$$St = \frac{f_v c}{V} \quad (1)$$

where f_v is the vortex shedding frequency, c is the chord length and V is the inflow velocity.

Vortex induced vibration is by nature an aeroelastic problem. However, here an attempt was made to identify the aeroelastic stability limits by means of prescribed motion computations where the airfoil was subjected to forced oscillations along the chord line. The load-displacement plots and the mean power were extracted from the computations. The instantaneous aerodynamic power per unit length of the system was defined as the product of the instantaneous speed of the airfoil and the component of the aerodynamic loading per unit length in the displacement direction, $R_x(t)$. Then, the mean value during a whole number of periods was calculated:

$$\bar{P} = \frac{1}{nT}\int_0^{nT} R_x(t)\frac{dx}{dt}dt \quad (2)$$

The time-series length in the power calculations was 10 oscillation periods in the case of 2D flows, and 30 periods in the case of 3D. Assuming that the damping in the system is linear, the power is directly proportional to the damping coefficient. Therefore, even though the aerodynamic damping is not necessarily linear, using power to determine the aeroelastic stability limits is somehow intuitive. When the power was positive, the flow fed energy to the oscillating system. In other words, an elastically mounted airfoil model of the same aerodynamic characteristics would vibrate with the same frequency under the same flow conditions. The same qualitative result would be obtained by integrating the loading over the displacement during a whole number of periods, and therefore obtaining the aerodynamic work.

A number of computations were made at different vibration periods, T. Then, the mean dimensionless power was plotted as a function of the dimensionless vibration period $T^*=T\,V/c$. Such a plot representing an exemplary vibrating cylinder is shown in Figure 4 (where c is the diameter). The corresponding Reynolds number was $2\cdot10^6$. The dimensionless mean power presented in the figure was obtained by normalization of the mean power with density, chord length, vibration amplitude and vibration period:

$$P^* = \frac{T}{\rho c A V^2}\bar{P} \quad (3)$$

The motivation for such a non-dimensionalization is as follows. The power is the product of the loading and airfoil velocity, i.e. $P = R_x(t)\dot{x}$. The loading is directly proportional to the square of the flow speed, i.e. $R_x \sim V^2$. The airfoil velocity is directly proportional to the ratio of the

amplitude and period of oscillation, i.e. $\dot{x} \sim \frac{A}{T}$. Therefore, the loading was non-dimensionalized by $\rho c V^2$, and the airfoil velocity was non-dimensionalized by $\frac{A}{T}$ which resulted with Eq. (3).

3 Results and Discussion

3.1 Computations on a circular cylinder

Figure 4 presents the dimensionless power of the oscillating cylinder as a function of the dimensionless oscillation period. The figure presents results of 2D computations with the A^*/T^*=0.01. There is a significant similarity between Figure 4 and the lower graph of Figure 1 which points to the analogy between the current work and the experiment by Feng. It is as follows: Regarding the x axis, since the dimensionless flow velocity in Figure 1 is defined as $V_r = V/Df_n$, and the dimensionless vibration period in Figure 4 was defined as $T^*=T\,V/c$, both represent the same number. Regarding the y axis, in order for the dimensionless amplitude presented in Figure 1 (lower) to increase, the flow needs to feed energy into the vibrating system. In other words, the dimensionless power, as presented in Figure 4, would be relatively large. Such an increase is visible in Figure 4, however, at a different value on the x axis than the increase in amplitude in Figure 1 (lower). This difference was due to a higher vortex shedding frequency, namely St=0.3, in the computations. The higher Strouhal number and therefore the vortex shedding frequency stemmed from a higher Reynolds number in the computations than in the experiment, and were in agreement with the literature [11].

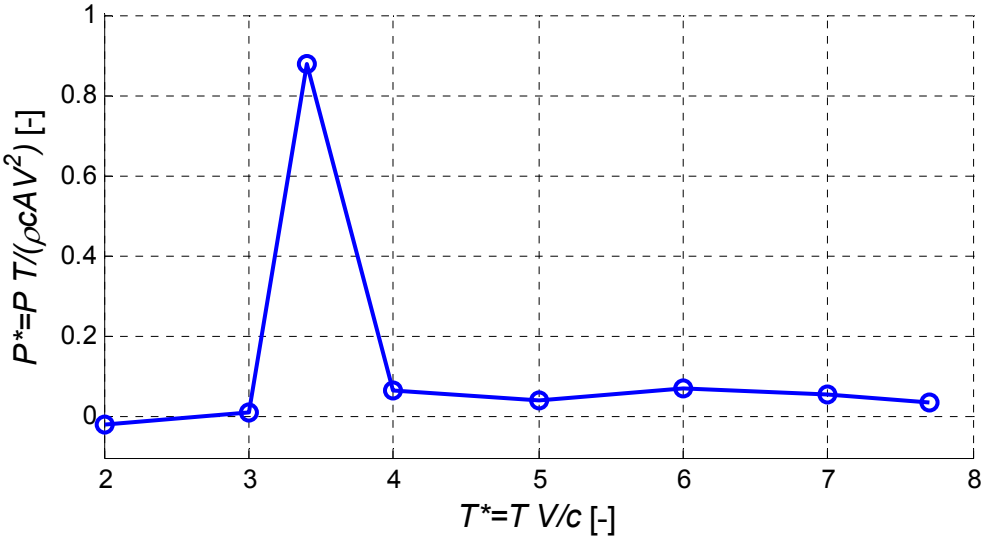

Figure 4: Dimensionless power as a function of dimensionless period of forced oscillation of a cylinder; the peak in the value indicates that the corresponding elastic system with the corresponding eigenfrequency could show negative damping.

To confirm that the power peak in Figure 4 was associated with a resonance between the vortex shedding and the motion of the cylinder, the associated load spectra and the load-displacement plots are presented in Figure 5. In the upper graphs of Figure 5 the results of a computation with the displacement frequency equal to the vortex-shedding frequency are presented. The load spectrum showed only one peak. The load-displacement plot was of deterministic shape.

The shape was exactly repeated over a number of displacement periods. The direction of the loop was clockwise. Computations made in a relatively narrow frequency band around the frequency considered in this figure showed similar behaviour. On the other hand, the lower graphs of Figure 5 show the results of a computation made with the dimensionless displacement period of 4. The corresponding dimensionless displacement frequency was 0.25. The dimensionless vortex shedding frequency, and therefore the Strouhal number, was approximately 0.3 which was in agreement with the literature [11]. The displacement frequency and the vortex shedding frequency were not close enough for the lock-in to occur. Therefore the associated dimensionless power presented in Figure 4 was relatively low. The shape of the load-displacement curve changed over consecutive displacement periods, as seen in the lower left graph of Figure 5. The load spectrum showed two distinct peaks. One peak corresponded to the vortex-shedding frequency and the other to the displacement frequency.

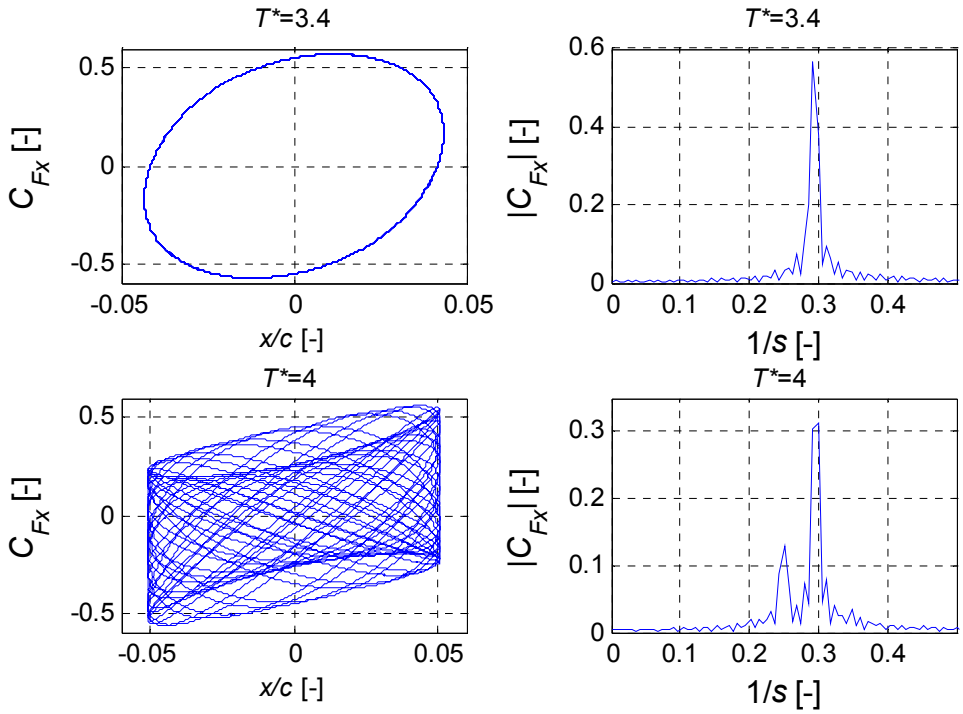

Figure 5: (upper) Load-displacement plot and load spectrum at T^*=3.4; (lower) Load-displacement plot and load spectrum at T^*=4

3.2 Computations on the DU96-W-180 airfoil

In the current work, computations similar to those presented on the cylinder were carried out on the DU96-W-180 airfoil at 90 deg angle of attack, both in 2D and 3D. The drawback of performing 3D DES computations in deep stall was the relatively long computation time. Such long computational times would make optimization of blades with respect to standstill vibrations based on 3D computations extremely expensive. Therefore, faster methods such as either 2D transient computations or engineering-type models are appealing if they reflect enough of the physics to simulate the main flow behaviour.

3.2.1 Computations on the non-moving airfoil

The upper graph of Figure 6 presents the time series of the chordwise force coefficient, C_{Fx}, of the DU96-W-180 airfoil at 90 deg angle of attack. The figure shows both the results of the 2D and 3D DES computations, both for 80 dimensionless time units, *s*. The 2D time series was more regular than the 3D series, with amplitude twice as large as the 3D series. This is visible in the lower graph of Figure 6 which shows the single-sided amplitude spectrum of the load coefficient based on the time series of 100 dimensionless time units. The Strouhal number values of the 2D and 3D computations were 0.13 and 0.16, respectively.

The instantaneous 3D loading was spatially averaged in the spanwise direction of the extruded profile. The time series of C_{Fx} related to three equidistant cross sections of the extruded profile are presented in Figure 7. The time series were well correlated. On the other hand, the profile was extruded by a single chord length. Therefore, the three sections were relatively close to each other while it is intuitive that an increase in the spanwise distance between the sections may decrease the load correlation. It is also observed and described in [1,6,11,28] that the spanwise pressure correlation between two points of a circular cylinder decreases when the distance between the points increases.

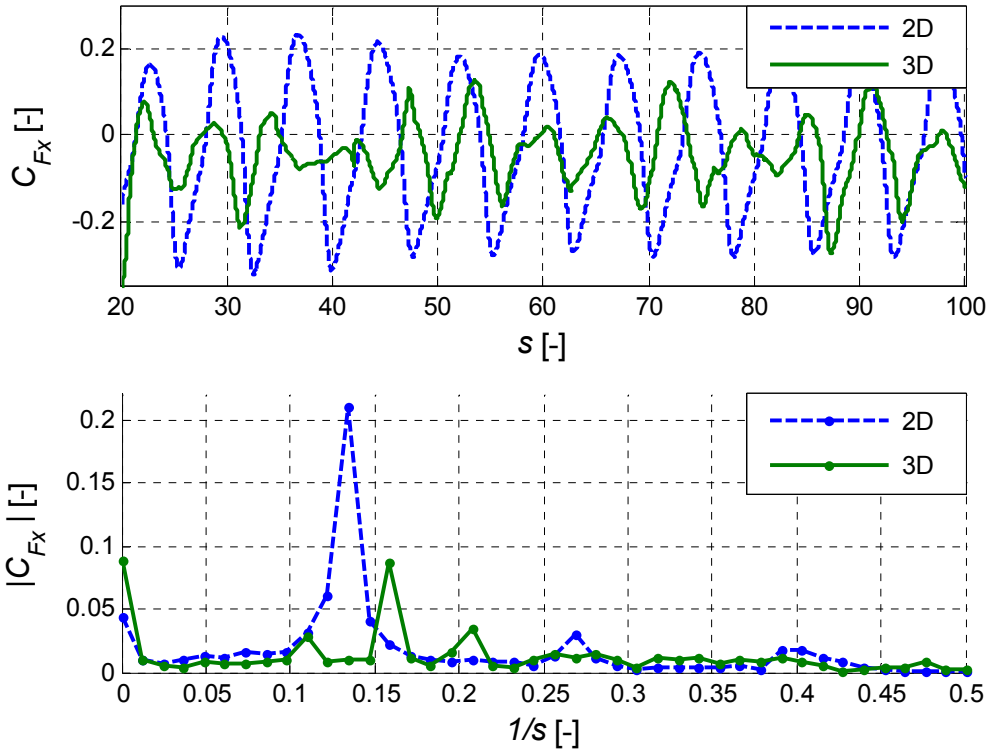

Figure 6: (up) Time series of the load coefficient in the chordwise direction, C_{Fx}; (lower) Single-sided amplitude spectrum of the chordwise load coefficient

It is noteworthy that at 90 deg angle of attack, C_{Fx} is the same as the negative lift coefficient. The lift coefficient of the 2D and 3D computations was 0.022 and 0.044, respectively. The measured lift coefficient is 0.11 [14]. The drag coefficient of the 2D and 3D computations was 3.1 and 2.5, respectively. The measured drag coefficient is 1.9 [14]. Therefore, both 2D and 3D computations overestimated the drag and underestimated the lift. However, possible occurrence of wind tunnel effects like tunnel blockage might have compromised the accuracy of the

measurements. Such effects are pronounced at high angles of attack and may cause experimental results to vary depending on the tunnel at which the measurements are taken. On the other hand, CFD computations may be laden with inaccuracies due to modelling limitations. To obtain higher agreement between the computations and experimental data, the computations would likely have had to include the tunnel walls and identical model aspect ratio.

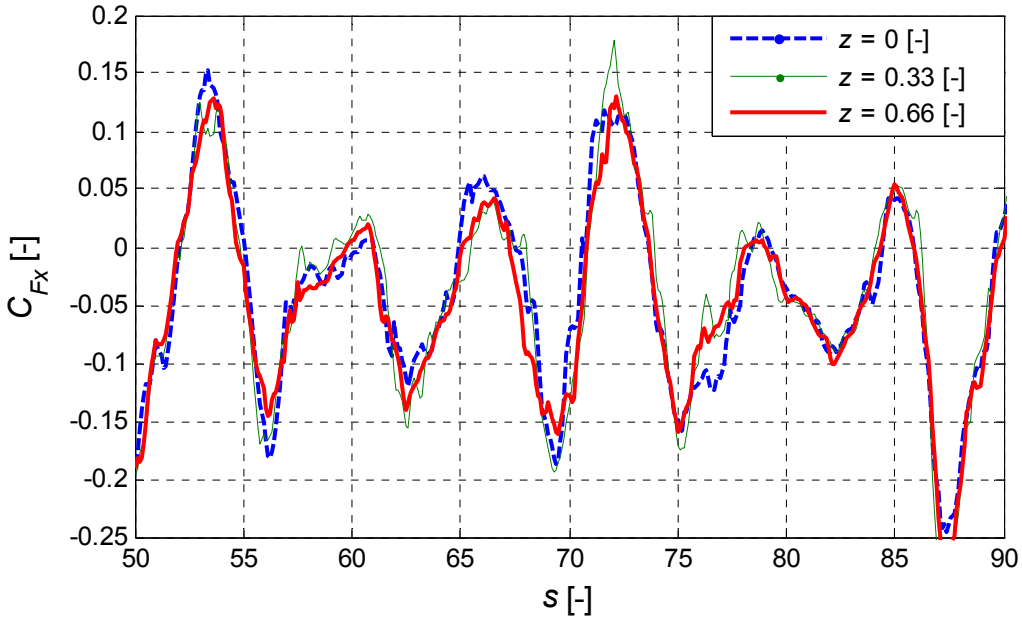

Figure 7: Time series of the force coefficient in the chordwise direction, C_{Fx}, from three equidistant cross sections of the extruded profile

To further illustrate that the force oscillations are caused by the vortex shedding, two snapshots of the 3D flow are presented in Figure 8. The figure presents vorticity magnitude. Dark areas correspond to high values. In the snaphot on the left side, a vortex is being shed off the leading edge. The vortex is marked with a circle. In the snaphot on the right side, a vortex is being shed off the trailing edge – also marked with a circle. This was confirmed by analysis of the animation showing pressure variation. It is noteworthy that a 2D computation made on Risø A1-21 returned the Strouhal number value of 0.13 which was the same as that of the DU profile obtained with 2D CFD. This indicated that at high angles of attack where separation is well defined, the Strouhal number is relatively independent of the airfoil shape.

After the values of the Strouhal number were obtained from the non-moving computations, 2D and 3D prescribed motion computations were carried out. The reason was to investigate the aeroelastic stability limits of the airfoil at 90 deg angle of attack.

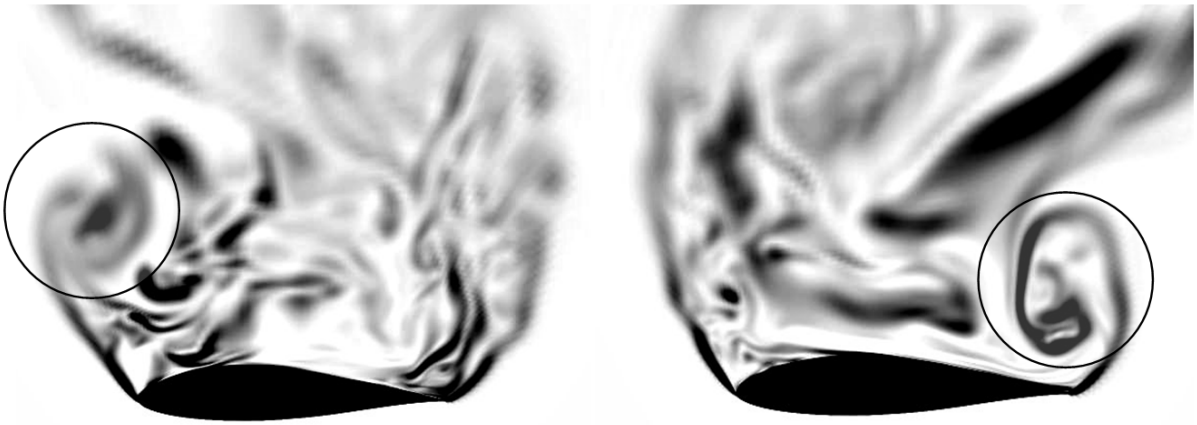

Figure 8: Snapshots presenting vorticity magnitude of the 3D flow around the DU96-W-180 airfoil

3.2.2 Prescribed motion computations

Figure 9 presents the results of the 2D computations with three curves showing the dimensionless power, P^*, as a function of the dimensionless forced-oscillation period, T^*, of DU96-W-180. The power was defined in Eq. (3). Each of the curves corresponds to simulations carried out at a specific A^*/T^* ratio. The reason for that was as follows. A^*/T^* or f^*A^* – where f^* is the dimensionless oscillation frequency – can be thought of as the level of perturbation imposed by the airfoil motion on the flow. If A^* was constant in a set of computations, then such a level of perturbation would grow with f^*. Then, computations with high oscillation frequency would drive the vortex shedding and create the lock-in. After a simple calculation, one may show that there exists the following relation between the A^*/T^* ratio, airfoil maximum velocity, and the maximum variation in the angle of attack:

$$\frac{A^*}{T^*} = \frac{\frac{A}{c}}{\frac{TV}{c}} = \frac{A}{T\,V} = \frac{1}{2\pi}\frac{|\dot{x}|_{max}}{V} = \frac{1}{2\pi}\tan\alpha_{max} \qquad (4)$$

where $\dot{x}$ is the velocity of the airfoil and α is the angle of attack. Therefore, maintaining a constant A^*/T^* ratio in a series of computations assures a constant ratio between the maximum airfoil velocity and the flow velocity. It also assures a constant maximum variation in the relative angle of attack independent of the oscillation frequency. The dimensionless vortex shedding period of the three cases was 7.7. As the figure shows, the dimensionless power in all three cases increased to a peak with positive sign when the oscillation period reached 7.7. This indicated that an actual DU96-W-180 airfoil with the natural frequency of the edgewise mode close to the frequency of vortex shedding could have issues with dynamic instability. In order to confirm that the vortex shedding was in resonance with the oscillation, load-displacement plots of the 2D simulations of all three cases at $T^*=7.7$ are presented in Figure 10. In the figure, the direction of all the loops is clockwise.

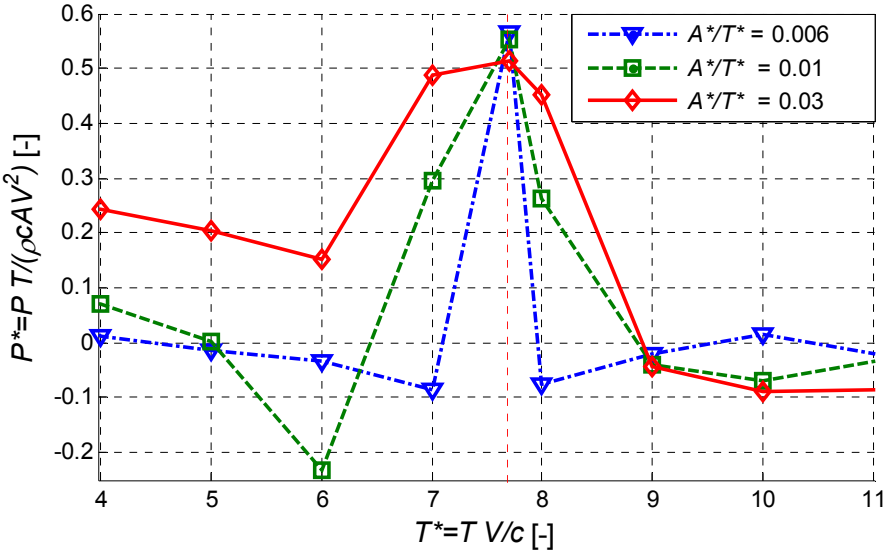

Figure 9: Dimensionless power related to prescribed oscillation of the DU96-W-180 airfoil; 3 different *A*/T ratios; 2D computations.**

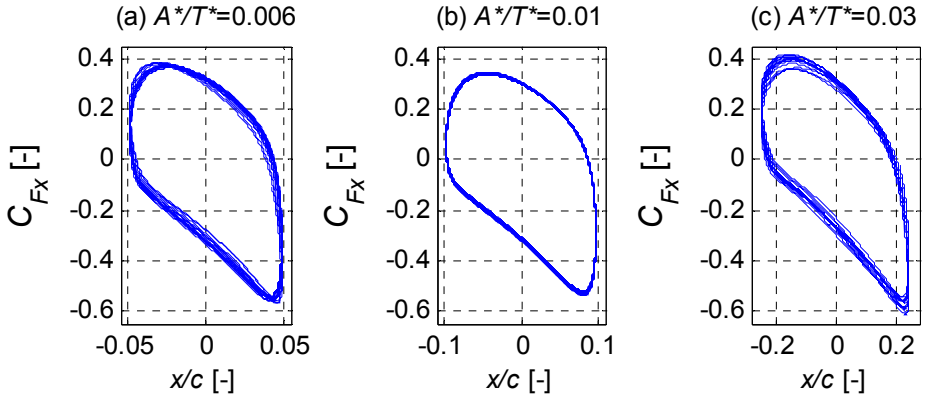

Figure 10: Load-displacement plots of DU96-W-180 at *T=7.7 and *A*/T**= (a) 0.006, (b) 0.01, (c) 0.03; 2D computations.**

Plots presented in Figure 9 also indicated what is mentioned by Sumer and Fredsøe [11] in the context of a vibrating cylinder, i.e. the larger the oscillation amplitude is, the wider the lock-in range is. Here, the larger the *A*/T** ratio was, the wider the *T** band in which the power increased was. This was further indicated by the load-displacement plots of the three systems at *T**=7 (see Figure 11), i.e. 9% or 0.7 dimensionless time units away from the vortex shedding period. There, the system with the highest oscillation amplitude, *A*/T**=0.03 (c), appeared fully locked-in. Positive direction of the loop was clockwise. The system with *A*/T**=0.01 (b) appeared as locked-in through a large part of the computation. Positive direction of the loop was also clockwise. The system with the smallest ratio – *A*/T**=0.006 – didn't show the resonance at all as the curve changed shape in every consecutive oscillation period.

Also, the sensitivity of the dimensionless power with respect to the changes in the angle of attack and angle of vibration was studied. The results are presented in Figure 12, where β is the angle between the chord line and the vibration direction. β is zero when the direction of vibration coincides with the chord line, and it is positive counter-clockwise. The results showed that a 10-deg variation in β from the default value of zero was less significant than the same

variation in the angle of attack. Increasing the angle of attack by 10 deg increased the computed power by 18%.

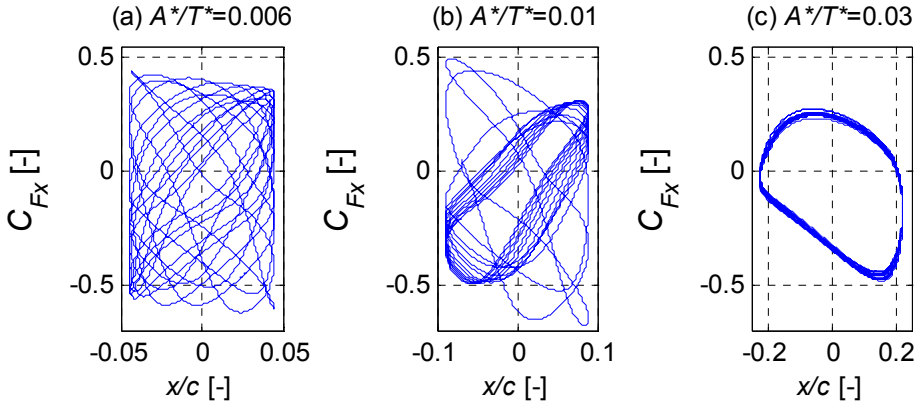

Figure 11: Load-displacement plots of DU96-W-180 at T^*=7 and A^*/T^*= (a) 0.006, (b) 0.01, (c) 0.03; 2D computations.

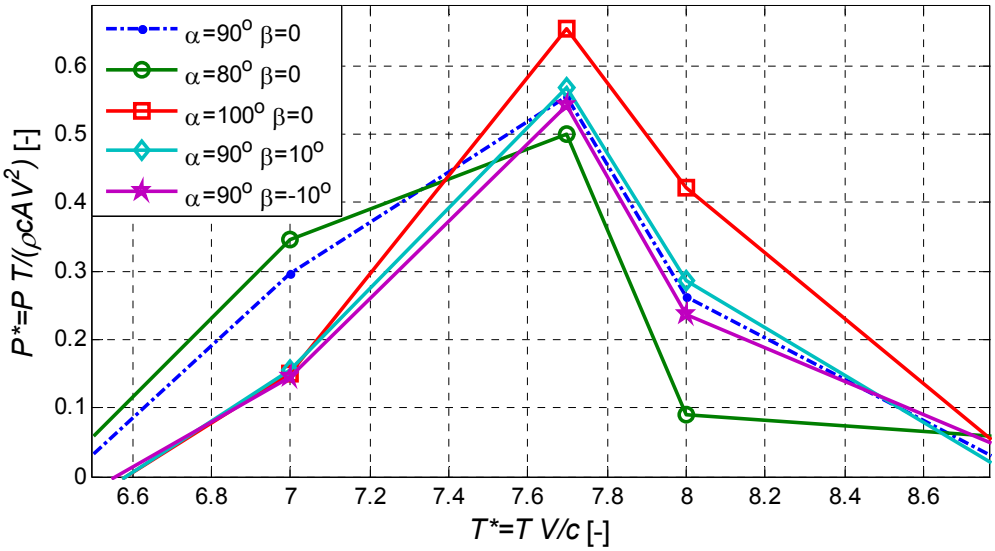

Figure 12: Sensitivity of the dimensionless power of DU96-W-180 on changes in the angle of attack and angle of vibration; 2D computations.

Figure 13 presents the dimensionless power as a function of the dimensionless period of forced vibration, comparing 2D and 3D computations. It is a comparison of the results of the 3D DES computations made at A^*/T^*=0.03 with the results of the 2D RANS computations presented in Figure 9. Surprisingly, the power peaked at T*=7.7 although the dimensionless stationary vortex shedding period in the 3D computations was 6.3 while the period in the 2D computations was 7.7.

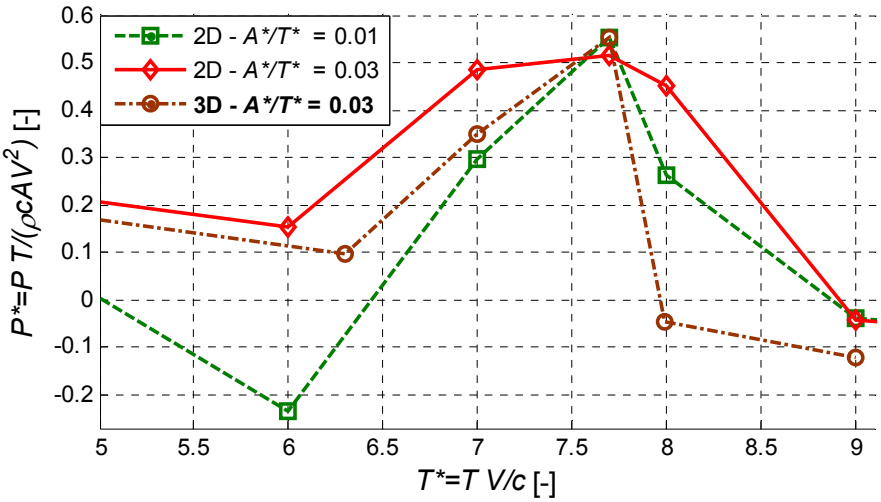

Figure 13: Dimensionless power related to prescribed oscillation of the DU96-W-180 profile; results of the 3D DES computations compared to the results of the 2D RANS computations

This may be clarified by looking at Figure 14 which presents the load-displacement plots from the 3D computations with three different eigen periods: T^* = 6.3, 7.7 and 8. These curves consist of 30 oscillation periods each. They are in very good agreement with the 3D power characteristic presented in Figure 13. Resonance between the displacement and the loading was clearly visible at $T^*=7.7$ where the shape of the curve remained practically constant for the whole time of the simulation. Direction of the loop was clockwise. T^*=7.7 is also where the power in Figure 13 peaked. The load-displacement curves corresponding to T^*=6.3 and 8 were not identical for all displacement loops and the corresponding power values were relatively small. This indicates that even though the 3D stationary vortex-shedding period was 6.3, when the airfoil was forced to oscillate, the loading characteristic resembled that of the 2D computations. The 3D prescribed motion load time series was relatively regular and resembled that of the non-moving 2D computation more than that of the non-moving 3D. Analysis, which is not presented here, of the present computations showed that the spanwise load correlation in the 3D flow was higher for the oscillating airfoil than for the non-moving. An increase in the spanwise correlation of the pressure distribution with increasing oscillation amplitude is also observed for a circular cylinder and described in [1,6,11,28]. One may therefore speculate that some characteristics of 2D simulations on oscillating airfoils may be applicable in 3D.

Moreover, the frequency analysis of the current loading not presented here indicated that a longer period of the forced motion resulted in a longer period of the vortex shedding. At T^*=3 the frequency analysis showed one peak at 3 (corresponding to the displacement period) and another at 7 (supposedly corresponding to the vortex-driven loading). However, at T^*=7 it showed one peak at 7 (corresponding to the displacement) and another at 7.7 (equal to the 2D stationary vortex shedding period). At T^*=7.7 only one peak was visible. In both the 2D and 3D computations, the power peaked to the values between 0.5 and 0.55 which were relatively close to each other.

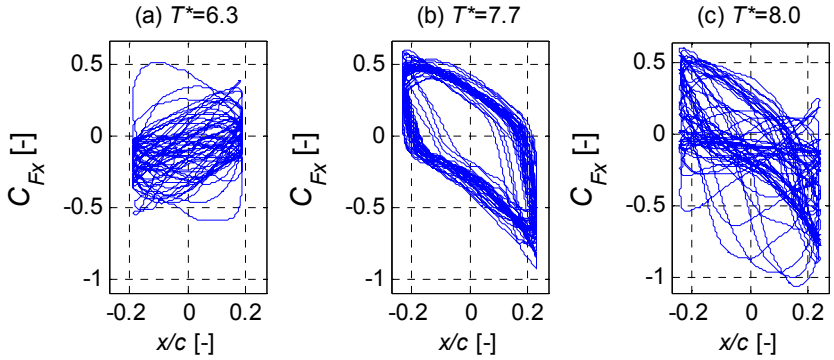

Figure 14: Load-displacement plots from the 3D DES computations of DU96-W-180 at A^*/T^*=0.03 and T^*= (a) 6.3, (b) 7.7, (c) 8.0

3.2.3 Elastically mounted airfoil computations

The current section presents results of the CFD computations performed with the aid of the structural model described in Chapter 2.3. The computations on the elastically mounted 2D structural model of the DU96-W-180 airfoil coupled with 2D CFD were performed at 90 degrees angle of attack. The model had one degree of freedom of movement in the edgewise direction. Figure 15 presents the dimensionless edgewise displacement time series. In the case of the elastically mounted airfoil computations, T^* represented the edgewise eigen period of the isolated structural system which was not necessarily the exact period of the oscillation of the aeroelastic system. The results of these computations supported the results of the 2D CFD prescribed motion computations. The motion in the edgewise direction had increasing amplitude in time when the eigen frequency of the system approached the frequency of vortex shedding (Figure 15 c). The growth of the amplitude in the edgewise-displacement time series was approximately constant in time. This made the calculation of logarithmic decrements inaccurate as these would change over time. Detailed investigation of limit cycles was outside the scope of the current work.

Figure 16 shows the dimensionless displacement of the same setup except with three degrees of freedom. At the beginning of the time simulations, the model was displaced by the drag in the flapwise direction by approximately 0.3 of the chord length. In the three cases where no violent vibrations occurred (a, b and d), the flapwise and edgewise displacements were of the same order of magnitude. In the case where the model showed growth of its displacement amplitude in time (c) the edgewise mode was dominating.

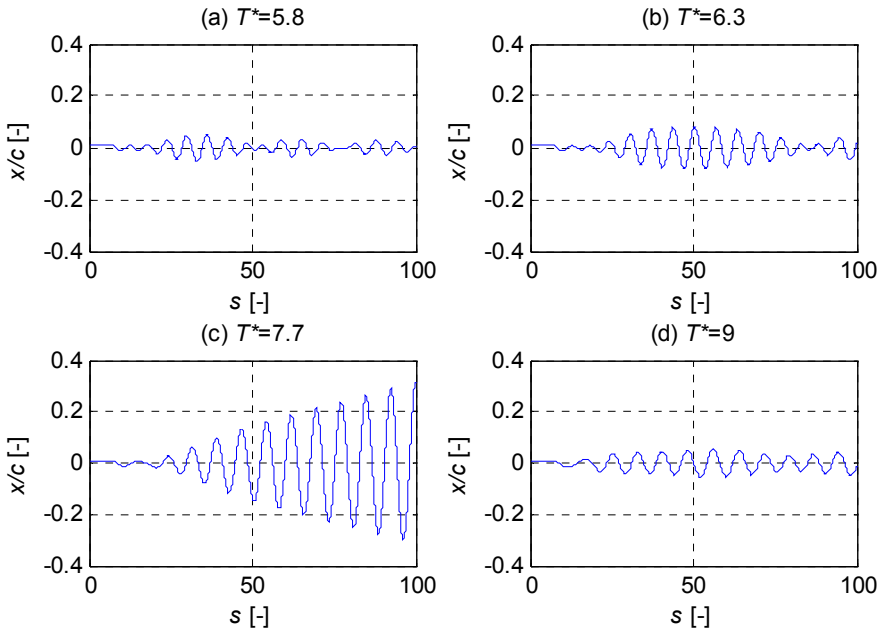

Figure 15: Dimensionless displacement in the edgewise direction of the elastically mounted 2D model of the DU96-W-180 at 90 deg angle of attack with one degree of freedom of movement. 2D CFD, 1DOF structural model.

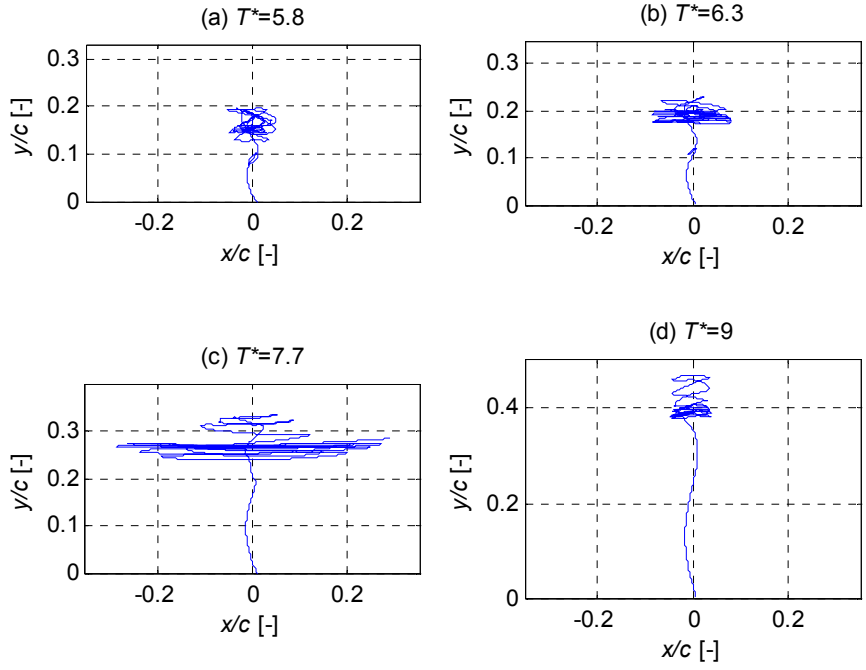

Figure 16: Displacement of the elastically mounted 2D, 3DOF structural model of DU96-W-180 coupled with 2D CFD; 90 deg angle of attack

Figure 17 presents dimensionless edgewise displacement time series of four different simulations made with the elastically mounted 2D, 3 DOF structural model of DU96-W-180 coupled with 3D CFD. The angle of attack was 90 degrees As in the case of the 2D CFD computations, it was impossible to determine constant values of damping ratio of the system. The model - like in the 2D CFD case - had four variations with different eigen periods. Cases (b) T^*=6.3 and (c) T^*=7.7 showed the highest maximum amplitude values within 100 time

units. It was shown previously that 6.3 was the period of the stationary vortex shedding of the 3D system. None the less, the displacement time series of the computation made with the eigen period 6.3 (c) did not indicate that there was a resonance between the system and the vortex-generated forcing. Moreover, the displacement time series (a),(b) and (c) were similar to that of a dynamic system subject to the beating phenomenon in which the frequency of forcing is relatively close to the system's eigen frequency, but not close enough to create a resonance. This indicated that the period of vortex shedding of the 3D CFD aeroelastic system in motion might be different than the period of stationary vortex shedding (6.3) or the period of vortex shedding of the system in prescribed motion (7.7). This was verified by a frequency analysis of the load time series of the computations (b) and (c). The analysis of both time series showed single peaks in the response corresponding to a period of 6.8 in the case of computation (b) and 7.1 in the case of computation (c). One may speculate that the difference comes from the elastically mounted system having three degrees of freedom while the prescribed motion system oscillated in a single direction.

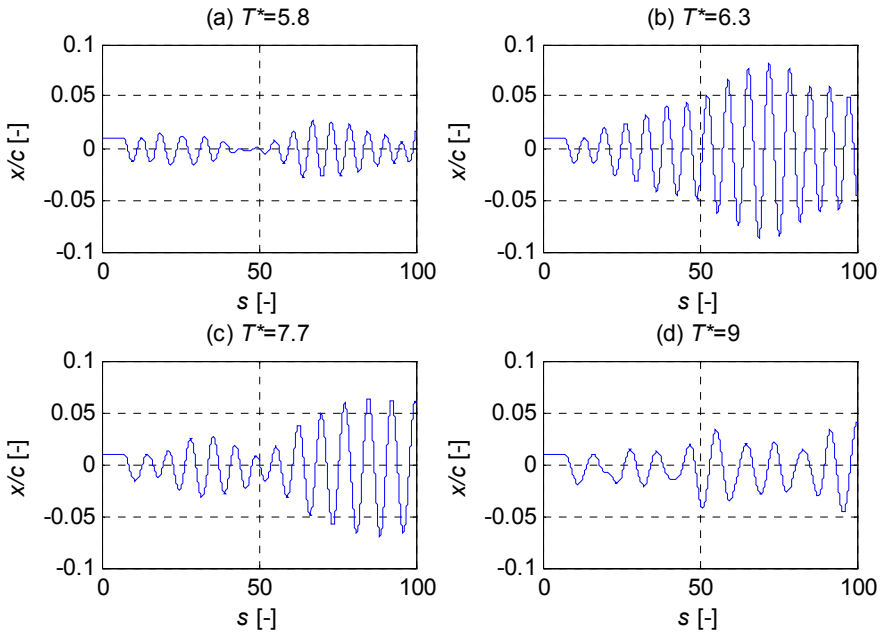

Figure 17: Dimensionless displacement in the edgewise direction of the elastically mounted 2D, 3DOF structural model coupled with 3D CFD; DU96-W-180 at 90 deg angle of attack; four different eigen periods of the edgewise mode

This fact spurred another computation with the eigen period of 7.0. The edgewise-displacement time series of that computation is presented in Figure 18. The displacement reached a higher amplitude than any of the 3D displacements presented above. The time series resembled more that of a dynamic system at resonance than at beating conditions.

A comparison of the 1 DOF and 3 DOF 2D CFD models with the 3 DOF 3D CFD model in terms of the maximum amplitude reached within 100 time units is presented in Figure 19. The comparison showed that the 1 DOF 2D CFD model over predicted the amplitudes at T^*=7.7 and 9 relative to the 3 DOF 2D CFD model. Both 2D CFD models showed the same tendency. The amplitudes were the highest at T^*=7.7 which was the 2D CFD stationary vortex shedding period. In the case of the 3D CFD model – as it was mentioned above - the maximum amplitude showed at T^*=7.0.

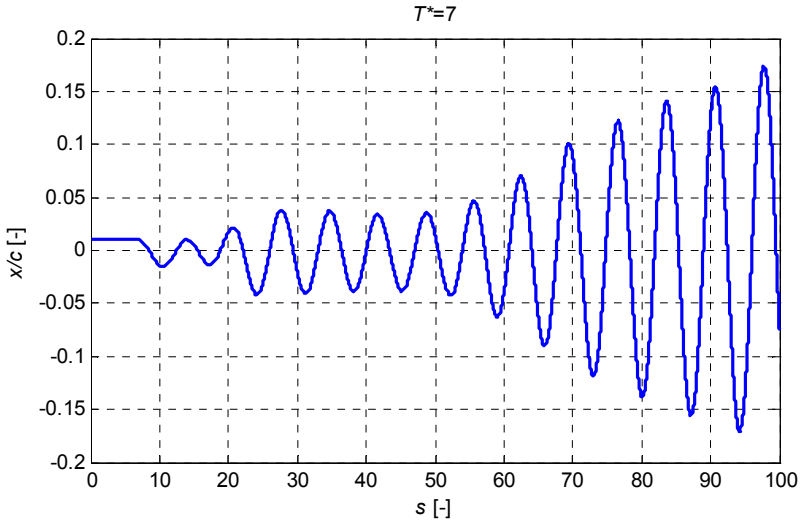

Figure 18: Dimensionless displacement in the edgewise direction of the elastically mounted 2D, 3DOF structural model coupled with 3D CFD; DU96-W-180; 90 deg angle of attack; edgewise dimensionless eigen period of 7.0

An important observation is that, the 3D CFD computations showed significantly lower maximum displacement, and occurring at a different eigen period than the corresponding 2D computations. Assuming that 3D CFD is more accurate in the present context, the results indicated that 2D computations can simulate the qualitative behaviour of the aeroelastic system while 3D computations are necessary to deliver more accurate quantitative results. However, it was not explicitly shown in the present work that 3D CFD is a better representation of the real life situation.

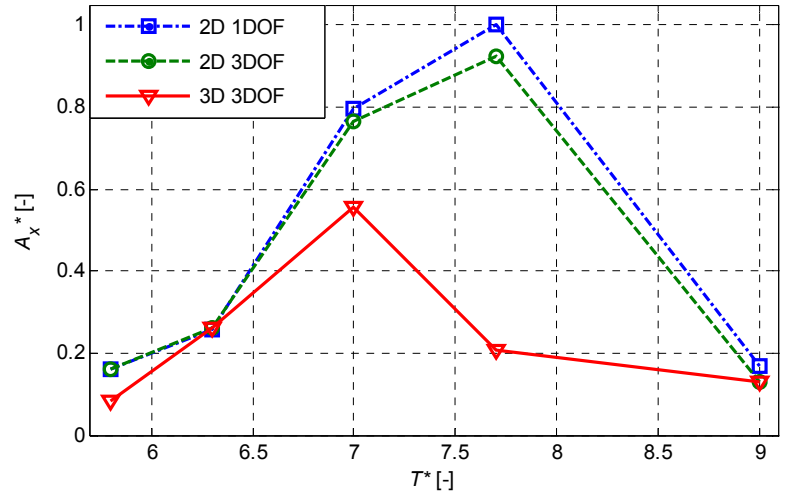

Figure 19: Comparison of the maximum amplitude reached within 100 time units by the 1 DOF and 3 DOF 2D CFD models with the 3 DOF 3D CFD model.

Several of the computations presented in this work were also performed on the Risø-A1-21 airfoil. The results were similar to those of the DU96-W-180 indicating that the phenomena described here were rather general and not exclusively specific to the DU profile.

One of the most significant implications of the current findings is that – according to the dimensionalization of T^* at which the vibrations occurred in the simulations – vortex-induced vibrations may show on modern wind turbine blades, assuming that the average chord length is 2 m and the frequency of the first edgewise mode is approximately 1 Hz.

Besides vortex-induced vibrations, another potential kind of blade vibrations is stall-induced vibrations (SIV) also referred to as galloping. However, the phenomena presented in this article were most likely solely related to vortex shedding. This was verified by the analysis of basic characteristics of galloping of bluff bodies [11]. The fact that vibrations modelled in 2D and 3D CFD occurred only in frequency bands around the corresponding frequencies of vortex shedding indicated that they were vortex related. Moreover, if these vibrations were stall related they would most likely show in lower frequencies, cover a wider range of frequencies and grow with the vibration period.

4 Conclusions

2D and 3D non-moving, prescribed motion and elastically mounted airfoil CFD computations of the DU96-W-180 airfoil were carried out in this work. The computations aimed at investigating the phenomenon of vortex-induced vibrations of an elastically mounted airfoil section.

The majority of the simulations showed negative aerodynamic damping in the vicinity of the corresponding stationary vortex-shedding frequencies. Analysis of the data indicated possibility of the lock-in phenomenon for airfoils.

Dimensionalization of the dimensionless eigen period at which the vibrations were predicted in the simulations indicated possibility of vortex-induced vibrations of modern wind turbine blades.

There was a difference between the 2D and 3D CFD results in terms of the frequency at which the vibrations were predicted.

Surprisingly, both the 2D and 3D prescribed motion computations showed an increase in power around the 2D stationary vortex shedding period.

The amplitude reached within 100 dimensionless time units was significantly lower in the case of the 3D CFD elastic computations than the 2D CFD elastic computations.

A shorter time series was sufficient in order to verify the sign of aerodynamic damping in the case of elastic computations than prescribed motion.

5 Future work

Based on the current study and literature review a number of issues were identified that need to be investigated in future work. Below is the list of the most important of:

- Investigate the effects of blade twist and taper as well as airfoil shape on the aerodynamic stability limits. The current work indicated that the VIV characteristics

described in this paper are general and not specific to the DU96-W-180 airfoil. The effects of twist and taper were outside the scope of the present work.

- Investigate the effects of the shear and turbulence in the incoming flow. Experiments carried out on circular cylinders showed that both the shear and turbulence decrease the amplitude of vibrations. These factors were outside the scope of the current work.

- Investigate the amplitudes of limit cycles in vortex-induced vibrations of wind turbine blades. Knowing the levels of these amplitudes would help to determine the risk of turbine failure due to VIV.

- Perform a 3D DES time-marching computation on a full wind turbine blade to investigate further the limitations of 2D and 3D computations on airfoils.

- Create an engineering model for predicting vortex-induced vibrations in aeroelastic codes.

Acknowledgements

The authors of this article would like to thank Nando Timmer for making the coordinates and aerodynamic characteristics of the DU96-W-180 airfoil used in this work available.

Computations were made possible by the use of the PC-cluster provided by Danish Center for Scientific Computing (DCSC) and the Risø-DTU central computing facility.

6 Nomenclature

A = Vibration amplitude [m]
A^* = Dimensionless vibration amplitude [-]
α = Angle of attack [deg]
β = The angle between the chord line and the direction in which the vibration occurs [deg]
C_{FX} = Force coefficient in the chordwise direction, $\frac{F_x}{\frac{1}{2}\rho V^2 c}$ [-]
c = Chord length [m]
D = Diameter of the cylinder [m]
f = Vibration frequency [Hz]
f^* = Dimensionless vibration frequency, $\frac{c}{TV}$ [-]
f_n = Natural frequency of the vibrating cylinder [Hz]
f_v = Vortex-shedding frequency [Hz]
$\bar{P}$ = Mean power during a whole number of periods in prescribed motion [W]
P^* = Mean dimensionless power in prescribed motion [-]
$\vec{R}$ = Net aerodynamic loading on the airfoil in prescribed motion [N/m]
St = Strouhal number [-]
s = Dimensionless time, $t\frac{V}{c}$ [-]

T = Vibration period [s]
T^* = Dimensionless vibration period, $\frac{TV}{c}$ [-]
V = Flow velocity [m/s]
Vr = Dimensionless flow velocity [-]
$\overrightarrow{V_x}$ = Instantaneous velocity of the airfoil in prescribed motion, $\frac{dx}{dt}\hat{\imath}$ [m/s]

7 References

[1] Dowell, E.H.; Clark, R.; Cox. D.; Curtiss, H.C. Jr.; Edwards, J.W.; Hall, K.C.; Peters, D.A.; Scanlan, R.; Simiu, E.; Sisto, F.; Strganac, T.W.: *A Modern Course in Aeroelasticity, Fourth Revised and Enlarged Edition*; Kluwer Academic Publishers; 2004

[2] Gaunaa, Mac; Larsen, Torben J.: *Stilstandslaster*; chapter in *"Forskning i Aeroelasticitet"*; ed. Christian Bak; Risø-R-1434(DA) in Danish, Risø DTU National Laboratory for Sustainable Energy; 2002

[3] Buhl, Thomas: *Edgewise vibration instand still*, chapter in *"Research in Aeroelasticity EFP-2006"*; ed. Christian Bak; Risø-R-1611; 2006

[4] Skrzypinski, Witold; Gaunaa, Mac: *Wind turbine blade vibration at standstill conditions – the effect of imposing lag on the aerodynamic response of an elastically mounted airfoil*; Proceedings of The Science of Making Torque from Wind; Heraklion, Greece; June 28-30 2010

[5] Parkinson, G.V.; Smith, J.D.: *A square prism as an aeroelastic non-linear oscillator,* The Quarterly Journal of Mechanics and Applied Mathematics; Vol. XVH, Ft. 3; 1964

[6] Pantazopoulos, M.S.: *Vortex-induced vibration parameters: critical review*; Proceedings of the International Conference on Offshore Mechanics and Arctic Engineering; American Society of Mechanical Engineers; 1994

[7] Bertagnolio, F.; Rasmussen, F.; Sørensen N.N.; Johansen, J.; Madsen, H.Aa.: *A stochastic model for the simulation of wind turbine blades in stochastic stall*; Wind Energy; 13:323-338; 2010

[8] Riziotis, V.A.; Voutsinas, S.G.; Politis, E.S.; Chaviaropoulos, P.K.: *Stability analysis of parked wind turbine blades using a vortex model*; Proceedings of TORQUE 2010: The Science of Making Torque from Wind; Crete, Greece; June 28-30 2010

[9] Hansen, M.H.: *Bias effect of self-induced turbulence on the stall-flutter limit of an airfoil section*; The sixteenth international congress on sound and vibration; Kraków, 5-9 July 2009

[10] Feng, C.C.: *The measurement of vortex-induced effects on flow past stationary and oscillating circular D-section cylinders;* M.Sc. Thesis; The University of British Columbia; 1968

[11] Sumer, M.; Fredsøe, J.: *Hydrodynamics around cylindrical structures, Advanced Series on Ocean Engineering – Volume 12*; World Scientific; 1997

[12] Williamson, C.H.K.; Roshko, A.: *Vortex formation in the wake of an oscillating cylinder;* Journal of Fluids and Structures; 2:355-381; 1988

[13] Timmer, W.A.; van Rooij, R.P.J.O.M: *Summary of the Delft University wind turbine dedicated airfoils*; AIAA-2003-0352; 2003

[14] Timmer, W.A.: *Aerodynamic characteristics of wind turbine blade airfoils at high angles-of-attack;* Proceedings of TORQUE 2010 The science of making torque from wind; Heraklion, Crete, Greece; June 28-30, 2010

[15] Michelsen J.A.: *Basic3D – a platform for development of multiblock PDE solvers;* Report AFM 92-05; Dept. of Fluid Mechanics, Technical University of Denmark, DTU; Denmark; 1992

[16] Michelsen J.A.: *Block structured multigrid solution of 2D and 3D elliptic PDE's;* Report AFM 94-06; Dept. of Fluid Mechanics, Technical University of Denmark, DTU; Denmark; 1994

[17] Sørensen N.N.: *General purpose flow solver applied to flow over hills;* PHD Dissertation, Risø-R-827(EN); Risø National Laboratory, Roskilde, Denmark; 1995

[18] Menter, F.R.: *Zonal two equation k-omega turbulence models for aerodynamic flows*; AIAA Paper 932906; American Institute of Aeronautics and Astronautics;1993

[19] Strelets, M.: *Detached eddy simulation of massively separated flows*; AIAA Paper 2001-0879, Russian Scientific Center 'Applied Chemistry'; St. Petersburg; 2001

[20] Menter F.R.; Kuntz M.: *Adaptation of eddy-viscosity turbulence models to unsteady separated flow behind vehicles*; In The Aerodynamics of Heavy Vehicles: Trucks, Buses, and Trains (volume 19 of Lecture Notes in Applied and Computational Mechanics); Springer; Berlin; 339–352; 2004

[21] Menter F.R.; Langtry R.B.; Likki S.R.; Suzen Y.B.; Huang P.G.; Völker S.: *A correlation-based transition model using local variables - Part I: model formulation*; Proceedings of ASME Turbo Expo 2004, Power for Land, Sea, and Air; Vienna, Austria; ASME GT2004-53452; 14–17 June 2004

[22] Sørensen N.N.: *CFD modelling of laminar-turbulent transition for airfoils and rotors using the* $\gamma - \widetilde{Re}_\theta$ *mode*; Wind Energy; 12: 715–733; 2009

[23] Sørensen N.N.; Schreck, S.: *Computation of the National Renewable Energy Laboratory Phase-VI rotor in pitch motion during standstill*; Wind Energy; DOI: 10.1002/we.480; 2011

[24] Leonard B.P.: *A stable and accurate convective modelling procedure based on quadratic upstream interpolation*; Computer Methods in Applied Mechanics Engineering; 19: 59–98; 1079

[25] Sørensen N.N.: *HypGrid a 2-D Mesh Generator;* Risø National Laboratory; Roskilde, Denmark; 1998

[26] Heinz, J., Sørensen, N.N.; Zahle, F.: *Investigation of the load reduction potential of two trailing edge flap controls using CFD*; Wind Energy; 14: 449–462; DOI: 10.1002/we.435; 2011

[27] Buhl, T.; Gaunaa, M.; Bak, C.: *Potential Load Reduction Using Airfoils with Variable Trailing Edge Geometry;* Journal of Solar Energy Engineering; Vol. 127; Nov. 2005

[28] Novak, M.; Tanaka, H.: *Pressure Correlations on a Vibrating Cylinder*; Proceedings of the Fourth International Conference, Wind Effects on Buildings and Structures; pp. 227-232; Heathrow, England; 1975

[IV]

Self-induced vibrations of a DU96-W-180 airfoil in stall

Witold Skrzypiński (wisk@risoe.dtu.dk)

Mac Gaunaa (macg@risoe.dtu.dk)

Niels Sørensen (nsqr@risoe.dtu.dk)

Frederik Zahle (frza@risoe.dtu.dk)

Joachim Heinz (jhei@risoe.dtu.dk)

DTU Wind Energy

Abstract

This work presents an analysis of 2D and 3D non-moving, prescribed motion and elastically mounted airfoil CFD computations. The elastically mounted airfoil computations were performed by means of a 2D structural model with two degrees of freedom. The computations aimed at investigating the mechanisms of both vortex-induced and stall-induced vibrations related to a wind turbine blade at standstill conditions. In this work, a DU96-W-180 airfoil was used in the angle of attack region potentially corresponding to stall-induced vibrations. The analysis showed significant differences between the aerodynamic stability limits predicted by 2D and 3D CFD. A general agreement was reached between the prescribed motion and elastically mounted airfoil computations. 3D computations indicated that vortex-induced vibrations are likely to occur at modern wind turbine blades at standstill. In contrast, the predicted cut-in wind speed necessary for the onset of stall-induced vibrations appeared high enough for such vibrations to be unlikely.

1 Introduction

Vibration of airfoils or whole wind turbine blades in standstill has recently received increased attention due to wind turbine failures potentially caused by blade vibration at standstill conditions. It is currently considered an important subject of research although no one has officially reported any turbine failures due to standstill vibrations so far. Blade vibration at standstill is potentially related to two separate phenomena: vortex-induced vibration (VIV) and stall-induced vibration (SIV). Both are well recognised in general aeroelasticity, civil engineering and hydrodynamics. In vortex-induced vibrations, the body vibrates in a particular mode at the wind speed for which the von Karman frequency of vortex shedding coincides with the natural frequency of the structural mode [1]. Several authors shed light on this phenomenon in the context of standstill vibrations of wind turbine blades [2,3,4,5]. One of the facts indicating that this phenomenon actually influences wind turbines is that according to simple predictions the frequency of vortex shedding in deep stall on modern wind turbine blades is relatively close to the eigenfrequency of the first edgewise mode of these blades. In stall induced vibrations [6,7,8,9,10] – often referred to as galloping, stall flutter or bluff-body flutter – a small displacement of the body causes an increase in the aerodynamic force in the direction of its motion, resulting in negative aerodynamic damping. The classic example of SIV is vibration of ice-coated power lines. Bluff bodies usually vibrate in the direction perpendicular to the flow. Slender bodies – including airfoils – usually vibrate in the direction of their largest span. In the case of bluff bodies and airfoils at 90 deg angle of attack, such an instability may be predicted by use of the so-called den Hartog condition or the necessary condition for galloping [11]. The condition says that the body is prone to galloping when the sum of the slope of stationary lift-coefficient and drag coefficient is negative:

$$\frac{dC_L}{d\alpha} + C_D < 0 \qquad (1)$$

Square or rectangular sections of relatively small aspect ratio are the most prone to such an instability [12]. Gaunaa and Larsen [8] and later Hansen [13] present the necessary condition for galloping that also accounts for the direction of rectilinear vibration and the angle of attack. It is therefore applicable to airfoils at angles of attack different from 90 deg:

$$C_{DA} = \sin\beta\cos\beta\left(C_{L\alpha} + \frac{dC_{D\alpha}}{d\alpha}\right) + \cos^2\beta\frac{dC_{L\alpha}}{d\alpha} + (1+\sin^2\beta)C_{D\alpha} < 0 \qquad (2)$$

where C_{DA} is the dimensionless coefficient of linear damping. The angles α and β from Eq. (2) are defined in Figure 1. Whether the condition is fulfilled is dependent on the underlying aerodynamic airfoil characteristics. Measured lift and drag curves at high angles of attack are often laden with inaccuracies due to tunnel effects while computed polars are laden with inaccuracies due to modelling limitations. Gaunaa and Larsen also show that at high angles of attack, a change in the underlying polars below their certainty level can significantly influence the airfoils' aeroelastic stability limits. In this light, a need for more accurate and reliable measurements of airfoil polars at high angles of attack emerges [14] together with the need for a realistic engineering model. The present work utilized Eq.(2) in order to find the angle of attack at which the DU96-W-180 airfoil [15] is the most prone to stall induced vibrations.

Note that the assumption of quasi-steady aerodynamics under which Eq. (2) was derived may be unrealistic in the present flow case. It is known that the aerodynamic response from the

onset of separation until the flow is fully separated is characterized by temporal lag which may be modelled by so-called dynamic stall models [16,17,18,19].

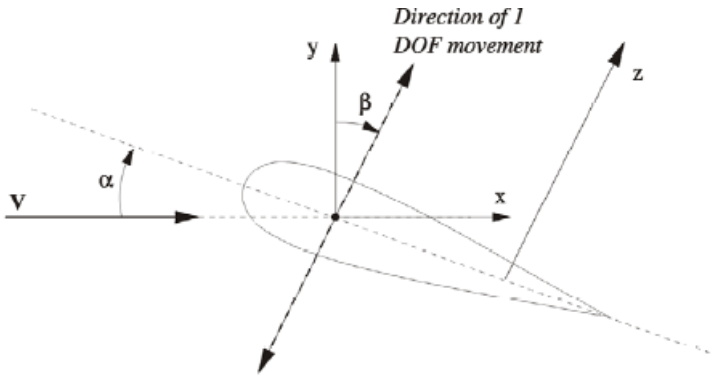

Figure 1: Definition of the angle of attack and angle of vibration from Eq.(2); reproduced from Gaunaa and Larsen [8]

The present work is partly inspired by the work of Parkinson and Smith [20] who study a one degree of freedom flexibly-mounted, galloping cylinder of a square cross section, exposed to air flow of varying speed. The direction of its displacement is perpendicular to the free stream. Figure 2 presents the result of their engineering calculations which is in good agreement with their experiments, presented in the same article. It presents the stationary amplitude of the limit cycle plotted against wind speed. No vibrations are present for wind speeds below U_0. If the flow speed is increased from zero and then decreased, the amplitude of the limit cycle shows path 012343510. The presence of the hysteresis loop itself was not of particular interest in the present work but it may have an effect on vibrating blades, if this phenomenon exists for blades too. That is, if the maximum speed of a wind gust during vibration of a blade exceeds the speed represented in Figure 2 by U_2, the amplitude of the blade vibration may remain relatively large until the wind speed drops below what is represented in Figure 2 by U_1. More importantly in the context of the present work, Parkinson and Smith show that there exists a certain cut-in wind speed necessary for the vibrations to emerge. They also argue that if there was no viscous damping in the system, it would start to vibrate at any flow speed different than zero. This argument was verified in the present work. Another question was – assuming that a certain minimum value of the flow speed is required for the vibrations to emerge – what the dimensional value of this flow speed in the case of modern wind turbines is.

The present work also focused on a study of the effective differences between 2D and 3D time-marching CFD computations, as well as on the effective differences between the prescribed motion and elastically mounted airfoil computations. The motivation for including computations with both the prescribed motion and the elastically mounted airfoil airfoil suspensions was as follows. Elastically mounted airfoil computations are the best reflection of real-life blade vibration. On the other hand, prescribed motion computations allow us to learn about the basic mechanisms of feeding energy into the vibrations. It is also easier to derive analytic models from the results when clearly defined forcing of prescribed motion computations was applied.

Flows in the deep-stall regime are inherently three-dimensional. Therefore, it is common to simulate those using computationally expensive 3D DES simulations [21,22]. The motivation for including 2D simulations in the current work was to investigate whether relevant flow characteristics may be resolved by 2D computations. This would be beneficial because of the high computational efficiency of 2D simulations compared to the much heavier 3D simulations.

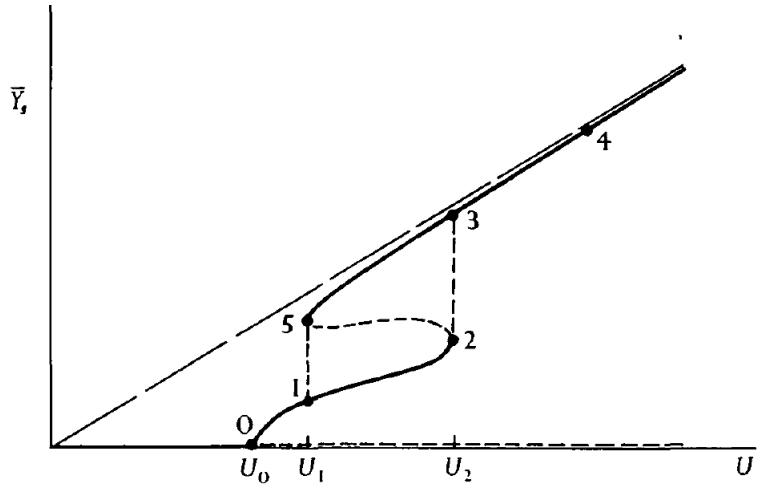

Figure 2: Characteristic of the limit cycle amplitude presenting the cut-in wind speed, U_0, and limit-cycle hysteresis (1235); reproduced from Parkinson and Smith [20]

2 Methods

2.1 2D and 3D Navier-Stokes solvers

All the computations were unsteady, made both in 2D RANS and 3D DES. The Navier-Stokes solvers used in the present work were EllipSys2D and EllipSys3D, developed by Michelsen [23,24] and Sørensen [25] at Risø DTU National Laboratory for Sustainable Energy and the Technical University of Denmark. The turbulence model used was the k-ω shear-stress transport (SST) [26]. It was used in both its standard RANS form and as a DES model as proposed by Strelets [27] with the delayed DES (DDES) technique of Menter and Kuntz [28]. The effects of laminar-to-turbulent transition in the boundary layer on the airfoil were modelled with the $\gamma - \widetilde{Re}_\theta$ correlation-based transition model of Menter [29]. For the present implementation, see Sørensen [21,22].

The airfoil motion was simulated by a moving mesh method. The grid points in the computational mesh were all moved together as a solid body. EllipSys2D and EllipSys3D are second-order accurate in time. The codes use a second-order backward differencing time discretization. Sub-iterations are used within each time step. In the present 2D and 3D computations, the diffusive terms were discretized with a second-order central differencing scheme. The convective fluxes in 2D and 3D RANS regions were computed using the third-order accurate QUICK scheme of Leonard [30]. The convective fluxes in 3D where the DDES model switched to large-eddy-simulation technique were computed with a fourth-order central differencing scheme.

The 2D computations were made in an O-grid with $32.8 \cdot 10^3$ grid cells. The height of the domain in both 2D and 3D was 30 m. The dimensions of the 2D grid were 256 cells (parallel to the airfoil surface) by 128 cells (perpendicular to the airfoil surface). The 3D computations were made in an O-grid with $12.6 \cdot 10^6$ grid cells. The mesh was extruded in the span-wise direction by a single chord length. The dimensions were 256 cells (parallel to the airfoil surface) by 384 cells (perpendicular to the airfoil surface) by 128 cells (spanwise direction).

The grids for 2D and 3D computations were made in HypGrid2D [31]. The grid around the DU96-W-180 profile [15] used in the 2D computations is presented in Figure 3.

The boundary condition on the 3D lateral boundaries was periodic. The aim of setting such a boundary condition was to limit the effect of finite span. The airfoil surface was specified by a no-slip condition. Outlet condition was specified at angles +/- 45 degrees downstream the airfoil, in the perimeter of the O-grid. The rest of the perimeter was specified by the inlet condition.

The time step was 0.01 seconds except for a few 2D computations where the time step was decreased to 0.005 seconds. The Reynolds number of all the computations was $6 \cdot 10^6$. The airfoil boundary layer was simulated assuming free transition with ambient flow turbulence intensity, I, of $1.1 \cdot 10^{-3}$%. This corresponded to the turbulent kinetic energy, k, of $1.5 \cdot 10^{-4}$ m^2/s and the specific dissipation, ω, of 10^6 s^{-1} at the inlet.

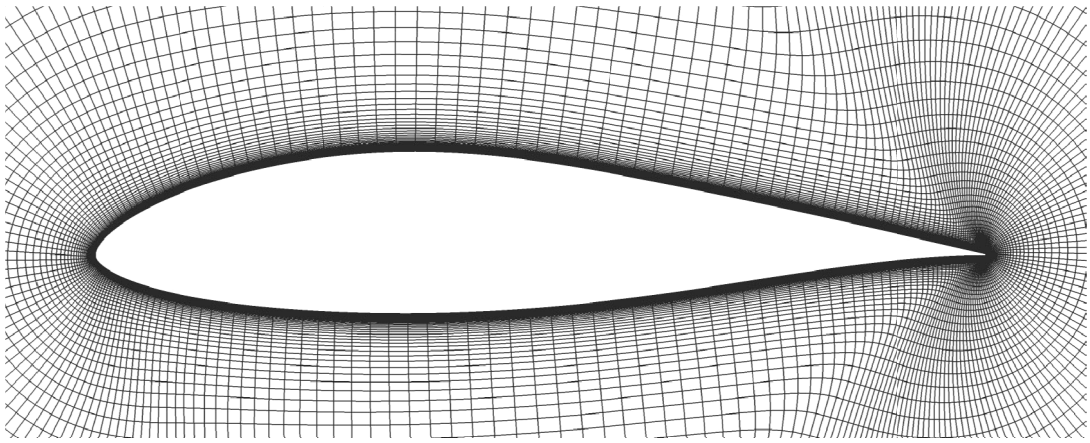

Figure 3: CFD grid around DU96-W-180 airfoil, used in the 2D CFD computations

2.2 2D elastic model for 2D and 3D CFD computations

The EllipSys add-on for 2D structural elastically mounted airfoil computations was developed by Heinz [32]. The structural model was coupled with both 2D and 3D CFD computations. All CFD computations were time marching.

The airfoil model was dimensionalized in the structural code with the following parameters. The chord length was 2 m. Air density was 1.225 kg/m^3. Mass per unit depth of the airfoil was 80 kg/m. The coefficients of viscous damping in all three directions of motion were zero. The parameters used were not meant to represent any specific position on a specific wind turbine blade. However, an airfoil with the present specifications could be found on the outer parts of large modern wind-turbine blades. The eigen frequency was varied in the parameter studies described later.

2.3 Calculation of the aerodynamic power transferred to the structure

Blade vibration is by nature an aeroelastic problem. However, in the present work the aeroelastic stability limits were also investigated by means of prescribed motion computations where the airfoil was subjected to forced oscillations in the direction of the chord line. The mean dimensionless aerodynamic power was extracted from the computations. The

instantaneous aerodynamic power per unit length of the system was defined as the product of the instantaneous speed of the airfoil, $\frac{dx}{dt}$, and the component of the aerodynamic loading per unit length in the displacement direction, $R_x(t)$. Then, the mean value during a whole number of periods was calculated:

$$\bar{P} = \frac{1}{nT}\int_0^{nT} R_x(t)\frac{dx}{dt}dt \qquad (3)$$

Note that positive power corresponds to negative aerodynamic damping, C_{DA}, and vice versa. The time series used for the power calculations were 20 oscillation periods long in the case of 2D flows, and up to 30 periods long in the case of 3D. The reason for using Eq. (3) was that, assuming that the damping in the system was linear, the power would be directly proportional to the damping coefficient. For this reason, even though the aerodynamic damping was not necessarily linear, using power to determine the aeroelastic stability limits is intuitive. Positive power means that the flow feeds energy into the oscillating system, and vice versa. A number of computations were made at different periods of oscillation, *T*. Then, the mean dimensionless power was plotted as a function of the dimensionless vibration period $T^*=T\,V/c$. Note that in the case of elastically mounted computations, $T^*=T\,V/c$ denotes the dimensionless eigen period of the isolated structural system where *T* denotes the dimensional eigen period. This period is not necessarily the same as the period of oscillation of the aeroelastic system. The dependency between T^* and the well know reduced frequency, $k = \varpi c/2V$, is $k = \pi/T$.

The dimensionless mean power was obtained by normalization of the mean power per unit length with density, chord length, the amplitude and period of vibration:

$$P^* = \frac{T}{\rho c A V^2}\bar{P} \qquad (4)$$

The motivation for such a non-dimensionalization is described below. The power per unit length is the product of the loading per unit length and airfoil velocity, i.e. $P = R_x(t)\dot{x}$. In first-order modelling, the loading would be directly proportional to density, chord length and the square of the flow speed, i.e. $R_x \sim \rho c V^2$. A representative airfoil velocity is directly proportional to the ratio of the amplitude and period of oscillation, i.e. $\dot{x} \sim \frac{A}{T}$. Therefore, the loading was non-dimensionalized by $\rho c V^2$, and the airfoil velocity was non-dimensionalized by $\frac{A}{T}$ which resulted in Eq. (4).

In the present work, every set of prescribed motion computations presented in a single figure was characterised by a constant A^*/T^* ratio, where $A^*=A/c$. The reason for that was that A^*/T^* or f^*A^* – where f^* is the dimensionless oscillation frequency – can be thought of as the level of perturbation imposed by the airfoil motion on the flow. If A^* was constant in a set of computations, then such a level of perturbation would grow with f^*. Then, computations with high oscillation frequency would drive the vortex shedding more than the computations with the low frequency would, and create the lock-in. After a simple calculation, one may show that A^*/T^* is directly proportional to the maximum velocity of the airfoil, i.e. $A^*/T^* \sim \dot{x}_{max}$, where $\dot{x}$ is the velocity of the airfoil.

3 Results and Discussion

3.1 Validation of the method by computations on a square section

3.1.1 Prescribed motion computations

The two methods for assessing the aeroelastic stability limits were validated by a comparison with the results from the reference experiment [20]. The difference between the experimental and computational setups was that in the computations the Reynolds number was kept constant at $4 \cdot 10^3$ while in the experiment it varied between $4 \cdot 10^3$ and $22 \cdot 10^3$. This was because in the experiment, the flow speed varied while in the computations, it was the period of oscillation that was the parameter. Therefore, the authors speculated that the change in the Reynolds number was insignificant in the range used in the experiment. Both approaches resulted in a change of the same dimensionless number, T^*. It was therefore possible to directly compare the results.

Figure 4 presents the dimensionless power as a function of the dimensionless period of forced oscillation. It includes results of the 2D and 3D CFD computations. It also includes the cut-in flow speed at which the vibrations occurred in the reference experiment. This cut-in flow speed is denoted in Figure 2 as U_0. The corresponding value of T^* – which is approximately T^*=11 – is marked in Figure 4 as the circle. This is in relatively good agreement with the current CFD results, especially 2D. The prescribed motion CFD computations were made with A^*/T^*= 0.01. The curve representing the 2D computations appeared positive approximately at $T^*=12$. The curve representing the 3D computations appeared positive approximately at $T^*=14$.

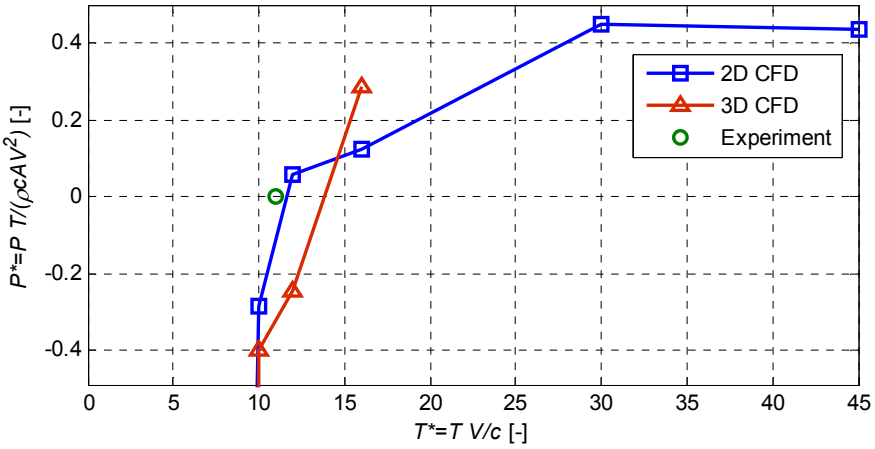

Figure 4: Dimensionless power of the oscillating square as a function of the dimensionless period of forced oscillation

If in the experiment, A corresponded to the amplitude of the limit cycle, and $1/T$ corresponded to the eigenfrequency of the isolated structural system, experimental A^*/T^* would be approximately 1.7. The authors speculate that A^*/T^* needs to be lower in the prescribed motion computations than in the corresponding elastically mounted system in order for the aerodynamic power of the prescribed motion computations to be positive where the corresponding elastic system shows limit-cycle behaviour. This was also indicated by the elastically mounted computations presented in the next section.

3.1.2 Elastically mounted computations

The 2D prescribed motion CFD computations were verified by elastic CFD computations on the same square section, performed with 2D CFD coupled with the 2D structural model of Heinz [32] with one degree of freedom. All the structural parameters in the computations were the same as in the experiment [20]. The exception was that while the Reynolds number was kept constant, the eigen period of the isolated structural system, T, was the free parameter in the elastically mounted computations. Six computations were carried out, each with different dimensionless eigen period, T^*. The initial displacements were equal to the displacement amplitudes in the corresponding prescribed motion computations. The resulting displacement time series are presented in Figure 5. The elastic computations showed the same characteristics as the prescribed motion. This is because the aerodynamic damping predicted by the elastic computations appeared negative for T^* values between 10 and 12. In other words, 12 was the lowest value of T^* at which the displacement amplitude grew in time.

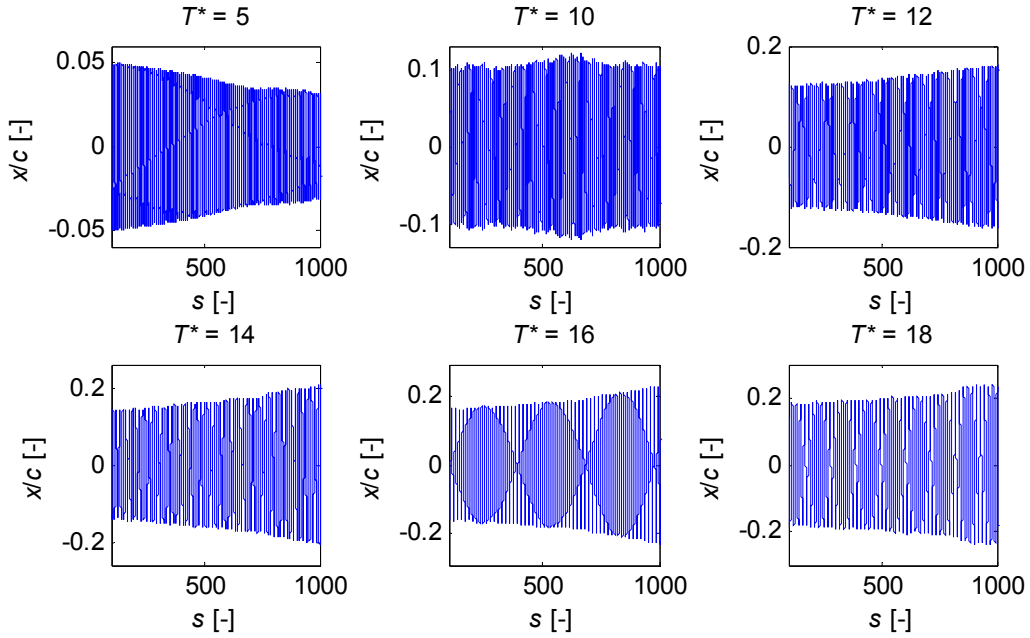

Figure 5:Displacement time series resulting from the elastic computations performed with the 2D structural model coupled with 2D CFD

3.2 Airfoil aerodynamic data

The publically available DU96-W-180 airfoil used in the computations was designed at TU Delft at the Faculty of Aerospace Engineering [15]. This airfoil is widely used and suitable for outer parts of modern wind turbine blades. The aerodynamic performance of the airfoil at the Reynolds number of $0.7 \cdot 10^6$ – including that at high angles of attack – is investigated by Timmer [14] and presented in Figure 6.

In order to facilitate the process of finding the angle-of-attack region of the highest risk of stall-induced edgewise vibrations, Eq. (2) was applied to the polars presented in Figure 6, indicating where the vibrations could emerge. The result is presented in Figure 7. Four regions showed negative quasi-steady aerodynamic damping, i.e. -171° to -165° (1st), -15° to -9° (2nd),

5° to 25° (3rd) and 163° to 172° (4th). After comparing this result with the results of CFD simulations presented later, it was decided that 26 degrees and 24 degrees were the angles of attack investigated further in 2D and 3D, respectively.

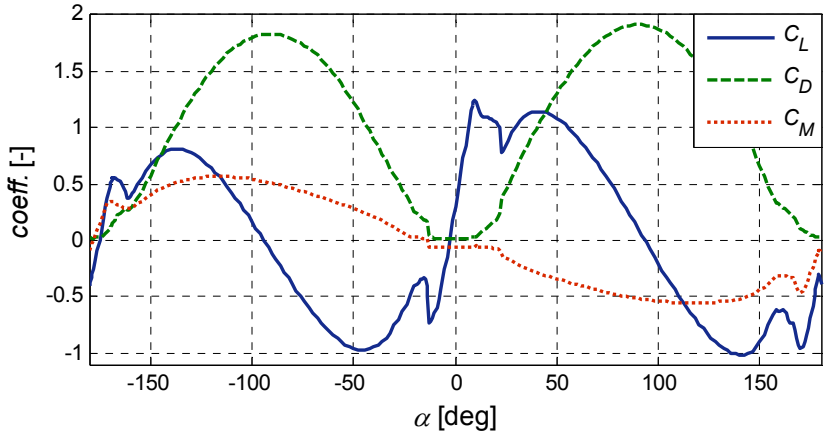

Figure 6: Aerodynamic force coefficients of the DU96-W-180 airfoil measured by Timmer [14]

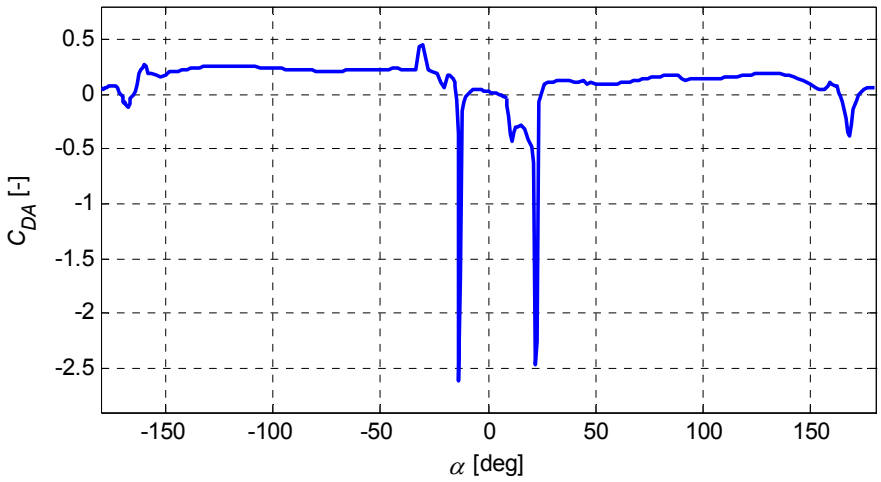

Figure 7: Eq. (2) being applied to the ref. polars [14] presented in Figure 6.

3.3 CFD computations with non-moving airfoil suspension

2D and 3D non-moving, time-marching computations of the DU96-W-180 airfoil were performed in order to identify the exact angles of attack at which the airfoil was the most prone to stall-induced edgewise vibrations according to Eq. (2). The computations were also performed to study how the lift and drag curves as well as the aerodynamic damping depend on the Reynolds number. Moreover, the differences between the 2D and 3D computations were of interest because although 3D CFD may be a better representation of real-life physics in deep stall, it is be beneficial to investigate to what extent the 2D computations resolve relevant flow characteristics.

The computed polars are presented in Figure 8. In the range of angles of attack between 21 and 29 deg, the mean 2D lift coefficient increased with the Reynolds number while the mean drag coefficient decreased. The stall delayed and became less abrupt when the Reynolds number

increased. This led to Eq. (2) showing higher C_{DA} values when the Reynolds number increased. This indicated that the risk of SIV decreases when the Reynolds number increases. However, a Reynolds number is one of many factors related to SIV. Figure 9 presents C_{DA} as a function of angle of attack.

The aerodynamic force resulting from 3D computations was spatially averaged in the spanwise direction of the extruded profile. The main difference between the 2D and 3D computations was that, at a given Reynolds number, the 3D flow stalled 2-4 deg of angle of attack before the 2D lift coefficient did. This corresponded to the angle most prone to vibrations being smaller in 3D than 2D.

The results of the non-moving computations at Re=$0.7 \cdot 10^6$ were also compared with the wind-tunnel measurements by Timmer [14] performed at Delft University of Technology at the same Reynolds number. The measurements show lower mean lift coefficients. Further, stall occurs approximately 2 deg after it occurred in the respective 3D computations, and 2 deg before it did in the respective 2D computations. The drag coefficient of the 2D computations was in relatively good agreement with the experiment until 24 deg angle of attack. After 24 deg, computed C_D increased in value more rapidly than in the experiment. The mean 3D drag was higher than the experimental drag except at 18-20 deg where it was in good agreement.

Generally, the present results were not in good agreement with the experiment. However, possible occurrence of wind tunnel effects like tunnel blockage or 3D effects stemming from wall interference might have compromised the accuracy of the measurements. Such effects are pronounced at the considered angle-of-attack range and may cause experimental results to vary depending on the tunnel at which the measurements are taken. On the other hand, CFD computations may be laden with inaccuracies due to modelling limitations. To obtain higher agreement between the computations and experimental data, the computations would likely have had to include the tunnel walls and identical model aspect ratio.

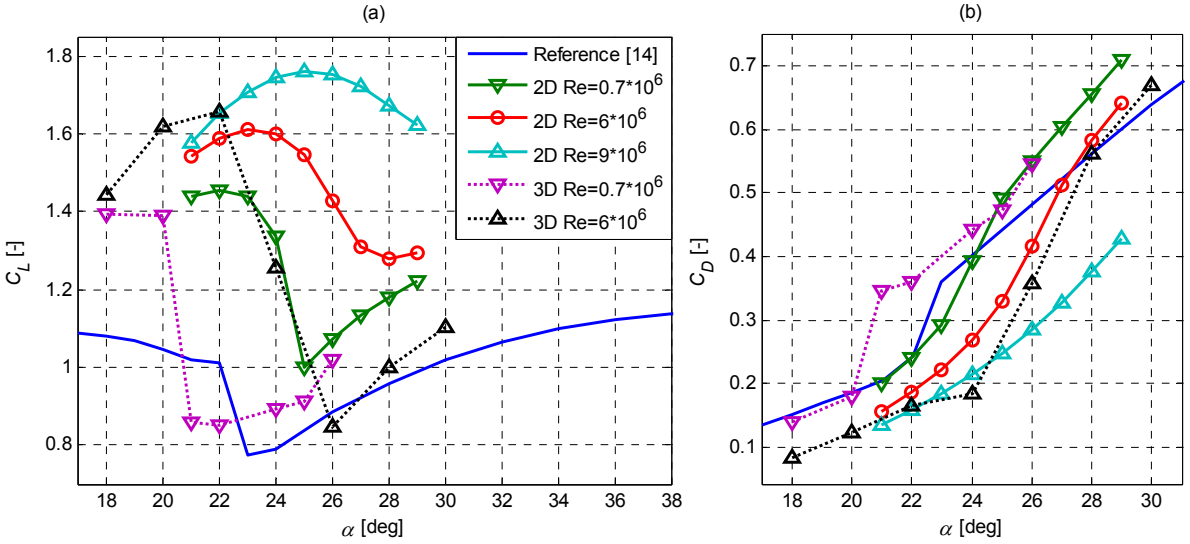

Figure 8: Polars from the 2D and 3D time-marching CFD computations of the DU96-W-180 airfoil; reference data are experiment results from Timmer [14]

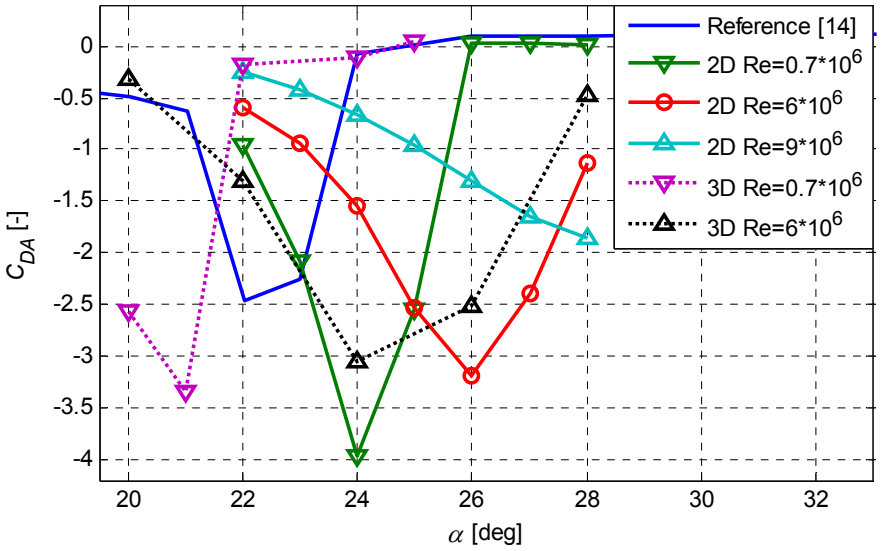

Figure 9: Eq. (2) being applied to the polars presented in Figure 8. The lowest values indicate the angles of attack corresponding to the highest risk of stall induced vibrations

An important issue of 3D blade computations is sensitivity to spanwise length. In the present work, 3D computations at 25 deg angle of attack were performed on both a grid extruded by a single chord length and a grid extruded by a double chord length. Virtually no difference between the computed loading was observed.

In order to perform the computations at a Reynolds number representing a modern wind turbine blade subject to stall-induced standstill vibrations, the prescribed motion and elastic computations were performed at $Re=6\cdot10^6$. This was because preliminary computations indicated that SIV occur at relatively high wind speeds. The angles of attack at which the prescribed motion and elastically mounted computations were performed in 2D and 3D were 26 and 24 deg, respectively.

3.4 Study of flow separation

A study of the 3D flow over the DU96-W-180 in prescribed motion at 24 degrees angle of attack is presented to give the reader a better overview of the flow characteristics including the level of flow separation. The parameters of the presented simulation are T^*=1.8 and A^*=0.018. Figure 10 presents the vorticity magnitude of a single section of the 3D profile at an instant at which the profile moves towards the leading edge. The dark areas represent high vorticity. In the figure, the separation of the boundary layer is visualized by the dark stream starting at the suction side approximately at the third of the chord length, and following into the wake.

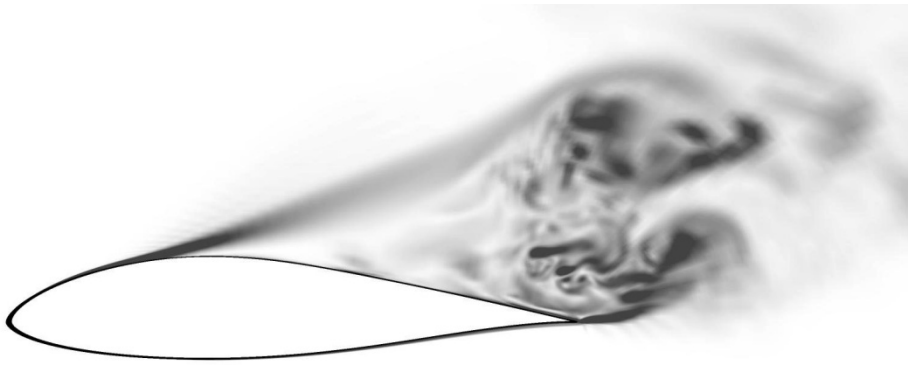

Figure 10: Vorticity magnitude of the 3D flow over DU96-W-180 at 24 deg angle of attack

Figure 11 presents the distribution of the pressure coefficient. It was plotted during both the motion towards the leading edge (curve 1) and the motion towards the trailing edge (curve 2). At x/c=0, curve 1 peaked at C_P=10.3 and curve 2 at C_P=13.5. The stagnation point indicated by curve 1 was at x/c=0.06. The stagnation point indicated by curve 2 was at x/c=0.08. It was expected that the separation point of curve 1 would be closer to the leading edge due to the geometric angle of attack being smaller because of the airfoil motion at that instant. Assuming that a flat shape of the curves is the sign of flow separation, both flows separated approximately between x/c equal 0.2 and 0.3. Also, the higher pressure at the pressure side shown by curve 2 may be justified by the higher geometric angle of attack due to airfoil motion.

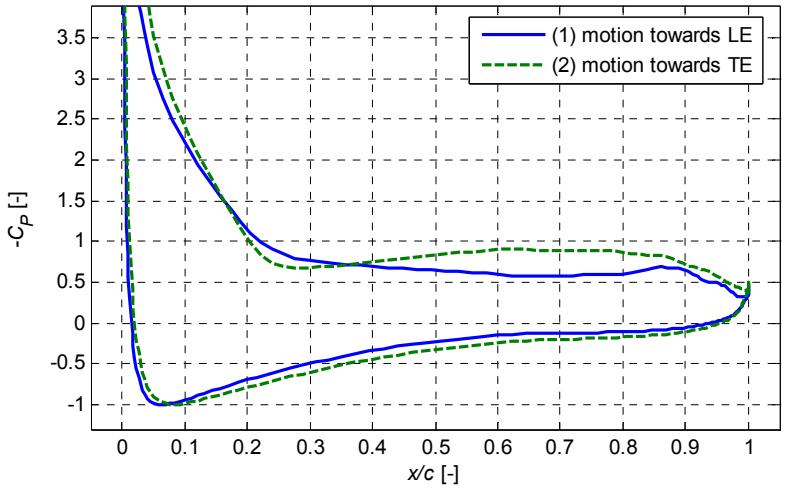

Figure 11: Pressure coefficient of oscillating DU96-W-180 plotted during the motion towards LE and the motion towards TE. 3D computation.

3.5 CFD computations on prescribed motion airfoil

Figure 12 presents the results of both 2D and 3D prescribed motion computations of the DU96-W-180. The dimensionless power was plotted as a function of the dimensionless displacement period for A^*/T^*=0.01 which corresponds to the angle of attack amplitudes of 1.6 deg in 2D and 1.5 deg in 3D. The difference comes from the fact that the angle of attack of the non-moving airfoil was 26 degrees in 2D and 24 degrees in 3D, because of the results presented in Figure 9. The curves representing 2D and 3D computations differed significantly which will be discussed in the following section.

Figure 13 presents the curve corresponding to the 3D computations from Figure 12. The power appeared positive in two T^* regions. The first was approximately between 1 and 15 while the second was approximately above 44. The first region contained relatively high values of P^* with steep rise and fall. The underlying values of T^* contained the dimensionless period of stationary vortex shedding. These facts indicated that the increase in power was associated with vortex induced vibrations. The same kind of vibrations is shown by both 2D and 3D prescribed motion and elastically mounted airfoil CFD simulations of the same airfoil at 90 deg angle of attack [5].

Note that – according to the present work – vortex-induced vibrations are likely to occur on modern wind-turbine blades. This is because the predicted frequency of vortex shedding is relatively close to the frequency of the first edgewise mode being approximately equal to 1 Hz.

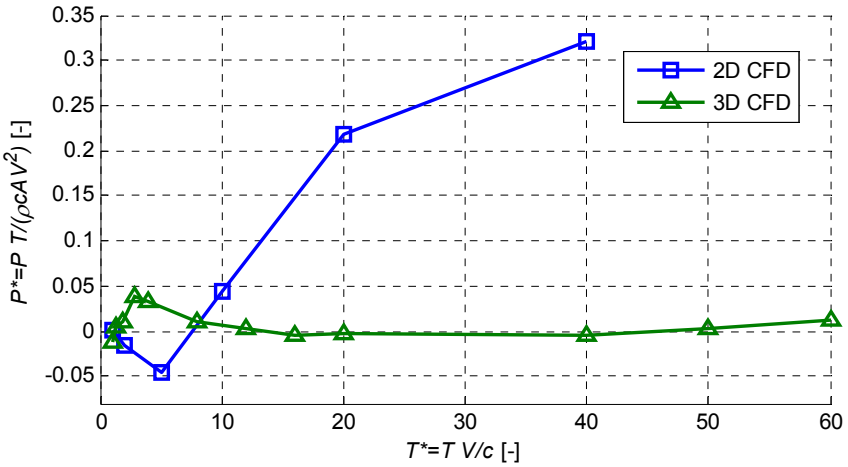

Figure 12: Dimensionless power related to prescribed motion 2D and 3D CFD simulations of DU96-W-180

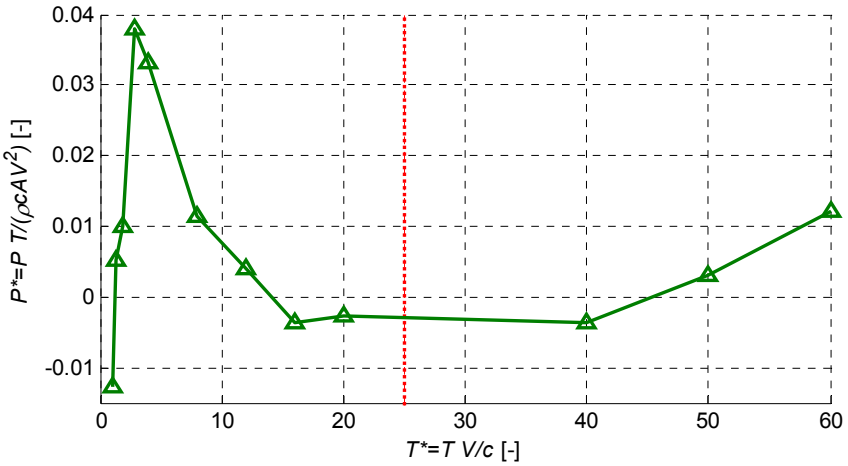

Figure 13: Dimensionless power related to prescribed motion 3D CFD simulations of DU96-W-180

The second region contained T^* values larger than the frequency of stationary vortex shedding by an order of magnitude. This indicated the presence of stall induced vibrations. However, the present model indicated that if such vibrations occurred on a modern wind turbine, the associated wind speed would be far from any realistic regime. Assuming that the chord length of the blade section was 2 m and the frequency of the first edgewise mode 1Hz, that mode would be excited if the wind speed exceeded 88 m/s. The thick vertical dotted line in Figure 13

shows the value of T^* corresponding to the wind speed of 50 m/s which is generally agreed on as the extreme value. On the other hand, in order for the T^* value of 44 to correspond to the wind speed of 50 m/s, the frequency of the first edgewise mode of the blade with 2 m chord would need to be as low as 0.56 Hz. In the case of a blade with 1 m chord this frequency would need to be 1.1 Hz. Given the average relation between the blade chord length and the frequency of the first edgewise mode of modern wind turbine blades, the risk of the onset of stall induced vibrations seems small.

Note that the present simulations included only a single angle of attack, airfoil design and direction of rectilinear vibrations. Therefore, the present results were not meant to describe vibrations at different conditions. Further, the conclusions based on the 2D results are drastically different, predicting vibrations at a wide range on T^* values while it was not explicitly shown in the present work that 3D simulations represent the real-life mechanisms of airfoil vibrations under the current flow conditions better than 2D. However, Shur *et al.* [33] and Strelets [34] indicate that 3D DES computations resolve stalled flows around airfoils better than 2D RANS.

It may also be concluded that CFD computations confirmed Eq. (2). This is because both 2D and 3D CFD simulations indicated a growth of stall-induced vibrations with increasing T^*. Further, the higher the T^* value is, the slower the oscillation is and the closer the aerodynamic response is to quasi-steady. On the other hand, Eq. (2) was derived based on the assumption of quasi-steady aerodynamics. Therefore, when the aerodynamic response approaches quasi-steady characteristics, the aerodynamic damping predicted by CFD approaches the negative value predicted by Eq. (2).

3.6 Analysis of the time series from the prescribed motion computations

In order to shed more light on the reasons for the 2D and 3D results to be different as well as on the nature of suspected vibrations, the normalized edgewise-displacement and edgewise-loading time series are presented in Figure 14. The figure presents the T^* regime corresponding to vortex induced vibrations. The mean loading was subtracted from the time series before plotting. The 2D results are presented in Subfigures (a), (b) and (c). The 3D results are presented in Subfigures (d), (e) and (f). The plots include three dimensionless displacement periods, i.e. T^*=1 (Subfigures (a) and (d)), T^*=2 (Subfigures (b) and (e)) and T^*=4 (Subfigures (c) and (f)). Note that the exact values of the frequency of vortex shedding differed between the respective 2D and 3D computations – among other reasons – because of the 2-deg difference in the angle of attack. Further, even if the angles were the same, there would be a difference in the frequency of stationary vortex shedding between the 2D and 3D computations. Such a difference was observed in past research and is described in [5]. The results presented in Figure 14 indicated that the band of T^* for which there existed the lock-in was wider in 3D than in 2D. In 3D at T^* values of 1, 2 and 4, only one frequency was visible in the load response. On the other hand, in 2D, a single peak in the frequency response was visible only at T^*=2. At T^* values of 1 and 4 both the frequency of vortex shedding and the frequency of oscillation were distinguishable in the load response. One could speculate that the reason was that the 3D flow was less correlated and therefore easier to be driven by an oscillation of frequency different than that of vortex shedding.

The plots also indicate why 2D simulations showed negative power where 3D showed positive. In order for the power to be positive, the loading cannot lag the displacement in phase. In all the 2D results presented in Figure 14, the displacement led the loading. This corresponded to

negative power, as presented in Figure 12. In the case of the 3D results, the displacement led at T^*=1 which corresponded to negative power, as presented in Figure 13. At T^*=2 the loading slightly led the displacement. At T^*=4 the loading led significantly. This corresponded to the power peak at T^*=4, visible in Figure 13.

The other region of positive power in the 3D simulations appeared at relatively high T^*. Figure 15 presents the time series of the normalized edgewise displacement and loading at T^*=40. 2D results are presented in Subfigure (a) while 3D results are presented in Subfigure (b). It also presents the 3D results of normalized edgewise displacement and loading a T^*=60 in Subfigure (c). It is visible in Subfigure (a) that the loading significantly led the displacement in phase. The same simulation corresponded to a large power value. However, the loading time series corresponding to the 3D simulations presented in Subfigures (b) and (c) were less deterministic and closer in phase to the corresponding displacement time series. Therefore, it would not be evident just by looking at the loading whether the power was positive.

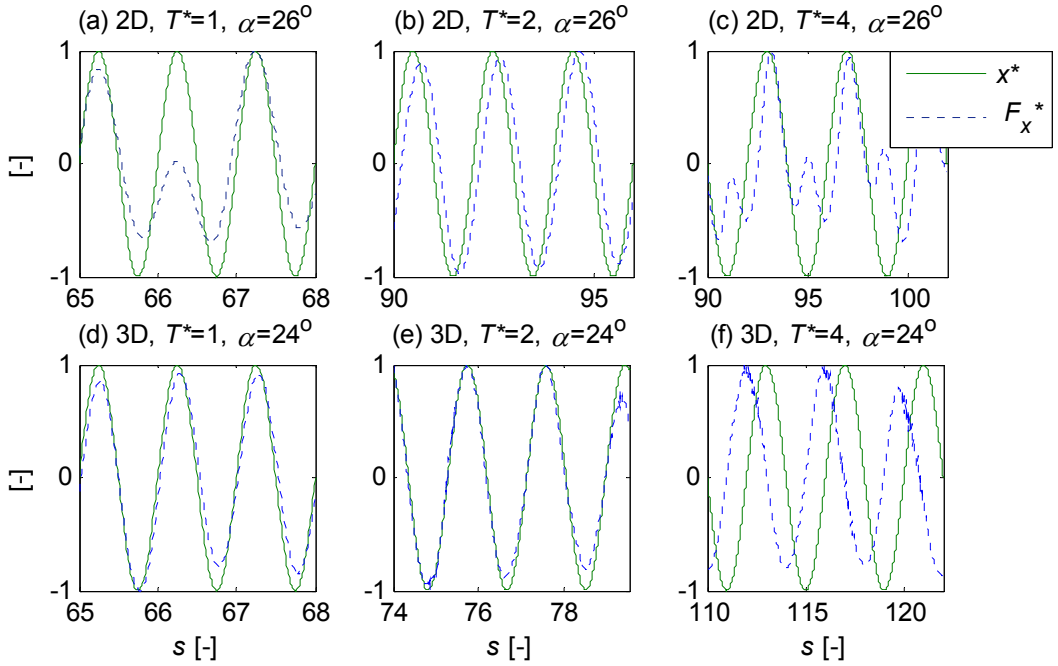

Figure 14: Normalized edgewise displacement and loading from the 2D and 3D CFD prescribed motion simulations of DU96-W-180 at low dimensionless oscillation periods

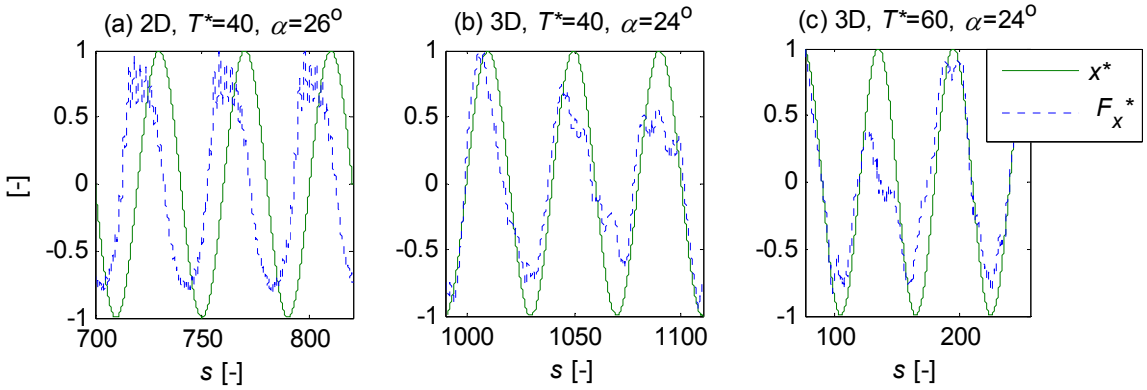

Figure 15: Normalized edgewise displacement and loading from the 2D and 3D CFD simulations of DU96-W-180 at high dimensionless oscillation periods

It was observed in the present work that for high oscillation periods where the vortex shedding was decoupled from the oscillation, there were two values of the frequency of vortex shedding present. A higher value appeared during the motion towards the leading edge while a lower appeared during the motion towards the trailing edge. The authors believe that the difference stemmed from the relative flow velocity being different in both cases. The approximate values of the periods of vortex shedding at T^*=40 are listed in Table 1.

Table 1: Dimensionless period of vortex shedding in prescribed motion at T^*=40; 2D and 3D simulations

	Motion towards LE	Motion towards TE
2D	1.4	2.5
3D	1.0	1.5

3.7 1, 2 and 3 DOF Elastic Airfoil Computations

The effective differences between using one, two and three degrees of freedom in the 2D elastically mounted airfoil model coupled with 2D CFD were investigated by comparison of predicted displacement amplitudes. The airfoil under consideration was DU96-W-180 at 26 degrees angle of attack and a Reynolds number of $6 \cdot 10^6$. The models had an edgewise dimensionless eigen period of 3. The ratio between the periods of the edgewise and flapwise modes of the isolated structure was 0.7. The ratio between the periods of the edgewise and rotational modes was 7. Compared to the 3 DOF structural system, the 2 DOF system was constrained in rotation. The 1 DOF structural system was only free to move in the edgewise direction. The amplitude values of edgewise displacement were compared after 10 and 100 periods of oscillation. All three systems showed an increase in the amplitude in time. The highest amplitude was shown by the 1 DOF system. The 3 DOF system showed the lowest. The differences relative to the 3 DOF system are listed in Table 2.

Table 2: The effective differences between using one, two and three degrees of freedom in the 2D elastically mounted airfoil model coupled with 2D CFD; the amplitude of edgewise displacement after 10 and 100 periods of oscillation

	Number of periods [-]	**10**	**100**
2 DOF system	$\left\lvert\frac{A_{3DOF} - A_{2DOF}}{A_{3DOF}}\right\rvert$ [%]	**0.7 %**	**5.6 %**
1 DOF system	$\left\lvert\frac{A_{3DOF} - A_{1DOF}}{A_{3DOF}}\right\rvert$ [%]	**1.0 %**	**7.3 %**

One of the problems with using the 3 DOF model was that the springs needed to be preloaded in order to avoid unwanted nonlinear effects. Secondly, some of the investigated values of T^* were relatively high. Therefore the corresponding values of spring stiffness were low. Accordingly, the airfoils needed to be displaced by a large distance in order to preload the springs. In the case of the rotational degree of freedom, that would correspond to a large change in the angle of attack which would change the aerodynamic characteristics of the system, and make the study very difficult. Because of this issue, and the fact that after a moderate number of oscillation periods the differences in the amplitude were relatively low, the elastic computations employed the 2 DOF system.

3.8 CFD computations with elastic airfoil suspension

The results of the prescribed motion computations were verified by performing three 2 DOF elastic computations. Results are presented in Figure 16. Note that y-axis range differs between subfigures. The displacement time series are presented in Subfigures (a), (b) and (c). The dimensionless eigen periods of the first model coupled with 2D CFD presented in Subfigures (b) and (e), and the model coupled with 3D CFD presented in Subfigures (c) and (f), were T^*=3. The dimensionless eigen period of the second model coupled with 2D CFD presented in Subfigures (a) and (d) was T^*=1.8. This was the period of stationary vortex shedding in 2D. The ratio between the frequencies of the flapwise and edgewise modes was 0.7 – similar to that on modern wind turbines. Viscous damping was set to zero. The 3D CFD model showed negative aerodynamic damping with an exponential growth in its displacement amplitude presented in Subfigure (c). The corresponding plot of the displacement history indicated lock-in (Subfigure (f)) by showing that the displacements in three consecutive periods were of similar shape. The direction of the loop was clockwise. The 2D CFD model with T^*=3 showed positive aerodynamic damping (Subfigure (b)) and a lack of lock-in (Subfigure (e)) as the plot of the displacement history changed shape in consecutive periods. The 2D model with T^*=1.8 showed lock-in (Subfigure (d)) and negative aerodynamic damping (Subfigure (a)). The direction of the loop in Subfigure (d) was clockwise. However, the displacement amplitude showed asymptotic growth with relatively small limit. Further, the limit was lower than the displacement amplitude used in the prescribed motion computations. That explains why the prescribed motion computation showed negative power while the elastically mounted computation showed an increase in the displacement amplitude. Generally, the three elastic computations verified the respective prescribed motion computations.

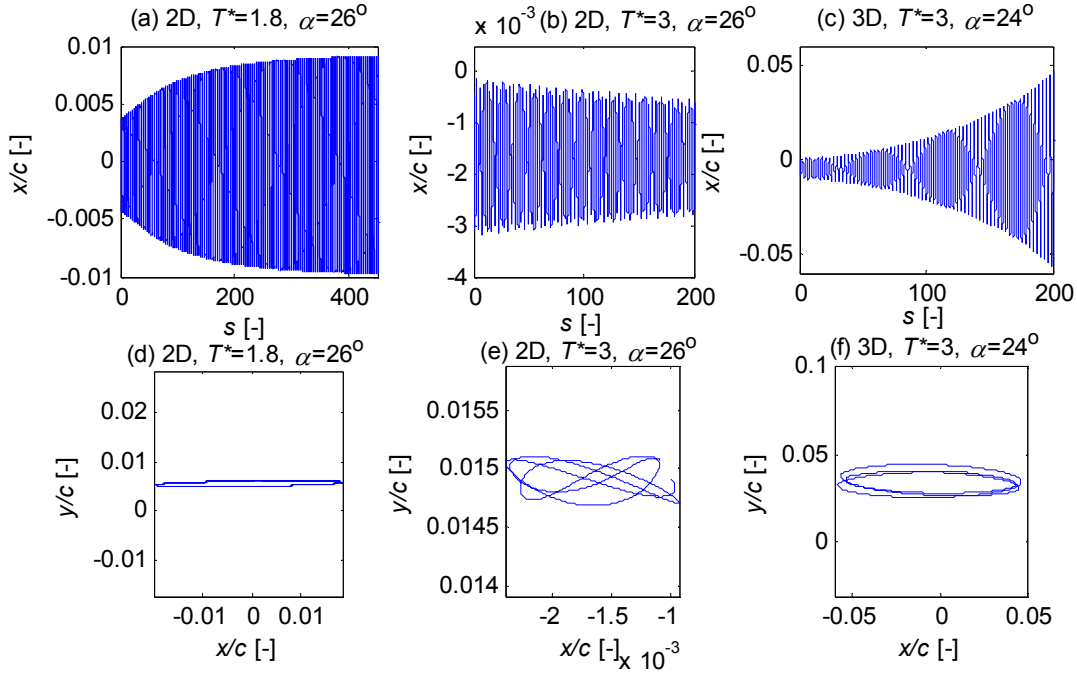

Figure 16: Displacement time series and displacement history of the elastic computations; displacement history plotted over 3 consecutive displacement periods

4 Conclusions

2D and 3D non-moving, prescribed motion and elastically mounted airfoil CFD computations were carried out in this work. The computations aimed at shedding light on the phenomena of both vortex-induced and stall-induced vibrations of an elastically mounted airfoil. In this work a DU96-W-180 airfoil was used.

The analysis showed significant differences between the aerodynamic stability limits predicted by 2D and 3D CFD simulations.

A general agreement was reached between the prescribed motion and elastically mounted airfoil computations.

Vortex-induced vibrations are likely to occur at modern wind turbine blades at standstill. The predicted frequency of vortex shedding can be relatively close to the frequency of the first edgewise blade mode.

The predicted cut-in wind speed necessary for the onset of stall-induced vibrations according to 3D CFD appeared high enough for such vibrations to be unlikely in the current setup.

5 Future work

Based on the current study and literature review a number of issues were identified that need to be investigated in future work. Below is the list of the most important of:

- Verify whether 2D or 3D computations reflect real-life mechanisms of vibrations at the current conditions better.

- 3D CFD prescribed motion computations indicated that the aerodynamic damping becomes negative between T^*=40 and 50. Therefore, future work should include 2D CFD and especially 3D CFD elastic computations at T^*=40 and 50 to verify the aerodynamic stability limit predicted by the 3D CFD prescribed motion computations.

- Investigate the amount of temporal lag in the dynamic aerodynamic response of the present flow.

- Investigate the usefulness of the state-of-the-art dynamic-stall models in the current angle-of-attack regime.

Acknowledgements

The authors of this article would like to thank Nando Timmer for making the coordinates and aerodynamic characteristics of the DU96-W-180 airfoil used in this work available.

Computations were made possible by the use of the PC-cluster provided by Danish Center for Scientific Computing (DCSC) and the Risø-DTU central computing facility.

References

[1] Feng, C.C.: *The measurement of vortex-induced effects on flow past stationary and oscillating circular D-section cylinders*; M.Sc. Thesis; The University of British Columbia, 1968

[2] Bertagnolio, F.; Rasmussen, F.; Sørensen N.N.; Johansen, J.; Madsen, H.Aa.: *A stochastic model for the simulation of wind turbine blades in stochastic stall*; Wind Energy; 13:323-338; 2010

[3] Riziotis, V.A.; Voutsinas, S.G.; Politis, E.S.; Chaviaropoulos, P.K.: *Stability analysis of parked wind turbine blades using a vortex model*; Proceedings of TORQUE 2010: The Science of Making Torque from Wind; June 28-30; Crete, Greece; 2010

[4] Hansen, M.H.: *Bias effect of self-induced turbulence on the stall-flutter limit of an airfoil section*; The sixteenth international congress on sound and vibration; Kraków; 5-9 July 2009

[5] Skrzypiński, W.; Gaunaa, M.; Sørensen, N.; Zahle, F.; Heinz, J.: *Vortex-induced vibrations of a DU96-W-180 airfoil at 90 degrees angle of attack*; submitted for Wind Energy in 2012

[6] Dowell, E.H.; Clark, R.; Cox. D.; Curtiss, H.C. Jr.; Edwards, J.W.; Hall, K.C.; Peters, D.A.; Scanlan, R.; Simiu, E.; Sisto, F.; Strganac, T.W.: *A Modern Course in Aeroelasticity*; Fourth Revised and Enlarged Edition; Kluwer Academic Publishers; 2004

[7] Rasmussen, F.; Petersen, J.T.; Madsen, H.A.: *Dynamic Stall and Aerodynamic Damping*; J. Sol. Energy Eng.; Volume 121; Issue 3, 150 (6 pages); DOI:10.1115/1.2888426; August 1999

[8] Gaunaa, M.; Larsen, T.J.: *Stilstandslaster*; chapter in *Forskning i Aeroelasticitet*; ed. Christian Bak; Risø-R-1434(DA) in Danish, Risø DTU National Laboratory for Sustainable Energy*;* 2002

[9] Buhl, T.: *Edgewise vibration instand still*; chapter in *Research in Aeroelasticity EFP-2006*; ed. Christian Bak; Risø-R-1611; 2006

[10] Skrzypinski, W.; Gaunaa, M.: *Wind turbine blade vibration at standstill conditions – the effect of imposing lag on the aerodynamic response of an elastically mounted airfoil;* submitted for Wind Energy in 2011

[11] Den Hartog, J.P.: *Transmission Line Vibration Due to Sleet*; Transactions of the American Institute of Electrical Engineers journal; DOI: 10.1109/T-AIEE.1932.5056223; 1932

[12] Blevins, R.D.: *Flow-induced Vibrations*; Van Nostrand; 1977

[13] Hansen, M.H.: *Aeroelastic Stability Problems for Wind Turbines*; Wind Energy; DOI: 10.1002/we.242; November/December 2007

[14] Timmer, W.A.: *Aerodynamic characteristics of wind turbine blade airfoils at high angles-of-attack*; Proceedings of TORQUE 2010 The science of making torque from wind; Heraklion, Crete, Greece; June 28-30, 2010

[15] Timmer, W.A.; van Rooij, R.P.J.O.M: *Summary of the Delft University wind turbine dedicated airfoils*; AIAA-2003-0352; 2003

[16] Leishman, J.G.; Beddoes, T.S.: *A semi empirical model for dynamic stall;* Journal of the American Helicopter Society 34, 3 (1989); DOI:10.4050/JAHS.34.3 (15 pages); 1989

[17] Øye, S.: *Dynamic stall simulated as time lag of separation*; Proceedings of the EWEC; Thessaloniki, Greece; Oct. 1994.

[18] Hansen, M.; Gaunaa, M.; Madsen, H.Aa.: *Beddoes-Leishman type dynamic stall model in state-space and indicial formulations*; Risø-R-1354(EN); 40 p.; 2004

[19] Larsen, J.W.; Nielsen, S.R.K.; Krenk, S.: Dynamic stall model for wind turbine airfoils; Journal of Fluids and Structures 23 959-982; 2007

[20] Parkinson, G.V.; Smith, J.D.: *A square prism as an aeroelastic non-linear oscillator*; The Quarterly Journal of Mechanics and Applied Mathematics; Vol. XVH, Ft. 3; 1964

[21] Sørensen N.N.: *CFD modelling of laminar-turbulent transition for airfoils and rotors using the* $\gamma - \widetilde{Re}_\theta$ *mode*; Wind Energy; 12: 715–733; 2009

[22] Sørensen N.N.; Schreck, S.: *Computation of the National Renewable Energy Laboratory Phase-VI rotor in pitch motion during standstill*; Wind Energy; DOI: 10.1002/we.480; 2011

[23] Michelsen J.A.: *Basic3D – a platform for development of multiblock PDE solvers.* Report AFM 92-05, Dept. of Fluid Mechanics, Technical University of Denmark, DTU, Denmark; 1992

[24] Michelsen J.A.: *Block structured multigrid solution of 2D and 3D elliptic PDE's.* Report AFM 94-06, Dept. of Fluid Mechanics, Technical University of Denmark, DTU, Denmark; 1994

[25] Sørensen N.N.: *General purpose flow solver applied to flow over hills.* PHD Dissertation, Risø-R-827(EN), Risø National Laboratory, Roskilde, Denmark; 1995

[26] Menter F. R.: *Zonal two equation k-omega turbulence models for aerodynamic flows*; AIAA Paper 932906, American Institute of Aeronautics and Astronautics;1993

[27] Strelets M.: *Detached eddy simulation of massively separated flows*; AIAA Paper 2001-0879, Russian Scientific Center 'Applied Chemistry'; St. Petersburg; 2001

[28] Menter F.R., Kuntz M.: *Adaptation of eddy-viscosity turbulence models to unsteady separated flow behind vehicles*; In The Aerodynamics of Heavy Vehicles: Trucks, Buses, and Trains (volume 19 of Lecture Notes in Applied and Computational Mechanics). Springer: Berlin; 339–352; 2004

[29] Menter F. R., Langtry R. B., Likki S. R., Suzen Y. B., Huang P. G., Völker S.: *A correlation-based transition model using local variables - Part I: model formulation*. In Proceedings of ASME Turbo Expo 2004, Power for Land, Sea, and Air; Vienna, Austria; ASME GT2004-53452; 14–17 June 2004

[30] Leonard B. P.: *A stable and accurate convective modelling procedure based on quadratic upstream interpolation*; Computer Methods in Applied Mechanics Engineering; 19: 59–98; 1979

[31] Sørensen N.N.: *HypGrid a 2-D Mesh Generator* Risø National Laboratory, Roskilde, Denmark; 1998

[32] Heinz, J., Sørensen, N.N.; Zahle, F.: *Investigation of the load reduction potential of two trailing edge flap controls using CFD*; Wind Energy; vol. 14:449–462. doi: 10.1002/we.435; 2011

[33] Shur, M.; Spalart P.R.; Strelets, M.; Travin, A.: *Detached-eddy simulation of an airfoil at high angle of attack*; Engineering Turbulence Modelling and Experiments – 4; Elsevier Science Ltd.; 1999

[34] Strelets, M.: *Detached Eddy Simulation of Massively Separated Flows*; AIAA 2001-0879; 39th AIAA Aerospace Sciences Meeting and Exhibit January; Reno, NV; 8-11 January 2011

[V]

Modelling of unsteady airfoil aerodynamics for the prediction of stall induced vibrations

Witold Skrzypiński (wisk@risoe.dtu.dk)

Mac Gaunaa (macg@risoe.dtu.dk)

Niels Sørensen (nsqr@risoe.dtu.dk)

Frederik Zahle (frza@risoe.dtu.dk)

DTU Wind Energy

Abstract

In the present work, CFD simulations of the DU96-W-180 airfoil at 26 and 24 deg. angles of attack were performed. 2D RANS and 3D DES computations with non-moving and prescribed motion airfoil suspensions were carried out. The openings of the lift coefficient loops predicted by CFD were different than those predicted by engineering models. The average lift slope of the loops from the 3D CFD had opposite sign than the one from 2D CFD. Trying to model the 3D behaviour with the engineering models proved difficult. The disagreement between the 2D CFD, 3D CFD and the engineering models indicates that further investigations are needed and that caution should be taken when applying engineering models in connection with aeroelastic simulations. Nonetheless, the results of the 2D CFD, 3D CFD and the engineering models indicate that the associated aerodynamic damping may be higher than that predicted by state of the art aeroelastic codes.

1 Introduction

Deep stall vibrations during standstill may be divided into two groups: vortex induced vibrations and stall induced vibrations. In the former, a bluff body vibrates when the frequency of vortex shedding coincides with the frequency of any of the modes of this body. In the latter, a body vibrates if the change of the aerodynamic loading on this body during its displacement is such that it facilitates the displacement. The current work deals with stall induced vibrations exclusively. Stall induced vibrations are currently well recognised in the context of blade standstill vibrations [1]. This is mainly because such vibrations appear in the state of the art aeroelastic codes. Whether the aeroelastic codes accurately predict vibrations is problematic because the underlying aerodynamic models usually assume quasisteady aerodynamics in deep stall. This, in turn, is problematic for several other reasons. Assuming that the actual aerodynamic response is quasisteady, Gaunaa and Larsen [2] show that changes made in the underlying polars below the level of their accuracy can significantly change the prediction of the aeroelastic stability limits in deep stall. Further, the accuracy of the measurements may be compromised by possible occurrence of wind tunnel effects like tunnel blockage. Such effects are pronounced at high angles of attack and may cause experimental results to vary depending on the tunnel at which the measurements are taken. On the other hand, CFD computations may be laden with inaccuracies due to modelling limitations.

Moreover, Skrzypiński and Gaunaa [3] show that even a relatively low amount of temporal lag in the aerodynamic response of an airfoil model in deep stall may dramatically decrease the range of angles of attacks at which the aerodynamic damping of this model is negative. Under the assumption that the actual aerodynamic response of airfoils in deep stall is slower than quasi-steady, this indicates that present aeroelastic codes may over-predict deep stall standstill vibrations.

The focus of the current work was on determining the amount of temporal lag of an airfoil in deep stall. For this purpose, one specific angle of attack in 2D and another in 3D were chosen. The chosen angles were the ones related to the highest risk of stall induced vibrations. In order to find these angles, the equation for the aerodynamic damping proposed by Gaunaa and Larsen [2] is applied by Skrzypiński *et al.* [4] on the full polars of the DU96-W-180 airfoil designed at the Delft University of Technology [5]. The measurements of airfoil performance were carried out by Timmer [6] in the wind tunnel of the Delft University of Technology. Then, the same equation is applied by Skrzypiński *et al.* on the aerodynamic data obtained by 2D and 3D time-marching CFD simulations. The analysis indicates that 26 and 24 degrees angles of attack are where the 2D and 3D CFD models are the most prone to vibrations, respectively. The angles deviate because of a difference in steady airfoil characteristics. In the present work, the same airfoil was subjected to forced translatory edgewise oscillation which allowed for a thorough study of the involved physical phenomena. Computations were performed in 2D and 3D, at the aforementioned angles of attack. The tools used for the simulations were 2D RANS and 3D DES CFD solvers, i.e. EllipSys 2D/3D [7,8,9,10] codes developed at the Risø DTU National Laboratory for Sustainable Energy and Technical University of Denmark. The effective differences between the 2D and 3D simulations were investigated.

Flows in the stall regime are inherently three dimensional. It is therefore reasoned that it is necessary to compute these using computationally expensive 3D DES simulations. The reasoning behind including 2D simulations in the present work was to study whether relevant flow characteristics may be properly resolved by 2D RANS computations. This would be

beneficial because of their high computational efficiency compared to the much heavier 3D simulations.

Moreover, the possibility of analytically modelling the aerodynamic response with the tools previously proposed by Skrzypiński and Gaunaa [3] was studied.

Note that the present work performed in the context of blade standstill vibrations, simplifies the problem by omitting the effects of blade twist and taper as well as the shear and turbulence in the incoming flow. The reason for this is to learn about the most basic mechanisms involved in vibrations of wind turbine blades, before embarking on the full very complex problem as it occurs on actual turbines.

2 Tools and Methods

2.1 Description of the procedure

All the simulations were performed at the relatively high Reynolds number of $6 \cdot 10^6$. This was because the application of the present research is on large wind turbine blades potentially subject to high wind speeds.

In the present work, temporal lag of the aerodynamic response was quantified by means of the engineering aerodynamic model proposed by Skrzypiński and Gaunaa [3]. In the model, the parameters were adjusted to match the dynamic lift coefficient and dynamic drag coefficient loops obtained during the CFD simulations. Then, these parameters were considered representative of the respective CFD simulations.

Note that the angles of attack used in the present work were defined with respect to the flow velocity relative to the airfoil. The motion of the airfoil was therefore taken into account. The rotor induction was not considered.

2.2 2D and 3D Navier-Stokes solvers and computational setup

All the computations were unsteady, made both in 2D RANS and 3D DES. The turbulence model used was the *k-ω* shear stress transport (SST) [11]. It was used in both its standard RANS form and as a DES model as proposed by Strelets [12] with the delayed DES (DDES) technique of Menter and Kuntz [13]. The effects of laminar to turbulent transition in the boundary layer on the airfoil were modelled with the $\gamma - \widetilde{Re}_\theta$ correlation-based transition model of Menter [14]. For the present implementation, see Sørensen [15,16].

The airfoil motion was simulated by a moving mesh method. The grid points in the computational mesh were all moved together as a solid body. EllipSys2D and EllipSys3D are second order accurate in time. The codes use a second order backward differencing time discretization. Sub-iterations are used within each time step. In the present 2D and 3D computations, the diffusive terms were discretized with a second order central differencing scheme. The convective fluxes in 2D and 3D RANS regions were computed using the third order accurate QUICK scheme of Leonard [17]. The convective fluxes in 3D, where the DDES model switched to the large eddy simulation technique, were computed with a fourth order central differencing scheme.

The 2D computations were made in an O-grid with $32.8 \cdot 10^3$ grid cells. The height of the domain in both 2D and 3D was 30 chord lengths. The dimensions of the 2D grid were 256 cells (parallel to the airfoil surface) by 128 cells (perpendicular to the airfoil surface). The 3D computations were made in an O-grid with $12.6 \cdot 10^6$ grid cells. The mesh was extruded in the span-wise direction by a single chord length. The dimensions were 256 cells (parallel to the airfoil surface) by 384 cells (perpendicular to the airfoil surface) by 128 cells (spanwise direction). The grids for the 2D and 3D computations were made in HypGrid2D [10]. The grid around the profile used in the 2D computations is presented in Figure 1.

The angles of attack were 26 and 24 deg in 2D and 3D, respectively. The boundary condition on the 3D lateral boundaries was periodic. The aim of setting such a boundary condition was to limit the effect of finite span. The airfoil surface was specified by a no slip condition. Outlet condition was specified at angles +/- 45 deg. downstream the airfoil, in the perimeter of the O-grid. The rest of the perimeter was specified by the inlet condition.

The time steps were 0.005 and 0.01 seconds in 2D and 3D, respectively. The Reynolds number of all the computations was $6 \cdot 10^6$. The airfoil boundary layer was simulated assuming free transition with ambient flow turbulence intensity, I, of $1.1 \cdot 10^{-3}$%. This corresponded to the turbulent kinetic energy, k, of $1.5 \cdot 10^{-4}$ m^2/s and the specific dissipation, ω, of 10^6 s^{-1} at the inlet.

The lift and drag coefficients obtained from the 3D computations were averaged in the spanwise direction.

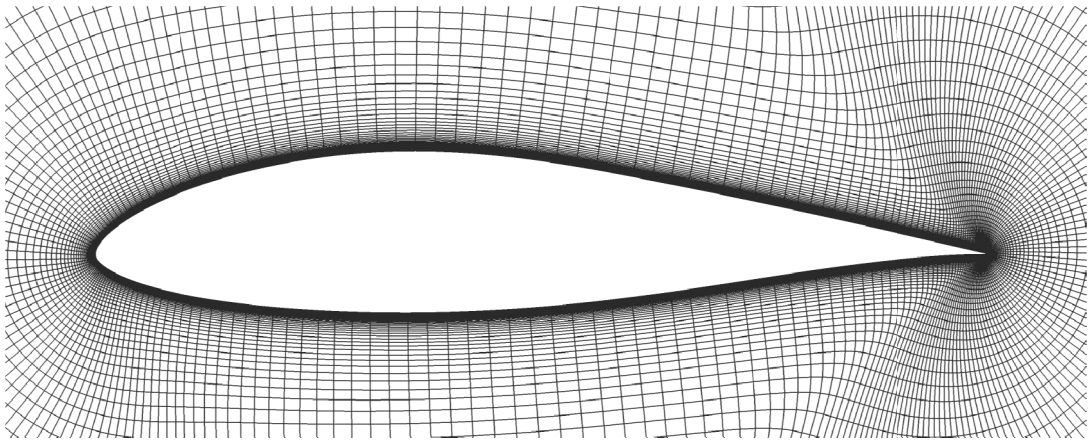

Figure 1: CFD grid around the DU96-W-180 airfoil, used in the 2D CFD computations

2.3 Description of the engineering model

In the engineering model proposed by Skrzypiński and Gaunaa [3], the dynamic lift coefficient is calculated as the static lift coefficient at the effective angle of attack. The original equation included four added mass terms, i.e. edgewise acceleration, flapwise acceleration, pitch rate and pitch acceleration terms. However, Skrzypinski and Gaunaa [3] show that only the pitch rate and flapwise acceleration terms have any influence on the stability limits while there was no motion in the flapwise direction or rotation in the present model. Therefore, all the added mass terms were excluded in the present application:

$$C_L^{Dyn} = C_L^{St}(\alpha_E) \quad (1)$$

The effective angle of attack (α_E) is the lagged angle of attack, defined as:

$$\alpha_E = \alpha_{3/4}(1 - A_1 - A_2) + x_1 + x_2 \quad (2)$$

where $\alpha_{3/4}$ is the angle of attack as observed at the three-quarter chord. In the present implementation, the angle of attack was constant along the chord because no rotation of the airfoil was present. The use of the effective angle of attack resembled that in the dynamic stall model described by Hansen et al. [18]. A_1 and A_2 constitute the first half of the parameters defined in the following description of the unit response function, ϕ, defined as:

$$\phi = 1 - A_1 e^{-b_1 s} - A_2 e^{-b_2 s} \quad (3)$$

where s is the dimensionless time, $\frac{V_0}{c} t$. Further, x_1 and x_2 are the aerodynamic state variables governed by the differential equations:

$$\dot{x}_i + \frac{2V_{rel}}{C} b_i x_i = b_i A_i \frac{2V_{rel}}{C} \alpha_{3/4}; \quad i = 1, 2 \quad (4)$$

where V_{rel} is the flow velocity relative to the airfoil, and b_i constitute the second half of the parameters defining the unit response function. The choice of four parameter values characterizes temporal behaviour of the aerodynamic model, represented by the unit response function.

The dynamic drag coefficient was calculated as:

$$C_D^{Dyn} = C_D^{St}(\alpha_E) + (\alpha - \alpha_E) C_L^{Dyn} \quad (5)$$

The first term is the steady drag coefficient defined with respect to α_E. This term ensures that the dynamic drag converges to the static value. The second term represents the induced drag which is a concept stemming from thin airfoil theory [19,20]. This term arises due to the change of the effective inflow direction due to the effect of shed vorticity. When the airfoil is in motion, the angle of attack is defined with respect to the relative flow velocity taking into account the motion.

3 Results

3.1 Time-marching 3D CFD computation of the non-moving DU96-W-180 airfoil

The complex nature of the flow field is shown in Figure 2 where the vorticity magnitude of the 3D flow over the non-moving DU96-W-180 at 24 deg angle of attack is presented. The flow was computed using a 3D DES. The figure represents a single section of the extruded profile. The dark areas represent high vorticity magnitude. Generally, separation of the boundary layer corresponds to high velocity gradient and therefore high vorticity magnitude. The latter is

visible in the figure. Separation of the boundary layer is visualized by the dark stream starting at the suction side approximately at one third of the chord length from the leading edge. The turbulent wake behind the profile is also visualized in the figure.

Figure 2: Vorticity magnitude of the 3D flow over the DU96-W-180 at 24 deg angle of attack; extruded from a single section of a 3D DES simulation

In order to provide background for the prescribed motion computations presented in the following chapter, Figure 3 presents polars of the DU96-W-180 airfoil computed in time-marching 2D RANS and 3D DES simulations. As it is seen in the figure, in the 3D computations the airfoil stalled faster than in the 2D. The values of the drag coefficient computed by the 2D and 3D simulations were relatively close.

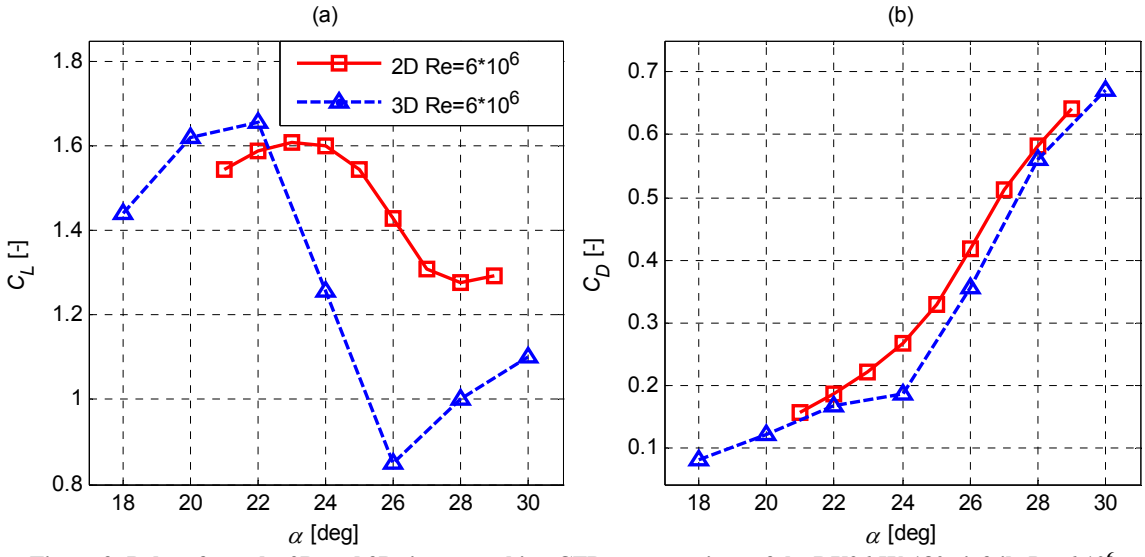

Figure 3: Polars from the 2D and 3D time-marching CFD computations of the DU96-W-180 airfoil; *Re*=6·10^6

3.2 Time-marching 2D CFD computation of the DU96-W-180 airfoil performing prescribed linear oscillation in the edgewise direction

The reduced frequency of the prescribed oscillations was k=0.079 (with $k=\omega C/2U$). The amplitude of the oscillation was $A=0.4C$. Figure 4 presents the following curves:

- Static lift coefficient resulting from the time-marching 2D CFD with the non-moving DU96-W-180
- Dynamic lift coefficient loop resulting from the prescribed motion 2D CFD
- Dynamic lift coefficient loop modelled to match the dynamic 2D CFD response based on the 2D CFD polars
- Dynamic lift coefficient loop modelled assuming inviscid response; based on the 2D CFD polars
- Dynamic lift coefficient loop modelled using Beddoes-Leishman type [21,22] dynamic stall model; based on the 2D CFD polars

The direction of the presented loops was clockwise. The results showed that the dynamic lift response resulting from prescribed motion 2D CFD was slower than the one modelled using the inviscid parameters for the temporal response. Neither the dynamic lift coefficient loop modelled using the Beddoes-Leishman type dynamic stall model resembled that of the prescribed motion CFD computations.

The approximate dynamic 2D CFD response was modelled by tuning values of two (A_1 and b_1) out of four available parameters in the aforementioned engineering model [3]. The other two were set to zero. However, the exact shape of the CFD response was impossible to obtain. The dynamic lift coefficient loop resulting from the prescribed motion 2D CFD was averaged over 20 periods of oscillation in order to decrease the influence of the higher frequency fluctuations associated with vortex shedding.

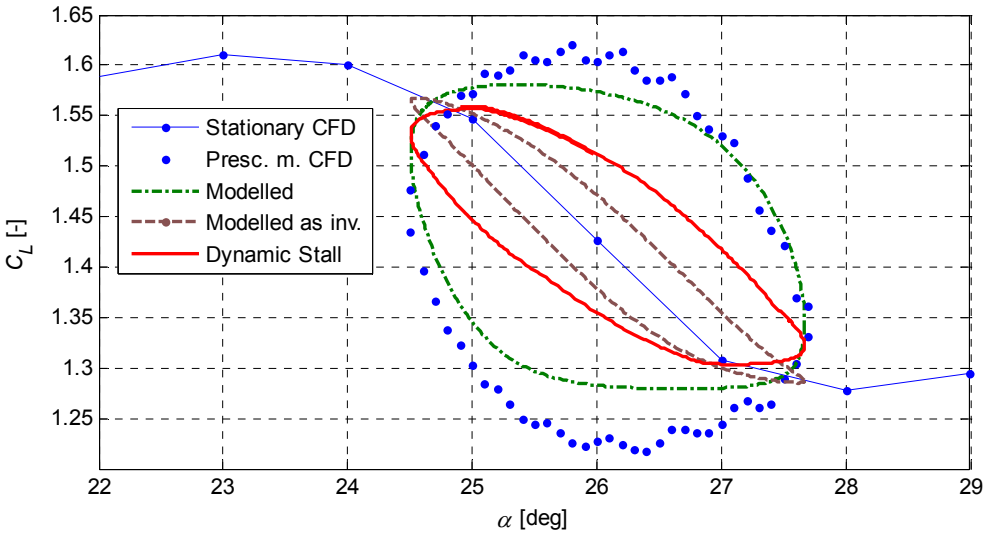

Figure 4: Lift coefficients from the 2D CFD with the non-moving DU96-W-180, 2D prescribed motion CFD and from two engineering models.

Figure 5 presents:

- Static drag coefficient resulting from the time-marching 2D CFD with the non-moving DU96-W-180
- Dynamic drag coefficient loop modelled using the same parameters as for modelling the dynamic 2D CFD response of C_L
- Dynamic drag coefficient loop modelled assuming inviscid response; based on the 2D CFD polars

- Dynamic drag coefficient loop resulting from the prescribed motion 2D CFD
- Dynamic drag coefficient loop modelled using Beddoes-Leishman type [21,22] dynamic stall model; based on the 2D CFD polars

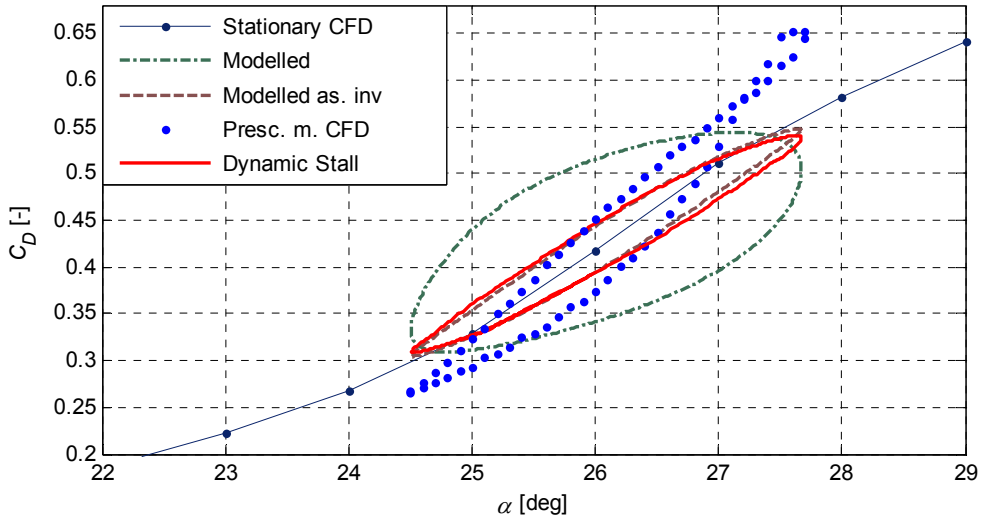

Figure 5: Drag coefficients from the 2D CFD with the non-moving DU96-W-180, 2D prescribed motion CFD and from two engineering models.

The direction of the presented loops was counter clockwise. The opening of the loop resulting from the prescribed motion 2D CFD simulation resembled that of the inviscid response and the one modelled using the Beddoes-Leishman model. However, the mean slope of the CFD loop was higher than of that representing inviscid response and the Beddoes-Leishman model.

From the results it was evident that it was not possible to model C_L and C_D simultaneously with the model from [3] as after tuning the parameters to match the prescribed motion CFD dynamic lift, the opening of the corresponding dynamic drag loop was larger than that of the prescribed motion CFD. On the other hand, Skrzypiński and Gaunaa [3] show that the aerodynamic damping is more sensitive with respect to the lift than drag. Therefore, it is possible that modelling the dynamic lift is sufficient in order to predict stall-induced vibrations.

3.3 Time-marching 3D CFD computation of the DU96-W-180 airfoil performing prescribed linear oscillation in the edgewise direction

Figure 6 presents:

- Static lift coefficient resulting from the time-marching 3D CFD with the non-moving DU96-W-180
- Dynamic lift coefficient loop resulting from the prescribed motion 3D CFD
- Dynamic lift coefficient loop modelled assuming inviscid response; based on the 3D CFD polars
- Dynamic lift coefficient loop modelled using Beddoes-Leishman type [21,22] dynamic stall model; based on the 3D CFD polars

The direction of the presented loops was clockwise. The results were surprising as the characteristic of the prescribed motion CFD dynamic lift loop was completely different from the corresponding 2D loop. The loop averaged over 30 oscillation periods had the opposite

slope, as if the static values were of positive instead of negative slope. Modelling the 3D CFD dynamic lift with the tools from [3] used in the present work or the Beddoes-Leishman model [21,22] was difficult and will require further investigation and possibly another approach. This is because these models are not developed to model loops with a slope of opposite sign to that of the steady values.

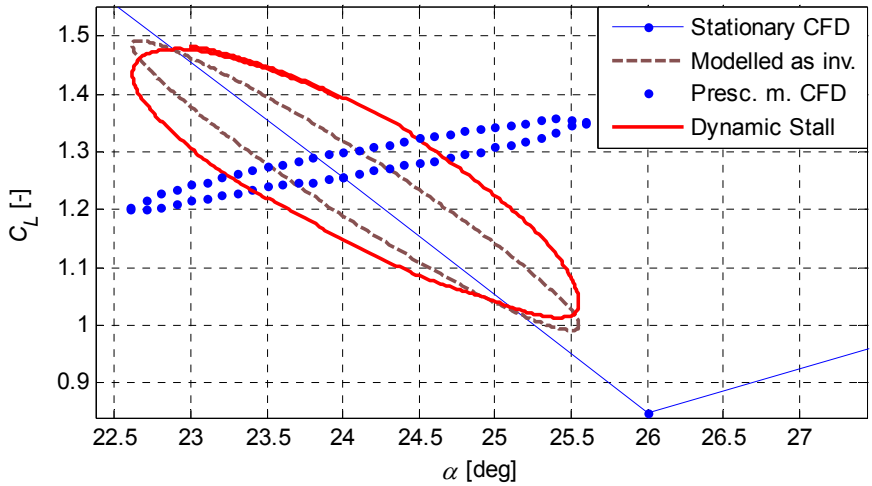

Figure 6: Lift coefficients from the 3D CFD with the non-moving DU96-W-180, 3D prescribed motion CFD and from two engineering models.

Figure 7 presents:

- Static drag coefficient resulting from the 3D CFD with the non-moving DU96-W-180
- Dynamic drag coefficient loop resulting from the prescribed motion 3D CFD
- Dynamic drag coefficient loop modelled assuming inviscid response; based on the 3D CFD polars
- Dynamic drag coefficient loop modelled using Beddoes-Leishman type [21,22] dynamic stall model; based on the 3D CFD polars

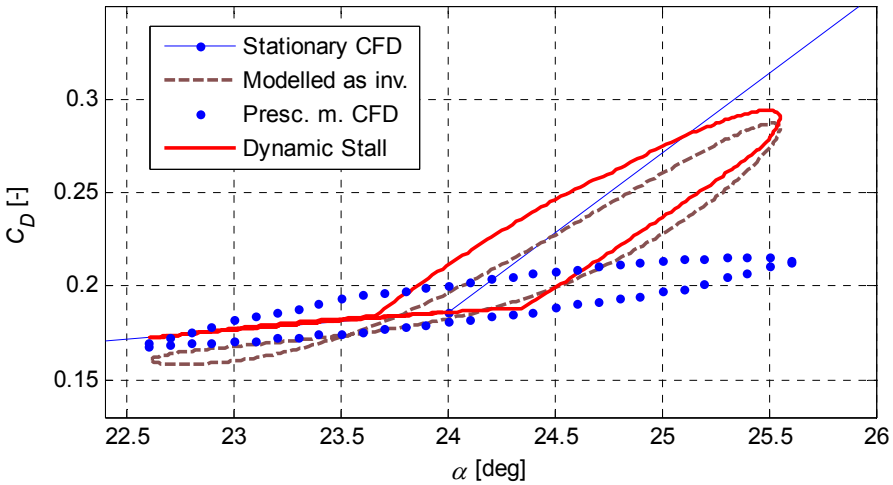

Figure 7: Drag coefficients from the 3D CFD with the non-moving DU96-W-180, 3D prescribed motion CFD and from two engineering models.

The direction of the presented loops was counter clockwise. The opening of the CFD loop was similar to that representing inviscid response. The opening of the loop obtained by the

Beddoes-Leishman model [21,22] was larger. The slope of the CFD loop did not follow the slope of the static drag coefficient while the slope of the loops representing the two models did.

Generally, both 2D and 3D simulations showed some temporal lag of the dynamic lift and dynamic drag coefficients indicating that the state of the art in modelling the dynamic lift and drag in deep stall in the aeroelastic codes may be inaccurate. Therefore, the present results indicate that the aeroelastic codes may to some degree overpredict edgewise vibrations as Skrzypiński and Gaunaa [3] show that temporal lag in the aerodynamic response of an airfoil model increases the level of aerodynamic damping. Further, Skrzypiński *et al*. [4] indicate that the positive slope of the lift loop of 3D computations may correspond to an increased aerodynamic damping compared to the negative slope of 2D computations. This is because in [4] a prescribed motion 3D CFD computation with similar behaviour to the one in the present work is shown to poses the positive aerodynamic damping while a corresponding prescribed motion 2D CFD computation is shown to poses the negative aerodynamic damping.

Further, it should be investigated whether 2D or 3D CFD simulations reflect the actual stall characteristics better as it was not explicitly shown in the present work that 3D simulations represent the real life flow conditions better than 2D. However, Shur *et al.* [23] and Strelets [24] indicate that 3D DES computations resolve stalled flows around airfoils better than 2D RANS.

It should also be investigated whether it is possible to tune the parameters of the Beddoes-Leishman [21,22] model to accurately represent the dynamic lift and drag loops obtained by CFD. The inability of the present model [3] to model the dynamic lift and drag using the same set of parameters indicates that the present engineering approach may be insufficient.

4 Conclusions

In the present work, CFD simulations of the DU96-W-180 airfoil at 26 and 24 deg. angle of attack, using 2D and 3D, non-moving and prescribed motion airfoil suspensions, were performed.

The openings of the lift coefficient loops predicted by 2D and 3D CFD were different than predicted by the engineering model [3] with constants based on inviscid attached flow or the Beddoes-Leishman type [21,22] engineering model.

The characteristics of the dynamic lift coefficient and dynamic drag coefficient loops were studied. The approximate average loop resulting from the 2D CFD simulation was modelled by the engineering model in [3].

The average slope of the dynamic lift loops from the 3D CFD simulation had opposite sign compared to the 2D CFD simulation. Trying to model the 3D behaviour with the engineering models proved difficult, indicating that the present engineering approach may be insufficient.

The opening of the average 2D CFD dynamic lift loop and the opposite slope of the average 3D CFD dynamic lift loop indicated that the associated aerodynamic damping may be higher than that predicted by state of the art aeroelastic codes.

The disagreement between the 2D, 3D and the engineering models indicates, first of all, that further investigations are needed and that caution should be taken when applying engineering models in connection with aeroelastic simulations.

5 Further work

Based on the current study and literature review a number of issues were identified that need to be investigated in future work. Below is the list of the most important of:

- Perform similar investigation at other angles of attack.
- Analyze the effect the change in the sign of the lift slope has on the aerodynamic damping.
- Investigate whether 2D or 3D CFD simulations reflect the actual stall characteristics better.
- Investigate the influence of ambient turbulence, skewed inflow and inflow varying along the blade span on the relevant aerodynamic characteristics.
- Investigate the influence of blade twist and taper on the relevant aerodynamic characteristics.
- Investigate whether it is possible to tune the parameters of the Beddoes-Leishman model to accurately represent the dynamic lift and drag loops obtained by CFD.

Acknowledgements

The authors would like to thank Nando Timmer for making the coordinates and aerodynamic characteristics of the DU96-W-180 airfoil used in this work available.

The dynamic lift and drag coefficients modelled with the Beddoes-Leishman type dynamic stall model [21,22] were delivered by Leonardo Bergami.

Computations were made possible by the use of the PC-cluster provided by Danish Center for Scientific Computing (DCSC) and the Risø-DTU central computing facility.

References

[1] Rasmussen, F.; Petersen, J.T.; Madsen, H.A.: *Dynamic Stall and Aerodynamic Damping*; J. Sol. Energy Eng.; Volume 121, Issue 3, 150 (6 pages) doi:10.1115/1.2888426; August 1999

[2] Gaunaa, M.; Larsen, T.J.: *Stilstandslaster*; chapter in *"Forskning i Aeroelasticitet"* 2002, ed. Christian Bak; Risø-R-1434(DA) in Danish, Risø DTU National Laboratory for Sustainable Energy; 2002

[3] Skrzypiński, W.; Gaunaa, M.: *Wind turbine blade vibration at standstill conditions – the effect of imposing lag on the aerodynamic response of an elastically mounted airfoil*; submitted for Wind Energy; 2011

[4] Skrzypiński, W.; Gaunaa, M.; Sørensen, N.N.; Zahle, F.; Heinz, J.: *Self-induced vibrations of a DU96-W-180 airfoil in stall*; submitted for Wind Energy; 2012

[5] Timmer, W.A.; van Rooij, R.P.J.O.M: *Summary of the Delft University wind turbine dedicated airfoils*; AIAA-2003-0352; 2003

[6] Timmer, W.A.: *Aerodynamic characteristics of wind turbine blade airfoils at high angles-of-attack;* Proceedings of TORQUE 2010 The science of making torque from wind; Heraklion, Crete, Greece; June 28-30, 2010

[7] Michelsen J.A.: *Basic3D – a platform for development of multiblock PDE solvers.* Report AFM 92-05, Dept. of Fluid Mechanics, Technical University of Denmark, DTU, Denmark; 1992

[8] Michelsen J.A.: *Block structured multigrid solution of 2D and 3D elliptic PDE's.* Report AFM 94-06, Dept. of Fluid Mechanics, Technical University of Denmark, DTU, Denmark; 1994

[9] Sørensen N.N.: *General purpose flow solver applied to flow over hills.* PHD Dissertation, Risø-R-827(EN), Risø National Laboratory, Roskilde, Denmark; 1995

[10] Sørensen N.N.: *HypGrid a 2-D Mesh Generator;* Risø-R-1035(EN) (1998) 36 p.; Risø National Laboratory, Roskilde, Denmark; 1998

[11] Menter F.R.: *Zonal two equation k-omega turbulence models for aerodynamic flows*; AIAA Paper 932906, American Institute of Aeronautics and Astronautics; 1993

[12] Strelets M.: *Detached eddy simulation of massively separated flows*; AIAA Paper 2001-0879, Russian Scientific Center 'Applied Chemistry'; St. Petersburg; 2001

[13] Menter F.R., Kuntz M.: *Adaptation of eddy-viscosity turbulence models to unsteady separated flow behind vehicles*; In The Aerodynamics of Heavy Vehicles: Trucks, Buses, and Trains (volume 19 of Lecture Notes in Applied and Computational Mechanics). Springer: Berlin; 339–352; 2004

[14] Menter F.R., Langtry R. B., Likki S. R., Suzen Y. B., Huang P. G., Völker S.: *A correlation-based transition model using local variables - Part I: model formulation*. In Proceedings of ASME Turbo Expo 2004, Power for Land, Sea, and Air; Vienna, Austria; ASME GT2004-53452; 14–17 June 2004

[15] Sørensen N.N.: *CFD modelling of laminar-turbulent transition for airfoils and rotors using the* $\gamma - \widetilde{Re}_\theta$ *mode*; Wind Energy 2009; 12: 715–733; 2009

[16] Sørensen N.N.; Schreck, S.: *Computation of the National Renewable Energy Laboratory Phase-VI rotor in pitch motion during standstill*; Wind Energy; DOI: 10.1002/we.480; 2011

[17] Leonard B.P.: *A stable and accurate convective modelling procedure based on quadratic upstream interpolation*; Computer Methods in Applied Mechanics Engineering 1979; 19: 59–98; 1979

[18] Hansen, M.; Gaunaa, M., Madsen; H.Aa.: *Beddoes-Leishman type dynamic stall model in state-space and indicial formulations*; Risø-R-1354(EN); 40 p.; 2004

[19] Theodorsen, T.: *General theory of aerodynamic instability and the mechanism of flutter;* National Advisory Committee for Aeronautics; Report No. 496; 1949

[20] Øye, S.: *Instationære, aerodynamiske kræfter på todimensionalt vingeprofil*; Afdelingen for Fluid Mekanik, Den Polytekniske Læreanstalt Lyngby, Nov. 1981

[21] Leishman, J.G.; Beddoes, T.S.: *A semi empirical model for dynamic stall;* Journal of the American Helicopter Society 34, 3 (1989); DOI:10.4050/JAHS.34.3 (15 pages); 1989

[22] Hansen, M.; Gaunaa, M.; Madsen, H.Aa.: *Beddoes-Leishman type dynamic stall model in state-space and indicial formulations*; Risø-R-1354(EN); 40 p.; 2004

[23] Shur, M.; Spalart P.R.; Strelets, M.; Travin, A.: *Detached-eddy simulation of an airfoil at high angle of attack*; Engineering Turbulence Modelling and Experiments – 4; Elsevier Science Ltd.; 1999

[24] Strelets, M.: *Detached Eddy Simulation of Massively Separated Flows*; AIAA 2001-0879; 39th AIAA Aerospace Sciences Meeting and Exhibit January; Reno, NV; 8-11 January 2011